UNIVERSITY OF LEICESTER

Mobile laser scanning in forests: Mapping beneath the canopy

Thesis submitted for the degree of

Doctor of Philosophy

at the University of Leicester

by

Thomas L. Potter, BSc (Hons) MSc

Centre for Landscape and Climate Research
School of Geography, Geology and Environment

Supervised by:
Professor Heiko Balzter
Professor Kevin Tansey
Professor Nicholas Veck MBE

2019

Abstract

Mobile laser scanning in forests: mapping beneath the canopy

Thomas L. Potter

Laser scanning is a modern technique used in forest mapping and monitoring. Airborne laser scanning (ALS) has been extensively used in medium-resolution, wide-area mapping. Terrestrial laser scanning (TLS), which delivers high-resolution data, has increasingly been used to map precise forest structural detail in discrete forest plots. Handheld mobile laser scanning (HMLS), a medium-to-high-resolution technique, sits between ALS and TLS methods and was first assessed in forestry in 2015. This thesis builds on existing research in evaluating the utility of HMLS sensors in forest mapping.

GeoSLAM ZEB-1 and ZEB-REVO HMLS sensors were deployed in a variety of UK forests and woodlands. Study sites were chosen to reflect a mixture of forest type, tree density, height, structural complexity and topographic variety. Scans were acquired alongside reference measurements and TLS scans. Experiments were devised to assess relative performance of HMLS sensors in the measurement of DBH, height, stem position, crown extent and volume with novel analyses performed in *3D Forest* and *CloudCompare*.

Results indicated DBH could be measured to accuracies of 0.016-0.026 m RMSE, agreeing with existing research. HMLS tree position compared with TLS was subject to 0.1-0.3 m error but superior to manual techniques. HMLS sensors could not resolve tree height or crown structure due to limited range, identified as 10-12 m from sensor. A combination of HMLS and ALS data fusion yielded more accurate results determining height, crown extent and crown volume. These findings indicate that HMLS are suitable for sub-canopy forest mapping. HMLS sensors with increased range are becoming widely available in tandem with increasingly lightweight portable mobile laser scanning (MLS) solutions attached to UAV platforms. This research contends that HMLS will play a major role in multi-sensor integrated forest mapping and is ideal in supporting remote and proximal airborne mapping by providing a rich and accurate ‘ground-up’ dataset.

Acknowledgments

I would like to thank my supervisors, Professor Balzter and Professor Kevin Tansey, for their excellent support, guidance, encouragement and constructive criticism throughout. *Thank you*. I also thank Dr Nicholas Tate and Professor Ross Hill for putting me through my paces in a tough but fair viva voce in the run up to Christmas 2018.

I am immensely grateful for the support offered by Veebha Dandikar and Charlotte Langley. Both were always 'on call' to help with excellent advice, effective delegation and in picking-up the pieces when the admin became overwhelming. I would also like to thank Adam, Bill, Gemma and Simon for their technical expertise. I certainly made the most of the facilities and couldn't have done my PhD without the excellent technical and admin teams at the University of Leicester. Outside the University, I am also indebted to Dr Sally Gadsdon at Epping Forest and Ian Bromley at the Forestry Commission.

My research was funded by the Central England NERC Training Alliance (CENTA). Many thanks to all affiliated with CENTA for the numerous opportunities to carry out my research, explore industrial collaborations and to network. My PhD experience was further supported by the Satellite Applications Catapult, where I worked alongside some passionate and inspirational earth observation experts. Many thanks to all of you – Dan in particular.

I owe a special gratitude to GeoSLAM Limited for enthusiastic advice, technical support and inspiration in the field of mobile laser scanning. GeoSLAM very generously loaned me a ZEB-REVO scanner on numerous occasions, and what great kit it proved to be.

I'm forever grateful to have shared my PhD journey with first-class friends, colleagues and tireless field assistants. Among them: Alex C, Ana Maria, Bashir, Chloe, Ciaran, David Ackerley, Helen, Isah, James, Jono, Marc, Mariano, Maryam, Matt, Pedro, Polyanna, Sarah, Sara, Sherri, Syrena, Tom Codd, Thomas Wong Hearing, Valentin and many others over the years. Wherever our paths cross, I'll buy you a beer. I owe Dr Ackerley in particular a crate of beers for his patient field assistance over the years – an absolute LiDAR superstar. Cheers!

Mum, Dad, Jake, Meg and Denise – you've put up with me through thick and thin. Thank you. I can only imagine the limitless fun you had watching me ride the creaky, tired rollercoaster that was my PhD adventure… I told you all I wanted a challenge and heck, I certainly found one! Cheers for supporting me in your numerous ways. Late-night pep talks, inspirational trips into Mallorquin countryside and philosophical debates in a variety of very fast cars among them. Love you all.

Were it not for the limitless, unremitting, patient and forgiving love of my partner Lowri, I doubt I'd be here today. Let alone adding the final touches to a PhD thesis. Which, for four years, I never thought I'd complete. All while battling to finish her own PhD at the very same time. I can't thank you enough, Lowri. Diolch yn fawr, cariad. Caru chdi.

Dedication

I dedicate this thesis to the memory of Jean Margaret Potter (1939 – 2016), a bottomless well of strength and inspiration both in life and death. ‘Nanny’ Jean fought adversity in all its forms her entire life. She taught me to persevere, even in the absence of hope.

Table of contents

List of tables

List of figures

List of abbreviations

AGB	Aboveground biomass
AGC	Aboveground carbon
ALS	Airborne laser scanning (not to be confused with 'airborne LiDAR')
ALOS-2	Advanced Land Observation Satellite (Japan)
ALOS-PALSAR	As above, plus 'Phased Array L-band synthetic aperture radar"
AOI	Area of interest (e.g. the subset of a point cloud used for analyses)
BIOMASS	Forthcoming (2021)m P-band SAR satellite mission
CORSAIR	COSMO-SkyMed Radar Science and Innovation Research programme
CSF	Cloth simulation function (algorithm)
DBH	Diameter at breast height (c.f. tree diameter 1.33 m above ground)
DTM	Digital terrain model
ESA	European Space Agency
FOSS	Free and open-source software
GEDI	Global Ecosystem Dynamics Investigation lidar (USA)
GLAS	Geoscience laser altimeter system (USA)
GNSS	Global Navigation Satellite System (generic)
GPS	Global Positioning System (USA)
GSV	Growing stock volume
HMLS	Handheld mobile laser scanner (-ing)
ICESat	Ice, Cloud, and land Elevation Satellite (USA)
IMU	Inertial measurement unit
JAXA	Japanese Space Agency
LCS	Local coordinate system
LiDAR	Light detection and ranging
LSR	Least squares regression (algorithm)
M3C2	Multiscale Model to Model Cloud Comparison
MIMICS	Michigan microwave scattering model
NASA	National Aeronautics and Space Administration (USA)
OHM	Outer hull model
QSM	Quantitative structure model
MLS	Mobile (vehicle-mounted) laser scanner
RADAR	Radio detection and ranging
RHT	Randomized Hough transform (algorithm)
RMSE	Root mean square error
RQ	Research question
RTK	Real-time kinematic (i.e. GPS correction, boosting accuracy)
SAR	Synthetic aperture radar
SfM	Structure from motion
SLAM	Simultaneous localization and mapping
SRTM	Shuttle radar topography mission
TLS	Terrestrial laser scanning (can also refer to 'terrestrial LiDAR')
UAV	Unmanned aerial vehicle (also known as 'sUAS' and 'drone')
UAV-LiDAR	LiDAR acquired from remotely piloted unmanned aerial vehicles
USB	Universal serial bus (port)

1. Introduction

There are in excess of two hundred and fifty definitions of ‘forest’ in the scientific literature. These range from binary ‘forest/non-forest’ classifications to complicated, fuzzy-set ecotone maps. Perhaps the most logical is that offered by Whittow (1984; In: Grainger, 2010) who described a forest as "a continuous tract of trees". Baccini et al. (2012), similarly, defined forests as areas of "live woody vegetation". However, there are circumstances where land can be classified as forest in the complete absence of trees (FAO, 2000).

Forests cover over thirty per cent of the terrestrial environment, contribute to thirty-three per cent of net terrestrial productivity (Chen et al., 2015) and play a vital role in carbon budget globally (Carvalhais et al., 2014; Ahmed et al., 2015; Mitchard, 2018). Forty-six per cent of Earth's forests lie in both the humid and dry tropics between the Tropic of Cancer and Tropic of Capricorn (Grainger, 2010) whilst in Great Britain, woodland coverage exceeds 3 170 000 Ha – some 13% of all land area (Forest Research, 2018). With improved understanding of the carbon cycle (Herold et al., 2011; Mitchard, 2018) and with increasing concern in the potential impacts of anthropogenic climate change (Carvalhais et al., 2014; Mitchard, 2018, forests have become a significant and very widely-discussed topic of scientific research (Baccini et al., 2012; Hansen et al., 2013; Mitchard, 2018).

Forest mapping is well-represented in the scientific literature with decades of scientific research documenting approaches which have made use of satellite (Kaasalainen et al., 2015), airborne (Lefsky et al., 2002; Mascaro et al., 2014; Adão et al., 2017) and terrestrial sensors in the microwave, optical and thermal domains. With the advent of programmes such as NASA’s Landsat and the recent ESA Sentinel constellation, the state-of-the-art focusses on deriving new information from established archives and the relatively-recent phenomenon of high temporal – as well as spatial – resolution between complementary sensors. In recent years, the advent of affordable LiDAR (light detection and ranging)

sensors has led to unparalleled detail and accuracy measuring forest structure from the air and the ground.

Forests are of critical importance, both in terms of ecology and the global economy (de Sassi et al., 2015). Aboveground forest biomass – the amount of woody vegetation stored in forests globally – is an Essential Climate Variable under the framework of global efforts to account for the fluxes within the carbon cycle (Sileshi, 2014; Li et al., 2015; Sinha et al., 2015). This variable is directly related to the volume of carbon currently stored in forests worldwide and thus it is imperative that we accurately and reliably understand and monitor carbon stocks as a huge piece of the climate change puzzle (Harris et al., 2012; Sileshi, 2014).

Aboveground biomass has become more and more widely reported within ecological science in recent years, especially in studies which have allied forest ecology with remote sensing (Sileshi, 2014; Li et al., 2015). Key to this increase in scientific attention is the advent of multiple-scale LiDAR (Sinha et al., 2015) and the rapid development of RADAR analysis leading to all-weather, wide-area forest mapping capability (Le Toan et al., 2011; Woodhouse et al., 2012; Joshi et al., 2017). In the past five to ten years, high-profile studies by research groups at NASA (Saatchi et al., 2012; 2014) and other institutions have endeavoured to map aboveground biomass globally, regionally and locally using various combinations of remotely-sensed and ground-based datasets (Saatchi et al., 2007; Cartus et al., 2012; Baccini et al., 2012; Avitabile et al., 2012; Englund et al., 2017; Rodriguez-Veiga et al., 2016; 2017).

However, while there is a growing body of scientific publications reporting aboveground biomass magnitudes around the world (Grace et al., 2014), there is an increasingly complicated picture of disagreement and widely-divergent estimates (Mitchard et al., 2014; Saatchi et al., 2014; Schimel et al., 2014; Sileshi, 2014; Avitabile et al., 2016; Rodriguez-Veiga et al., 2016; 2017). Numerous studies exist employing all manner of statistical, machine-learning and allometric modelling approaches to attempt to quantify biomass at the forest level, but comparatively few give much attention to ground-based validation (Clark and Kellner, 2012; Saatchi et al., 2012) and it can prove troublesome

making an informed decision as to which biomass map might be most-appropriate (Englund et al., 2017). Indeed, it is rare to find studies which even agree on the definition of 'forest'. Given this lack of consensus at almost every level, it seems folly to claim biomass maps are accurate or precise (Woodhouse et al., 2012).

Aboveground biomass is, to all intense and purposes, a measure of density. It attributes a variety of mass measurements or estimates – specifically, the variable of wood specific gravity – to an estimate of volume, usually at the individual tree level (Chave et al., 2014). These figures often derive from statistical models (Woodhouse et al., 2012), themselves based on highly selective sub-sampled ground data aggregated at the database level of a number of decades (Mitchard et al, 2014; Saatchi et al., 2014). Even assuming the samples used in allometric models are unbiased and entirely representative, the ground data collected within inventory plots and fed into these models is in itself biased and unrepresentative (Clark and Kellner, 2012; Sileshi, 2014; Sagang et al., 2018).

There is a need to increase consistency of sampling, analysis and reporting of forest structure and biomass magnitude at tree, forest plot, forest stand, regional and global levels (Le Toan et al., 2011; Schimel et al., 2014). Key to this could be an approach that leverages a new generation of mobile mapping systems – handheld mobile laser scanners (HMLS) – to rapidly and accurately map areas of forest (Ryding et al., 2015; Talbot, 2017; Bienert et al., 2018; Liang et al., 2018; Pierzchala et al., 2018). It was hypothesised that by focussing solely on accurate measurement of forest structure and hence volume, biomass estimates could be refined (Liang et al., 2016; Paynter et al., 2016; Oveland et al., 2018). It was further proposed that the volume of all physical entities within a forest plot should be measured. Ratios of the constituent parts of a given forest biome could then be developed. Combined, this information could be of use in the calibration and validation of remotely sensed data products (Putman et al., 2018; Shendryk et al., 2018; Stovall et al., 2018; Wilkes et al., 2018) such as COSMO-SkyMed, Sentinel-1 and ALOS-2 radar and Landsat 8, Sentinel-2 and other optical satellite sensors.

The research presented in this thesis sought to determine how well HMLS systems work beneath the forest canopy. It assessed how they compared with 'traditional' forest inventory methods as well as measurements derived from tried-and-tested, tripod-

mounted TLS systems. Novel two- and three-dimensional analyses were performed in cutting edge, open source software (*3D Forest v0.42*: Kruček, 2017; Trochta et al., 2017; *CloudCompare v2.9.1*: CloudCompare, 2018) and basic sensor fusion was explored, addressing technical limitations identified in current-generation HMLS sensors. Based on the results of this research, the most likely role HMLS technologies could play in forest mapping was proposed. Broadly, as part of an integrated forest inventory approach.

1.1 Research aims and objectives

The primary aim of this research was to explore the real-world performance of HMLS sensors in mapping areas of forest – specifically from the ground toward the crown. In recent years, there has been a swift rise in the number of research projects exploring airborne and then terrestrial LiDAR as a tool to measure and model forest structure. Yet in the four or five years in which HMLS sensors have been available, fewer than ten projects have critically assessed them in comparison with other forest mapping techniques. The primary objective of this thesis was to assess the accuracy and error of HMLS tree mensuration in comparison with TLS and forest inventory approaches.

A secondary aim was to identify the factors that most influenced point density and distribution in point clouds acquired with HMLS instruments. In terrestrial laser scanning, maximum point density per scan decreases in a linear manner with distance and as a function of beam angle. In airborne LiDAR data, point density is a function of aircraft velocity, altitude and sensor frequency. At the time of writing, no studies had sought to characterise point distribution in HMLS data. As point density and distribution are key parameters influencing the biophysical parameters that can be extracted from a point cloud, an opportunity was identified to develop a 'best practice' field protocol. Therefore the second objective of this research was to devise a protocol to collect an optimal density and distribution of point data in a time-efficient, consistent and repeatable way.

Within this research, a final aim was to assess the extent to which 'sensor fusion' might address shortcomings identified when deploying HMLS sensors beneath the forest canopy. It became apparent that sensor range was the principle limitation. Whilst the manufacturer advertised a range of 20 to 30 m, in reality this fluctuated between 10 and 15 m. Accordingly, HMLS data were acquired in areas where ALS data was also available and a process of data 'fusion' – alignment, vertical adjustment and merging of multi sensor point clouds – was designed. Biophysical parameters extracted from these datasets were compared with reference parameters extracted from coincident, reference TLS data. Therefore, the final objective of this thesis was to determine what tree and forest variables could be measured with a combination of HMLS and airborne datasets.

1.2 Research questions

Three research questions were posed:

RQ1: What forest inventory variables can be measured with HMLS sensors? What is the magnitude of error inherent in these measurements when compared with a reference, TLS-derived dataset?

RQ2: How does HMLS sensor range and proximity to a target influence point density and distribution? Is it possible to increase point density in areas of marginal sensor range by increasing scan repetition alone?

RQ3: To what extent can a fusion of HMLS and ALS data address limitations in the range of HMLS sensors? What 2D and 3D forest inventory measurements can be extracted from a fused dataset and how do they compare to TLS-derived measurements?

1.3 Thesis structure and organisation

1.3.1 Thesis structure

This thesis begins with a chapter dedicated to the comprehensive review of the scientific literature (***Chapter 2***, from page 21) undertaken throughout the research process. It is followed by a detailed chapter describing the methods (generic and bespoke) and materials (datasets and derived variables) used in the research (***Chapter 3***, starting on page 44).

Three standalone research chapters then follow, with each reporting on analyses designed to answer a specific research question (***Chapter 4***, from page 101; ***Chapter 5***, from page 148; and ***Chapter 6***, from page 178).

Chapter 7 (page 200 to 235) comprises a comprehensive discussion of all results, both in terms of specific research questions and in the context of the broader research aim. This chapter synthesises the full body of research presented here, highlights major findings and proposes areas of future research.

A conclusion (***Chapter 8***) follows, then a full bibliography (***Chapter 9*** from pages 240 to 265).

Finally, an Appendix presents three tables of results not featured in ***Chapters 4*** to ***6*** directly.

2. Literature review

2.1 Introduction

In this chapter, the body of scientific literature encompassing various aspects of forest remote sensing is reviewed and the state-of-the-art in three-dimensional forest mapping explored. As of April 2019, many hundreds of papers can be found which have explored themes as diverse as forest biology (Chave et al., 2014), ecology (Shugart et al., 2010), health (Mitchard, 2018), history (Herold et al., 2011) and extent (Saatchi et al., 2012). Of these, many employed multiple remote sensing techniques to detect (Shimada et al., 2015), measure and characterise (Hall et al., 2011; Ahmed et al., 2015) forests.

In the course of delving into the body of knowledge for this literature review, a particular focus was placed on studies which used LiDAR or RADAR (often both) to measure structural forest parameters (Lucas et al., 2005; Cartus et al., 2012; Kaasalainen et al., 2015; Ferraz et al., 2016). The majority of these leveraged airborne laser scanning (ALS) to derive forest metrics at continental, regional (Bolton et al., 2011; Wulder et al., 2011; Hansen et al., 2014), forest (Shendryk et al., 2018) and stand level. Such metrics were typically upscaled or extrapolated over larger areas of forest – either alone or in tandem with coarser-resolution data from satellite optical and radar platforms.

From the mid-2000s (Hopkinson et al., 2004; Bienert et al., 2006; Danson et al., 2007), the emergence of terrestrial laser scanning (TLS) became apparent (Calders et al., 2015) with an ever-increasing volume of studies using this technology year-on-year. Increasingly, the focus of these studies has honed-in on the precision and data density afforded by survey-grade LiDAR technology to glean new insights into forest structure and processes. This, and the advent of handheld mobile LiDAR systems, appeared to represent the 'leading edge' in what remains a very fast-paced area of active and international research (Liang et al., 2016; Liang et al., 2018). Over the following pages, ever-evolving sensor technologies

and their application in forestry are described in depth. Gaps in knowledge are identified, and research questions proposed and justified.

2.2 Forest structural parameters

Forest structure is best-detected with laser-based instruments (i.e. LiDAR) which offer dense, accurate and precise measurements of forest structure in three dimensions. **Table 1.1** (page 24) introduces key forest parameters measured directly or derived from a combination of LiDAR data, allometric models and third-party inventory data. Of the variables described in **Table 1.1**, aboveground biomass is most commonly cited as it is an Essential Climate Variable (Grainger, 2010; Hall et al., 2011) and a major parameter in the carbon cycle (Le Toan et al., 2011). In the terrestrial carbon cycle, forests are the dominant dynamic (Ahmed et al., 2015) with standing aboveground biomass (AGB) a major parameter (Chave et al., 2005; Le Toan et al., 2011; Baccini et al., 2012; Chen et al., 2015; Kaasalainen et al., 2015).

Aboveground carbon (AGC) comprises roughly 50 per cent of estimated standing AGB in a given forest (Grainger, 2010; Hall et al., 2011). Forests, in turn, store 46 to 50 per cent of the AGC associated with terrestrial vegetation (Grainger, 2010; Chen et al., 2015) - a total estimated at 228.7 Pg carbon (Baccini et al., 2012). AGB can be measured through destructive sampling, or estimated with non-destructive sampling (Brown et al., 1989; Calders et al., 2014; Stovall et al., 2018). For destructive sampling, entire trees are felled and their constituent parts (steam, branches, leaves, roots) weighed pre- and post-heating at pre-defined temperatures (Calders et al., 2015a; 2015b) which determines wet and dry mass. Another form of destructive sampling requires extraction of small cores from tree stems (Brown et al., 1989; Chave et al., 2006). The resultant cylinder of wood is also weighed in wet and dry form. In both destructive and non-destructive sampling, tree parameters such as diameter at breast height (DBH), tree height and tree species are identified. These parameters are then input into allometric equations, usually on a per-species or otherwise on a forest-type basis, to estimate aboveground live biomass and

aboveground carbon density based on established multiple regressions (Chave et al., 2014).

Brown et al. (1989) introduced a general model for calculation of AGB with required parameters including tree height, DBH, wood density and Holdridge life zone (Holdridge, 1967) derived from a series of regressions established with data from over 5 000 trees collected from 43 plots. More recently, pantropical allometric models have been established and species wood density and biomass databases created (Chave et al., 2003; 2004; 2006; 2014). These have all been very widely cited throughout the literature, although studies do not always reach consensus regarding the parameters required for in situ sampling (Mitchard et al., 2014; Saatchi et al., 2014).

Many sub-canopy variables (DBH, basal area, stem density, growing stock volume, etc) are vital to forest applications such as biomass mapping, carbon accounting and understanding fuel balance in context of forest fires (Garcia et al., 2017). These variables are typically inferred from coarser datasets (e.g. airborne LiDAR; ALS; satellite data) or measured with high-precision TLS instruments. As such, there seem to be two 'extremes' represented in the literature: wide-area mapping at the expense of spatial resolution and absolute precision, and highly-precise but extremely-localised 3D mapping and modelling. Studies tend to map entire forests and forest stands - at an aggregate level - at one extreme. On the other extreme, research seems to focus on estimation of individual tree volume with highly precise data and sophisticated algorithms. There seems to be a clear 'gap', which this thesis aims to help populate.

Table 1.1: Summary of tree and forest parameters that can be measured with remote sensing

Parameter	Brief definition
A. Direct structural measurements	
Canopy cover	Essentially the vertical distribution of the forest canopy within a profile from treetop to ground. Calculated by Bolton et al. (2013) as the ratio of first returns above 2 m to the total number of first returns for a given bin size.
Canopy height	Probably the most commonly cited metric. To calculate canopy height, first and last returns are gridded to create DSM and DTM layers respectively. A raster calculation is performed subtracting DTM heights from the DSM. The resultant grid represents the top of the forest canopy.
Canopy profile	A vertical profile through the canopy indicating the distribution of tree stems, branches and foliage relative to the ground.
Crown radius	The horizontal measurement of an individual tree crown, determined by measuring the radius of the crown circumference. In a gridded discrete-return dataset, this might require segmentation to determine which bins/raster cells relate to a particular tree.
Canopy volume	Derived from canopy profile information. This can be estimated through calculations based on the relationship between canopy profile area and field-based volume measurements, as established in multiple field studies.
Leaf area index	The ratio between leaf cover and gaps in leaf cover for a given bin, plot or hemispherical photographic image. A strong correspondence between LiDAR and hemispherical image estimates was demonstrated by Morsdorf et al. (2006). This is particularly useful in estimating the penetration of natural light within a forest canopy, e.g.: in determining photosynthesis and primary productivity.
Tree height	A simple measurement of the highest point(s) per tree, obviously in some part dependent on the ability to discriminate between individual trees. Tree height statistics calculated in forestry-related studies include mean, SD, percentile heights and relative frequency of points at predefined height intervals (Lu et al., 2014). Knowing tree height and species type, a forester can estimate timber volume.
B. Parameters derived through further computation	
Basal area	This can be estimated through analysis of tree height and various allometric relationships (see: Wulder et al., 2007).
DBH	Diameter at breast height is usually measured with a tape measure around a tree trunk 1.37 m above the ground. With the use of field plots, this can be estimated from ALS through reference to tree height and other biophysical parameters.
Stand complexity	Inferred from point height variation (Bolton et al., 2013), this is in essence a measurement of the variability in return heights within the canopy – the 'topography' of the uppermost forest canopy surface. However, the literature recommends caution here as complexity is difficult to define in the field.
Texture	By considering the texture – or rugosity, i.e.: the complexity and shape - of the upper canopy surface, it is possible to better-estimate the volume of a given forest stand with ground classification.
AGB	Forest canopy height and density are correlated with AGB (Hansen et al., 2015). Numerous studies recommend use of 3D datasets over two-dimensional, field-based measurement in broader-scale AGB estimates, focussing on vertical and horizontal canopy structure (Lu et al., 2014).
AGC	AGC density is roughly 50% that of AGB, so estimated with a simple calculation.

2.3 Measuring forest structure with remote sensing

Forest structure and aboveground biomass are routinely modelled with LiDAR and estimated with LiDAR parameters. Structure and AGB are often estimated from SAR backscatter intensity, too, albeit indirectly (Woodhouse et al., 2012). Backscatter intensity is in part determined by interactions of a radar pulse with components of trees (leaves, branches and stems) within a given footprint (Ulaby et al., 1988; Balzter, 2001; Balzter et al., 2003; Shugart et al., 2010) and is sensitive to scattering mechanisms outside interactions the with parts of a tree. Other important parameters include radar wavelength, signal polarisation, forest type, dielectric properties of tree components, soil roughness and soil moisture (Dobson et al., 1992; Le Toan et al., 1992; Balzter, 2001; Balzter et al., 2013; Shugart et al., 2010).

Unlike LiDAR, which requires acquisition of data in strips analogous to the flightpath or orbit pattern of an air or spacecraft, SAR 'looks' cover vast areas (Kellndorfer et al., 2014) tens of km in dimension in periods no more than a few minutes per scene. This means SAR data offers a 'snapshot' of the state of all forested regions in a given scene at a known moment in time. LiDAR mosaics, whilst more precise, are generally a composite of data acquired on multiple dates – in some cases, dates covering periods of several years. Furthermore, with satellites such as Sentinel-1 operated by ESA (European Space Agency) and ALOS-PALSAR/ALOS-2 operated by JAXA (Japanese Space Agency) currently orbiting Earth, regular global coverage is made available (Kaasalainen et al., 2015).

Fusion of SAR and LiDAR data is likely to be of greatest relevance and utility (Lucas et al., 2005; Kellndorfer et al., 2010) in cases where field inventory data is patchy or non-existent and climatic conditions preclude regular optical imagery (Tsui et al., 2013). However, estimates can vary significantly to the order of several hundred $Mg.ha^{-1}$ (Mitchard et al., 2014) depending on upscaling and extrapolation methods employed. Disney et al. (2006) developed one of the first three-dimensional structural models for modelling optical reflectance and microwave backscatter, in a study with yielded significant potential for modelling even needle-level SAR interaction. Several studies have

sought to characterise forest structure with SAR (Cartus et al., 2012; Englhart et al., 2012; Kellndorfer et al., 2014; Mermoz et al., 2015; Garcia et al., 2018; Santoro et al., 2018; Shendryk et al., 2018). In a comprehensive review paper, Kaasalainen et al. (2015) compared sixteen individual studies which combined LiDAR and synthetic aperture radar sensors to estimate AGB. They noted that synergy between LiDAR (ground elevation) and large area SAR-derived biomass estimates looked particularly promising. Knowing precisely how much – and where - biomass is stored should enable pixel-level precision in biomass maps where upscaling and extrapolation is applied. This synergy is given further credence by Mitchard et al. (2014, p. 942) who controversially claimed "wood density cannot be detected from space", advocating use of regional algorithms for regional-scale studies. This was refuted by Saatchi et al. (2014), stating inappropriate use of field plot data which they alleged showed signs of sample bias. More recently, studies have examined the synergistic use of LiDAR and high-resolution SAR to model forest structure and contribute to calibration-validation activities (Qi et al., 2019).

For optimal results, wide-area SAR mapping should be combined with a comprehensive series of regular ALS campaigns (Mascaro et al., 2014) or a carefully distributed, statistically robust network of TLS ground-truth plots. Garcia et al. (2015) employed both ALS and TLS techniques to appraise canopy clumping and assess the quantity of light penetrating the forest canopy, determining that the relatively low point density of ALS data precluded the use of certain analyses otherwise used with TLS data. It was contended that the use of discrete multiple-return or full-waveform ALS could compensate for relative deficiencies in point density (Garcia et al., 2015). It was also suggested that TLS is superior to ALS when estimating AGB density as forest variables derived from lower sections of the canopy were shown to explain a greater portion of AGB density than those derived from canopy height measurement (Hansen et al., 2015).

Airborne laser scanning (ALS) is an active, laser-based sensing platform fitted to an aerial platform. These platforms are typically affixed to light fixed-wing or rotary aircraft and, in recent years, to small unmanned aerial vehicles (UAVs, sUAS or 'drones'). Such systems scan a full swath perpendicular to the aircraft's flight path multiple times per second and are typically closely coupled with an inertial measurement unit (IMU) combining

gyroscope, accelerometer and compass to measure pitch, yaw and roll. Further combined with real time kinematic (RTK) GNSS systems, the result is a three-dimensional point cloud dataset fully corrected for aircraft motion and accurately georeferenced to accuracies exceeding 0.01 m (Brede et al., 2017; Pierzchala et al., 2018). Whilst metrics such as tree height can be inconsistent and vary with forest type and structure (Disney et al., 2010; Simpson et al., 2017), data density and processing play an important role (Khorrami et al., 2018; Ørka et al., 2018). ALS systems typically fall into one of two common categories: full-waveform and discrete-return. Full-waveform systems emit a laser pulse and record the entire return signal to memory. Discrete-return systems differ in that several peaks in the pulse – usually four – are automatically digitised on-board (Heinzel and Koch, 2011). Full-waveform systems acquire the larger dataset of the two but at the expense of data utility (Reitberger et al., 2009). Discrete-return LiDAR data are more transferable and require much less memory but offer less structural insight as a compromise (Heinzel and Koch, 2011).

Several major studies have used full-waveform ALS data to characterise tree and canopy structure (Wulder et al., 2007; 2009; Reitberger et al., 2009; Heinzel and Koch, 2011; Hansen et al., 2014) and characterise and estimate aboveground biomass (Yao et al., 2012; Cao et al., 2014; Latifi et al., 2015). Discrete-return ALS systems have been similarly used in studies exploring forest canopy structure (Ferraz et al., 2012; Bolton et al., 2013; Görgens et al., 2015; Fisher et al., 2015; Palace et al., 2015), tree detection and classification (Dalponte et al., 2014; Saremi et al., 2014; Garcia et al., 2015; Gorgens et al., 2015) and estimation of aboveground biomass (Ene et al., 2012; Asner et al, 2014; Sheridan, 2014; Hansen et al., 2015; Palace et al., 2015; Takagi et al., 2015). In particular, a comprehensive study by Ioki et al. (2014) and similar studies by Asner & Mascaro (2014) and Asner et al. (2018) utilised ALS to characterise AGB in different forest types undergoing differing processes of forest degradation in northern Borneo. ALS systems have also been used to determine tree species (Brandtberg, 2007; Mascaro et al., 2014a; 2014b) and characterise the effects of wildfires on forested environments (Wulder et al., 2009; Garcia et al., 2017).

2.4 Estimating AGB with Earth observation techniques

The first high-resolution pantropical map of aboveground biomass was published by Saatchi et al. (2011) in a seminal paper much-discussed in subsequent literature. Utilising IceSAT/GLAS footprints converted to Lorey's Height, local-scale information on biomass magnitude and maps of forest stratification, biomass density was estimated at a resolution of 1 km using the maximum entropy algorithm. Three-parameter allometric equations were used to estimate aboveground biomass as a function of tree height, basal area and generalised wood density for in excess of 4 000 individual plots, each at least 0.1 ha in area (Saatchi et al., 2011).

In another broadly similar and widely cited study, Baccini et al. (2012) used the Random Forest algorithm proposed by Breiman (2001) to classify a variety of optical and radar-derived raster images, determine aboveground biomass density and output a wall-to-wall aboveground biomass map. In a similar vein, Cartus et al. (2014) also employed a maximum entropy algorithm to detect and quantify aboveground biomass and generate wall-to-wall biomass density and estimate uncertainty maps for Mexico. Tsui et al. (2013) combined C- and L-band SAR with discrete multiple-return LiDAR transects and a variety of co-kriging, regression kriging and regression co-kriging approaches to characterise AGB on the regional to national scale.

In recent years, several major pantropical forest carbon maps derived from remotely-sensed data fused with field inventory plots and upscaled through statistical techniques have been published at national, regional and global scales (Baccini et al., 2011; Harris et al., 2012; Saatchi et al., 2012; Cartus et al., 2014; Solberg et al., 2014; Avitabile et al., 2016; Rodriguez-Veiga et al., 2017). Yet despite the undoubted value of these maps to science, there remains significant and at times robust disagreement in their interpretation - and use - of field plot data and the subsequent estimates of aboveground carbon densities (Mitchard et al., 2014; Saatchi et al., 2014) derived thereafter. More recently, de Sassi et al. (2015) noted the substantial utility in such pan-tropical maps but

emphasised the apparent disconnect between large-scale maps and finer-scale, plot-level inventory data.

2.5 Terrestrial LiDAR in forestry

Terrestrial laser scanning (TLS) in forests can trace its roots back to the mid-2000s (Hopkinson et al., 2004; Bienert et al., 2006; Danson et al., 2007). One of the earliest studies to use TLS in tree measurement was Hosoi and Omasa (2006) who modelled trees using voxel cells to calculate leaf area density. Tansey et al. (2009) explored the utility of TLS in estimating various structural tree and stand parameters including DBH, basal area and tree density. Reporting high degrees of accuracy, they also cautioned that in dense forest stands, TLS was unable to accurately determine tree height due to occlusion. A further limitation in the use of TLS is in the discrimination between tree saplings, shrubs and herbaceous vegetation - all broadly similar in detected structure within unfiltered, dense point clouds (Brolly et al., 2013). A potential solution might be in operating the TLS in 'leaf off' conditions, although this would preclude species identification and subsequent classification (Brolly et al., 2013; Calders at al., 2015). This leaf-off approach was supported by Lu et al. (2014) who adopted a bottom-up approach in the segmentation of individual trees within a stand of deciduous tree species.

2.5.1 Estimating tree diameter at breast height

DBH was derived from TLS data in numerous studies including Tansey et al. (2009), Pueschel et al., (2013), Aijazi et al. (2017), Blakey et al. (2017), Koreň et al. (2017), Muir et al. (2018), who reported R^2 of 0.77, Bienert et al. (2018), Cabo et al. (2018a; 2018b) who quantified RMSE between 0.8 and 1.3 cm, Liang et al. (2018), Liu et al. (2018) and Oveland et al. (2018). The accuracy of estimated DBH often varied as a function of the chosen algorithm (Koreň et al., 2017; Liu et al., 2018; Cabo et al., 2018a; 2018b), software (Liang et al., 2018) and user-specified parameters. Evidently TLS offers a step change in accuracy compared to traditional, tape measured field inventory but results are only as good as the survey methodology and algorithm selection. Liang et al. (2018) further suggested that TLS sensors were the optimal hardware for forest scanning – superior to mobile sensors.

2.5.2 Estimating tree volume

There is an increasing need to understand both the two – and three – dimensional structure of global forests. This is particularly the case in quantifying ecosystem dynamics including aboveground biomass, the carbon cycle and the potential impacts of climate change (Shugart et al., 2010; Wilkes et al., 2017; Asner et al., 2018; Calders et al., 2017; Coomes et al., 2018; Stovall et al., 2018). Chief among structural variables is tree volume. In one of the first tree volume-centred studies, Bienert et al. (2010) successfully demonstrated the separation of individual trees in a TLS-derived voxel space model through the application of eigensystems, with substantially higher rates of success in coniferous stands than broadleaf stands.

Another early approach was to fit a polyline to each branch and use this to generate a sequential series of cylinders fitted to point cloud extent perpendicular to polyline orientation (Tansey et al., 2009; Dassot et al., 2012). An advantage of this approach was that it mitigated the effects of occlusion. Dassot et al. (2012) found that gaps between points did not necessarily limit the effectiveness of cylinder-fitting; TLS-derived estimates of solid wood volume of 42 trees fell within a range of +/- 10% compared with destructive samples. The concept was further-developed by Raumonen et al. (2013) who devised a scan-to-3D-model workflow ideally suited to precise estimation of tree volume. Calders et al. (2014b) used TLS to scan 65 trees within open Eucalypt forest. The same trees were then measured with traditional inventory techniques before destructively sampling to determine AGB density. Individual tree data was extracted from co-registered point clouds and parameters including tree volume, tree height and DBH were calculated through computation of quantitative structural models (QSM). In comparison with the reference AGB densities, TLS-derived analyses overestimated AGB by 98%; allometric equations derived from DBH and tree height, in contrast, underestimated AGB by up to 36.57% (Calders et al., 2014b).

Feliciano et al. (2014) assessed AGB in mangrove forests and reported strong results further advocating the use of TLS as a non-destructive means of estimating biomass. Kunz et al. (2017) performed similar work, estimating the volume of 24 young trees using both

a cylinder-fitting and voxel space approach. Estimates were compared with physical samples where volume was measured through water displacement. They found the voxel-based approach most accurate (R^2 = 0.98) with cylinder-fitting techniques achieving R^2 of 0.90 and 0.92.

However, not all laser scans are equal and approaches such as QSM can falter. Issues commonly encountered include tree detection and segmentation in highly heterogeneous stands as well as occlusion (shadowing) in dense forest. Whilst multiple studies demonstrated strong performance in automating the detection of trees in TLS-derived datasets, few have established a robust protocol for the detection of smaller, younger trees (Brolly et al., 2013). Hess et al. (2015) explored the effect of occlusion on TLS-derived, voxel-based small tree models and found volume estimates were very similar. However, they noted that in natural forests comprised of larger trees, occlusion may present a greater source of error in volume estimation. Errors in TLS-derived volume estimation also tend to be species-specific (Kunz et al., 2017). That said, error can be highly marginal. TLS sensors are sensitive to crenulations in tree bark; Cabo et al. (2018b) reported error of 0.001 to 0.004 m compared to reference, caliper-derived measurements attributed to presence of bark.

2.5.3 Estimating aboveground biomass with TLS

There is a pressing need to reduce uncertainty in our understanding of the role forests play in the carbon cycle (Wilkes et al., 2018). Using allometric models – transfer functions relating structural measurements such as DBH, tree height and crown dimension to individual tree biomass – researchers have been able to estimate AGB magnitude in multiple forest types around the world (Shugart et al., 2010; Calders et al., 2014a; 2014b). Quantitative structure models have increased in popularity in recent years and are a robust method for estimating tree and stem volume (Paynter et al., 2016; Kunz et al., 2017; Bienert et al., 2018; Stovall et al., 2018; Wilkes et al., 2018). Combined with accurate wood density information, they offer the most promising means of estimating aboveground biomass (Calders et al., 2016; Wilkes et al., 2018). Several recent studies have leveraged TLS data and software like *Computree* (Raumonen et al., 2013;

Hackenberg et al., 2015; Calders et al., 2015; 2016; Sheppard et al., 2017; Stovall et al., 2017; 2018; Putman et al., 2018; Wilkes et al., 2018) to build quantitative structure models. A leading study was published by Stovall et al. (2018) in which AGB for 329 trees, with DBH as large as 1.23 m, was estimated in a demonstration of non-destructive AGB estimation using TLS and QSM. The authors discovered that TLS-derived AGB estimates had lower RMSE and higher magnitude than those derived from national allometry. Stovall et al. (2018) also determined that modelling tree stems is especially appropriate in reducing uncertainty at larger scales (e.g. landscape).

Wilkes et al. (2018) applied a similar approach, in tandem with ALS data, to urban trees in London. Biomass magnitude comparable to that of both temperate and tropical forests was reported. However, the authors also noted uncertainties associated with wood density data. Stovall and Shugert (2018), in turn, proposed that TLS-derived allometry could substitute the need to conduct TLS campaigns locally when calibrating and validating forthcoming SAR and LiDAR missions. Huerta-García et al. (2018) reported the first study exploring the utility of HMLS in estimating tree biomass, with an R^2 of 0.945 suggesting high accuracy compared with field data-derived estimates.

Stovall et al. (2017) proposed a novel approach to biomass estimation in coniferous forest through an 'Outer Hull Model (OHM)'. OHM was applied to tree stems whilst a voxel model was used to estimate the volume of branches and foliage. This approach is computationally similar to the crown volume tool in *3D Forest* (Krůček et al., 2016; Trochta et al., 2017) in that both created convex hull mesh structures. Whole-tree biomass estimates were very accurate in comparison with destructive sampling (R^2 = 0.98, RMSE = 20.4 kg) (Stovall et al., 2017), suggesting a powerful new approach to AGB estimation in pine forests. The state-of-the-art in TLS-based forest surveying lies in novel applications benefitting from very-high-resolution 3D forest data over wider areas than typical forest plots (Calders et al., 2018; Wilkes et al., 2018). These studies clearly demonstrate the potential for TLS technology to significantly improve AGB estimates in comparison with well-documented field protocols, offering substantial time and cost savings.

2.5.4 Further applications of TLS in forest research

Airborne laser scanning is not consistent in its ability to penetrate forest canopies to detect canopy strata or understorey vegetation. TLS offers a considerable advantage in that it can detect multiple layers with minimal bias. Some studies have computed vegetation profiles (Ashcroft et al., 2014). These profiles may yield further insight into forest biomass, forest classification, canopy closure and may even facilitate improved radiative transfer modelling (Avitabile et al., 2016; Calders et al., 2018). Tree volume estimates are prone to the effect of tree complexity (Hess et al., 2015) and the effect of vegetation in 'leaf on' conditions can further complicate this (Calders et al., 2018). Vegetation profiles may therefore simplify otherwise-complex forest structure into metrics more suited to coarser-resolution sensors such as spaceborne SAR.

TLS is now a mature technology widely utilised within forest research (particularly in mapping tree and forest structure and forest topography) for almost decade. More recently, TLS has 'revolutionized' the field of forest ecology. Blakey et al. (2017) explored the utility of TLS data in modelling forest traits to better-understand relationships between forest structure and bat communities. Following broadly similar lines of investigation, Eichhorn et al. (2017) revealed a 68% reduction in density of understorey vegetation in woodlands with high populations of deer. Combined, these studies show the potential for TLS to be used as tool to capture rich, 3D habitat structure and derive an array of metrics suited to numerous ecological applications beyond forest structure in itself. The pace of development is rapid and novelty in the field includes ever-improving sensor range, sensor accuracy and even dual-wavelength hyperspectral (Danson et al., 2018) capabilities.

Another promising strand of research is a movement towards lightweight, highly portable TLS sensors such as the Compact Biomass LiDAR (CBL) (Paynter et al., 2016), BLK360 (Leica Geosystems, 2017), RTC360 (Leica Geosystems, 2018) and BLK2GO. These sensors are designed to be rapidly deployed with minimal set-up and to capture a high volume of data efficiently. For example, by facilitating a higher density of scan set-ups than conventional TLS instruments. Another major bottleneck of TLS-based forest observation

is slow data capture, which can be accelerated through use of mobile platforms (Liang et al., 2018).

2.5.5 Limitations of TLS in forested areas

TLS techniques do have shortcomings which may limit their use. The biggest hurdle in terms of continuous coverage is occlusion (shadowing) as the laser pulse clearly cannot pass through solid objects. Geometrically, occlusion is influence by proximity to vegetation (i.e. a tree stem) and vegetation extent. The larger an object, the greater the proportion of scan (percentage of up to 360 degrees about the scanner) in which shadows are cast. In areas of forest with a high density or magnitude of obstruction, then a higher density of scan is required to maintain coverage. This ultimately means more time and resource is required to scan a given area.

Another limitation of TLS is that sensor range, specifically given that point density – in an unhindered, occlusion-free set-up - decreases in a linear manner with distance from scanner. As the TLS instrument is static, point density is a function of beam angle separation. The further from a scanner, the greater the distance between beams. Additionally, range noise increases with distance. The density of scanner set-ups once again has a direct effect on maximum point density. Whilst this can be mitigated to some extent with very high-detail scan configurations, all scanners are limited by the quality of their hardware, and higher detail requires longer scan times.

2.6 Mobile laser scanning in forestry

2.6.1 Vehicle-based platforms

Further efficiencies in forest structural mapping have been achieved through use of 'mobile' laser scanners mounted to ground vehicles (e.g. cars, vans, quad bikes) and unmanned aerial vehicles (UAV, sUAS, RPAS or 'drones') in recent years. Several studies have been published in which LiDAR sensors mounted to vehicles such as quad bikes and 4x4 all-terrain vehicles were deployed in forested environments (Kukko et al., 2017;

Bienert et al., 2018). One of the first studies to use mobile laser scanning to capture forest structural information over wide areas was Liang et al. (2014). Forsman et al. (2016) used the two-dimensional SICK LMS 511 line laser scanner to estimate tree DBH. Bienert et al. (2018) combined TLS and MLS to develop forest inventory data. They found that MLS data is comparable to TLS data and both could be similarly processed to derive DBH, tree height and tree position. However, MLS data was not suitable for derivation of QSM models. Herrero-Huerta et al. (2018) also deployed vehicle-mounted MLS LiDAR to map trees and develop semi-automated parameter extraction, albeit in an urban context. DBH estimation compared with in situ reference data had strong correlation (R^2 = 0.92, further confirming the suitability of MLS in forestry.

In recent years, LiDAR systems integrated with UAV platforms have been used to survey forested areas (Carbomap, 2017; Brede et al., 2017). Unmanned, robotic ground vehicles have also been used in forests. Pierzchala et al. (2018) combined a Velodyne VLP-16 laser scanner, an IMU, GNSS and graph-based SLAM processing to create 3D forest point clouds and derive tree parameters. Where DBH was estimated, RMSE was 2.38 cm (9%) and mean error for tree position 0.048 m (Pierzchala et al., 2018). Forsman et al. (2018) noted that MLS methods often led to DBH overestimation as a function of diameter bias.

2.6.2 Portable mobile laser scanning

Portable laser scanners are those operated by a single surveyor, typically worn as a backpack, such as the Leica-manufactured *Pegasus: Backpack* or 3D Laser Mapping (2018) *ROBIN*. Others, such as the GeoSLAM ZEB-1 and ZEB-REVO, are hand-held (Bosse et al., 2012; Ryding et al., 2015; Bauwens et al., 2016; Díaz-Vilariño et al., 2017; Lehtola et al., 2017; Nocerino et al., 2017; Oveland et al., 2017; Cabo et al., 2018a; Huerta-García et al., 2018; Oveland et al., 2018; Tucci et al., 2018). Many portable laser scanners use SLAM (simultaneous localization and mapping) – originally developed in the robotics field – to fuse LiDAR data with IMU inputs (pitch, roll, yaw, acceleration). SLAM is used to (1) locate a sensor within a field site and (2) to augment semi-automatic or automatic data processing.

Ryding et al. (2015) published one of the first studies to explore use of a SLAM-based HMLS (GeoSLAM ZEB-1) in forest survey. In comparison with reference TLS data, RMSE of DBH was 0.0015 m and tree position was 0.0021 m. They also found data capture to be two orders of magnitude faster than TLS (50 m^2/min vs 0.85 m^2/min) (Ryding et al., 2015). Huerta-García et al. (2018) also assessed ZEB-1 performance in urban deciduous forest in Mexico, reporting similar accuracies in mapping DBH and tree height. The ZEB-1 was also assessed by Oveland et al. (2018) alongside TLS and backpack sensing platforms; in this study, DBH RMSE was 0.031 m. Both ZEB-1 and ZEB-REVO scanners struggled to detect small trees with DBH less than 3 cm (Ryding et al., 2015; Bauwens et al., 2016; Oveland et al., 2018). However, this may be limited by the acquisition techniques employed (Liang et al., 2018).

A similar but manufacturer-independent SLAM-based approach was applied by Forsman et al. (2016) to estimate DBH of trees in five separate field sites, albeit with a 2D, line-based laser scanner from manufacturer SICK. A similar, graph-based SLAM approach was applied to MLS data from various sensors by the Finnish Geospatial Institute (FGI). This included all-terrain vehicle-mounted data captured within boreal forest (Kukko et al., 2017). In similar research, Oveland et al. (2017) devised a custom, backpack-based mobile LiDAR system and reported high-accuracy DBH and stem position estimates compared with reference TLS data. A limitation of SLAM-based sensing platforms, especially those that lack GNSS integration, is that spatial errors can propagate and in forestry, multiple copies of each stem may appear in the data (Kukko et al., 2017). These effects were minimised where forest complexity and heterogeneity increased. Conversely, TLS sensors struggle in areas of denser vegetation (Ashcroft et al., 2014). An advantage of HMLS is that they offer a theoretically-infinite number of scan ‘positions’. Dynamic, mobile platforms such as HMLS thus offer the opportunity to successfully-detect the forest floor in all but the most-impenetrable vegetation. With filtering algorithms such as the novel Cloth Simulation filter (CSF; Zhang et al., 2016), mobile LiDAR data has been shown to be especially well-suited to this task (Cai et al., 2018).

In recent months, innovation in the survey industry has seen the development of improved portable LiDAR technology which could further boost efficiency and accuracy

when measuring forest. Both Leica Geosystems and 3D Laser Mapping offer wearable, backpack-based hardware ('Pegasus Backpack' and 'ROBIN' respectively) featuring greater range and sub-cm precision. Similarly, UAV-based LiDAR systems are emerging and are increasingly deployed over forested areas (citations). These sensors are yet to be fully-assessed in scientific research with one study – Brede et al. (2017) – the only one to leverage this type of mobile LiDAR within forest. At the time of writing, GeoSLAM had just announced the ZEB-HORIZON system, designed for handheld and UAV operations alike.

Meanwhile, there has been a recent emergence of non-commercial sensors and auxiliary hardware, with sensor development and forest applications of this technology gaining increasing traction in the literature (Kukko et al., 2017; Cabo et al., 2018a; Campos et al., 2018; Herrero-Huerta et al., 2018; Liang et al., 2018; Oveland et al., 2018; Pierzchala et al., 2018). Common to all of these systems is fusion of LiDAR data with GNSS position and IMU orientation information. Through this fusion, not only can points be precisely positioned relative to other points, but scans be accurately located in real-world coordinate systems. The near future thus offers substantial potential.

HMLS systems offer an immediate and accessible route to improved ground validation of remote sensing products. This ranges from the high- (e.g. "mapping trees") to low-level (e.g. "quantifying stem volume of Corsican pines in a steep-sloped hillside stand") applications. At one end of the spectrum, HMLS provide a means to rapidly determine the number of trees – and approximate volume of vegetation – underlying a Landsat 8 or Sentinel-2 pixel. At the other end, there is great potential for HMLS to contribute 3D information to physics-based calibration and validation datasets. Such research could build on similar work by Calders et al. (2018) who demonstrated the first application of a high-detail TLS dataset in radiative transfer modelling.

2.6.3 Field testing of multiple mobile mapping platforms

Lehtola et al. (2017) conducted a detailed analysis of 'rival' mobile laser scanning systems, including the commercially available Leica *Pegasus: Backpack* and GeoSLAM *ZEB-1* solutions, alongside three further commercial and tree research-facing sensor platforms.

The sensors were deployed in three separate field sites and tasked with mapping the same features, then compared with a reference TLS (Leica Geosystems P40) dataset. The ZEB-1 performed well, recording the second-highest radial accuracy and 0.02 m standard error where flat ground surfaces were recorded (Lehtola et al., 2017).

A further, comprehensive side-by-side assessment of mobile mapping platforms was conducted by Tucci et al. (2018) who established both indoor and outdoor field tests. Using a variety of 2D (cross-sections), 2.5D (cloud-to-mesh distance) and 3D (Multiscale Model to Model Cloud Comparison, or 'M3C2') data analyses, they compared wearable (Leica Pegasus) and handheld mobile (Kaarta Stencil; GeoSLAM ZEB-REVO) LiDAR data against a reference TLS dataset. The authors concluded that at best, any assessments regarding accuracy or precision were qualitative. They noted the ZEB-REVO showed least sign of 'double surface' reconstruction, but that the other sensors offered higher point density. Of the three sensors, only the Leica Pegasus stores LiDAR intensity values within the point cloud, potentially adding extra contextual value to derived data.

Other research has explored the utility of both the Microsoft Kinect and Google Tango devices to capture DBH and stem taper. Of these, the Kinect proved reasonably capable of estimating DBH (RMSE: 0.019 m) from a sample of 121 trees but the Tango yielded superior results (RMSE: 0.0073 m; bias: 0.003 m) (Hyyppä et al., 2018). Campos et al. (2018) developed an ultra-portable, ultra-low-cost backpack-mounted 'omnidirectional' camera, integrated with navigation sensors, and used it to map forested areas. Estimating DBH, they quoted centimetric (3.5 to 7 cm) accuracy but a maximum useful range of 5 m. Given that such devices (i.e. Kinect, Tango and omnidirectional cameras) are substantially less expensive than TLS sensors and also cheaper than HMLS technologies, they may be of increasing interest in forestry.

2.7 Research gaps and aims

TLS systems have been used to map forests for over a decade, but it is only in recent months that optimised protocols (Calders et al., 2018; Wilkes et al., 2018) and international benchmarking studies (Liang et al., 2018) have been conducted. As of September 2018, very little work had been undertaken in the field of terrestrial vehicle-based (Wu et al., 2013; Bienert et al., 2018), UAV-LiDAR (Brede et al., 2017), wearable (Kukko et al., 2017; Pierzchala et al., 2018) or handheld (Ryding et al., 2015; Bauwens et al., 2016; Aijazi et al., 2017; Huerta-Garcia et al., 2017; Cabo et al., 2018a; Oveland et al., 2018) mobile laser scanning in forests. Of these, very few explored sensor performance outside the confines of one or two formal field plots to explore the influence of methodology on data quality - or applications beyond basic tree mensuration. It therefore seems prudent to examine the potential of HMLS in the context of precision forestry along similar lines to these studies. Furthermore, there is a need to propose ways in which mobile laser scanning might augment calibration and validation of forest remote sensing products.

The GeoSLAM ZEB-1 and ZEB-REVO sensors were designed for the 3D mapping of complex, heterogeneous, indoor environments. In particular, the type of environments where local conditions limit use of line-of-sight-reliant, fixed-centre, reflective targets - and where accurate GNSS coverage was not available. HMLS sensors like these collect data continuously while the surveyor moves freely across a site, acquiring spatial data from almost every conceivable angle all-but-eradicating the risk of occlusion. Taking these design features at face value, it is reasonable to assume such sensors are perfect for forest survey, especially as the durability of the hardware itself means it is resistant to the typical forest environmental threats (moisture, humidity, particulate matter and abundance of rigid-and-sharp obstructions.

2.7.1 Gaps in the literature

Shugart et al. (2010, p. 13) identified a need for simultaneous capture of active and passive remotely sensed data and “well developed ground data”. In the years since, the

need to capture validation data with satellite data remains pressing. Dassot et al (2012) defined a need to develop time-efficient, semi-automatic algorithms to derive forest-relevant parameters from TLS data and ensure applicability of such approaches in the forestry industry. Most of the studies in the literature draw from esoteric programming libraries while few utilise bespoke software packages. A clear research gap existed in identifying intuitive, accessible and open-source packages which could work alongside one another in a series of coherent workflows.

Muir et al. (2018) recommended future research in the field of terrestrial LiDAR forest mapping should consider developing improved classification methods. Specifically, methods which can separate trees, shrubs and other forest components from one another. Stovall et al. (2018) noted that allometric models based on a sample size <100 trees can be prone to error and risk being biased where large trees are under-represented. There were few studies boasting such substantial sample sizes. This suggested a clear role for HMLS sensors in expanding the scope of ground-based LiDAR scans from typical TLS plots to a much broader spatial extent. To achieve this, absolute accuracy would be sacrificed in favour of spatial coverage. At the time of writing, nobody had yet quantified accuracy of HMLS-derived DBH in multiple plots of differing dimensions.

Ryding et al. (2015) identified that HMLS point cloud resolution – specifically those acquired using ZEB-1 scanners – might preclude feature extraction and recommended further examination in future work. While some studies performed a basic HMLS 'field test' in forests (Ryding et al., 2015; Bauwens et al., 2016; Cabo et al., 2018a; Oveland et al., 2018) none were as comprehensive as leading, non-forest-related field tests such as Lehtola et al. (2017), Nocerino et al. (2017) or Tucci et al. (2018). A clear research gap therefore existed to perform in-depth field tests of HMLS performance when mapping (i) individual trees and (ii) forested areas.

HMLS has been mentioned several times in the literature but it does not yet look to have been fully exploited. There are several known limitations of HMLS (range; noise) but almost no discussion on optimising the use of these sensors. In terms of SLAM

positioning, there was some uncertainty in its performance in varying forest type and complexity (Pierzchala et al., 2018). Liang et al. (2018) concluded, too, that there may be an effect of user operation on data quality in consequence of trajectory design (pre-fieldwork) and routing (in the field). In more complex forests, bias increased. Kukko et al. (2017) suggested further work remains to quantify the quality of MLS-derived tree parameters with those derived from UAV (Salach et al., 2018; Graham et al., 2019) and TLS data.

Huerta-García et al. (2018) noted a disconnect between UAV sensors (which can only see crown geometry) and HMLS (which lack the range to see tree crowns). They proposed simultaneous capture of terrestrial and airborne data. Bienert et al. (2018) agreed, describing MLS in forestry as an "emerging field of research" and suggesting future studies focus on semi-automated segmentation of trees scanned using mobile LiDAR sensors. Similarly, the use of lower-cost TLS and MLS sensors was justified (Wang et al., 2018) as a cost-effective path to data of high utility. Meanwhile, the untested potential seemed to extend beyond 3D mapping alone. Staats et al. (2017) identified surfaces might be identifiable through analysis of HMLS trajectory files where sensors were carried by human operators. Where a forest surveyor could follow a specific path, could trajectory data yield similar insight?

2.7.2 Emerging technology

At the time of writing (August 2018), the potential of HMLS has not been fully explored with less than 10 relevant studies currently published. Results in previous chapters of this thesis demonstrate the role HMLS can play measuring trees – individually and at plot-level. Several papers have tested HMLS sensors in the field (Ryding et al., 2015; Bauwens et al., 2016; Aijazi et al., 2017; Huerta-García et al., 2007; Oveland et al., 2018; Cabo et al., 2018). The research presented in this thesis places HMLS in the context of established ALS and TLS methods. It explores whether fused, multi-sensor datasets may yield useful results when compared with more costly or time-intensive approaches, at multiple scales. Several research gaps were identified in the literature:

Few studies (three assessing the GeoSLAM ZEB-1 and two the ZEB-REVO) had explored the role HMLS could play in the rapid acquisition of below-canopy forest structural data. This type of information is highly useful as ground validation data for forthcoming operational sensor technologies such as BIOMASS P-band SAR, NovaSAR S-band SAR and the GEDI spaceborne LiDAR altimeter. Each of these missions are designed to retrieve three-dimensional information on forest structure and this research proposes HMLS as a useful tool for rapid capture of calibration/validation datasets. No research had sought to fuse HMLS data with ALS data. By doing so, perhaps the limited range of HMLS could be overcome to some extent.

2.8 Research aims and objectives

The principal objective of this research is to assess the utility of HMLS sensors in forest mapping. Research questions were designed to (i) assess the impact of in-the-field decision making on data quality, (ii) compare HMLS-derived 2D and 3D tree measurements with a TLS-derived reference dataset and (iii) determine the possible roles HMLS might play in multiple-scale calibration of very high resolution, remotely-sensed datasets.

At the time of writing, (i) and (iii) had not been addressed whilst (ii) had only been explored in a handful of studies on a very local scale. The answers presented within the following chapters aim to build on exploratory research to develop a robust, rigorous and repeatable methodology for efficient capture, processing and quality control of 3D data using HMLS sensors (***Chapters 4*** and ***5***). The research also aims to define a realistic mechanism for semi-automated, time-efficient retrieval of biophysical parameters from HMLS point cloud data which may also be useful in LiDAR and optical satellite calibration and validation. Additionally, it seeks to define variables which may also be useful as inputs for RADAR scattering models (***Chapter 6***).

2.9 Summary

Terrestrial and handheld LiDAR sensors have developed as part of a revolution in forest mapping and forest ecology. At the time of writing, TLS techniques are well-understood and increasingly prevalent in research projects. Meanwhile, HMLS sensors are at the cutting edge of research and only just starting to be deployed in forests. Programmes such as AIRSAR, AfriSAR and CORSAIR (Satellite Applications Catapult, 2016) demonstrate a legitimate interest in extracting value from leading-edge remote sensing datasets, to support scientific research and drive development of new applications and markets.

LiDAR has been shown to be the optimum sensor for inferring aboveground biomass density in multiple studies (Calders et al., 2014b; Hansen et al., 2015; Sinha et al., 2015; Coomes et al., 2018) and has the tightest tolerances of all widely-used instruments in this context, although its costs and relatively-small spatial coverage rather limits its utility on broader-scale studies. Fused, SAR and LiDAR are increasingly proving to be a highly effective tool to map forested areas (Asner et al., 2018).

3. Methods

3.1 Introduction

This chapter details the equipment, methods and processes used, devised and applied throughout this research. **Figure 3.1**, below, illustrates chapter structure:

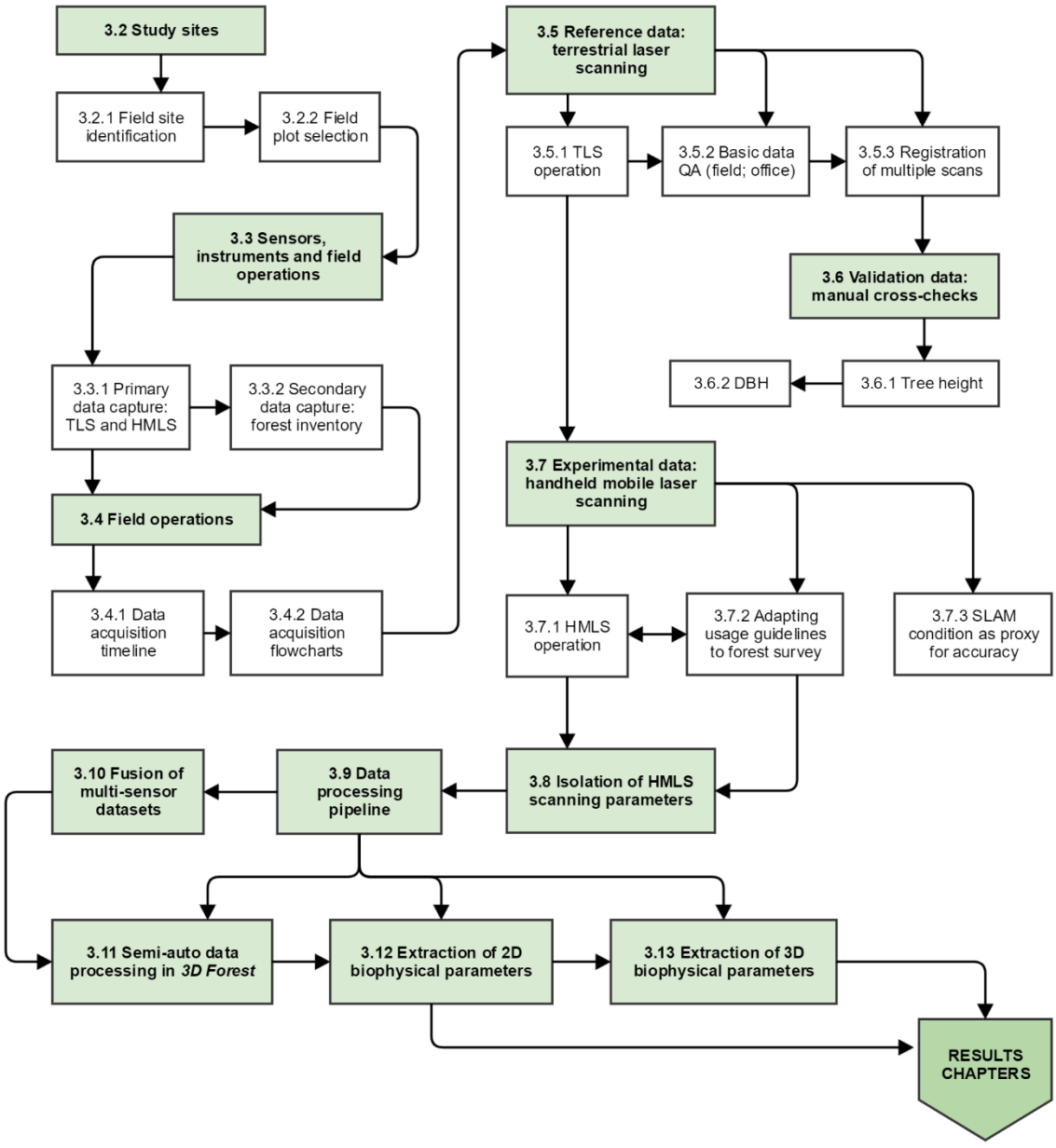

Figure 3.1: Flowchart showing the structure of this chapter.

3.2 Study sites

For the purposes of this research, the requirement was for study sites to encompass wide variety. This meant that the combination of sites chosen had to show a broad range of tree species, shape, size and density. As the research was principally concerned with development and assessment of a new technique for forest mapping, there were also spatial and geomorphological requirements. Among these, slope and complexity of the underlying terrain was deemed to be important. Between the study sites, these range from flat and even to hummocky or steeply sloped. Finally, as object detection was an important facet of investigation, it was important that different management regimes were assessed. This ensured that data were acquired in veteran woodland, unmanaged forest and young even-aged plantations alike.

3.2.1 Identification of suitable field sites

Data from several third-party organisations were used to determine potential study sites suitable for this research. This was principally done in collaboration with Environment Agency Geomatics who hold ALS data covering over 85% of the land area of England and Wales. ALS data were first gathered in March 2015, prior to the complete release of the entire dataset under the UK Government 'open data' initiative. Simultaneously, the National Forest Inventory (Forestry Commission, 2018) GIS dataset was interrogated to understand the spatial and compositional content of key UK forests, with particular focus placed on species homogeneity (i.e. monocultures) and heterogeneity (where a broad variety of tree dimension and species could be expected to be found).

Study sites were selected toward the start of active research (March 2015) in conjunction with Environment Agency Geomatics and chosen based on the availability of recent (< 90 day) ALS acquisitions. At the time, point cloud datasets were not readily available and the opportunity to access recent ALS acquisitions was deemed sufficiently important to determine study site selection. ALS data were accessed directly in spring 2015 (on-site during a work placement) and from 2017 onwards, via the Environment Agency 'Survey Open Data' portal (Environment Agency, 2018a; 2018b). Raw point clouds were identified

via interactive spatial query and downloaded in compressed (.LAZ) point cloud format. Data were processed entirely within *CloudCompare* with processing steps described later in the chapter.

GIS shape files encompassing both the National Forest Inventory and National Forest Estate (Forestry Commission, 2018) were accessed and downloaded. These contained a wealth of information on forest type, composition and age (among many other variables), reported at the sub-compartment and stand level. Further GIS data was supplied by Corporation of London, who own and manage Epping Forest and who kindly contributed data and expertise to support field planning and data capture.

Three UK forests were selected: Epping Forest (Essex), Stratfield Brake (Oxfordshire) and Tilgate Forest (West Sussex). These sites were chosen to provide as broad a range of tree diameters and heights as possible. Additionally, Victoria Park in Leicester served as a 'controlled-condition' study site to replicate a laboratory environment as much as possible. Basic location information is presented in **Table 3.1** (overleaf). Limitations in resource in-the-field and desk-based processing resource (i.e. available system RAM and disk storage space) subsequently restricted analyses to subplots extracted from wider-area scans acquired at each site. This meant that only a proportion of all scan data was analysed within this thesis. Stovall et al. (2018) advocated for sample sizes of at least 100 trees to mitigate error and bias. Nevertheless, this was not deemed to be a problem as the study was not intended to be representative of all forests or of a specific forest type. Instead, the scope of the study was designed to assess relative sensor performance in a variety of environments to confirm whether any error in HMLS mapping was a function of tree size and shape. Given the trade-off between processing time and broader research relevance, a smaller sample size became acceptable.

Table 3.1: Study site location and forest type

Study site	Code	Region	Lat/Lon (WGS84)	UTM 31U	Primary forest type	Secondary forest type
Bury Wood, Epping Forest	UEP-BW	Essex	51.643540, 0.014044	E: 293409 N: 5725615	Ancient wood pasture	
Stratfield Brake woodland	USB-C	Oxfordshire	51.803571, -1.284059	E: 618311 N: 5740583	Juvenile oak (20 – 21 years)	Even-aged mixed deciduous
Tilgate Forest	UTF-ROK	West Sussex	51.086099, -0.166021	E: 698473 N: 5663220	Mature mixed deciduous	Mature coniferous monoculture

3.2.2 Selection of field plots

Table 3.2 lists the sites, describes the sensor combinations deployed and summarises the spatial extent of each subplot extracted from wider-area scans. Subplot extents were adjusted to suit tree density, with a hard limit based approximately on the point at which *3D Forest* software crashed. Each subplot contained at least 20 individual trees at time of extraction, ensuring a minimum sample size of 10 per subplot (e.g. after accounting for error in point data or presence of complex structure at DBH height).

Table 3.2: Sensor combinations deployed at each study site

Site	**TLS** (P20)	**HMLS1** (ZEB-1)	**HMLS2** (ZEB-REVO)	**Subplot size** (m)
UEP-BW	Yes	Yes	Yes	40 x 40
USB-C	Yes	Yes	Yes	10 x 10
UTF-ROK (square plots)	Yes	No	Yes	20 x 20 (2)
UTF-ROK (circular inventory plots)	Yes	No	Yes	10 m (radius) x 2

3.2.3 Epping Forest, Essex

The first subplot was extracted from data acquired within managed woodland – Bury Wood – situated towards the southwest of Epping Forest, northeast of Chingford and southwest of Loughton (**Figure 3.2**). This site was chosen in conjunction with environmental stewardship officers at City of London Corporation, who recommended the site due to biodiversity and planned forest management activity. From an 'object-based analysis' point of view, Bury Wood comprises many trees of varying age and size. It therefore presented an ideal field site in that it encompassed natural variation in tree species, size and shape.

Wood pasture intervention encompassing pollarding (in part illustrated in **Figure 3.3**) and coppicing has been carried out regularly over the preceding century, and Bury Wood therefore presents atypical morphology in otherwise-typical UK tree species. One tree, Grimston's Oak, is believed to be over 350 years in age. Bury Wood is also home to an abundance of holly (*Ilex aquifolium*) characterised here as unwanted understorey vegetation. An opportunity arose to scan the site pre- ("A") and post-holly clearance ("B"). By scanning before and after this intervention, it became possible to assess HMLS sensitivity to smaller-scale woody vegetation. However, in this chapter, research is concerned only with post-clearance data. A potential HMLS-derived change detection workflow is introduced in ***Chapter Six***.

Figure 3.2: Google Earth-derived (Google, 2018) image of Bury Wood in relation to the greater extent of Epping Forest as well as Chingford (southwest; bottom-left) and King George's Reservoir (west; left-centre). Bury Wood is approximately 3.5 x 3.4 km.

Figure 3.3: Photograph of the UEP-BW site looking SE from NW corner of site. Note that most trees have been pollarded. Image captured immediately prior to HMLS2 (ZEB-REVO) scan of the plot; these are leaf-on conditions.

Figures 3.4 (below) and **3.5** (overleaf) illustrate UEP-BW scan data in plan and side profile. Note that the HMLS2 scan was acquired over a larger area.

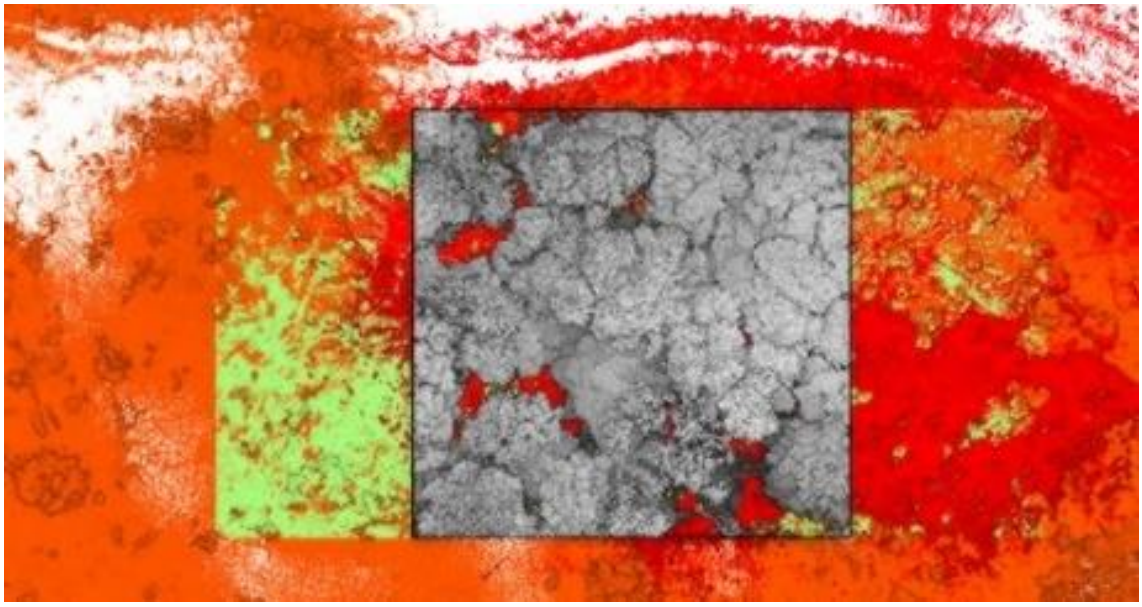

Figure 3.4: Plan view of three vertically clipped scans (TLS: green; HMLS1: red; HMLS2: orange) acquired at UEP-BW with full-height subplot (greyscale colour ramp). Subplot was 40 x 40 m and randomly located within an area of overlap between the three scans.

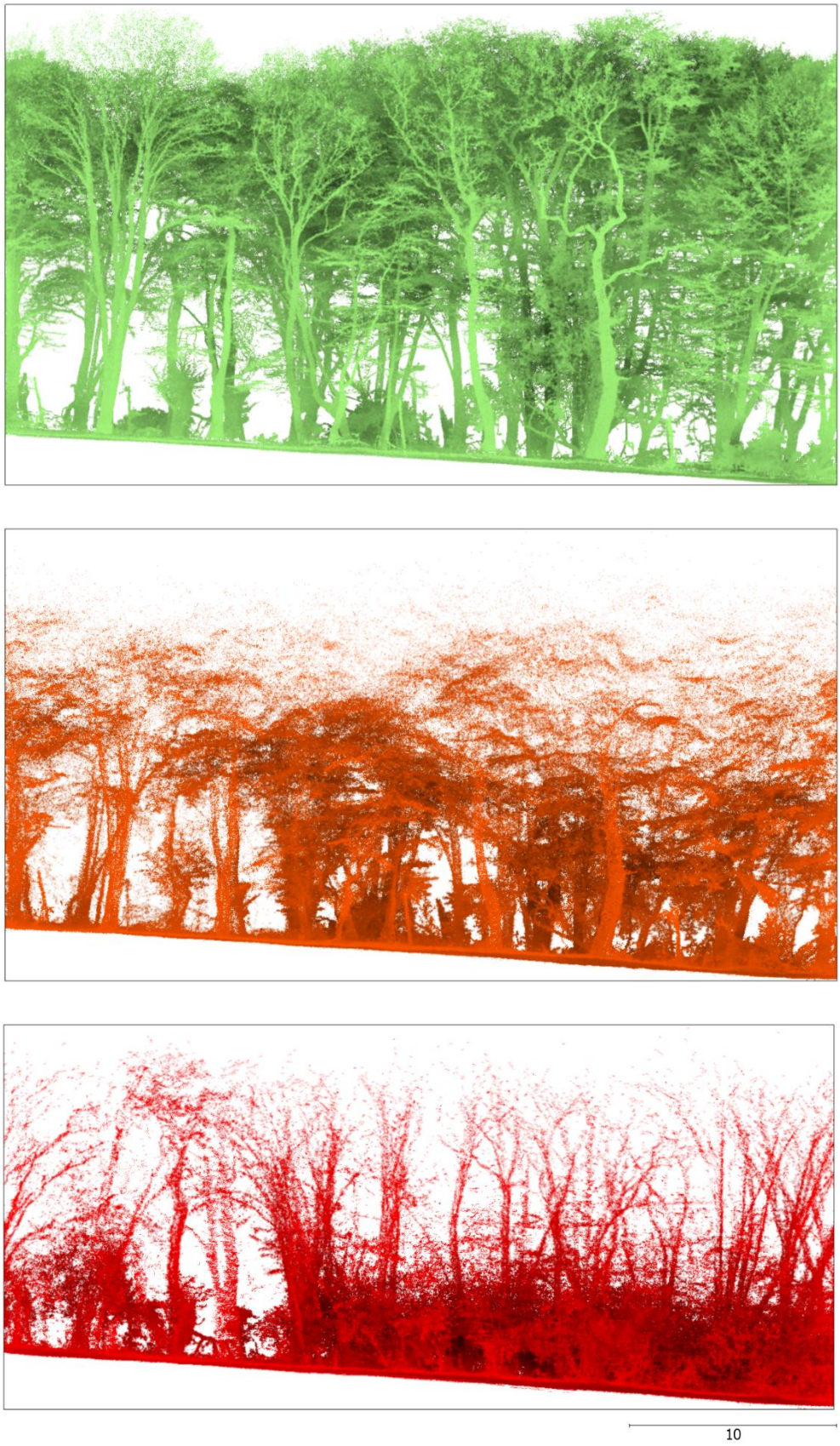

Figure 3.5: Profile views of the UEP-BW 40 x 40 subsets coloured by sensor (TLS: green; HMLS1: red; HMLS2: orange). Note the high density of holly in HMLS1 profile (region of red noise to bottom-centre/bottom-right). All views to scale. Bounding boxes are 40 m wide but heights vary: TLS = 23.1 m, HMLS1 = 18.5 m, HMLS2 = 21.7 m.

3.2.4 Stratfield Brake, Oxfordshire

At Stratfield Brake, data were acquired along a north-south transect within a small (80 x 250 m) tract of juvenile woodland (**Figure 3.6**). The site is described as secondary woodland (Woodland Trust, 2014) and within the highlighted region, trees are even aged (planted in 1997-8.) The stand comprises of mixed-deciduous tree species. Trees were observed growing in parallel rows and appeared to be of similar height. Unfortunately, individual tree crowns overlapped and intersected each another and the canopy was closed. Due to close proximity of tree stems (see **Figure 3.7**), occlusion presented a major logistical challenge in the context of TLS scan coverage. As a result, a high density of scan stations was set-up. Data from all three sensors were acquired along a north-south transect (**Figure 3.6**; **3.8)** marked in-field with orange twine. All data were acquired within a 14-day period.

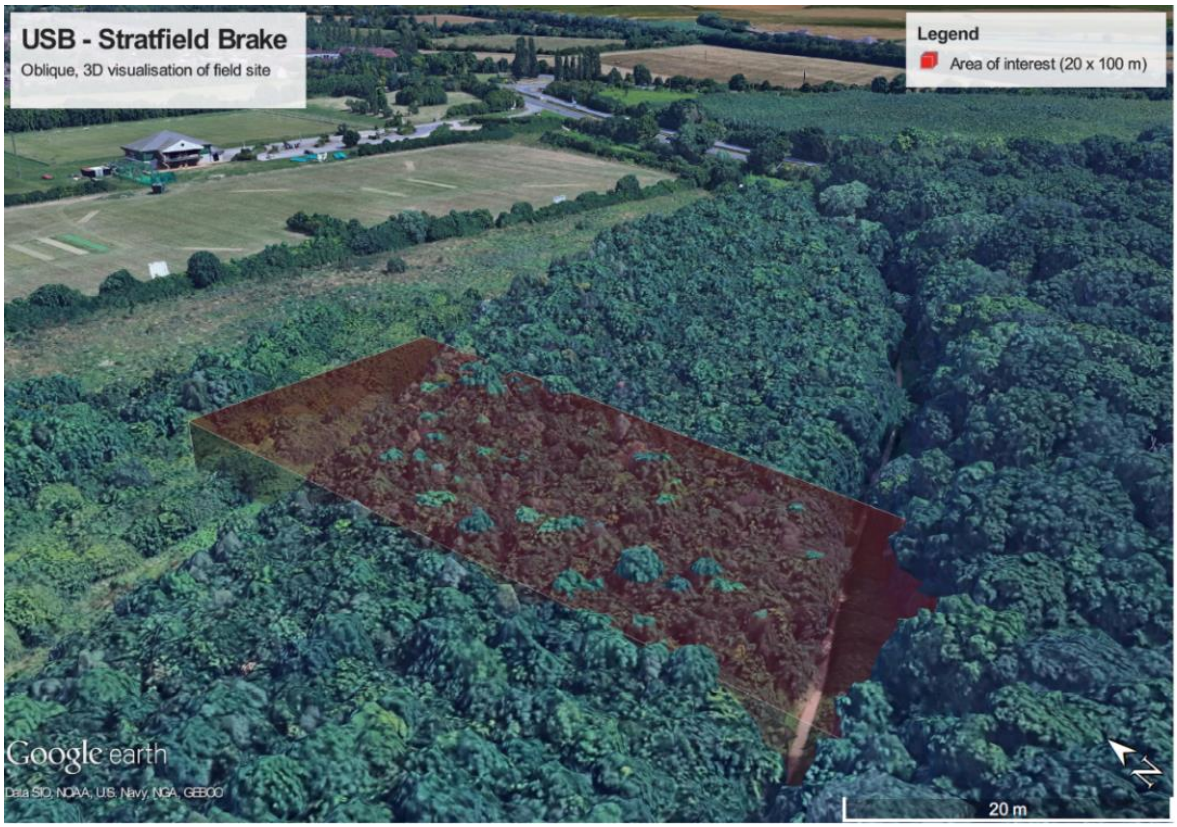

Figure 3.6: Google Earth-derived (Google, 2018) image of USB-C (red polygon) in relation to the greater Stratfield Brake woodland. Two paths can be seen extending from W (left of image) to NE (top-right corner) bordering the juvenile plantation area.

Figure 3.7: Photograph of the USB-C field site taken from the centre of the sub-plot looking north. Also in shot is the TLS (Leica P20) instrument atop a tripod.

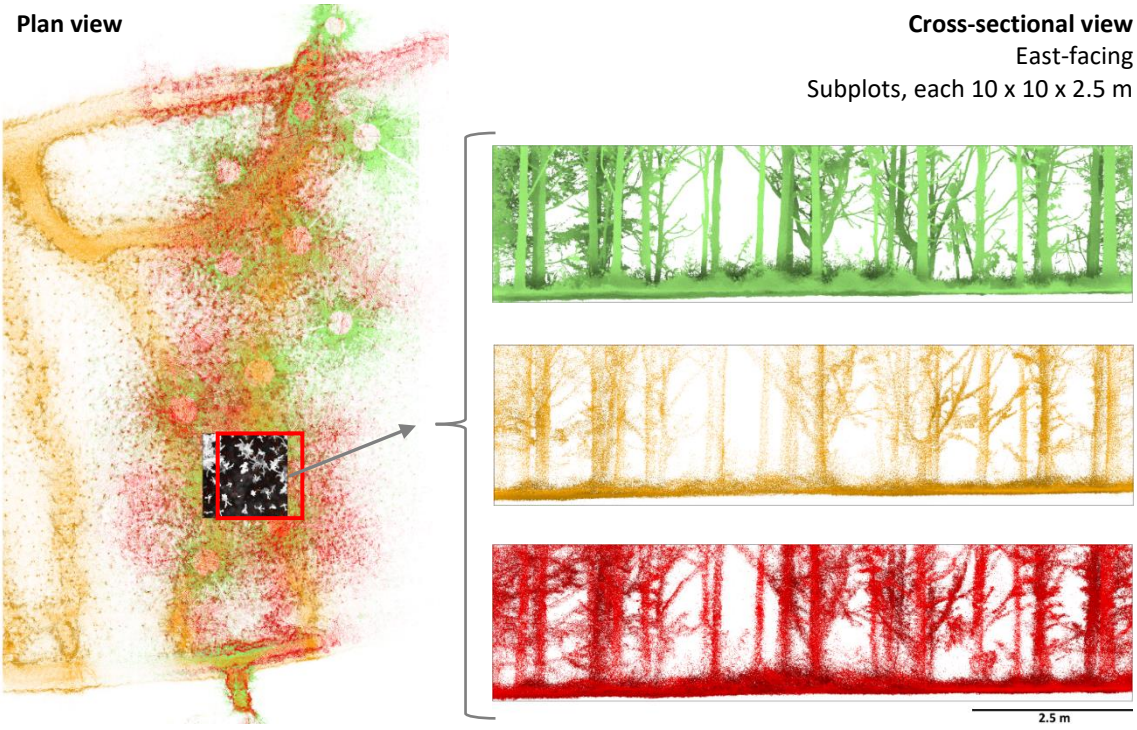

Figure 3.8: Plan (left) and profile (right) views of subplot data coloured by sensor (TLS: green; HMLS1: red; HMLS2: orange). As previously, all subplots to scale.

3.2.5 Tilgate Forest, West Sussex

Tilgate Forest is a relatively small (1.2 x 2 km) mixed-type forest located two miles south of Gatwick Airport (see **Figure 3.9**). The forest is laid out into separate compartments, often comprising monoculture assemblages adjacent to one another. According to the National Forest Inventory (Forestry Commission, 2018) the forest is dominated by coniferous monoculture compartments and mixed deciduous compartments with a few single-species deciduous compartments, too. For this chapter, data acquired in two red oak compartments to the southeast of the forest were analysed. These compartments are illustrated in **Figures 3.10** and **3.11**.

Figure 3.9: Oblique orthophoto image of Tilgate Forest with the study area, UTF, highlighted with a semi-transparent red polygon. Image produced with the permission of Google (Google Earth, 2018) using Google Earth Pro (version 7.1.2.2041).

Figure 3.10: Photograph of the UTF-ROK field site looking due west. This site comprises of 100% red oak (*Q. rubra*), widely spaced, with an understorey mostly comprised of bracken (*P. aquilinum*). The photo was taken at the time of HMLS2 scanning. The TLS reference scan was acquired the following year during leaf-off conditions.

UTF-ROK was scanned with the TLS and HMLS2 sensors. The trees at this site were relatively sparse in terms of point density. Two 20 x 20 m subplots were randomly located (**Figure 3.11**), each encompassing approximately 10 trees. To mitigate edge effects, trees 'partially inside' both subplots were manually clipped to their fullest extent beyond subplot edges, maximising sample size (n = 25) across the two subplots.

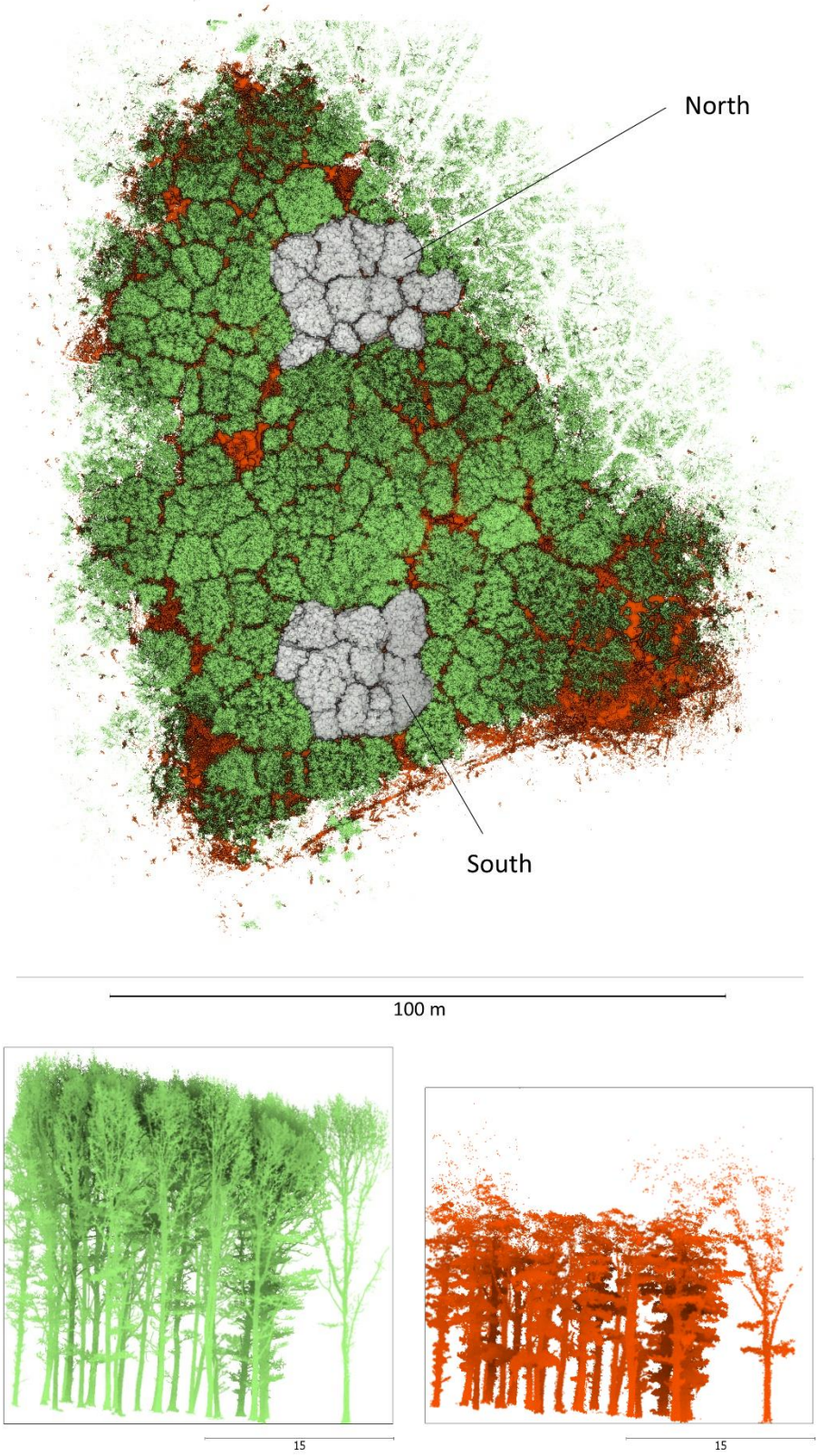

Figure 3.11: Plan (**top**) and north-facing profile (**bottom left** & **right**) views of TLS (green) and HMLS2 (orange) UTF-ROK data subplots. Note subplots (plan view; grey) extend beyond 20 x 20 m square subplot boundary preserving full crown extent.

3.2.5 Victoria Park, Leicester

TLS and HMLS scans were acquired in Victoria Park, Leicester (UK) (**Figure 3.12**) adjacent to the University of Leicester, in a plot subsequently referred to as 'UVP'. Four trees with overlapping crowns (inset, **Figure 3.12**) were clustered in an otherwise flat and featureless area of open grassland. Initial estimates suggested the tree heights were in the range of 11 to 12 m above ground, within the quoted range of the ZEB-1 HMLS sensor tested in this chapter (GeoSLAM, 2018). This cluster of trees appeared to offer a good test site for assessing the influence of HMLS geometry on target reconstruction. The presence of an adjacent goalpost offered an additional feature to assist scan co-registration.

Figure 3.12: Detail map showing the position of the target tree cluster, UVP, within the broad, flat expanse of the Victoria Park sports pitches. Inset image illustrates the closed, merged canopy of the four trees during 'leaf on' conditions. Imagery reproduced from 3D photogrammetric Google imagery accessed via Google Earth Pro (Google, 2018).

3.3 Sensors, instruments and field operations

3.3.1 Primary data capture: terrestrial and mobile LiDAR

A Leica Geosystems HDS ScanStation P20 (hereon, 'P20') tripod-mounted TLS was used to collect reference data in all four study sites. The P20 is a time-of-flight system capable of capturing up to 1,000,000 points per second with 360-degree horizontal and 270-degree vertical viewing angles (Leica Geosystems AG, 2014; see **Figure 3.13** overleaf for an annotated schematic). The system operates in visible (658 µm) and near-infrared (808 µm) domains, has a range of 120 m and an accuracy of 0.006 m at maximum range (Leica Geosystems AG, 2014). Beam divergence is 0.2 mrad; the P20 can resolve points 0.6 mm apart at a distance of 10 m from the scanner.

The P20 has a dual-axis compensator; all captured data was level. Black-and-white targets, also mounted on tripods, were situated within each field plot and used to align scans in three axes. This constrained multiple perspectives (i.e. multiple scan set-ups) of a given forest plot in terms of vertical and horizontal alignment. Full hemispherical scans typically took 6 to 9 minutes each to complete. Data were stored on a solid-state drive, copied to an external USB drive and imported into *Leica Cyclone* software for processing.

Two HMLS systems were used in this research, both manufactured by GeoSLAM Limited: the ZEB-1 and ZEB-REVO (**Figure 3.14**, also overleaf). At the time of writing, the ZEB-REVO RT (modified version with real-time SLAM coverage presented via a visual interface) was about to be released to market but was not tested. Both the ZEB-1 and ZEB-REVO systems contained the same scanner hardware, a rotating (horizontal axis) Hokuyo UTM-30LX 2D time-of-flight laser rangefinder, with a nominal range of 30 m operating at 40 Hz (Bosse et al., 2012; GeoSLAM, 2018). This laser operated in the near-infrared domain (905 µm), with a resolution of 0.625° (horizontal) and accuracy of 0.02 to 0.03 m (at 10 m range). Field-of-view was 270-degrees and a hemispherical view achieved through mechanical movement (vertical axis) of the laser through sprung oscillation (ZEB-1) or electro-mechanical rotation via a motor (ZEB-REVO).

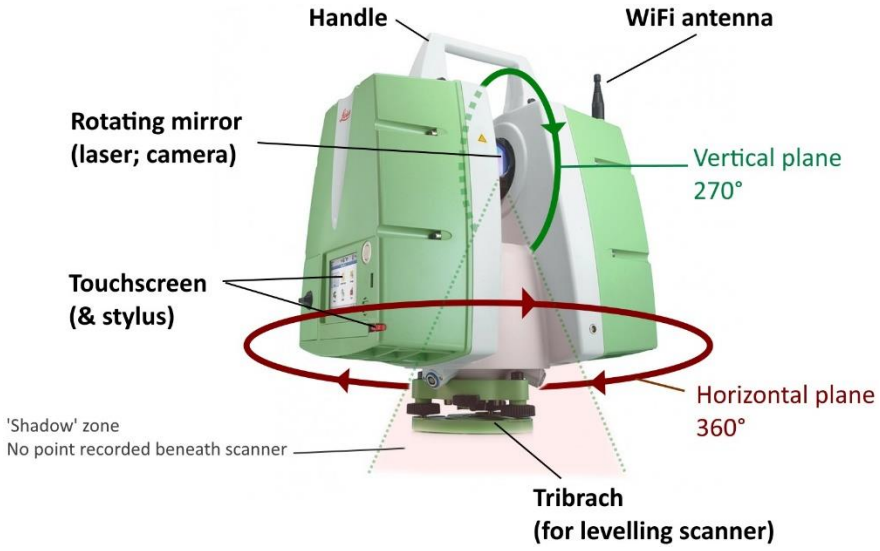

Figure 3.13: Schematic diagram of a P20 TLS illustrating key components, planes of rotation (vertical and horizontal) and a 'shadow zone' where no points are logged immediately beneath the scanner.

Source: author's own illustration.

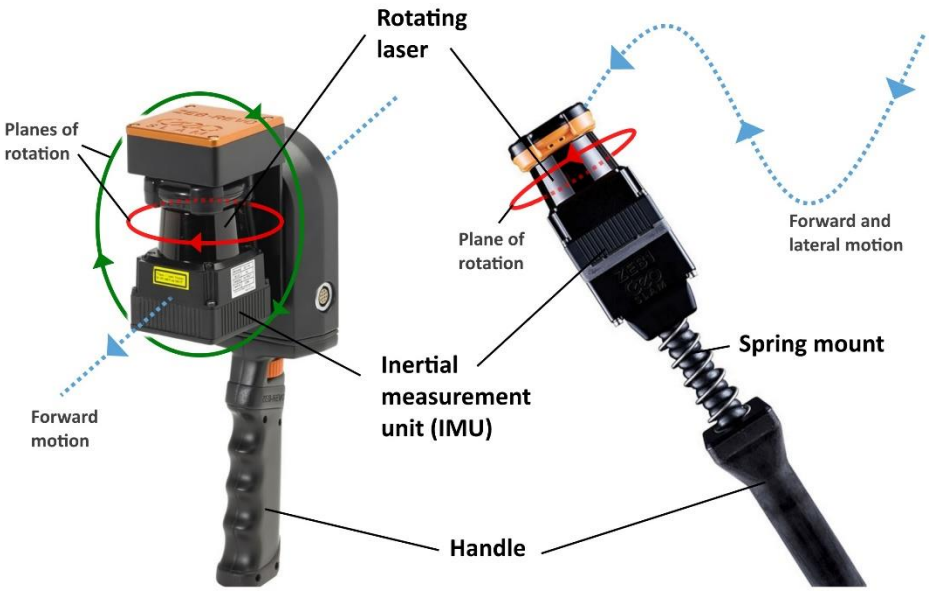

Figure 3.14: Schematic diagram illustrating ZEB-REVO (left) and ZEB-1 (right) HMLS sensors. Blue dotted lines indicate scanner trajectory: the ZEB-REVO is held steadily in one hand while the ZEB-1 oscillated to and fro and side-to-side as a surveyor traverses a site.

Source: author's own illustration.

Both HMLS systems use the same Hokuyo laser system and the same IMU but whilst these were spring-mounted on the ZEB-1, a second motorised plane-of-rotation was integrated into the ZEB-REVO. Consequently, point distribution was more uniform. The two systems each captured 43,200 points per second and data were logged to identical data loggers. The two HMLS instruments were specified to have a proportionally greater point separation than the TLS, but this was felt unlikely to have a significant effect given most objects were scanned from distances < 10 m.

Whilst the TLS and HMLS instruments operate in slightly different wavelengths (808 and 905 µm respectively), the two systems are unlikely to record differing structural data. Both sensor types operate on a time-of-flight basis and in all scans, both dry and moist vegetation was recorded with no obvious clusters or gaps in point data. Neither the ZEB-1 nor ZEB-REVO sensors recorded a measure if intensity, so no further investigation was possible.

3.3.2 Secondary data capture: forest mensuration

A wide variety of instruments were also used in the field. To calibrate TLS and HMLS measurements, a Leica TS16 total station (used to confirm TLS distances were within manufacturer specification before each field visit) and Leica GS16 SmartNet GNSS receiver (for precise, sub-cm positioning) were deployed. This latter sensor was not available for data collection at the UEP, USB and UTF field sites but briefly used at the UVP site to validate scan positions. In any case, SmartNet RTK positioning was found to degrade in forest as it relied upon an intermittently unavailable GSM signal to receive GNSS corrections.

A small selection of additional, consumer-grade instruments were taken to the field. These included a Garmin eTrex handheld GPS receiver (maximum accuracy: 5 m), a Bosch GLM 250 VF laser measure, an ikeGPS IKE4 measurement system and a set of Mitutoyo 500 AOS series digital calipers (0.01 mm resolution) for DBH measurement. The eTrex was used to locate plots: initially, to provide a heading for forest inventory, then to coarsely determine where to conduct HMLS scans of certain forest inventory plots several months

later. The Bosch laser measure was used to shoot vertical observations in forested areas to confirm maximum TLS heights were reasonable. Similarly, the IKE4 was used to measure tree height and stem location (UVP site only). However, it was found that the TLS signal was more reliable and thus TLS data became the benchmark. Finally, the Mitutoya calipers were used to precisely measure DBH as reference data.

3.4 Field operations

3.4.1 Data acquisition timeline

Figure 3.15 (below) outlines dates at which data were acquired with LiDAR instruments. **Figure 3.16** (page 62) describes the general flow of data while **Figure 3.17** (page 63) offers a more granular overview of processes performed in-the-field to acquire all required data. All acquired HMLS scan data is aggregated and illustrated in the **Appendix**.

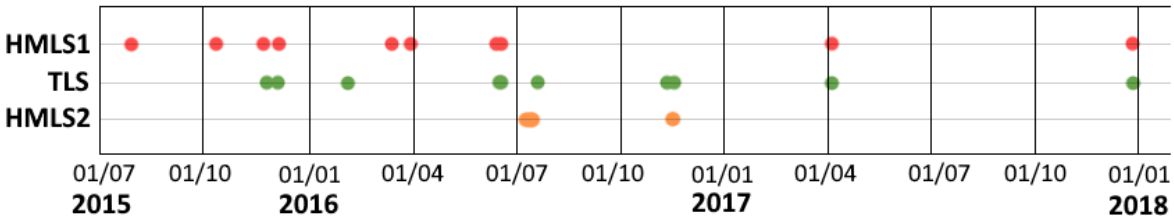

Figure 3.15: Timeline of field data acquisition using TLS (Leica P20) and HMLS (GeoSLAM ZEB-1 [HMLS1] and ZEB-REVO [HMLS2] sensors).

3.4.2 Data acquisition flowcharts

Figure 3.16 describes the process of data capture on a given date within a given field plot. Not all sensors were readily available – for example, the ZEB-REVO was only available on hire for a period of 5 and then 2 working days, limiting potential data capture opportunities. The scale of data capture was itself limited by available field assistance (staff) and equipment (e.g. number of tripods and targets). **Figure 3.17** details the specific steps undertaken to obtain comparable TLS and HMLS point clouds ready for analysis.

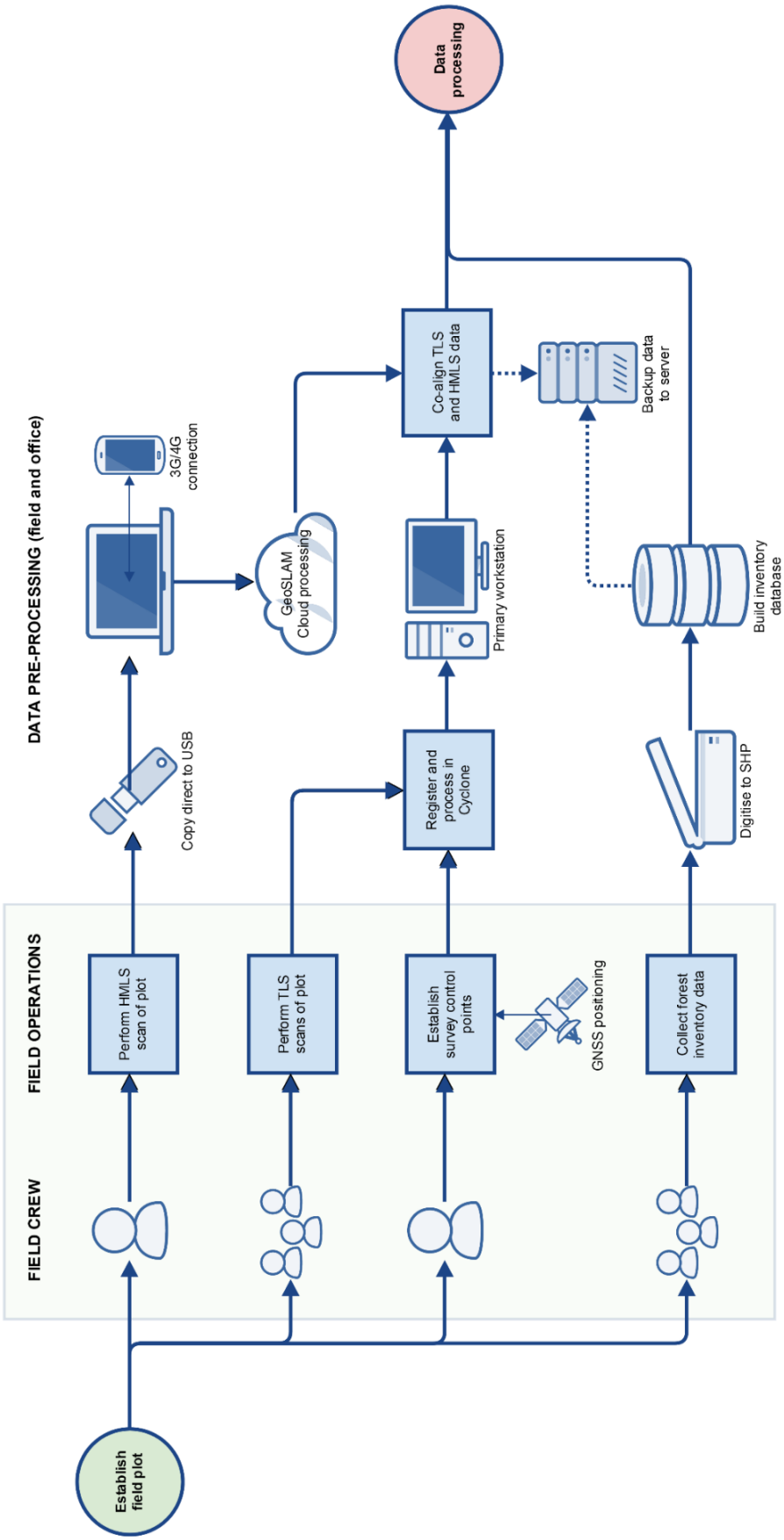

Figure 3.16: Flowchart indicating key fieldwork and data pre-processing steps.

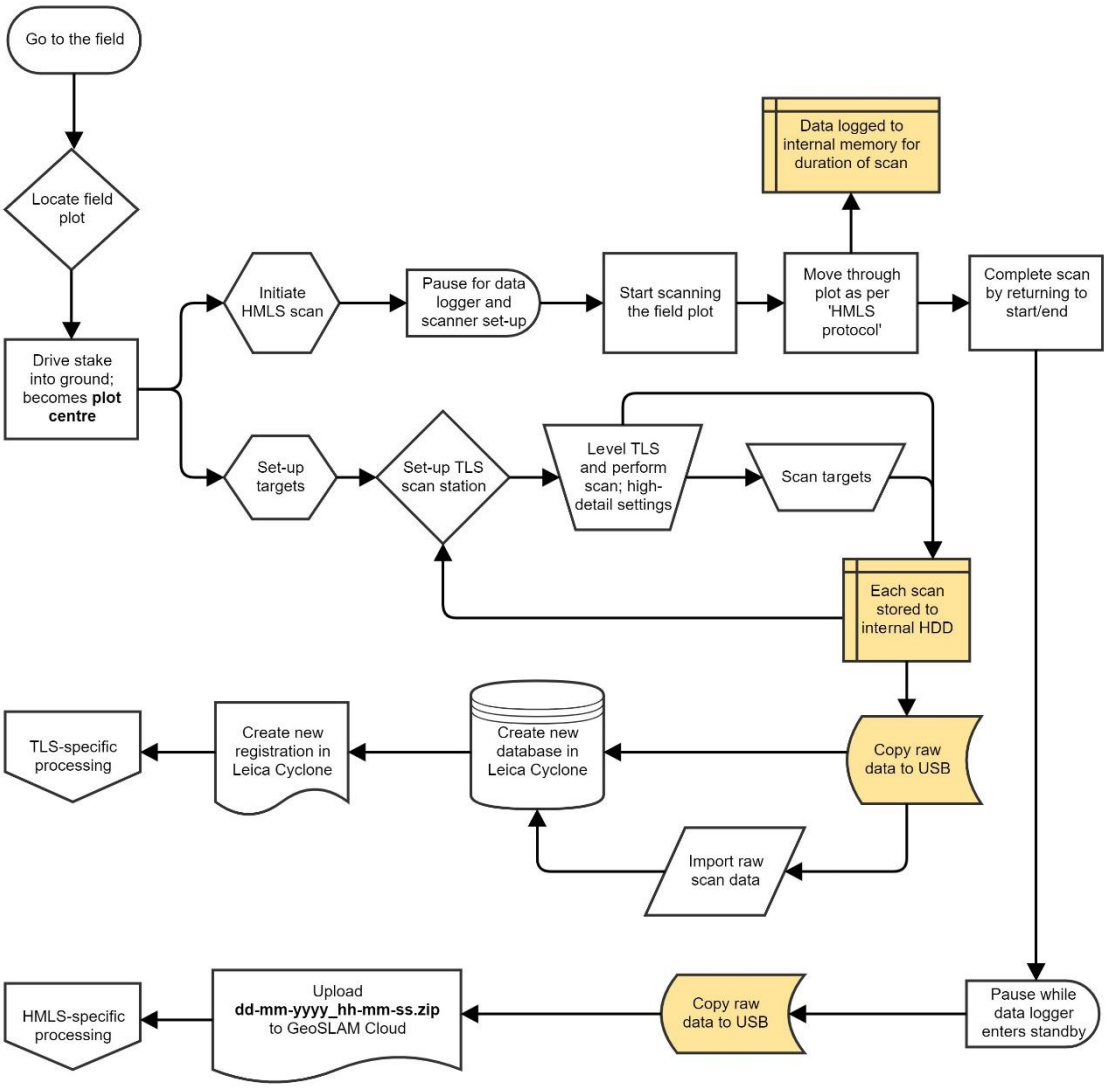

Figure 3.17: Flow of data as captured in the field, stored to removable media and imported into software for processing.

3.5 Reference data: terrestrial laser scanning

3.5.1 TLS operation

Scans were acquired from static, levelled tripods sequentially with a period of set-up required between each scan. TLS instruments capture 3D data by rotating about a fixed plane with precision servo motors incrementally rotating the scanner by the manufacturer's stated beam divergence (in this case, 0.2 mrad; Leica Geosystems AG, 2014). To mitigate shadowing where objects like tree stems 'occlude' the laser pulse,

multiple scan set-ups were distributed throughout each field site (as illustrated in **Figure 3.18**, below). Tripod-mounted targets were used to provide common reference tie points between individual scans, facilitating precise co-registration into a single, coherent TLS point cloud dataset. Targets were iteratively swapped with the TLS using the same tripods, so that three targets were visible in each individual TLS scan.

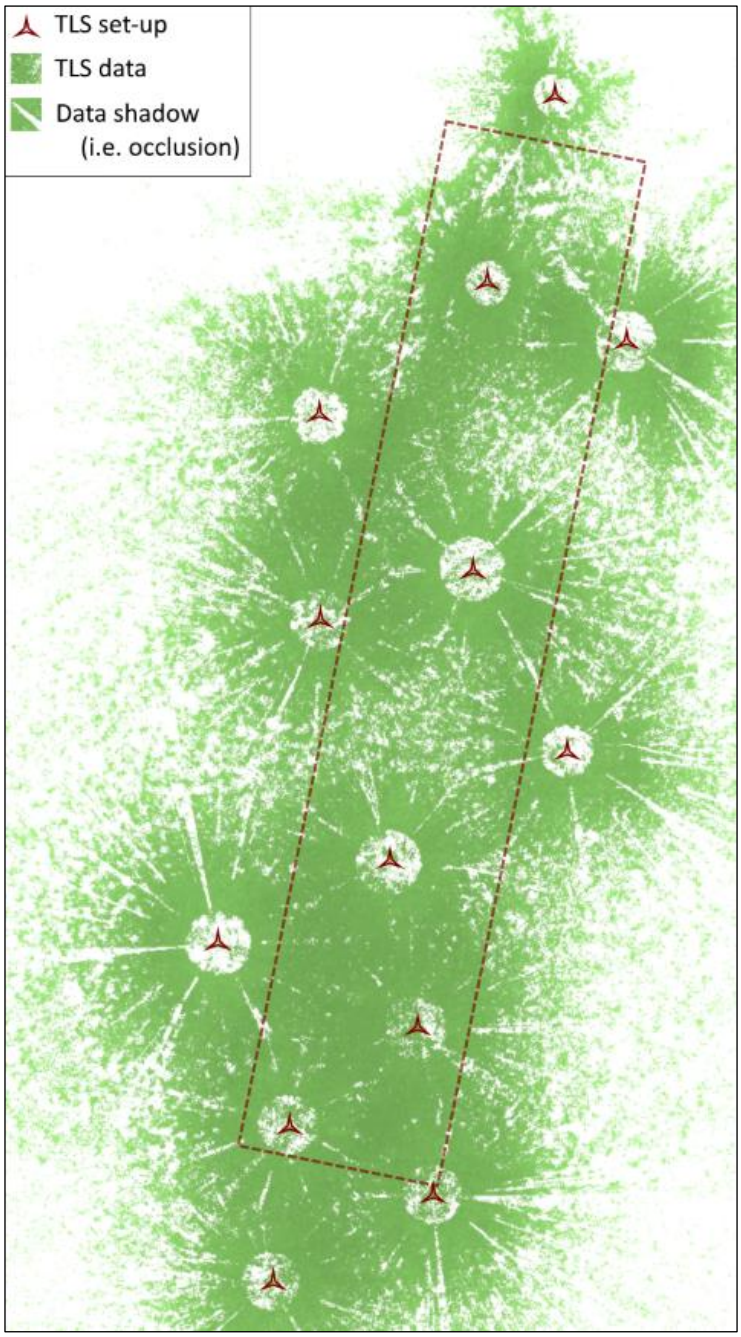

Figure 3.18: Schematic showing typical P20 scan and target set-up. The dashed box shows the survey AOI, the red icons the TLS/target tripod set-ups, and the green the TLS data. In this example, scan set-up density was high to mitigate against occlusion in the data.

3.5.2 Basic data QC: field versus office

Only TLS data could be quality checked in the field as of the scanners used in this research, only the Leica P20 included a display. In this instance, the display was a full-colour LCD which afforded an option to visually check data coverage (hemisphere, as panoramic image) and quality (by zooming in on the data preview). HMLS scans were conducted 'blind', with data QC not possible until after raw data had been processed into point cloud data. This is a major limitation of current-generation HMLS sensors. Once field activity concluded and point cloud data had been downloaded from scanners, it was loaded into *CloudCompare* where basic QC was performed. This encompassed a gross height ("Are minimum and maximum heights realistic?"), point density and point distribution checks from plan and cross-sectional views.

3.5.3 Registration of multiple scans

Individual TLS scans were registered in *Leica Cyclone* (Leica HDS, 2017) using 'visual registration' or the target-based 'registration' techniques. The former saw point clouds, two at a time, visually aligned and rotated in the horizontal then vertical planes. Scans were considered both levelled and calibrated, so no warping or stretching was applied. The latter technique required the geometric fitting of target-centre vertices between scans. Accuracies typically fluctuated between 0.001 and 0.005 m per survey.

3.6 Validation data: manual cross-checks

TLS instruments are inherently accurate and precise, rivalled only by total stations when making 3D measurements with minimal error. However, instruments can drift out of tolerance between calibrations. Furthermore, not all surveys are equal, and it is possible factors such as occlusion, scanner set-up and data processing can affect data. Therefore, a series of independent, cross checking measurements were made at each of the field sites. Due to intermittent availability of field equipment, certain instruments were only available for very specific periods and sadly could not be used across all field sites.

3.6.1 Tree height calculated with tripod-mounted laser disto

Two such instruments were deployed: a Bosch GLM 250 VF Professional and an ikeGPS IKE4. Both were specified to have decimetre accuracy at a distance of 20 m and each contained mathematical software to derive height from multiple distance measurements. The IKE4 contained a high-precision IMU and video target, offering increased precision. The use of a study tripod ensured both sensors were rotated about a centre of gravity aligned to the instrument reference plane, minimising angular error. **Figure 3.19**, below, illustrates a typical tree height measurement using one such sensor.

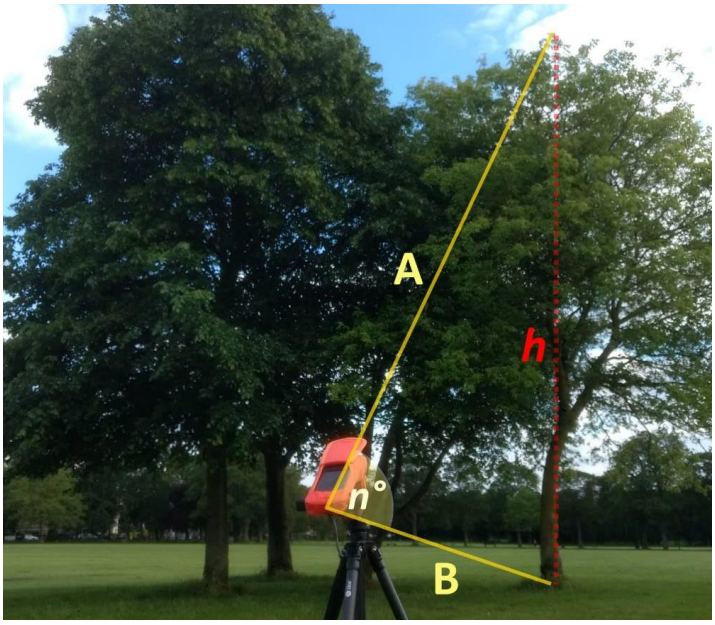

Figure 3.19: schematic diagram of tripod-mounted disto tree height measurement, overlaying a photo of an ikeGPS IKE4 set-up at the UVP field site. Angle *n* is measured at the instrument reference plane. Source: author's own photograph and annotation.

3.6.2 DBH measured with tape and calipers

Where laser distos were not useful was in validation of DBH measurement, principally due to the sheer number of observations required. Instead a combination of calipers and flexible tape measures were used. Calipers offered the highest accuracy in that measurement could be made at the sub-mm level. However, caliper-derived DBH only captured diameter at a specific part of the tree and assumed a cylindrical stem. Tape measurements were less accurate but captured the full stem circumference.

3.7 Experimental data: handheld mobile laser scanning

3.7.1 HMLS operation

Operation of HMLS scanners in-the-field was straightforward. Upon powering-up, the systems went through a brief period of initialisation before continuous data capture commenced. 3D data were logged throughout the field site traverse until the system was returned to the start point and left in a static position. The built-in MEMS inertial measurement unit (IMU) recorded orientation and acceleration while the scan was underway (Bosse et al., 2012; Pierzchala et al., 2018) and the scan was terminated once the IMU registered a period of inactivity. Both 3D distance and multi-datastream IMU data were fused, in real-time, in an on-board processing unit. These input data were utilised by the SLAM algorithm to repeatedly localise scanner position within the study site. This process mapped where the sensor was – and had been – during a scan.

3.7.2 Adapting OEM usage guidelines to forested environments

As previously discussed in ***Chapter 2***, HMLS systems were not developed for use in forested environments. Minimal guidance was available for best practice when scanning trees. So a series of operational considerations were developed as part of this research. These are detailed in **Table 3.3**, below.

Table 3.3: Operationalising OEM guidelines for HMLS forest survey

Guideline	**OEM recommendation**	**Operational consideration in forests**
Scan repetition	Must scan features >1 time. The more points per feature, the higher the likelihood SLAM will use the feature	Ensure all trees are looped *at least* once, additionally ensuring each tree can be seen from multiple passes <10 m distant
Feature significance	1:10 rule (objects can only be detected if their greatest dimension >10% of the distance from the scanner)	Strive to have at least one pass of target objects (e.g. tree stems) within 1 m to ensure trees with DBH of 0.1 m are captured sufficiently that DBH can be extracted
Feature richness	Ensure lots of features within range	Ensure trajectory routes loop to and from objects rather than heading in a linear path between widely separated objects

Loop closure	Must scan each loop closure from similar perspective	Ensure each loop encompasses a revolution of at least 360 degrees and includes some Euclidean overlap
Change in heading	Slow and careful. Ensure a period where both sides of a bend can be seen. Avoid abrupt changes in heading	When navigating a forest, be cautious not to trip over fallen branches. Rotate gently and when passing between trees, capture both stems in a looping motion
Transition between environments	Slow. Take bends slowly. Avoid 'abrupt' change of structure. Reverse/180deg turn if required	Crucial when passing between dense understorey and open forest. Side-step or reverse from closed into open areas and vice versa
Survey speed (walking velocity)	Slow. Need to preserve point density of features	Survey at a speed slower than typical walking speed. Use natural gait to oscillate the scanner (e.g. ZEB-1) and do not manually shake it

3.7.3 SLAM condition as proxy for data accuracy

SLAM condition is an indicative, qualitative measure which spatially describes the confidence that can be placed in the SLAM algorithm within a target area (i.e. forest plot) in the context of that specific scan. In this context, 'quality' refers to the performance of the HMLS sensor and subsequent processing in terms of resolving the scanned environment. SLAM condition can be affected by environmental factors (e.g. feature abundance, feature size and feature complexity) and survey characteristics (e.g. velocity, smoothness of survey, motion remaining IMU tolerance).

All HMLS data processed via GeoSLAM Uploader or GeoSLAM Hub includes two files which indicate SLAM 'condition' qualitatively via a blue-beige-red colour ramp. The first of these files is a de-densified (9% of all points) point cloud coloured by condition. This is coupled with a polyline indicating 3D trajectory, which should be considered the absolute path taken by the scanner IMU throughout each scan. In each, 'good' condition is indicated by a deep blue, 'poor' by bright red and intermediate quality by hues between. Results were generated by coarsening SLAM condition in *CloudCompare* using the 'Rasterize' tool at a spatial resolution of 1 m. Scans which mostly comprised blues were assigned the category 'good'. Conversely, those mostly comprising red hues were categorised as 'poor'. Scans encompassing predominantly beige hues – or a broad mixture of hues – were categorised as 'intermediate'.

3.8 Isolation of parameters likely to influence HMLS data

Four simulations (or 'scenarios') were designed to empirically assess ZEB-1 HMLS performance in controlled conditions. Experiments were designed to compare multiple, individual scans with varied geometry against a single, reference TLS dataset with defined precision (accuracy: 0.001 m; RMSE for network-adjusted coregistration of multiple scans = 0.001 m; maximum distance from scanner to nearest tree: 12 m). To assess performance, specific parameters – relative stem positions, tree rotational alignment, diameter at breast height and individual tree height – were extracted from each UVP scan. The first series of HMLS scans were designed to assess the effect of distance. These scans looped a fixed buffer around the cluster with each scan a separate, predefined distance: 1 m, 2 m, 5, 10 and 20 orbits. For the second series, each scan followed a 2 m buffer and the number of repetitions was varied: 1, 2, 5, 10 and 20. Two scans were conducted at a 5 m distance: at typical walking speed (8 km h-1) and at a faster velocity (15 – 20 km h-1). Thereafter, distance from the target trees increased incrementally with a secondary aim being to identify the point at which SLAM failed.

3.8.1 Reference datasets: HMLS and TLS

Benchmark TLS data was acquired with eight set-ups distributed as per **Figure 3.20** (following page). Two rows of three set-ups extended along a north-south axis either side of the four trees, with two scans acquired directly beneath the trees. Alongside benchmark TLS data, a reference HMLS1 dataset was acquired at the UVP field site with a sinuous and complex scan (trajectory illustrated in **Figure 3.20**) in which each tree – and three TLS set-ups – were looped at least three times from multiple directions. This guaranteed a high point density, particularly at DBH height. As only three TLS tripods were available, set-ups had to be staggered, so two could not be demarcated in the field for HMLS looping. An additional, larger loop was also undertaken encompassing all four stems (and the convex hull marking three further TLS scans) to augment SLAM. Three radial paths 'connected' stems to one another and formed loop closures in a further effort to minimise error propagation.

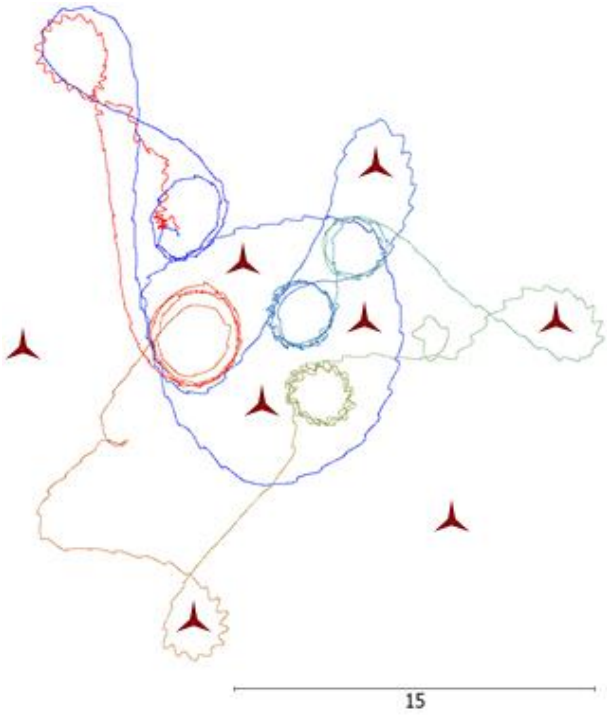

Figure 3.20: Visualisation of the UVP reference scan trajectory in plan view, aligned within this individual scan's reference frame. In this instance, the route taken is coloured by time (somewhat arbitrarily) ranging from blue at the start through to red at scan completion. TLS scanner set-ups are indicated by red 'tripod' graphics.

Further processing steps were applied to both the HMLS and TLS reference scans. The TLS cloud was manually rotated and the Y axis oriented approximately northwards. The HMLS point cloud was then rotated and translated to match, using the tripod-mounted targets as control features. All scans were acquired in 'leaf off' conditions. A laser rangefinder confirmed that top height achieved in the TLS scans was realistic. The density and distribution of points in all scans suggested occlusion was not a limiting factor. Given the density of HMLS trajectory paths beneath, adjacent to and outside the cluster of trees, it is likely the laser was able to achieve multiple lines-of-sight to the upper crown.

3.8.2 Isolation of variables

To assess effects of the various variables, the principle user-defined parameter was survey path which required planning trajectory routes (**Figure 3.21**, overleaf) through the UVP field site. It was critical each trajectory was the required distance from targets to

ensure only each independent variable was likely to affect point density and the proportion of tree successfully detected.

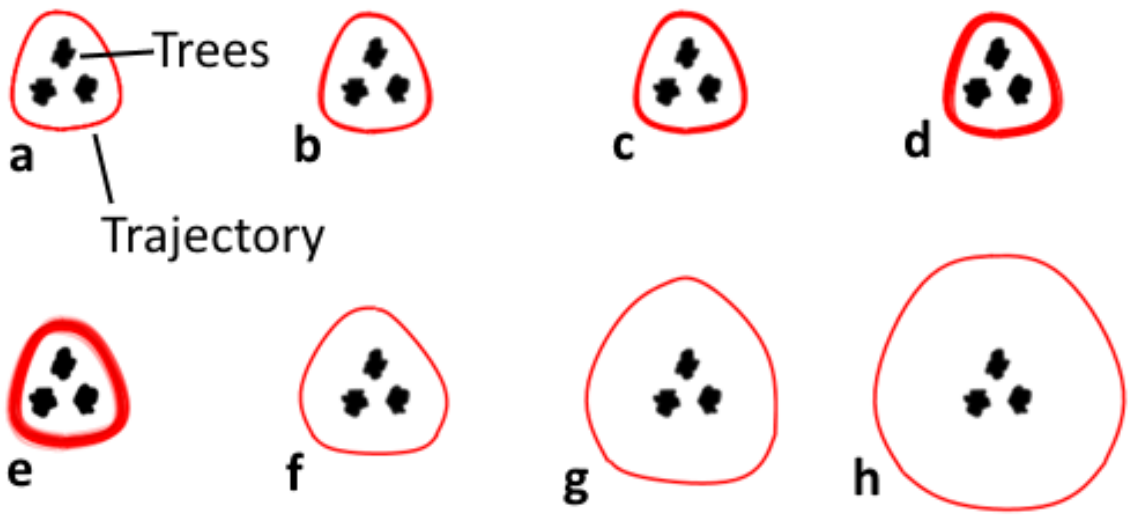

Figure 3.21: Simplified schematic diagram showing the permutations of scan geometry within this experiment. Hypothetical scan trajectory is shown as a red line and trees as dark grey clusters. Images **a** to **e** show a 2 m loop with varying degrees of repetition. Image **f** shows a 5 m buffer relative to trees, **g** a 10 m buffer and **h** a 20 m buffer.

With no visual feedback of scan extent in real-time, designated survey geometry was mapped on-site with embedded, highly visible marker pegs. Plastic, red 'camping' pegs were distributed at 2 m intervals at the required distance from targets, driven into the ground such that 0.05 m remained exposed. The pegs were precisely positioned with a tape measure to demarcate loci (buffers) at the appropriate distance from the closest tree (**Figure 3.22**, overleaf). All scans were conducted in a clockwise direction with a common start/end point. In each scan, the surveyor walked in a constant heading to the next peg. Remaining on the left-hand side of each peg ensured that distance was *at least* target distance, whilst the constant heading meant that distance did not fluctuate much more than the target distance.

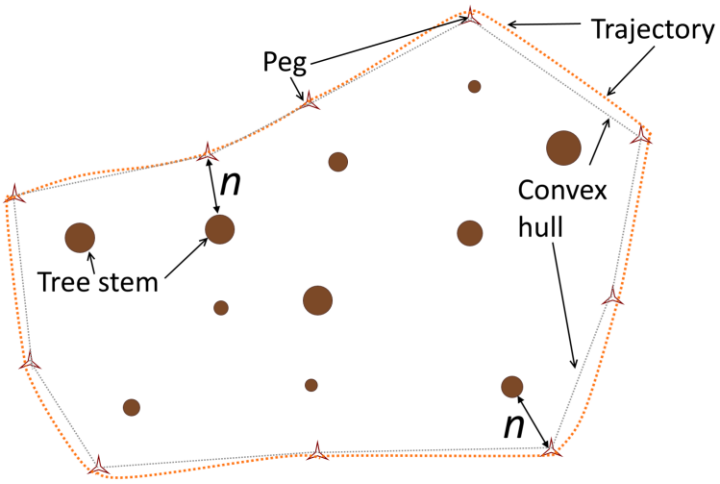

Figure 3.22: Schematic diagram showing a hypothetical HMLS survey trajectory around an area of woodland and how it would be marked-out with pegs. Distance *n* is the designed distance-from-target. Note that by design, the trajectory is never closer than *n* to a target.

3.8.3 Data capture

Field protocols were tailored for isolation of user variables which required accepting concessions in terms of data quality. The lack of intermittent loop closure meant increased risk of SLAM degradation due to error propagation, especially given the flat topography (Calders et al., 2014). There was a benefit in causing SLAM condition to degrade: it became possible to identify a threshold distance-to-target at which processing became problematic. The different geometries led to obvious effects in the output point clouds; this is described in both the results and discussion sections of the chapter.

While scan geometry was unique by design, all scans still required a 'closed loop' trajectory (GeoSLAM, 2018; Lehtola et al., 2017; Pierzchala et al., 2018). To ensure this, a common 'start/end point' was established which required precise (+/- 10 cm) placement of the HMLS scanning head on a pre-marked piece of board. In the reference scan, loop closure was achieved multiple times (**Figure 3.23**, following page). Deliberate loop closures are symbolised with dark black points. Intersections between tangential vectors (i.e. where an area is captured at different stages within the same survey) are symbolised by small grey points. As anticipated, quality of SLAM registration appears related to density of loop closure (Pierzchala et al., 2018).

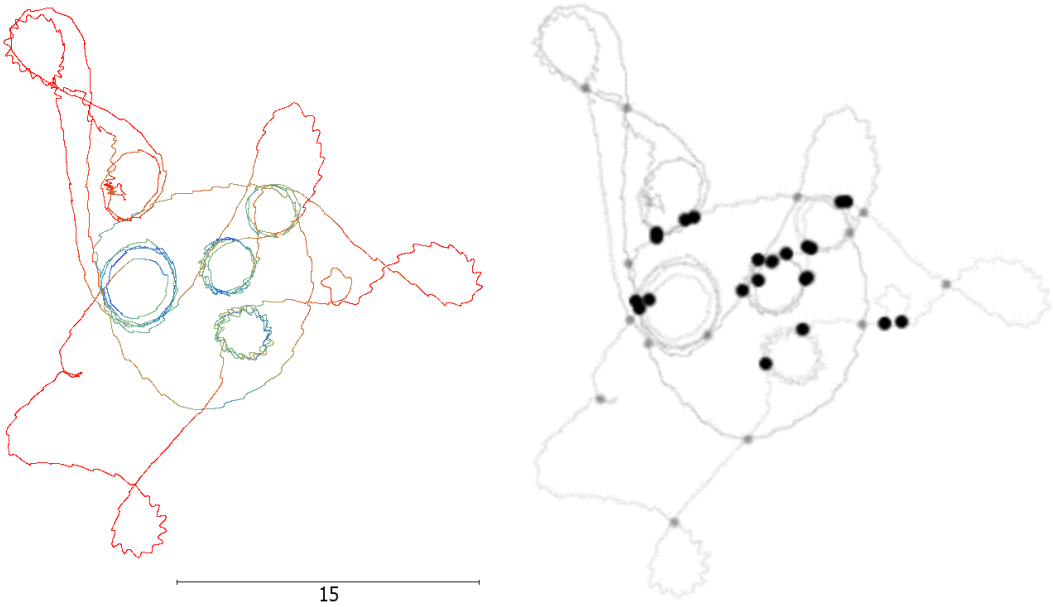

Figure 3.23: UVP reference scan (**left**) and showing loop closure/intersection with colouration removed (**right**).

At the time of writing, there was no real-time data capture module available for the HMLS systems used here. Accordingly, a manual process was required to track progress within each scan. In the case of repetition, this simply required a manual count each time the start/end point was passed. To enable accurate wayfinding in the UVP field site, markers pegs were installed. Measuring velocity proved trickier. This was achieved by recording typical walking pace and noting the period between each step. At 'typical' speed, velocity was equivalent to 2 steps per s^{-1}. At the faster rate of progress, this equated to 4 steps s^{-1}.

3.8.4 Data quality

This was a qualitative, visual comparison and assessment. Trajectory files, coloured by quality, were downloaded alongside processed point clouds. The alignment and orientation of all files associated with a single scan are identical and therefore share a local coordinate system. Part of the data pre-processing involved manually aligning, rotating and translating isolated-variable scans in *CloudCompare* with a north-oriented clone of the reference scan. By doing this, trajectory files could be superimposed on another, facilitating spatially explicit comparison.

The SLAM algorithm continually adjusts the position of targets based on spatial complexity already mapped (localisation) and in a perfect world, it would follow that alignment within a single scan should be perfect. However, error propagation (IMU 'dead reckoning'; insufficient loop closure) may mean that, for example, a tree stem may appear multiple times (Lehtola et al., 2017; Pierzchala et al., 2018). In the context of the UVP field site, persistent structural features included four trees, a largely flat horizontal surface, and a football goalpost comprising two vertical poles and a horizontal component (with two, 90-degree, intersections). These features proved useful collectively when assessing relative alignment between passes during a single scan, and between separate scans.

To assess alignment, two intersecting, 1 m-wide, perpendicular cross-sections (**Figure 3.24**, overleaf) were manually extracted from each scan. Projecting both a 'master' and 'comparison' scan simultaneously, a visual assessment was made. In each case, the reference scan was the 'master' against which the additional eight scans were systematically compared. Good alignment presented good overlap – features would appear in the same XY space on-screen. Poor alignment would manifest as a bias in one scan relative to the other, as per **Figure 3.25** (overleaf), where vertical separation between two scans would exist as a function of rotation about the scanner trajectory. This sort of error is unlikely, and if detected, probably caused by a glitch in pitch, roll or yaw measurements recorded by the built-in IMU. In this simulation, the black point cloud depicts a 'true' reconstruction of the field site, with reasonably flat and level terrain. The red point cloud has been rotated by several degrees with respect to the Z-axis; separation between the scans increases with distance from the centre of rotation, halfway between the two visible stems. For each of the UVP scans, vertically exaggerated cross-sections were used to explore the intricacies of co-alignment, e.g. in upper branches, or where point density might otherwise preclude the ability to pick out edges. Vertical exaggeration was performed at a magnitude of 20x original Z-axis height.

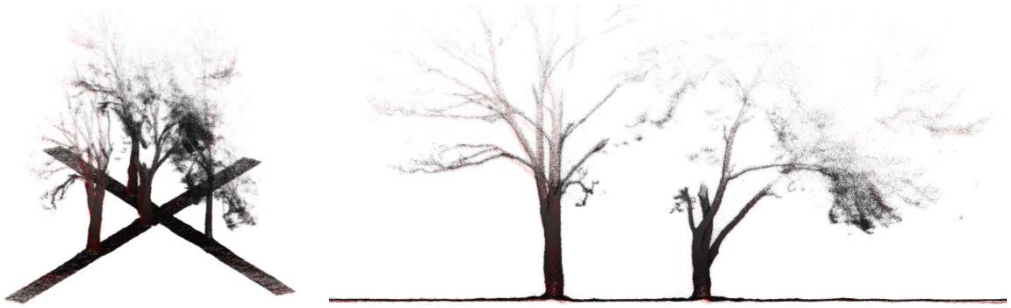

Figure 3.24: Oblique (**left**) and side profile (**right**) illustrations of alignment-checking cross-profiles extracted from HMLS data (black: reference; red: 10 m scan) acquired at the UVP field site. Each cross-section is 1 m wide.

Figure 3.25: Simulated example of misalignment between either different time portions of one scan, or between multiple scans.

Within this research, 'tree reconstruction' refers to the type and dimension of tree structure – stem, branches and twigs – resolved by HMLS sensors. In abstract terms, the parts of a tree that can be reproduced digitally in point cloud form by a given sensor in a particular set of circumstances. This is a qualitative measure as HMLS are not expected to detect objects sub-0.03 m in dimension (Bosse et al., 2012; GeoSLAM, 2018) and have limited range, a function of the laser hardware used in this sensor (Bauwens et al., 2016; GeoSLAM, 2018). As a result, only relative comparisons between the reference and isolated-variable scans were possible. This required exploring point density in 2D and 3D.

By cross-referencing point density at various parts of each tree, it was possible to locate where point density degraded such that objects could not be resolved. This also meant that a threshold 'maximum range' could be tentatively proposed.

2D density was calculated by projecting the number of points per cell into a raster dataset. This was done using the 'Rasterize' tool in *CloudCompare*. A cell size of 0.1 m was deemed most appropriate, balancing the need to preserve detail and information quality with limitations imposed by print resolution (e.g. 300 dpi required). More precise, 3D density estimates were carried out using the *CloudCompare* 'Density' tool. Here, the 'precise' method was applied and a radius set to 0.05 m (0.1 m diameter, superficially analogous to the 2D density calculation in spatial consideration of 'nearby' points). For output, volume density was chosen. Initial attempts to display these 3D plots on paper were unsuccessful, so representative slices were extracted from the density-coloured surface using the *Cross Section* tool, again in *CloudCompare*.

Two tests were devised to assess the maximum range of the sensor: a straightforward maximum height comparison and a three-dimensional distance of points from nearest trajectory. To assess maximum height, point clouds for each of the nine HMLS scans were individually processed in *3D Forest* and segmented into each of the four trees. The *Tree height* tool was then used to extract maximum tree height – height above a terrain-normalised surface. Measurement of the distance of points from the nearest trajectory was a more convoluted process, carried out entirely within *CloudCompare* and illustrated in **Figure 3.26** on the following page. A workflow was designed which required complete implementation one scan at a time. Initially, a scan and its corresponding trajectory files were imported and the 'Cloud-cloud distance' tool used to calculate an approximate three-dimensional distance with the trajectory file set as the reference. Once an initial, octree-based calculation had been completed, a more precise calculation was invoked. Finally, the colour ramp of the scan file was adjusted to match a new scalar field in which 3D distance-from-trajectory had been encoded for each individual point.

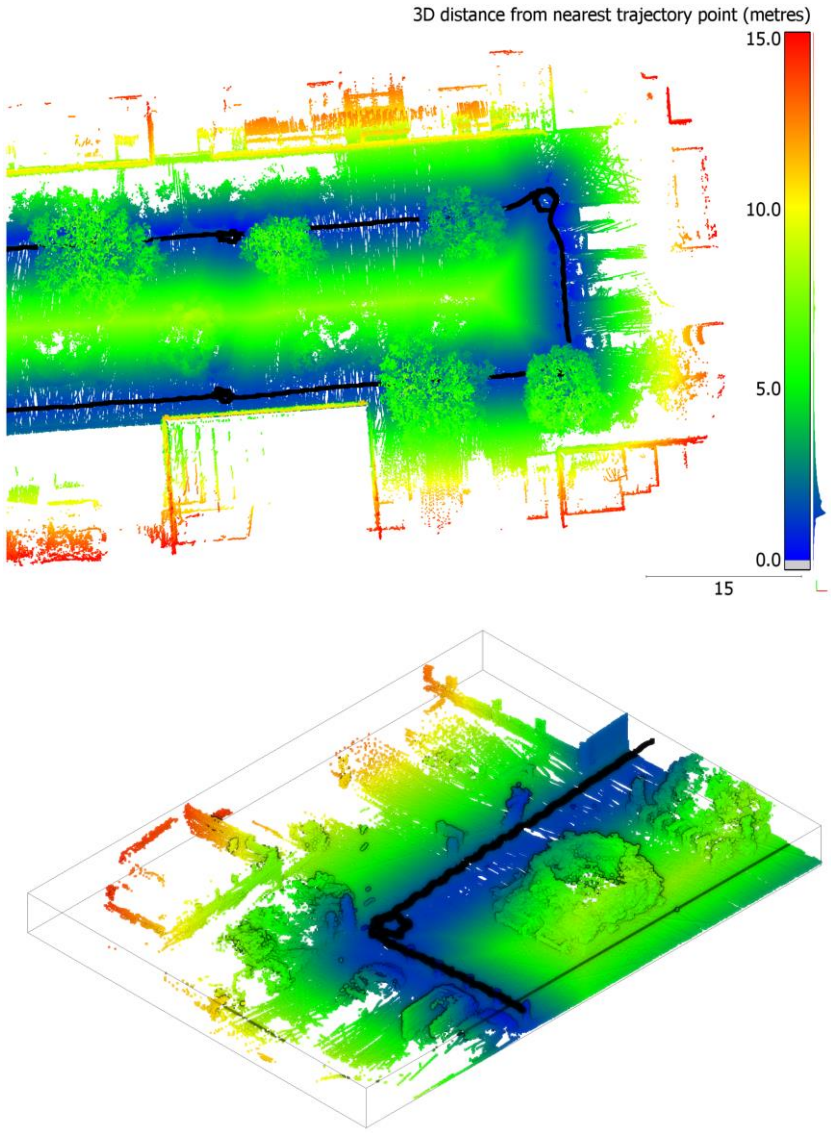

Figure 3.26: 2D plan (top) and 3D off-nadir (bottom) visualisations of a test scan acquired prior to UVP data capture, coloured by 3D distance-from-trajectory. Black points indicate trajectory points, themselves recorded in 3D space.

3.9 Data processing pipeline

Point clouds were obtained via multiple sensors: TLS (Leica P20), HMLS (GeoSLAM ZEB-1 and ZEB-REVO) and ALS (Environment Agency as third-party data provider). The various stages of data processing (pre-processing; alignment to a common grid; sensor fusion; classification; segmentation; extraction of 2D and 3D variables) are described in more granular detail over the following pages.

3.9.1 Data processing: hardware

A majority of the analysis and data processing within the research documented here was carried out on a bespoke data processing workstation. This workstation comprised of an eight-core Intel Xeon CPU, 64-bit Windows operating system, 64 GB DDR3-RAM and a dedicated GPU with 4 GB of RAM. The operating system was run from an OS-specific SSD and data stored locally on a separate SSD.

Additional processing was carried out on a Microsoft Surface 4 portable workstation. The specifications were substantially more restrictive, including a dual-core Intel i7-6500U CPU (2.2 GHz) and just 16 GB DDR3L-RAM. The GPU was an Intel Iris 540 chip with 1 GB dedicated RAM. Combined, the reduction in memory and processing capability limited the spatial extent of data which could pass through the processing pipeline.

3.9.2 Data processing: software

There are many software packages for processing and analysing LiDAR data, some commercial and others free and open-source (FOSS). Until recently, FOSS-licensed LiDAR software was dominated by relatively basic add-ons to GIS software. At the time of writing (July, 2018) several software packages incorporating tools for the extraction of information from point clouds were available. Of these, the overwhelming majority were commercial (e.g. Autodesk AutoCAD, Bentley PointTools, LAStools, and PointCab). Of the FOSS alternatives, a majority were command-line based. Whilst powerful, they did not offer fine-scale, interactive data manipulation at the object level precluding tasks such as manually identifying a tree branch common to separate scans. Command-line software were also of minimal use in manual point measurement (e.g. point-to-point distance). There was no way to task such software libraries to “measure the length of Branch A” or “calculate surface area of Feature B”.

Given the steady move toward ‘open access’ in science, this research advocates use of FOSS software. Several innovative software tools were identified and assessed including *CloudCompare* (2018), *Computree* (Othmani et al., 2011), *DendroCloud* (Koreň, 2017) and

3D Forest (Krůček et al., 2016; Trochta *et al*., 2017). The former is a powerful, user-interactive tool supporting import of almost all point cloud datasets and incorporating multiple generic and bespoke processing and analytical routines. *Computree* is a modular software package incorporating many modules, launched through nested scripts or via the command line. *DendroCloud* is a lightweight application designed to process and visualise TLS data for forestry applications (Koreň, 2017). *3D Forest* incorporates several forest-targeted algorithms including tree segmentation, DBH and height estimation, and calculation of crown geometry and volume. After a brief appraisal of software options, *3D Forest* was chosen as it was (i) the most intuitive, (ii) was easily installed, (iii) and offered real-time point cloud adjustment (removal of noise etc). It was chosen over other software (e.g. *Computree*; *DendroCloud*) as it worked out-the-box and had an intuitive graphical user interface.

In summary, a significant majority of LiDAR data processing was carried out using:

- *Leica Cyclone* (version 9.3.1)
- *CloudCompare* (versions 2.9.1 and 2.10.2)
- *3D Forest* (version 0.42)

3.9.3 Processing raw data to create unified point clouds

HMLS data were initially processed online via the *GeoSLAM Cloud* processing package which used a bespoke, black-box implementation of the SLAM (simultaneous localization and mapping) algorithm to self-register data within a common, local coordinate system (LCS). Output files included a self-registered point cloud and several auxiliary files including a simple polyline trajectory for each scan coloured by SLAM trajectory condition (i.e. quality). *GeoSLAM Cloud* is proprietary, 'black box' software with limited documentation on the specific processing steps undertaken and user interaction was limited to drag-and-drop to upload raw data and download processed data.

TLS data processing was rather more involved. The Leica P20 TLS can resolve targets at distances >100 m to a tolerance of +/- 0.006 m. Given that TLS instruments scan whilst

levelled, a target accuracy of 0.005 m was specified. To achieve this, high-precision, tripod-mounted black-and-white survey targets were randomly distributed throughout each study site during data acquisition. Targets were rotated in 3D space, each retaining a common 'dead centre' centroid position used to provide a series of three-dimensional vertex coordinates common in multiple scans. Each vertex was stored in a 'ModelSpace' database for each scan within *Leica Cyclone* (Leica HDS, 2017) software. An algorithm was initiated to best-fit scans together using these as tie points. Typical RMSE of registered scans was 0.001 m, occasionally degrading to 0.005 m where forest floor was less stable.

In certain scenarios, a fall-back 'cloud-to-cloud' visual registration approach was adopted. This was a manual process in which a 'master' and 'slave' point cloud were simultaneously rendered on-screen. The slave point cloud was manipulated in terms of rotation (about the Z axis; data were levelled by default) and translation (X and Y axes). Once the two clouds appeared to match both in plan and side elevations, an algorithm calculated statistical best-fit. Using this technique, RMSE remained between 0.001 m and 0.010 m, meeting survey specification. Coregistered scans were 'unified' in *Leica Cyclone,* removing redundant points to output a single point cloud at a user-selected resolution. The 'Unify' process downsampled the multi-scan point cloud at octree level, combining multiple points into a single point per unit area. This ensured all objects in 3D space were retained whilst a proportion of points were removed. This saved disk space and reduced RAM overheads in subsequent processing of the unified point cloud.

3.10 Fusion of multi-sensor datasets

A basic 'data fusion' workflow was devised to combine LiDAR datasets from different sensors. This allowed the development of a holistic, multi-sensor dataset combining ALS and HMLS data, offering similar spatial extent to reference TLS data.

3.10.1 Establishment of a common local coordinate system (LCS)

Of the LiDAR data acquired in this research, EA ALS was the only geocoded dataset. This data was considered the 'primary' dataset in context of geolocation, to which HMLS and TLS would be co-registered in 3D space. This was achieved using a 'visual registration' approach in *CloudCompare* in which the 'slave' TLS scan was 'dragged' by eye to align with ALS data, first vertically (from a side projection) and then horizontally (from an aerial perspective). Cross-sectional error checks implied data were matched to 0.1 to 0.01 m on the vertical plane and 0.1 to 0.2 m horizontally. *CloudCompare* works with 32-bit floating point numbers, and coordinates with precision in the region of 10^6 can be corrupted (CloudCompare, 2018) during certain geoprocessing routines. It is good practice to establish local coordinate systems when working with large-scale LiDAR to avoid the need to apply scale factors to datasets. A series of affine translation matrices were applied to EA ALS data once loaded into *CloudCompare* to reduce memory overheads, mitigating loss of precision associated with large coordinate values. An example matrix, used in the Tilgate Forest data processing, is reproduced below:

```
1.0   0.0   0.0   -526802.125
0.0   1.0   0.0   -132778.15625
0.0   0.0   1.0   -78.0
0.0   0.0   0.00  1.0
```

3.10.2 Multi-sensor point cloud coregistration

Prior to extraction of forest structural parameters, point clouds from different sensors were co-registered and georeferenced with respect to a global coordinate system and ellipsoid (OSGB 1936/Airy). Each dataset was considered internally registered –

demonstrably, in the case of TLS (with *Leica Cyclone* confirming scan registration accuracies of 0.001 to 0.005 m RMSE). In any given dataset, relative error was assumed minimal. Clouds were rotated and translated as individual entities about a centre of rotation defined as the centre of the point cloud bounding box. This was done in *CloudCompare* using the 'Rotate/Translate' tool. Prominent, overlapping geometries such as pathways, fences and low branches were used to align datasets. Where temporal intervals exceeded 60 minutes, non-natural features were used, minimising the effect of wind-blow. Vertical alignment was performed manually with a cross-sectional viewpoint, with one dataset 'dragged' about the Z-axis such that clear horizontal features (e.g. roads, prominent branches) were in alignment. Tie points were not required as no warping or distortion was necessary.

Although a visual process, results were good. Prior to analysis of coaligned data, alignment was verified - a crucial task when mapping dynamic environments such as forests, where data can be acquired in significantly different conditions. To assess vertical alignment, 2.5D meshes were created from each input dataset and pairs were iteratively compared using the cloud-to-mesh distance measurement tool. Only when datasets were vertically aligned to within several cm (residual error < 0.05 m) did they pass quality tests. To assess horizontal alignment, slices were iteratively cut through multiple datasets (e.g. 0 – 0.5 m; at DBH height; etc) and gross horizontal offsets measured on a point-to-point basis, with corresponding features identified across coaligned clouds.

3.10.3 Terrain normalisation

It is crucial LiDAR-derived relative heights are calculated with reference to a datum. Height measurements should not be made before a given point cloud has been terrain normalised (Calders et al., 2014). The Cloth Simulation Filter (Zhang et al., 2016), abbreviated to CSF, is a powerful example of such a tool, bundled as a plug-in with recent versions of *CloudCompare*. Although primarily designed for discrete, multiple-return ALS data, the tool has been applied to MLS data (Cai et al., 2018) and worked very well with both TLS and HMLS scans acquired throughout this research project. Upon initiation of the plug-in, several user options are selected and custom parameters then entered. For

the purposes of the UVP datasets, the scene 'Relief' was chosen and 'Slope processing' was also activated. A 'cloth resolution' – essentially raster resolution – of 0.1 m was selected. Default values for the number of iterations (500) and the classification threshold (0.5) were maintained and CSF ran. Upon completion, each scan was split into separate point cloud files: 'ground' and 'off-ground' (**Figure 3.27**, below).

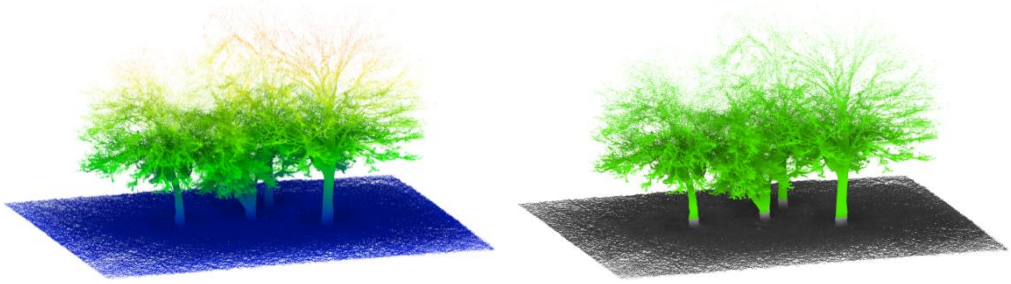

Figure 3.27: Visualisations of a UVP point cloud in *CloudCompare* before (**left**, coloured by height) and after (**right**: ground points are shaded grey, off-ground points shaded green) use of *CSF* to classify into ground and off-ground points.

These two files were compared via the 'Cloud-cloud distance' tool (**Figure 3.28**, below) with each fulfilling either the role of 'reference' (ground) or 'compared' (off-ground) cloud. As a result, a discrete vertical separation between each off-ground point and its closest neighbour in the ground layer was determined as stored in a new scalar field. Finally, the 'Apply scalar field to coordinate' tool was launched and height differences applied as height (i.e. passed into the *Z* axis field). Consequently, every off-ground point was reduced by the height of the ground layer above survey datum (in this case the scan origin, '0,0,0'). Each point cloud was 'sliced' horizontally at 0.5 m intervals. Slices were rendered from either east- or north-facing projections.

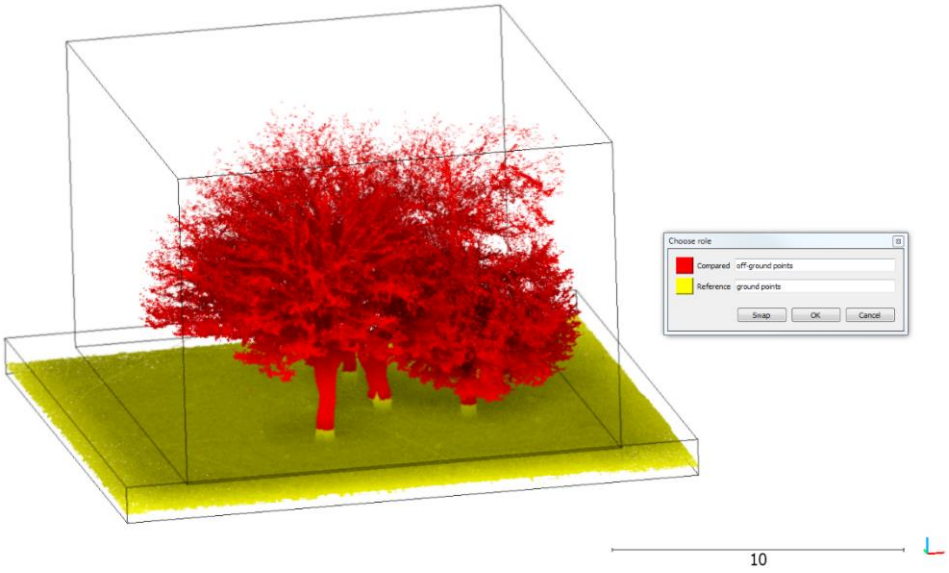

Figure 3.28: Visualisation of 'ground' and 'off-ground' points as input layers in an instance of *Cloud-cloud distance* calculation using *CloudCompare* software. Note that the respective bounding boxes do not overlap.

3.11 Semi-automated data processing using *3D Forest* software

3.11.1 Extraction of subplots and subsamples

TLS point clouds were downsampled to lower resolutions based on gross point count. As a rule, subplot data was reduced to 20,000,000 points per point cloud section using the *CloudCompare* 'subsample' tool and specifying the 'random' method. To each subsample, slices comprising full-resolution data, set-aside prior to downsampling, were merged back into the downsampled data. Slices encompassed full-resolution data between 1 and 3 m above ground. This 'multi-resolution' approach preserved individual tree geometry, as well as point density at DBH height, whilst optimising the quantity of RAM (random access memory) needed by *CloudCompare* and *3D Forest*. Geometry was preserved due to the octree-based algorithm retaining a point (per unit area) for every occupied octree cell. So, whether a tree crown apex was depicted by 1 or 1 000 points, the uppermost octree would persist with at least a single point at its centre. With Stratfield Brake (USB-C) data an additional, fixed (2.5 m) maximum height cut-off was also applied. This was due to (a) the significant point density associated with a low canopy (distance between points is a function of distance of an object from the scanner) as well as (b) intersecting crowns. The

phenomena of intersecting and 'touching' tree clouds repeatedly led *3D Forest* to crash during segmentation. Clipping the cloud at a 2.5 m height resolved this problem.

Subplots were extracted from HMLS data based on SLAM condition as stored in trajectory files, ranging from 'good' (blue) through to 'poor' (red). It proved difficult to quantify SLAM condition objectively given minimal documentation (GeoSLAM, 2016) but appeared optimal where trajectory loops were frequently closed and encompassed regular overlap. However, not all areas of 'good' condition matched reference TLS data. In some scenarios, homogenous forest structure 'spoofed' the SLAM algorithm into depicting some trees multiple times. These errors were consistent with jumps in scan trajectory where the surveyor may have temporarily lost their footing. The *CloudCompare* 'cross section' tool was used to physical extract subplots. Sites were located at random by defining a random coordinate pair within scan coordinates using a random number generator (Haahr, 2018). These values were used to define plot centre and requisite subplot dimensions (width, length) were then manually entered.

3.11.2 Definition of 'a tree' as a spatial object

The definition of a 'tree' in a biological context is straightforward. Defining a tree in terms of data structure proved more complicated as semantic meaning does not readily apply to irregular data like point clouds. So specific to this research, a tree was defined as:

> *A dense, columnar cluster of points extending in a direction broadly perpendicular to the 'terrain layer', to which it is connected by means of adjacent points within a user-defined threshold distance.*

All points belonging to a tree had to be within a threshold maximum distance (a user-determined parameter required for *3D Forest* segmentation). Secondly, the points within a segment had to resemble a cylinder. This meant that incomplete stems - cross-sections resembling parabola rather than circles – would be misclassified as 'non-tree vegetation' or 'noise'. Incomplete stems prevented *3D Forest* DBH algorithms from functioning correctly. Detail on the threshold values applied to the various subplots explored in this research can be found further in the chapter.

3.11.3 Working within resource limitations

Although not documented in the *3D Forest* user manual, limitations in terms of point cloud size (memory; spatial extent) were identified. Independent of resolution, point clouds greater than 400 m^2 in extent seemed to render the software unstable. Point counts >30,000,000 points also destabilise the software. In many cases, the application froze and crashed altogether – particularly when analysis moved from a high-power HP workstation to a more commercial-off-the-shelf Microsoft Surface 4 laptop part way through the research. A decision was therefore made to extract subplots from co-aligned point clouds to ensure transferability and repeatability of data and analysis, irrespective of platform or workstation configuration.

3.11.4 Semi-automated classification: vegetation and terrain

Prior to segmentation, *3D Forest* required point data to be classified into discrete 'vegetation' and 'terrain' point clouds. This was achieved through automated octree-based division decreasing to a user-input minimum. **Figure 3.29** (following page) illustrates this process iteratively with three different minimum-octree dimensions. The coarser octree resolution is, the greater the likelihood of vegetation being misclassified as terrain. With octree size as large as 1 m, sections of tree stem (bottom-right) were classified as terrain. Any parameters subsequently extracted from data would be erroneous due to consequential height underestimation.

There was a delicate balance to be struck between precision (fine-scale octrees) and preservation of vegetation. Perfect classification would result in an almost-continuous terrain surface with points >0.001 m above the terrain layer preserved as vegetation. Heights and height derivatives would then fall within absolute precision of the TLS sensor (e.g. RMSE of 0.001 m after optimal co-registration). In practice, an octree of 0.1 m proved sufficient for most terrains.

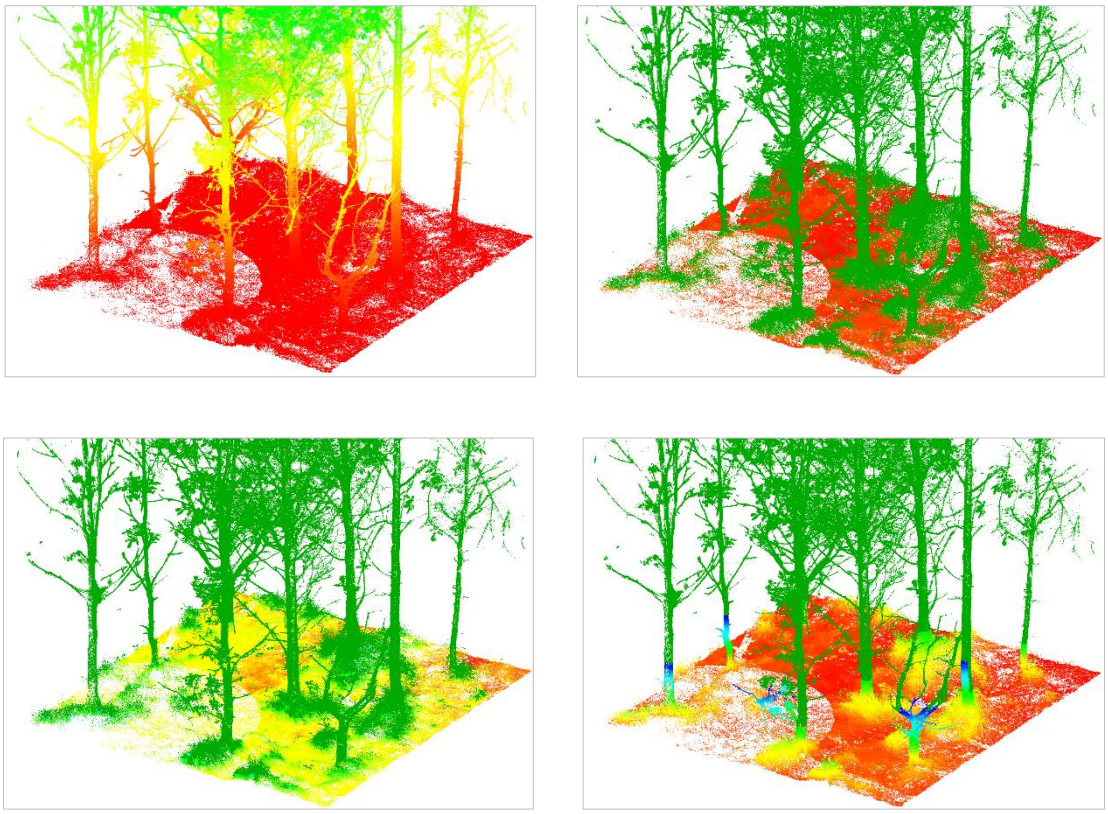

Figure 3.29: Oblique-angle illustrations of point cloud classification in *3D Forest* based on a sample of TLS data from USB-C. **Top-left**: raw point cloud coloured by height. **Top-right**: vegetation (green) and terrain (coloured by height) with octree size set to 0.05 m. **Bottom-left**: as previous, with 0.1 m octree. **Bottom-right**: as previous, with octree at 1 m.

3.11.5 'Vegetation' point cloud segmentation

Two approaches were applied sequentially: semi-automated, k-means nearest-neighbour clustering and manual-refinement based on iterative polygonal 'fences' isolating point cloud segments. Both were performed in *3D Forest*, unique in offering automated classification and manual adjustment in a single application. **Figure 3.33** (page 91) defines the workflow developed within this research to segment TLS and HMLS point clouds into individual-tree segments.

The subplots were pre-processed (to remove noise and other artefacts) then segmented within *3D Forest*. This led to the creation of individual, tree-specific point clouds and facilitated semi-automatic extraction of forest parameters – here, DBH and tree height among others. The 'Automatic segmentation' tool was then used to segment the layer

into individual trees. Within the UVP field datasets, an input distance of 0.15 m and a minimum points-per-cluster value of 100 were chosen based on initial experimentation. These settings were used for all scans acquired at the site. Elsewhere – the UEP, USB and UTF sites – different values were applied. The input variables used where defined through iterative experimentation on a qualitative basis. It was not possible to find a pair of input values that segmented all trees with no errors of omission or commission.

An effect of applying a low input distance was that outlier points at the top of the crown were often discarded as these points were most widely separated due to distance from sensor. Conversely, increasing the input distance meant that multiple trees were sometimes misclassified as a single tree. The maximum value used across all data was 0.5 m (UEP, where tree separation was greater) and the minimum 0.05 m (TLS acquired at UTF). Trees that physically touched neighbouring trees proved problematic – especially the case USB field site. In addition, occlusion caused problems associated with commission error. Points describing the same tree were sometimes segmented into two or more 'trees' where the shadow zone dimension exceeded the minimum point separation applied in the algorithm.

Each point cloud was measured in one, two and three dimensions and compared with TLS reference data. Bias, RMSE and other comparative statistics were then calculated. Two approaches were applied, in series: a semi-automated method based on k-means nearest neighbour clustering implemented within *3D Forest* and a manual-refinement technique based on iterative use of polygonal 'fences' to isolate point cloud segments for storage in separate files. Both were performed within *3D Forest,* unique at the time experiments were designed (September 2017) in offering automated classification and manual adjustment without needing third-party software. User interaction for the semi-automated approach was minimal with two user-defined parameters required: input distance and the minimum point count per segment. In many cases, manual refinement was required. Only points definitively belonging to a tree would be retained; the remainder would be stored separately as 'noise'. **Figure 3.30** (on the following page) illustrates this refinement.

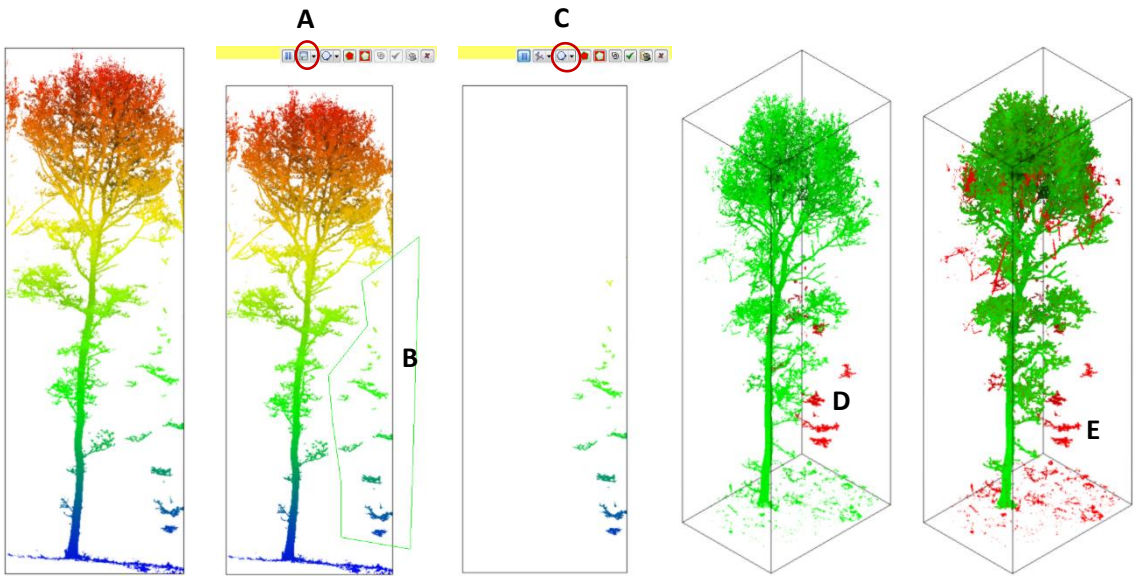

Figure 3.30: worked example of segment refinement as applied to a tree acquired by TLS in the USB-C subplot

The 'activate polyline selection' (**A**) tool was selected and a polygonal 'fence' (green line; **B**) was drawn around points requiring removal. The 'segment' tool (**C**) was used to isolate points within the fence in 3D space. This split the parent point cloud into 'remaining' (green) and 'segmented' (**D**; red) child point clouds. Removed points were merged and saved externally. Retained points were reimported to *3D Forest* as 'tree' point clouds for DBH estimation and derivation of 2D and 3D measurements. Further refinement continued until all points surplus to requirement were isolated (**E**).

Figures 3.31 and **3.32** illustrate two separate field plots which were successfully segmented and manually refined where appropriate. The full segmentation workflow is summarised in **Figure 3.33**, a flowchart, on page 91.

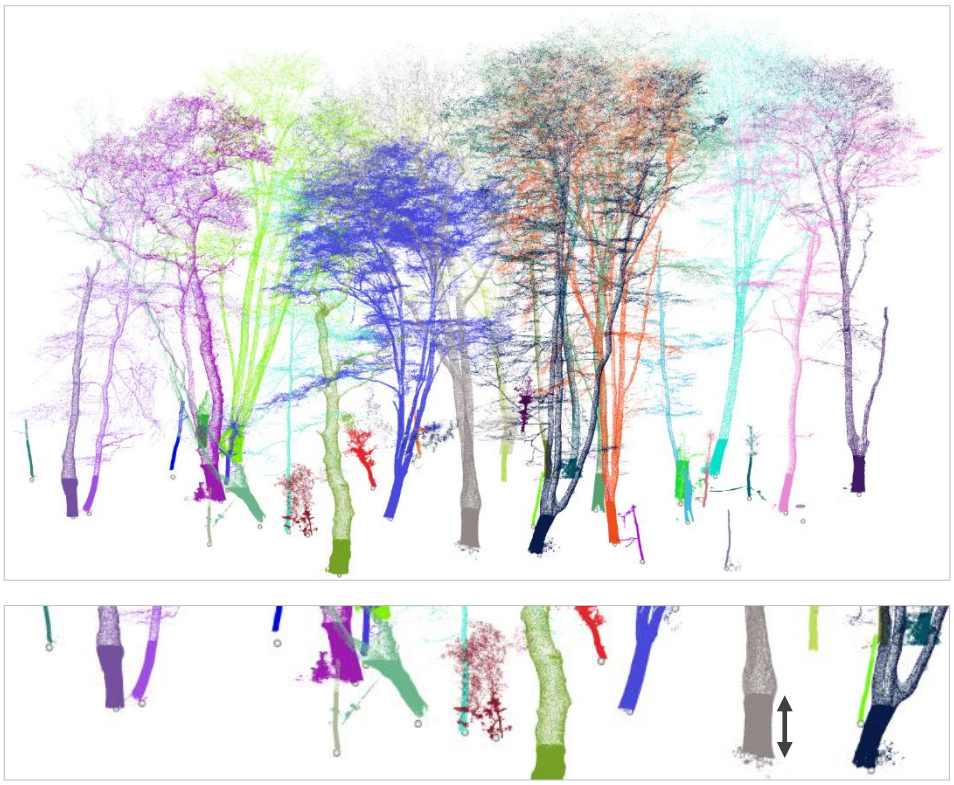

Figure 3.31: Segmented TLS point cloud of UEP-BW illustrating the fusion of two-resolution point clouds into a single file.

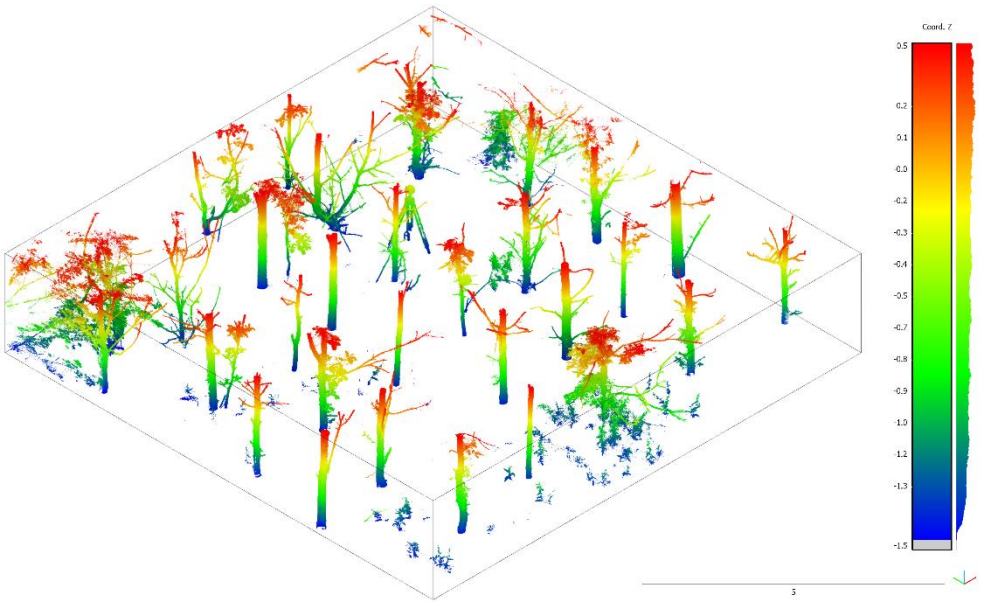

Figure 3.32: Subset of points acquired with the TLS (USB-C sub-plot) extracted between heights of 0.5 and -1.5 m with regard to the survey datum. Within this 10 x 10 x 2.5 m subset were 31 individual tree stems.

Figure 3.33:

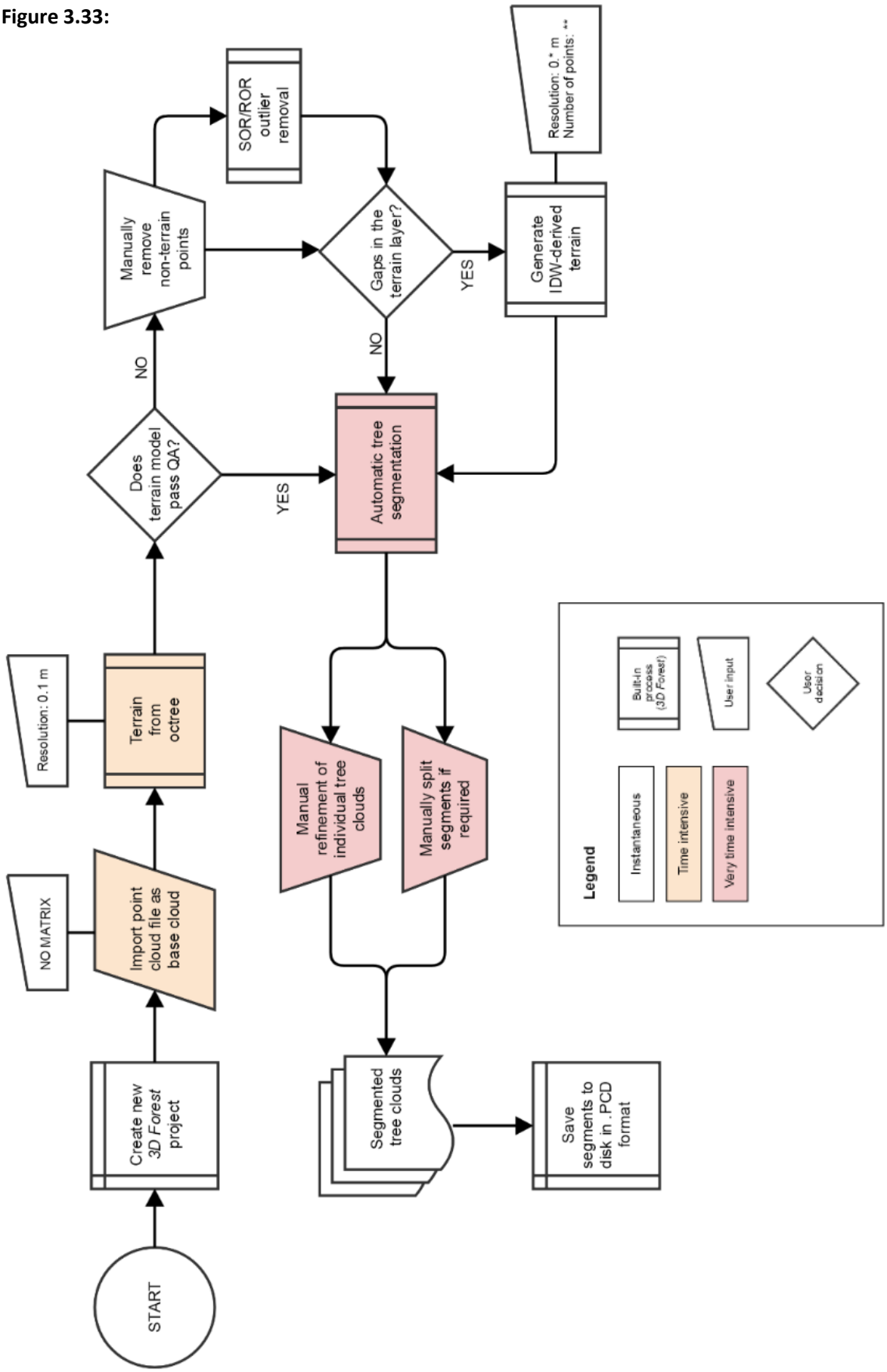
START
Create new 3D Forest project
Import point cloud file as base cloud
NO MATRIX
Terrain from octree
Resolution: 0.1 m
Does terrain model pass QA?
NO
YES
Manually remove non-terrain points
SOR/ROR outlier removal
Gaps in the terrain layer?
NO
YES
Generate IDW-derived terrain
Resolution: 0.* m
Number of points: **
Automatic tree segmentation
Manual refinement of individual tree clouds
Manually split segments if required
Segmented tree clouds
Save segments to disk in .PCD format
Legend
Built-in process (3D Forest)
User input
User decision
Instantaneous
Time intensive
Very time intensive

3.12 Extraction of 2D biophysical parameters

3.12.1 Stem position (more on manual approach)

Tree centroid locations were located most accurately using the 'Position lowest points' function. Here, after iterative experimentation, a threshold value of 0.5 m input as 'height above lowest point' was found to be optimal. In each case, a value of 20 points was input as the number to be recruited from the terrain model in deriving the lowest point and hence tree position. The 'Randomised Hough Transform' and 'Least Squares Regression' centroids were derived from semi-automated extraction of DBH, detailed below.

3.12.2 Diameter at breast height

To extract DBH from tree segments in *3D Forest*, the DBH RHT and DBH LSR tools were used (Krůček et al., 2016; Trochta et al., 2017). When calculating DBH with the RHT method, the number of iterations was left at the default value of 200, which yielded good results. There was no user input required for the alternative, LSR-based, method. A benefit of performing this semi-automatic derivation of DBH via a GUI (graphical user interface) such as *3D Forest* was that it was possible to manually edit DBH point cloud slices on-the-fly.

Upon segmentation, segments identified as trees were isolated and the 'position lowest points' algorithm initiated to generate tree centroids. Required parameters included the nominated terrain model, a threshold upper height limit (set at 0.6 m above ground) within which tree stem 'centroids' would be mapped, and a maximum number of points for the centroid search to include (with 50 found to be optimal value). These attributes were used across all tree segments. Both DBH estimation algorithms implemented in *3D Forest* - RHT (Randomized Hough Transformation) and LSR (Least Squares Regression) - were then applied consecutively. RHT accuracy was influenced by number of iterations with higher values (e.g. 2000) comparing better against reference TLS data than the default value (200), albeit at the cost of a marginal increase in processing time. As an example, mean processing time for a 10 x 10 m point cloud (USB-C) was 5 minutes and 20 seconds. LSR DBH estimation required no user-parameter inputs and mean processing

time for the same plot was 7 seconds. Documentation and literature (Krůček et al., 2016; Trochta et al., 2017) suggested the RHT algorithm would be most accurate. Both algorithms were run side-by-side and DBH estimates were cross-referenced via scatterplots to determine fit with respect to the 1:1 line. RMSE was also calculated.

An independent validation exercise was conducted in *CloudCompare* to ensure results obtained via *3D Forest* were realistic. Per-sensor tree data (saved to .PCD-format point cloud files) were imported into *CloudCompare,* fused at plot-level, coloured by sensor and terrain-normalised (0.2 m mesh created with the 'rasterize' tool). Cloud-to-mesh (C2M) distance was calculated between the fused point clouds and the terrain mesh associated with each sensor-plot pair. The resultant 'difference' values were passed into the Z-axis field as normalised height and a horizontal slice was automatically extracted with a height range of 1.2 m to 1.4 m above the normalised terrain surface. This effectively created a plot-level DBH cloud. From these, individual trees were randomly selected for validation. Manual measurements were made using the 'point-to-point measure' tool for each of these trees, with target points selected visually. As validation was less-precise than cylinder fitting as per the RHT and LSR algorithms, values obtained were ephemeral (not stored in memory) but in all cases, manually measured DBH fell within 95% of *3D Forest*-derived estimates. Where there was disagreement, extraneous points (i.e. branches/noise at DBH height) led to sampling bias in *3D Forest*; outlier points were not included in manual validation.

To test potential relationships between semi-automated DBH estimates processed in *3D Forest*, separation of successfully segmented trees common to both TLS and HMLS datasets was required, discarding trees only present in a single dataset. This was achieved by manually matching estimated tree centroids and identifying matching pairs within a visual threshold. Pairs that matched were spatially joined using GIS. Unique among the field sites included within this research was what can best be described as 'stem complexity' inside the USB-C subplot. This sub-plot was scanned by all three instruments: TLS, HMLS1 and HMLS2. As the trees were all 20 to 21 years of age (Woodland Trust, 2018), branches emerged from tree stems below DBH height. Due to the interconnected nature of the canopy – all trees were of similar height and individual crowns intersected

one another – initial attempts to segment the sub-plot proved unsuccessful. Of thirty-one trees included in the subplot, twenty-one exhibited this unique trait. The consequence was that DBH estimates were, to some extent, exaggerated where the *3D Forest* algorithms included branch points in the stem point cloud subsets. These 'complex' stems are depicted in **Figures 3.34** (below) and **3.35** (next page). Points >2.5 m above ground were removed, maintaining geographical separation between points associated with each tree. Despite this, sufficient structure for DBH estimation (points between 1.2 and 1.4 m above ground) was retained. The resultant vertically clipped plot was terrain-normalised using a mesh created using 'CSF' in *CloudCompare*, before extraction of a horizontal slice (red points in **Figures 3.34** and **3.35**). This is analogous to the way *3D Forest* derived DBH clouds using both the RHT and LSR algorithms.

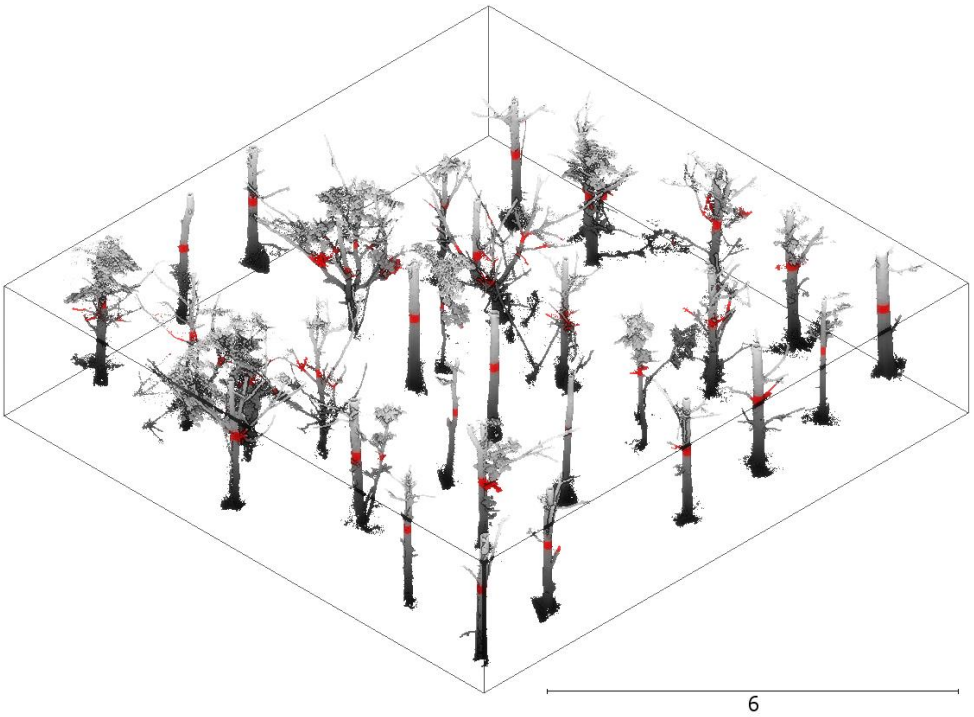

Figure 3.34: 'Front' view of the USB-C sub-plot extracted from the TLS reference dataset. Stems were truncated at 2.5 m above the lowest point to remove interconnection between adjacents stems and branches; they are shaded black fading to grey (with increasing height). The red points denote 'DBH height' (1.2 to 1.4 m above lowest point) and indicate that some points not directly associated with tree stem contribute to DBH overestimation.

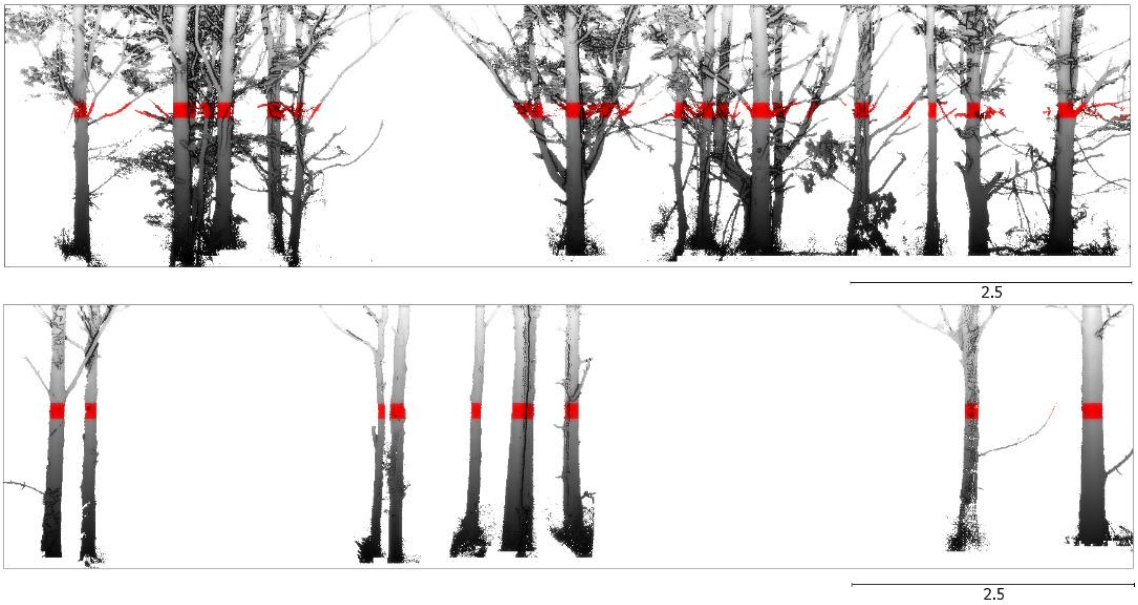

Figure 3.35: Side-view of the USB-C TLS sub-plot. In the uppermost panel, only 'complex'-structured trees are represented. 21 in total, these are the trees where DBH estimates were biased with the presence of non-stem material at DBH height. The lower panel shows only 'simple'-structured trees, 10 overall, where DBH estimates appeared accurate compare to manual mensuration within *CloudCompare* software.

3.12.3 Tree height

Tree height was calculated as the distance between the highest point of a given tree segment and the estimated position of a tree stem centroid. Tree height was estimated in *3D Forest* using the 'Compute tree height' tool. Results were displayed on-screen (as per **Figure 3.36**, below) and exported with other biophysical variables to a series of *CSV* files.

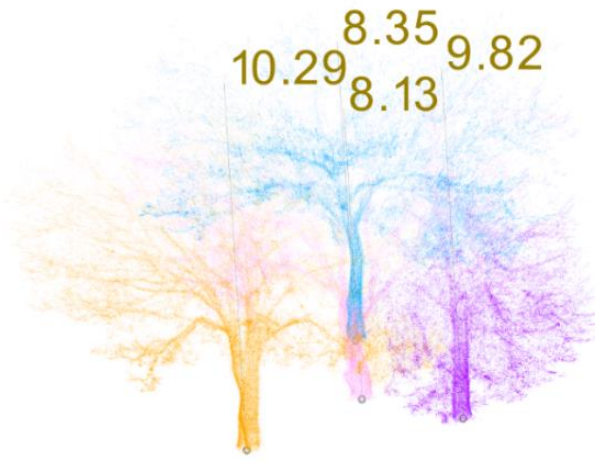

Figure 3.36: Tree height and tree position as derived using *3D Forest* software.

3.13 Extraction of 3D biophysical parameters

Three-dimensional object measurement was computationally intensive and quite challenging. Two approaches were tested: mesh-based and voxel-space volume estimation. Of the mesh-based approaches, two were applied: a convex hull technique applied to outermost points and a cross-sectional (higher-detail, akin to 'shrink wrapping' a crown) convex hull technique. The former was relatively swift whilst the latter required substantial processing effort. The cross-sectional approach required a user-specified cross-section depth to be applied – with smaller values causing slower data processing. A 'sweet spot' of 1 m was identified as optimal after iterative testing from 0.1 to 5 m.

3.13.1 *3D Forest*-derived biophysical parameters

3D Forest can extract various biophysical parameters at tree level. Several of these focussing on crown measurement were calculated from HMLS data within this research:

- Number of points per crown
- Crown height
- Crown bottom height
- Voxel volume
- Volume of concave hull sections
- Surface area of concave hull section meshes
- Volume of 3D convex hull
- Surface area of 3D convex hull

The processing workflow designed to extract 3D measurements from segmented TLS and HMLS data is illustrated in **Figure 3.37** overleaf. Note that at separate stages of the workflow, substantial processing time was required. Automated crown selection required substantial (>1 hour for 5 trees) processing time despite use of a high-specification workstation. Furthermore, *3D Forest* was prone to intermittent crashing, requiring significant repetition of processing. Unfortunately, as the software stores derived variables in RAM and not to storage media, data was lost each time the software crashed.

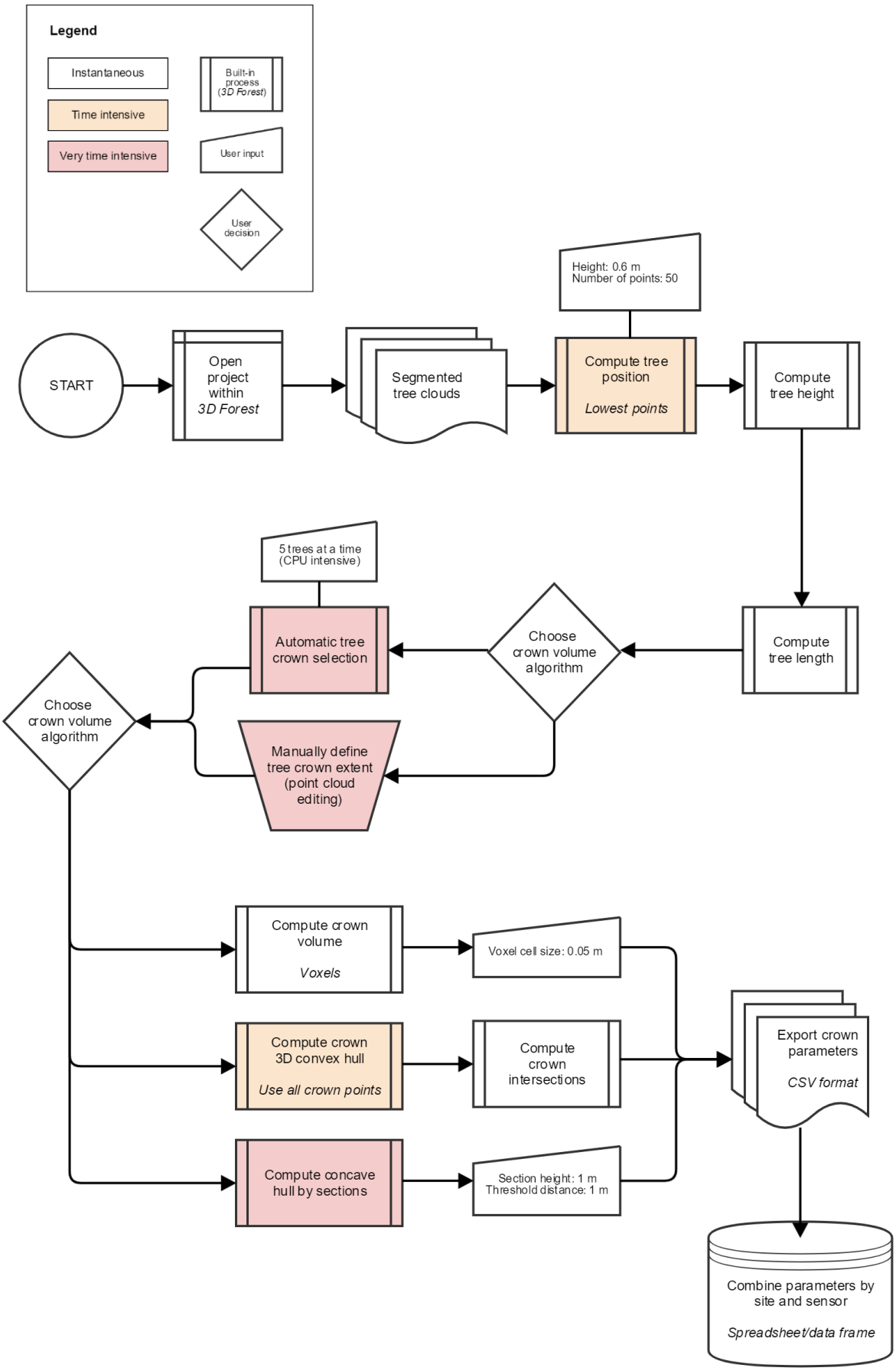

Figure 3.37: Flowchart describing the workflow for 3D measurement of tree crowns using *3D Forest* software. Refer to page 78 for detailed workstation specification.

3.13.2 Stem volume

In the literature search, stem volume was identified as a key parameter not commonly extracted from LiDAR data due to computational complexity. In this research, considerable effort went into developing a workflow (**Figure 3.38**, below) capable of resolving volume meshes. This was typically done in high-end commercial software but in 2018, a release of *CloudCompare* included a mesh-based volume estimation tool for the first time. After much trial and error, the below workflow was devised. There were numerous parameters at each of the processing steps. Overall, the biggest hurdle seemed to be computation of 'normals' (see ***2. Literature review***). Where normals were correctly computed, the software was able to correctly model the 'outside' of the stem and develop roughly cylindrical meshes. Where normals were ineffectively computed, the Poisson Reconstruction meshing algorithm (Kazhdan and Hoppe, 2013) created all manner of bizarre shapes and structures – doughnut or bone-shaped the most common.

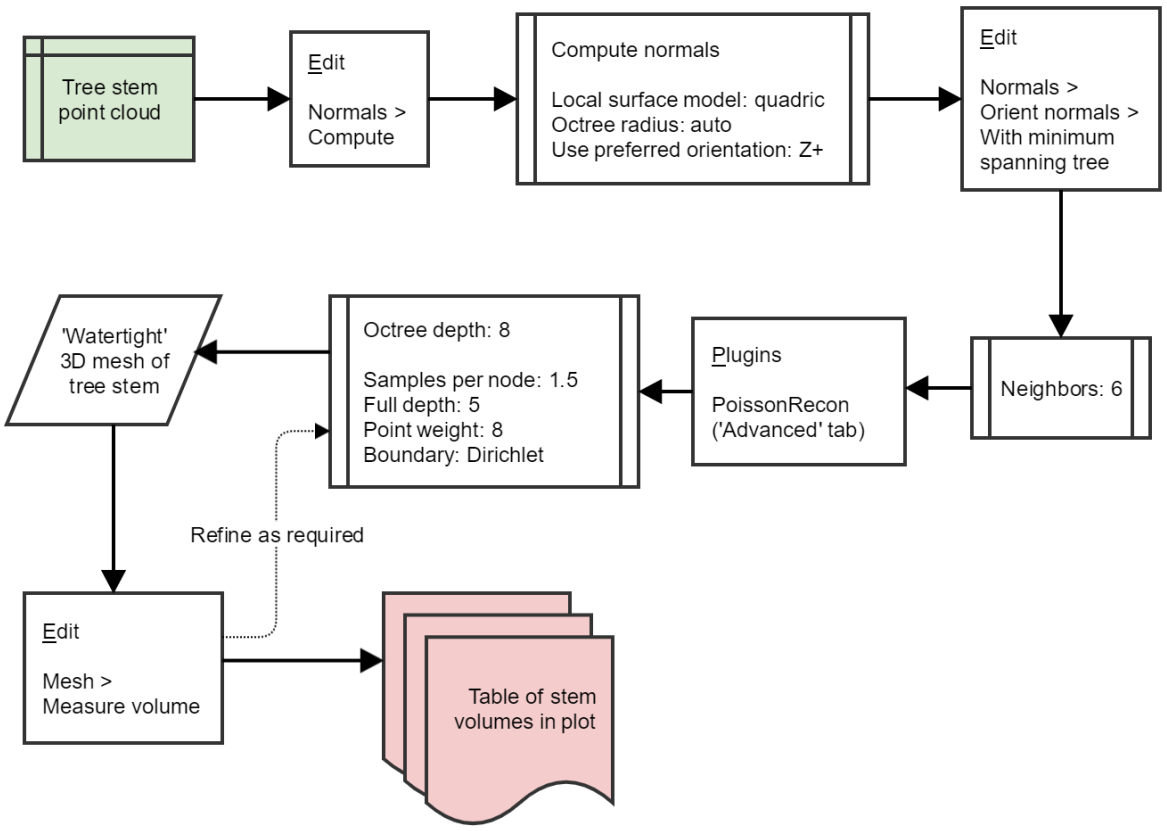

Figure 3.38: Experimental workflow designed to measure the volume of 2 m sections of tree stem using meshing via the Poisson Surface Reconstruction plug-in (*CloudCompare)*.

To verify these volume estimates were plausible, stem volume estimates were calibrated using the formula:

$$Volume = \pi r^2 h$$

In this equation, *r* represents stem radius and *h* height of the stem point cloud. **Figure 3.39** demonstrates there was a good level of agreement (R^2 of 0.893 for HMLS meshes and 0.760 for TLS meshes), suggesting the mesh-based approach is of some merit.

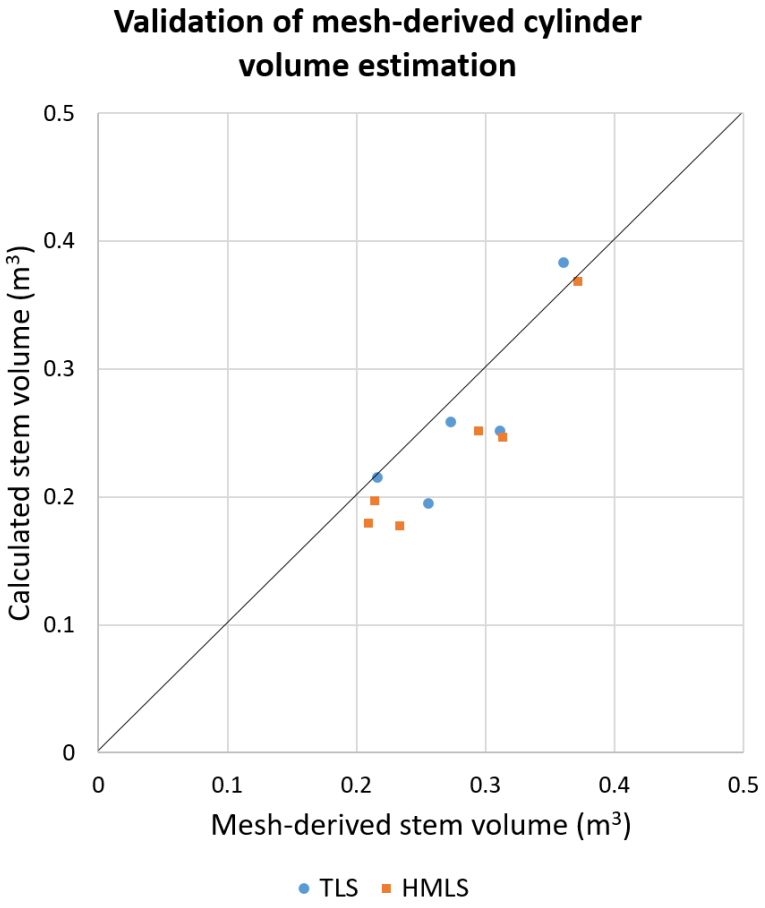

Figure 3.39: Scatterplot validating the stem volume approach. Manually calculated volume estimates (cylinder volume formula) were compared with mesh volume. For the HMLS comparison, R^2 was 0.893. For TLS R^2 was 0.760. However, this could feasibly be due to a poor fit at the DBH estimation stage.

3.14 Summary

This chapter set out to detail equipment, methods and the many processing stages devised, developed and refined throughout this body of research. Whilst it is difficult to condense four years of research methods into a single chapter, these topics were covered. The structure of the chapter was introduced graphically in flowchart format and followed with a detailed justification for the selection of study sites and field plots in each. Sensors and instrumentation were then technically described and field operations chronicled. Crucial to this research was the development a new protocol (in the absence of relevant literature) for the mapping of forested areas with a handheld SLAM-based scanning technology (***3.7 Experimental data*** and ***3.8 Isolation of parameters***). At the time this research began, there had been no published research on this topic – and at the time of writing there are fewer than 10 such studies. Another methodological innovation was the leveraging of the *3D Forest* software package, among other free and open source applications, to develop 'turnkey' solutions for the extraction of useful forestry information from rapidly acquired point data.

Over the following three chapters, these methods are applied to handheld, terrestrial and airborne LiDAR to answer the three research questions detailed in ***2. Literature review.***

4. Object-based measurement using HMLS

At the time of writing - May 2018 - few studies had been published using HMLS sensors in forest environments (Ryding et al., 2015; Bauwens et al., 2016; Oveland et al., 2018; Cabo et al., 2018a). These studies were limited in that they only described relative accuracy of DBH measurement, overlooking over forest structural measurements. In the context of forest inventory, none of the studies offered insight or information in terms of the smallest-size tree an HMLS sensor might detect. Additionally, neither study had objectively sought to determine what other tree measurements might be derived from HMLS data. Hence a need to quantify the size of trees and tree components which could be detected was identified. Building on the cited studies, the results presented in this chapter sought to determine which tree measurements both HMLS sensors could make. Furthermore, despite the opportunity to explore operational efficiencies mapping forested areas with HMLS, the cited studies each encompassed no more than a pair of single-loop scans. None of these articles sought to define a threshold 'minimum' object size or explore how the geometry of an HMLS scan might influence such a threshold.

4.1 Research aims

The aim of this chapter was to determine how well HMLS sensors performed in the context of object detection and measurement. Specifically, it examined performance of the GeoSLAM ZEB-1 and ZEB-REVO sensors. Accuracy was determined through direct comparison with TLS and field inventory (e.g. caliper) data. Trees of various size and shape, spanning different species across multiple forests, were scanned by the two HMLS sensors and compared with reference, multi-scan TLS-derived datasets. Each tree was extracted from a subset ('subplot') of larger-area scans, to mitigate hardware limitations. Subplots varied in size to preserve a consistent sample size (20 to 30 trees per subplot) and to mitigate the technological limitations identified in the pilot study.

4.2 Research question

> ***RQ1**: What forest inventory variables can be measured with HMLS sensors? What is the magnitude of error inherent in these measurements when compared with a reference, TLS-derived dataset?*

4.3 Results for RQ1

These results seek to answer RQ1 and are presented in the order in which they were derived within the documented workflows. The first section includes the results of point cloud classification and segmentation, followed by semi-automatically derived tree parameters. Hereafter an experimental series of one-, two- and three-dimensional measurements made interactively within the *3D Forest* application are presented in considerable detail. **Figure 4.1** on the following page 'maps' the sequence of result generation, some of which are reasonably novel.

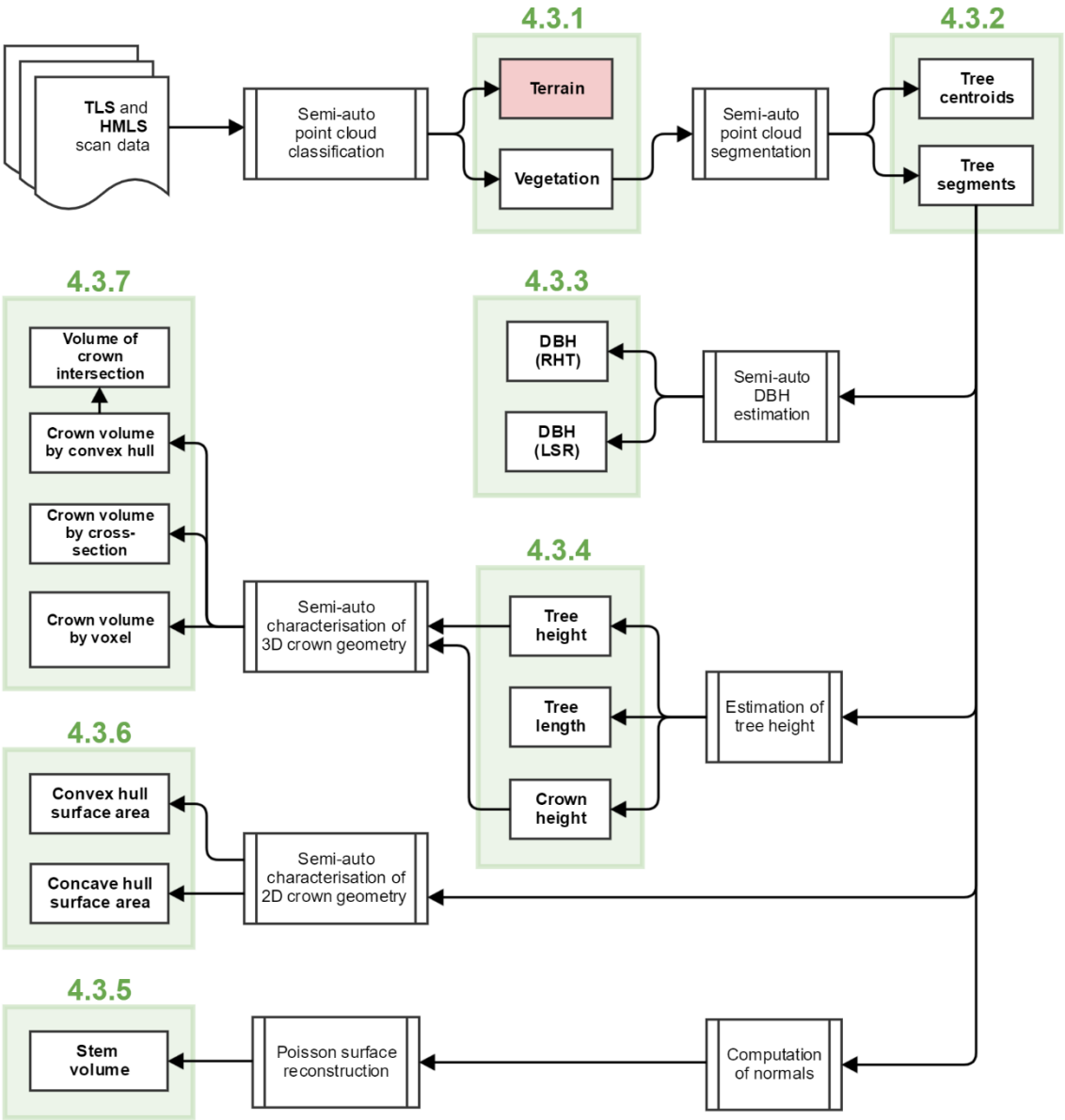

Figure 4.1: Flowchart illustrating the variables (plain white boxes) and results chapter subheadings (annotated green boxes). Boxes with double-sides indicate processing stages, as previously documented.

With the exception of 4.4.5 (stem volume), all results were derived from point cloud data in *3D Forest*. Terrain (red) is not a result itself.

4.3.1 Semi-automated point cloud classification

Each dataset - one per sensor - was separately imported into *3D Forest* and stored in an individual, dataset-specific project. Classification into 'terrain' and 'vegetation' was also performed project-by-project and the user parameters applied varied with each scan. These settings are described in **Table 4.1**.

Table 4.1: Settings for *3D Forest s*emi-automated point cloud classification

Site	Plot	Sensor	Method	Resolution	Terrain model
Epping Forest	UEP-BW	TLS	Octree	0.1 m	Default
		HMLS1		0.05 m	IDW
		HMLS2		0.1 m	Default
Stratfield Brake	USB-C	TLS			
		HMLS1			
		HMLS2			
Tilgate Forest	ROK	TLS			
		HMLS2			

The results of semi-automated point cloud classification are presented on a subplot-by-subplot basis. First, the proportion of points assigned to each class is summarised (**Tables 4.2**, **4.3** and **4.4**, on the next page). In each, the 'noise' column refers to points manually removed from the 'terrain' later post-classification – typically associated with discrete clusters of understorey vegetation. Note that in the UEP-BW TLS and both UTF-ROK HMLS2 datasets, terrain was extracted using the CSF algorithm and subsampled at 0.01 m resolution in *CloudCompare*. This helped mitigate the effect of dense understorey vegetation on accurate terrain modelling and reduced the size on disk of point clouds. By doing this, the risk of software crashing due to high RAM demand was reduced.

These tables are followed with three-dimensional renderings of post-classification results on a per-sensor basis. UEP-BW is illustrated in **Figure 4.2** (overleaf). This is followed by USB-C in **Figure 4.3** (also overleaf). Finally, the two UTF-ROK subplots – north and south – are illustrated in **Figures 4.4** and **4.5** (pages 108 and 109).

Table 4.2: Output point counts for post-classification **UEP-BW** data

	Number of points per point cloud			
Sensor	*Raw*	*Terrain*	*Vegetation*	*Noise*
TLS	*21,346,449*	817,500 (**3.7**%)	20,584,550 (**96.3**%)	*369,732*
HMLS1	*6,364,811*	2,673,358 (**42.0**%)	3,691,593 (**58.0**%)	*182,340*
HMLS2	*4,278,501*	2,586,081 (**60.4**%)	1,691,926 (**39.6**%)	*263,692*

Table 4.3: Output point counts for post-classification **USB-C** data

	Number of points per point cloud			
Sensor	*Raw*	*Terrain*	*Vegetation*	*Noise*
TLS	*17,658,743*	8,697,369 (**49.3**%)	8,961,374 (**50.7**%)	*176,741*
HMLS1	*1,158,208*	428,530 (**37.0**%)	729,702 (**63.0**%)	*177,534*
HMLS2	*430,936*	205,630 (**47.7**%)	225,276 (**52.3**%)	*25,764*

Table 4.4: Output point counts for post-classification **UTF-ROK** data

	Number of points per point cloud			
Sensor	*Raw*	*Terrain*	*Vegetation*	*Noise*
TLS N	*13,930,689*	6,727,724 **(48.3**%)	7,202,965 (**51.7**%)	*684,400*
TLS S	*13,252,828*	5,762,812 (**43.5**%)	7,562,016 (**57.1**%)	*110,751*
HMLS2 N	*583,050*	48,737(**8.4**%)	534,313 (**91.6**%)	*83,235*
HMLS2 S	*614,270*	20,373 (**3.3**%)	593,897 (**96.7**%)	*23,596*

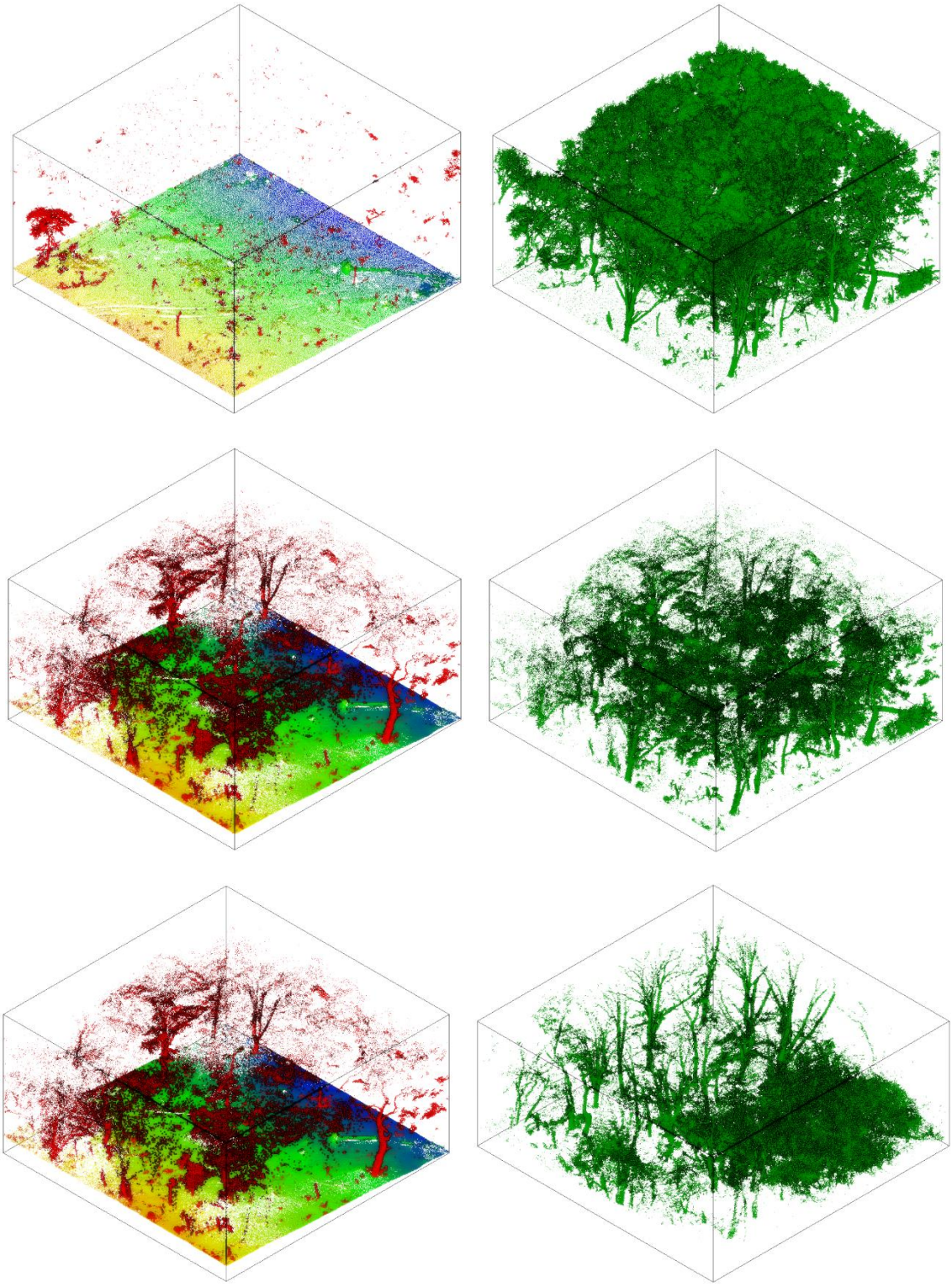

Figure 4.2: Visualisations of the UEP-BW sub-plot datasets, acquired using all three sensors (TLS, HMLS1, HMLS2). Each bounding box is 40 x 40 with varying height.

Left panels: terrain (rainbow colour ramp) and non-vegetation points (red). **Right** panels: vegetation (green) pre-segmentation.

Top row: TLS; **middle** row: HMLS2 (ZEB-REVO); **bottom** row: HMLS1 (ZEB-1).

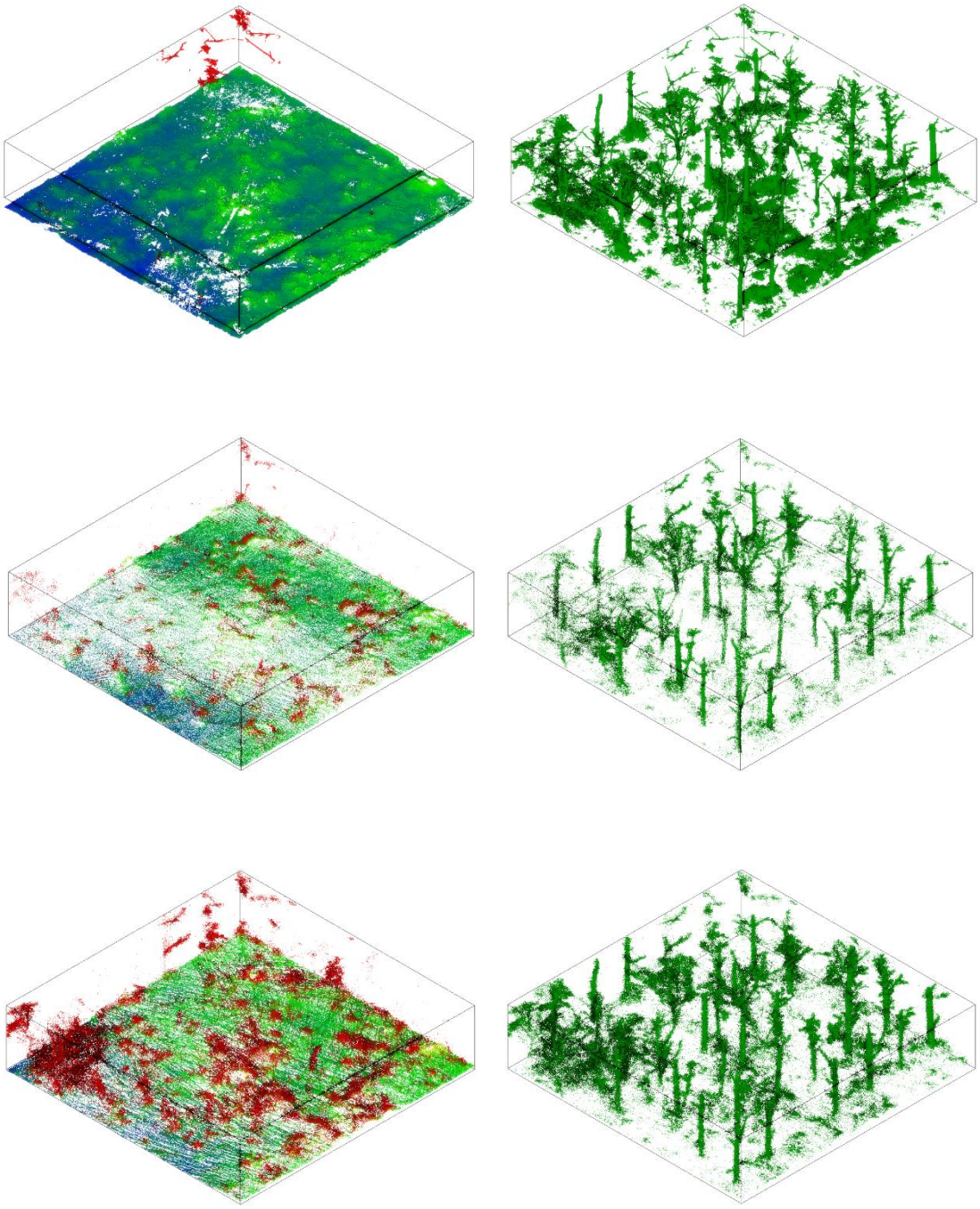

Figure 4.3: Visualisations of the USB-C sub-plot datasets, acquired using all three sensors (TLS, HMLS1, HMLS2) at a temporally coincident window of opportunity (July 2016). Each bounding box is 10 x 10 x 2.5 m in dimension. Number of points per category are summarised in **Table F** on the previous page.

Left panels: terrain (rainbow colour ramp) and non-vegetation points (red).
Right panels: vegetation (green) pre-segmentation.

Top row: TLS; **middle** row: HMLS2 (ZEB-REVO); **bottom** row: HMLS1 (ZEB-1).

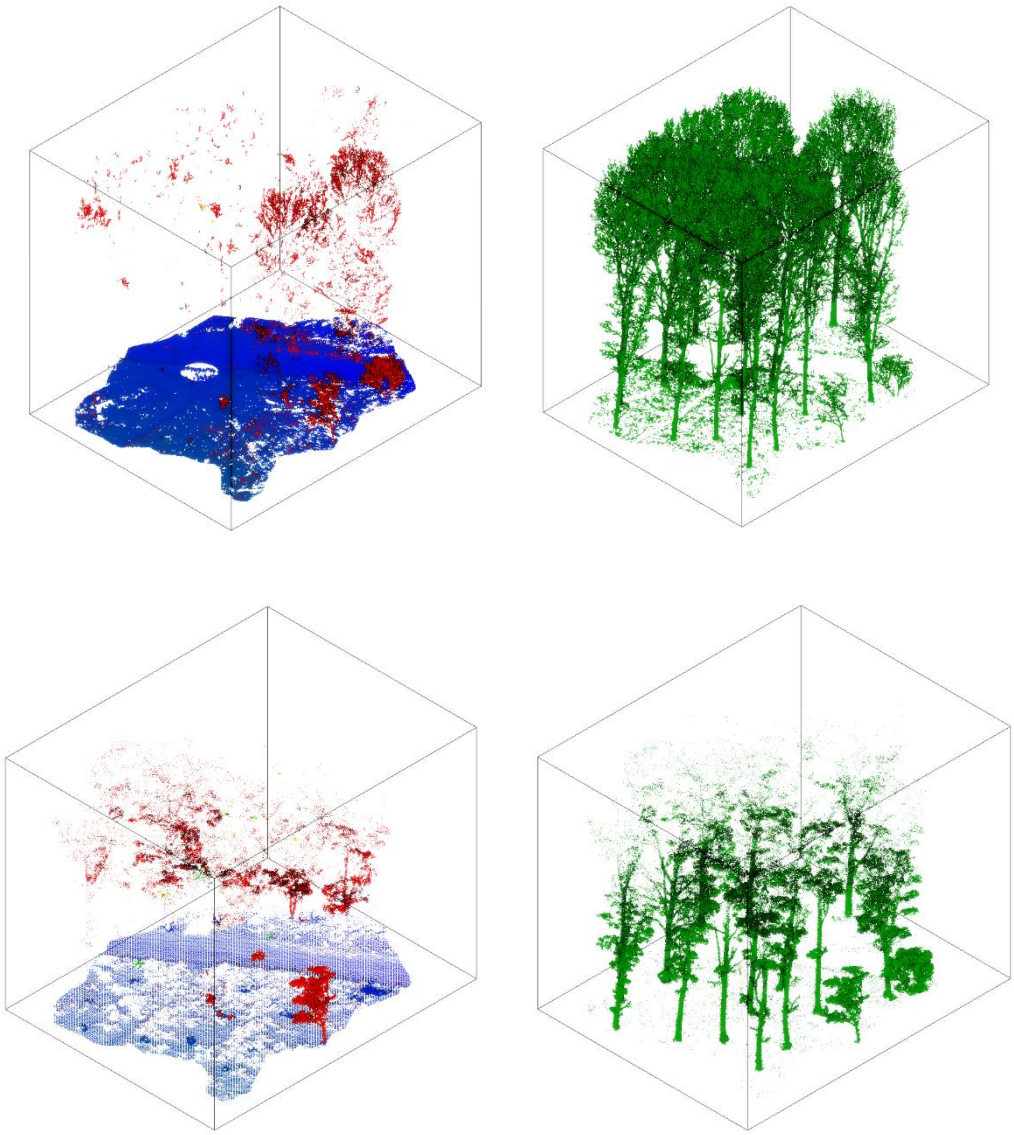

Figure 4.4: Visualisations of the UTF-ROK-North sub-plot datasets, acquired using TLS (P20, in 'leaf off' conditions) and HMLS2 (ZEB-REVO, in 'leaf on' conditions). Each bounding box is 20 x 20 m in dimension with varying height. Number of points per category are summarised in **Table F** on the previous page.

Left panels: terrain (rainbow colour ramp) and non-vegetation points (red).
Right panels: vegetation (green) pre-segmentation. **Top** row: TLS; **bottom** row: HMLS2.

Note the substantial variation in terrain layer point density. Also note the greater range of the TLS, evidenced by a more-detailed depiction of tree crowns. In both UTF-ROK-North and UTF-ROK-South, data were clipped to crown extent to mitigate against edge effects.

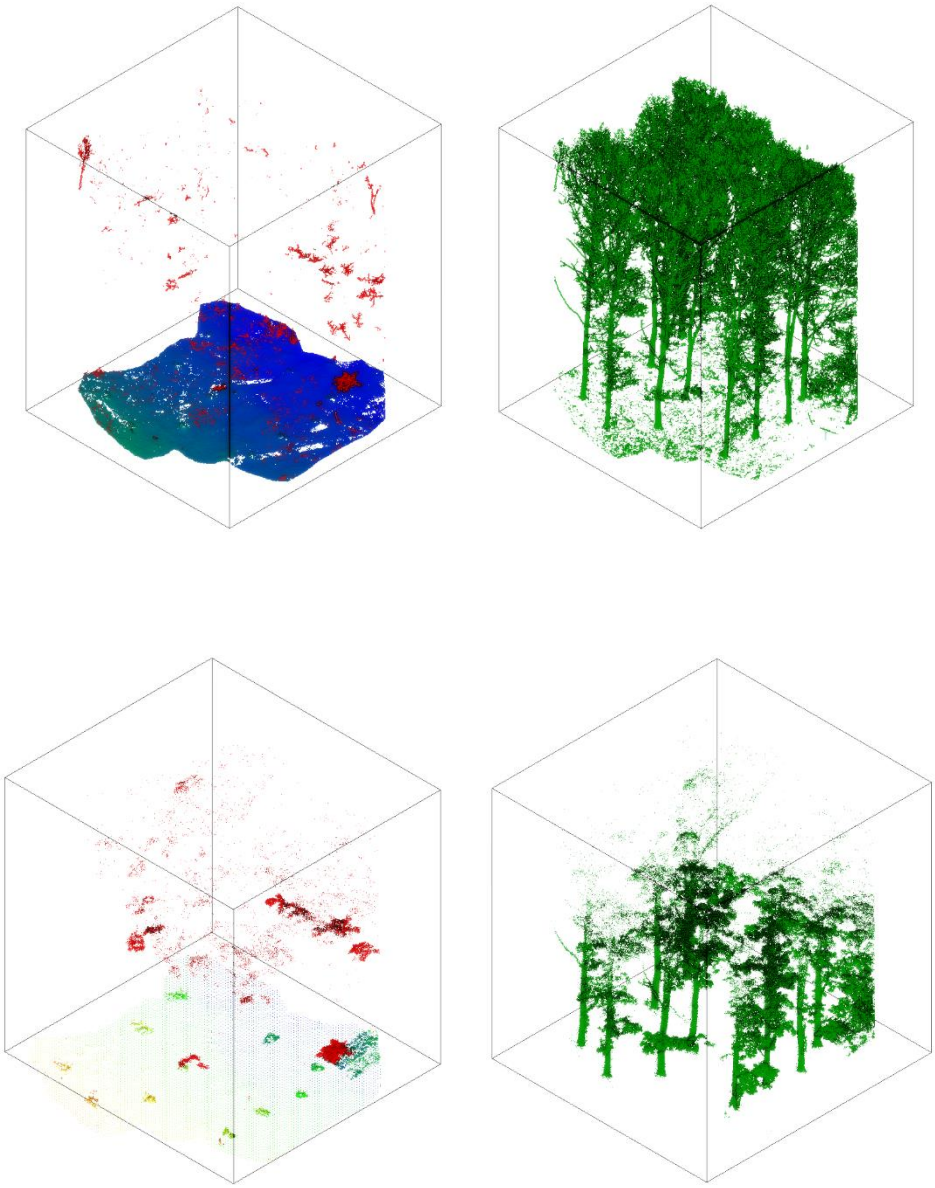

Figure 4.5: Visualisations of the UTF-ROK-South sub-plot datasets, acquired using TLS (P20, in 'leaf off' conditions) and HMLS2 (ZEB-REVO, in 'leaf on' conditions). Each bounding box is again 20 x 20 m in dimension with varying height. Once again, the TLS demonstrated a much better range in terms of its ability to resolve crown structure.

Left panels: terrain (rainbow colour ramp) and non-vegetation points (red).
Right panels: vegetation (green) pre-segmentation. **Top** row: TLS; **bottom** row: HMLS2.

4.3.2 Semi-automated point cloud segmentation

Once again, data processing in *3D Forest* was applied in a dataset-by-dataset approach. Segmentation parameters varied per sensor due to different point cloud geometry and point spacing but remained consistent between sub-plots. **Table 4.5** summarises the variables applied. Application was per project – with each row of the table denoting an individual *3D Forest* project.

Per project, segmentation averaged roughly 120 minutes in duration, with TLS-based projects taking an order of magnitude more time to process than HMLS equivalents. UEP-BW projects were notably slower, perhaps also due to the spatial (40 x 40 m) extent of each subplot. Where raw TLS data was imported, segmentation repeatedly failed. It is therefore recommended that a degree of downsampling is applied to TLS data prior to its import into *3D Forest*.

Table 4.5: Input parameters and output point counts for UEP-BW data

Site	Sensor	Input distance	Minimum points per cluster
UEP-BW	TLS	0.10 m	1000
	HMLS1	0.10 m	500
	HMLS2	0.10 m	500
USB-C	TLS	0.10 m	1000
	HMLS1	0.10 m	500
	HMLS2	0.10 m	500
UTF-ROK	TLS N	0.10 m	1000
	TLS S	0.10 m	1000
	HMLS2 N	0.15 m / 0.05 m	500 / 50
	HMLS2 S	0.15 m	500

Epping Forest, pre- and post-holly clearance

The UEP-BW dataset can be considered as two subplots as two time periods are reflected in the data: a large volume of holly in the form of understorey vegetation, pre- and post-removal by the Epping Forest stewardship team. TLS data were acquired both before and after this holly clearance. Meanwhile, HMLS1 was acquired with holly *in situ* and HMLS2 was acquired with no holly present. This meant significantly fewer stems were scanned in HMLS1 data - some stems were occluded by the abundance of holly. Segmentation of TLS and HMLS1 was successful on the first run. HMLS2 data, meanwhile, required manual adjustment (**Figure 4.7**, overleaf) as unexpected proximity of points from adjacent trees influenced segmentation success. Stem centroids for each segment are depicted in **Figure 4.6** below. Note the relative lack of HMLS1 centroids (these trees rendered invisible beyond the holly due to occlusion).

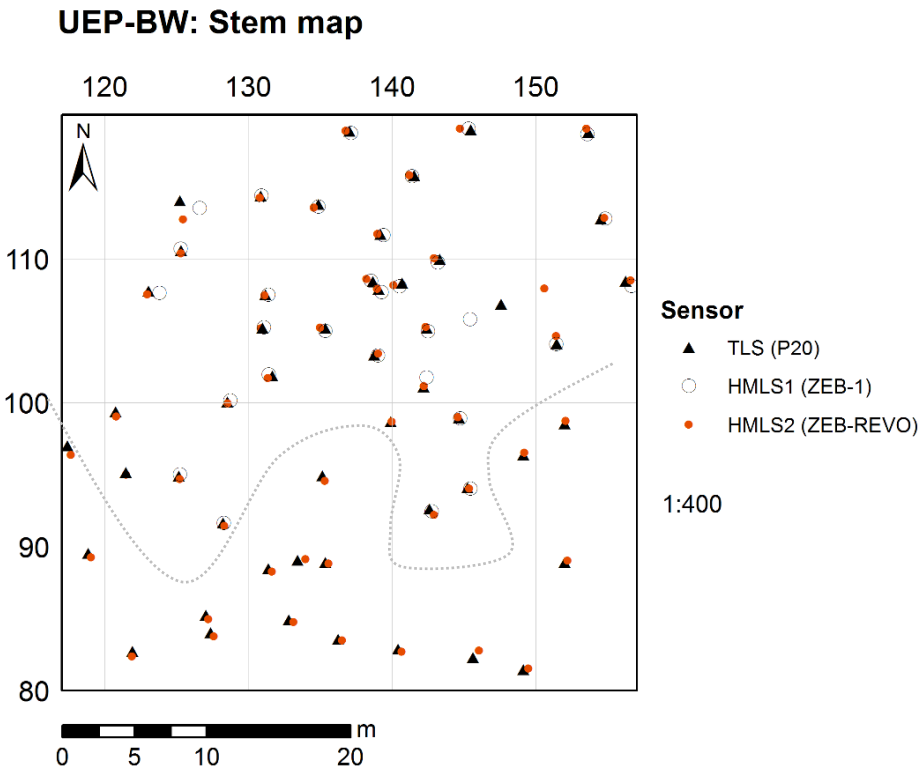

Figure 4.6: Map of stem centroids, as derived in *3D Forest* using the 'Position lowest points' algorithm. Coordinates refer to the origin coordinate of the first scan captured – the HMLS1 scan (pre-extraction of subplots). The dotted grey line marks the boundary of holly pre-removal – holly was extant south of the line. 'Up' reflects north.

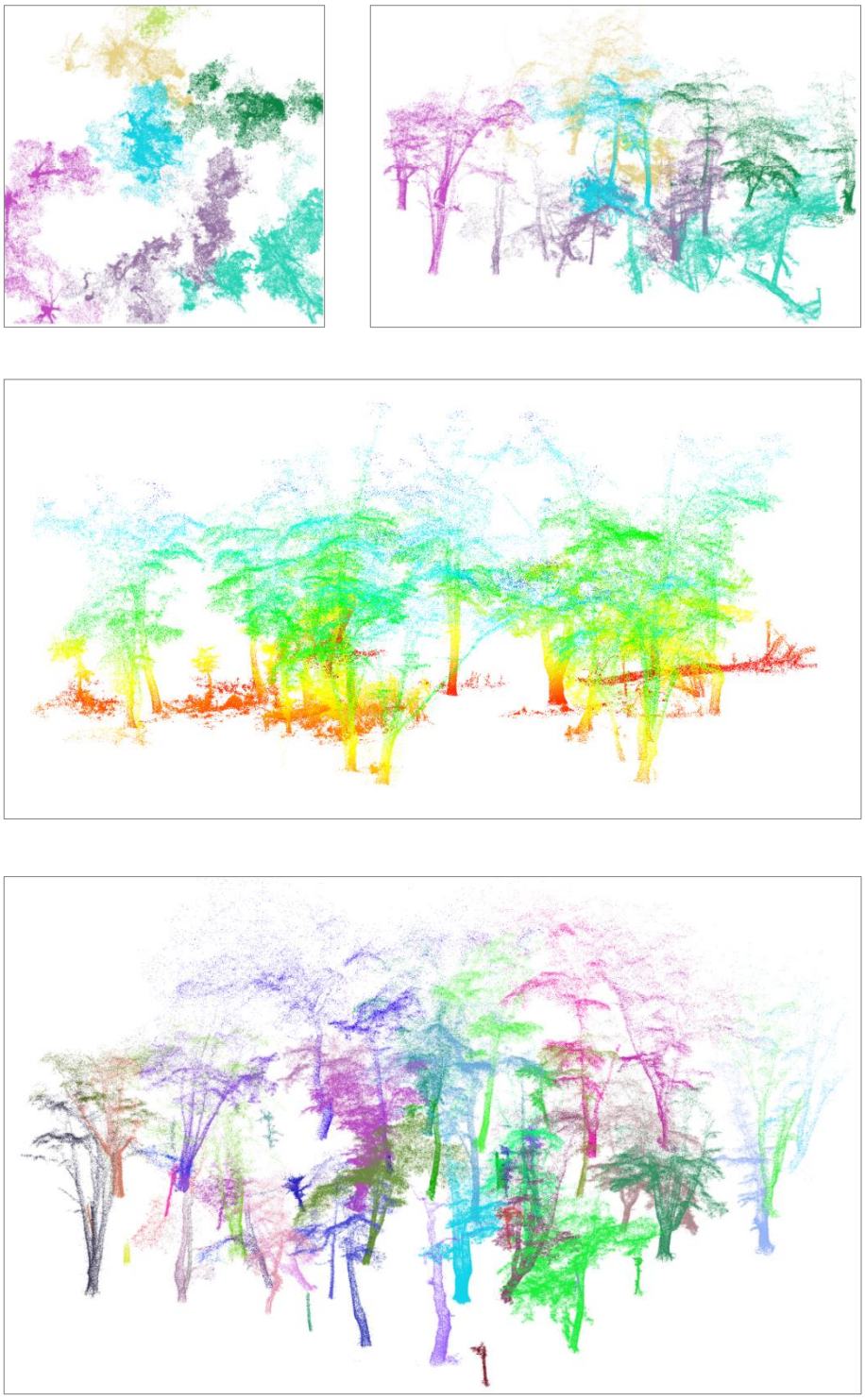

Figure 4.7: Plan (**top-left**) and oblique (**top-right**) renders of UEP-BW from ZEB-REVO HMLS data, depicting 7 clusters. Due to close proximity of points within the canopy, the algorithm could not distinguish between certain trees - so each cluster contains multiple trees. These 7 clusters were merged (**middle**; coloured by height) and individual trees manually extracted. In total, 56 trees which matched reference scan (TLS) segments were identified and are illustrated (**bottom**) coloured by segment. 4 of these were later removed as their complexity prevented *3D Forest* crown height detection from functioning correctly.

Stratfield Brake

All three sensors – TLS, HMLS1 and HMLS2 - were used at the Stratfield Brake site. Each sensor was deployed within a four-week window, ensuring tree structure and geometry remained stable between scans. All scans were co-aligned to within 0.1 m of one another and from each scan, a 20 x 20 m sub-plot was extracted. As the crowns of most trees in the plot were connected (branches fell within 0.1 m of one another), sub-plots were vertically clipped at 2.5 m above the lowest point. This removed crown data and ensured the segmentation algorithm could run in an optimal manner with minimum point thresholds tweaked to suit segmentation at the ground-level.

Upon segmentation, the reference TLS dataset detected 31 trees and several incomplete tree components which were removed. This was due to 'edge effects' where the bounding box of the 20 x 20 m plot intersected with trees whose stems lay beyond the box. The relative position of tree centroids retained is illustrated in **Figure 4.8**, below. Overleaf, **Figure 4.9** illustrates segmentation results per-sensor.

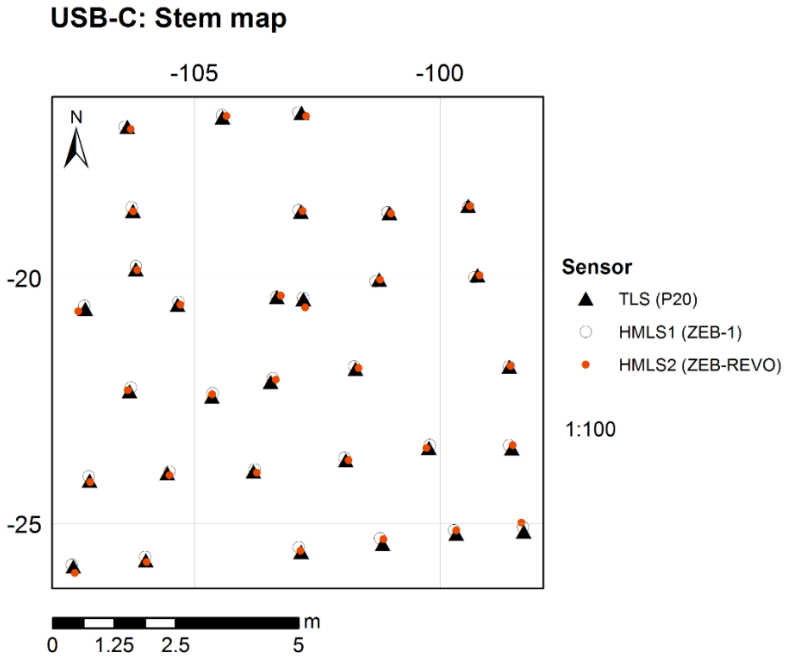

Figure 4.8: Another map of stem centroids. All 31 trees within the subplot were successfully detected in all three scans. Stems were correctly located with any X-Y offsets here a result of bias from the presence of understorey vegetation.

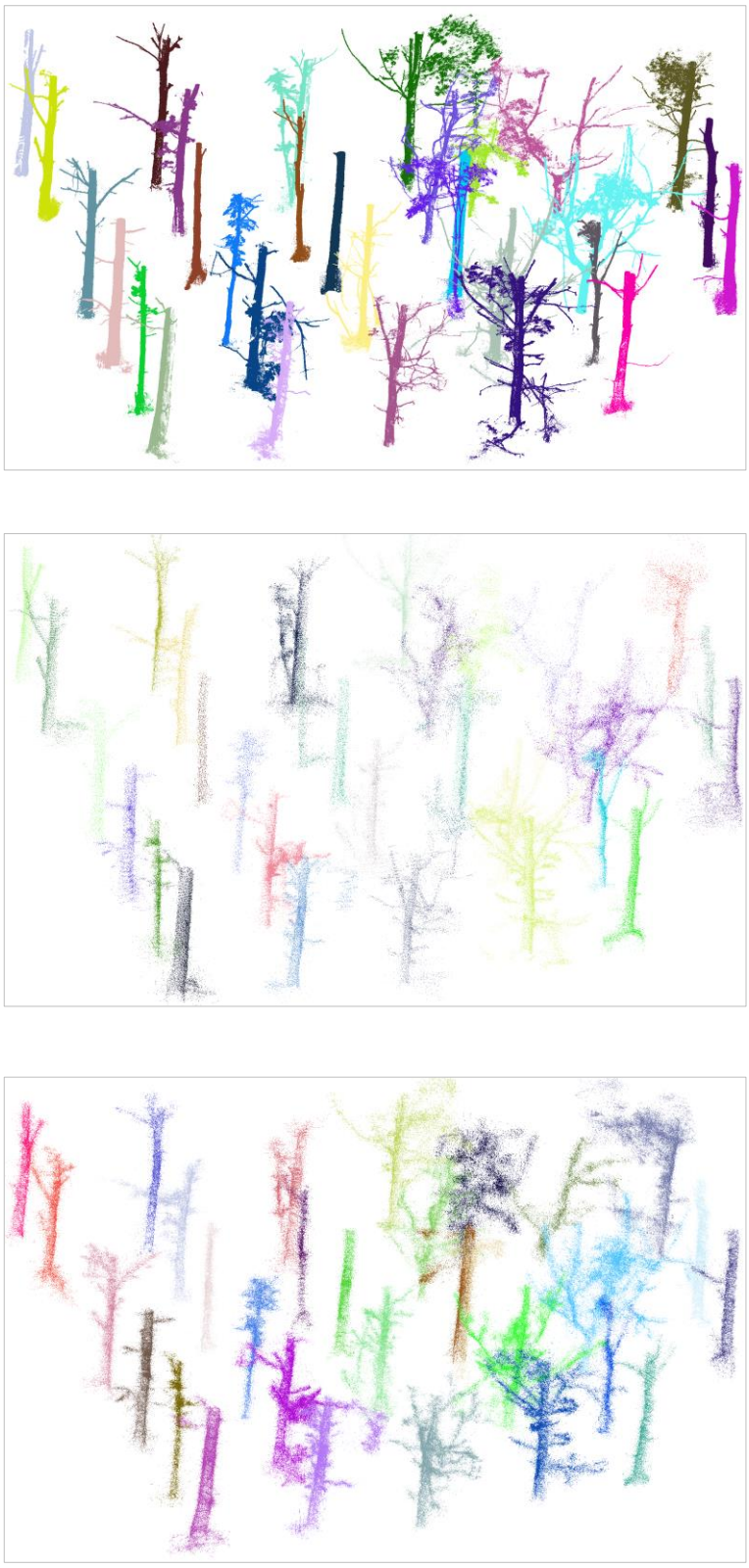

Figure 4.9: Oblique (NE-facing) renders of segmented point clouds acquired from TLS (P20; top), HMLS2 (ZEB-REVO; centre) and HMLS1 (ZEB-1; bottom) sensors. All trees were clipped at 2.5 m above ground to remove crown overlap which would otherwise prevent segmentation success.

Tilgate Forest: TLS and HMLS2

Two different subplots ('north' and 'south' rather than 'i004' and 'i006'; see ***3. Methods,*** pages 46 to 47) were extracted from the UTF-ROK site. To avoid edge effect bias, crowns outside the 20 x 20 m bounding box were also included. A useful benefit of this site, with leaf-off data, was that tree crowns exhibited 'crown shyness' and could be manually delineated as upper branches from adjacent crowns did not intersect. Only TLS and HMLS2 data were acquired at this site.

Figure 4.8 (page 113), as with previous subplots, illustrates stem centroid position. The same local coordinate system applies to both subplots (true origin lies between the two subplots on a north-south axis, and slightly west). Centroids can be seen to almost-perfectly align with one another. As in previous subplots, height obtained by HMLS2 fell short of true height extracted from TLS data. **Figure 4.11** on page 117 illustrates the results of segmentation.

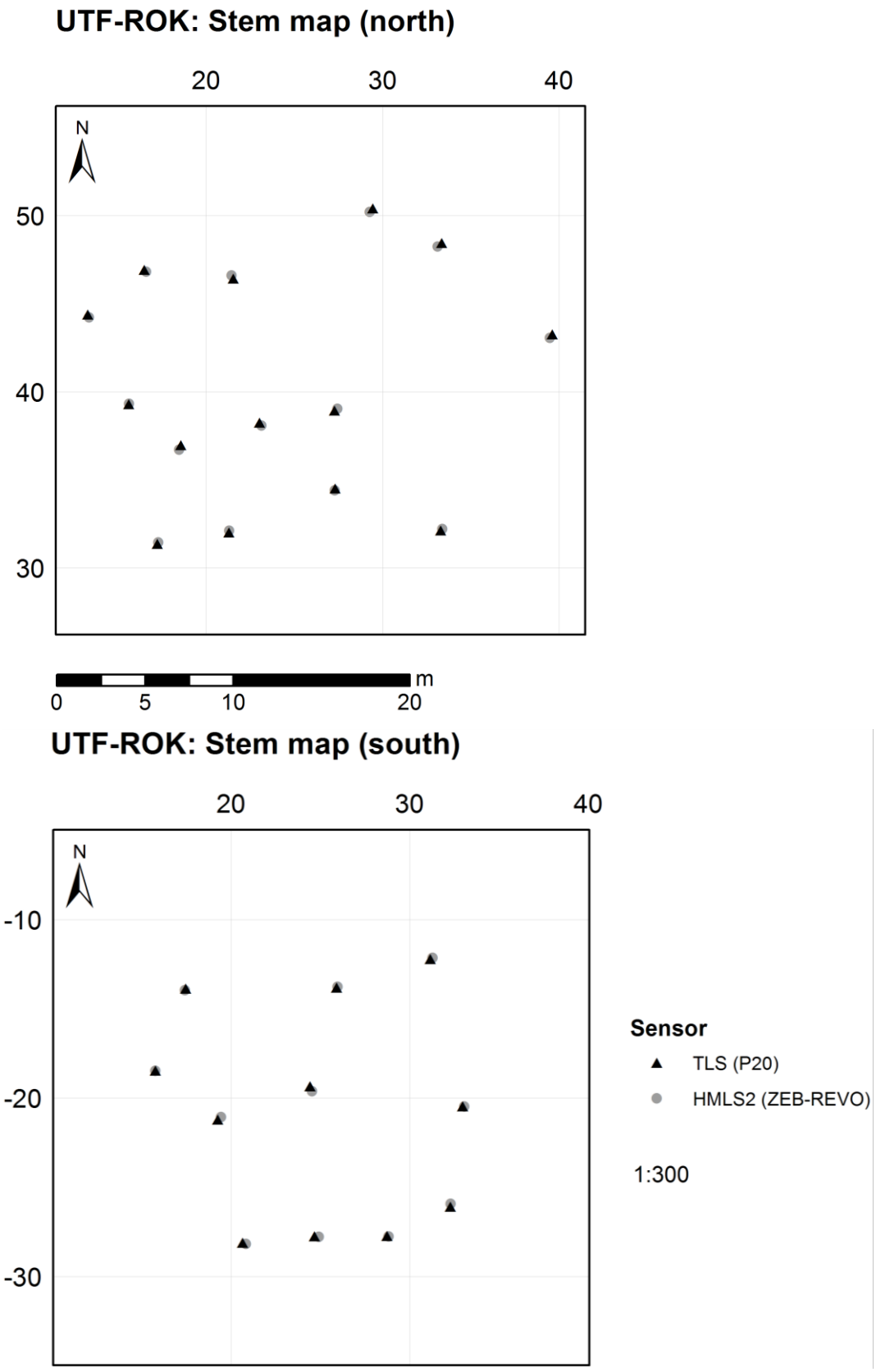

Figure 4.10: Final pair of centroid maps. All 14 trees in the UTF-ROK north (**left**) and 11 in the UTF-ROK south (**right**) plot were successfully detected and segmented in the TLS (triangle) and HMLS2 (circle) scans.

Figure 4.11: Visualisations of segmentation results for the UTF-ROK subplots.

Top row: TLS (**left**) and HMLS2 (**right**), with all 14 trees successfully segmented from each dataset. **Bottom row**: TLS (**left**) and HMLS2 (**right**), with 11 out of 11 trees successfully segmented.

Both datasets are projected from the same viewer perspective but are included solely as a visual communication of segmentation efficacy. Note the stark inter-sensor difference in resolve tree height and crown structure. Despite this, stems appeared to be nigh-on identical.

As per **Figure 4.8**, tree stem centroids for each sensor and plot pair were correctly positioned with almost no horizontal offset. Where offset was detected, this was due to noise in HMLS2 point clouds associated with understorey vegetation (i.e. ferns) present throughout the plot.

4.3.3 Diameter at breast height

Diameter at breast height (DBH) was extracted semi-automatically across all ten subplot datasets extracted from the three forest study sites. Results are presented in the form of scatterplots, with TLS-derived values acting as reference dataset on the X axis and HMLS-derived estimates on the Y axis. Numeric DBH values can be found in the ***Appendix***.

Epping Forest, pre-holly clearance (all 3 sensors)

Of the segments detected in *3D Forest* identified as trees, 51 matched between TLS and either HMLS1 or HMLS2 datasets. Of these, 31 trees were detected and segmented across all three sensors, with paired DBH estimates per algorithm (i.e. RHT; LSR; **Figure 4.12** on page 119). Two trees were subsequently removed as they failed a quality control test (i.e. branches were present in close proximity to the stem at DBH height). A further twenty trees were excluded from HMLS1 data due to occlusion caused by the presence of dense holly which effectively shielded tree stems within from penetration of laser pulses.

Epping Forest, post-holly clearance (TLS and HMLS2 only)

The Bury Wood plot (**Figure 4.11**, page 117) at Epping Forest was scanned a second time several months later, after Corporation of London had organised clearance of holly using a flailing technique (i.e. complete removal of all holly between veteran trees). In this instance, only HMLS2 and TLS datasets were acquired but both datasets encompassed a larger sample size (n = 49) once tree pairs common to both datasets were mapped. Of these, 39 had realistic DBH values whilst 10 were removed due to tree structural complexity which *3D Forest* could not resolve as realistic DBH estimates. In **Figure 4.13** (page 120)**,** TLS and HMLS2-derived DBH values extracted from the raw (left; n = 49) and modified (right; n = 39) are presented. Where anomalous DBH values were removed, R^2 rose from 0.718 to 0.976 whilst RMSE decreased from 0.196 to 0.029 m.

Epping Forest, pre-holly clearance: HMLS1 (ZEB-1) vs TLS

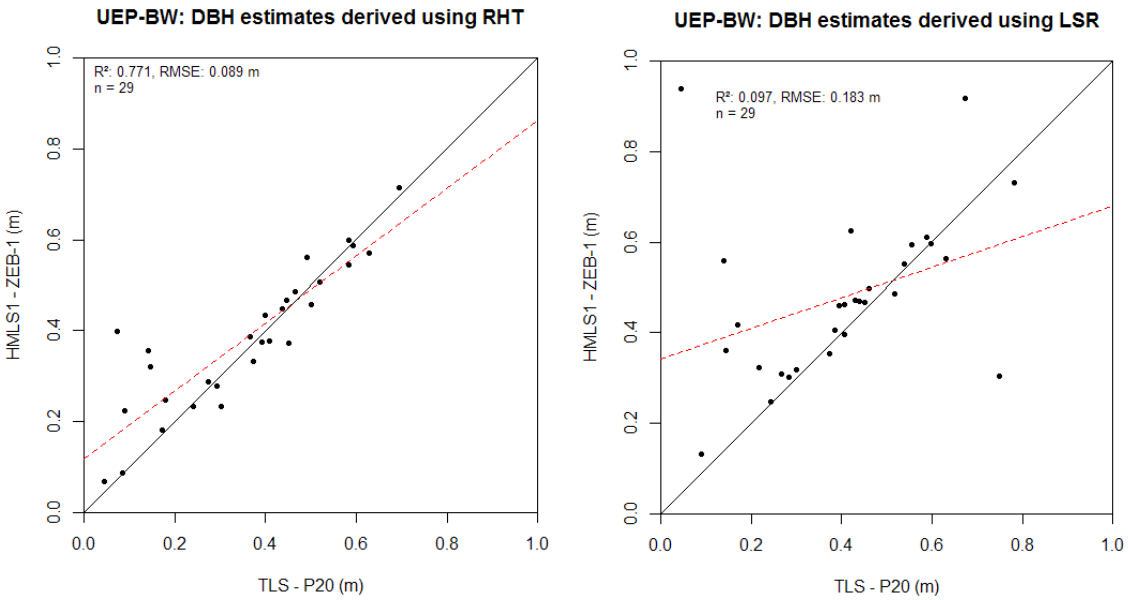

Epping Forest, pre-holly clearance: HMLS2 (ZEB-REVO) vs TLS

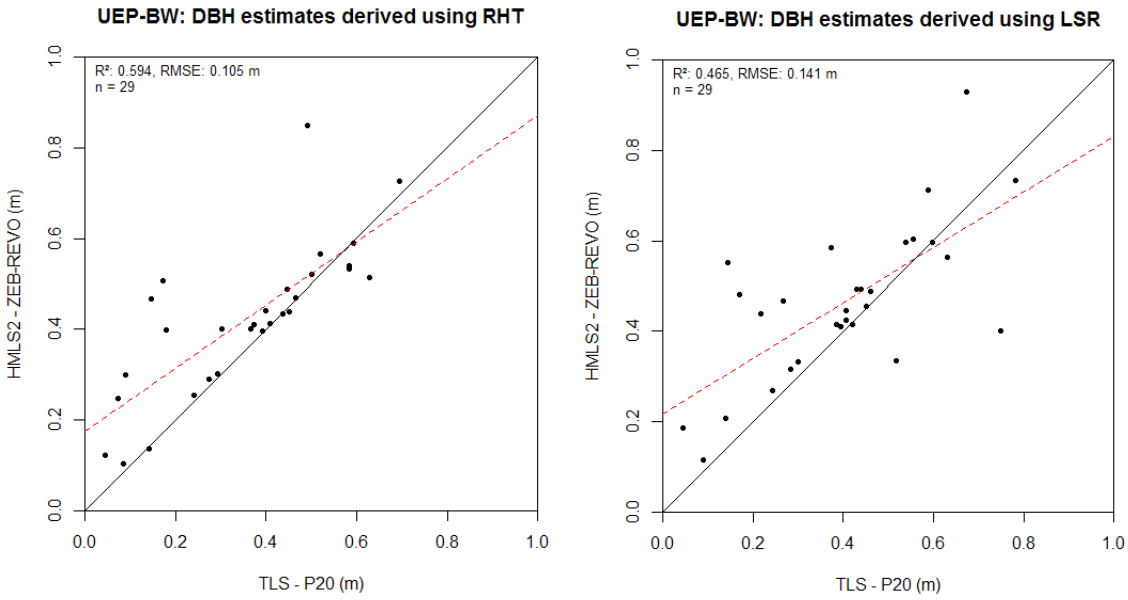

Figure 4.12: Sample size reduced to 29 segments, as measured using HMLS1 and HMLS2. In these plots, the 2 most-obvious anomalous values have been removed. As a result, R^2 improved in all four instances and RMSE decreased significantly.

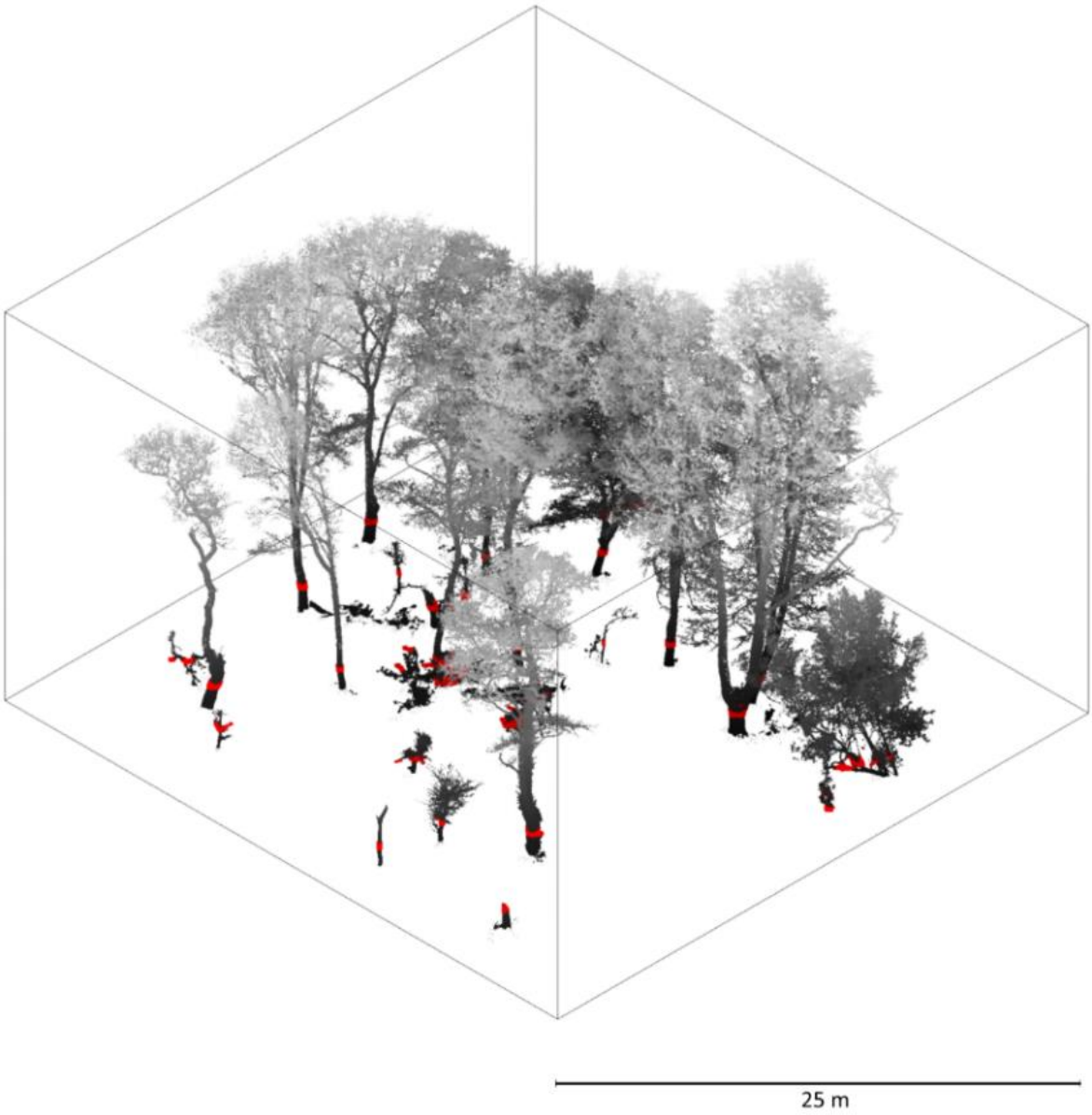

Figure 4.13: Oblique (NE-facing) render of UEP-BW showing the TLS data (greyscale, coloured by height which ranged from 0 to 22.68 m) and DBH (red) as a slice at 1.2 to 1.4 m above ground. Note that disparity in both diameter and height. This illustrates a wide range of dimensions, offering a good test of HMLS (ZEB-1 and ZEB-REVO) accuracy in comparison with this TLS data.

Epping Forest, post-holly clearance: HMLS2 (ZEB-REVO) vs TLS

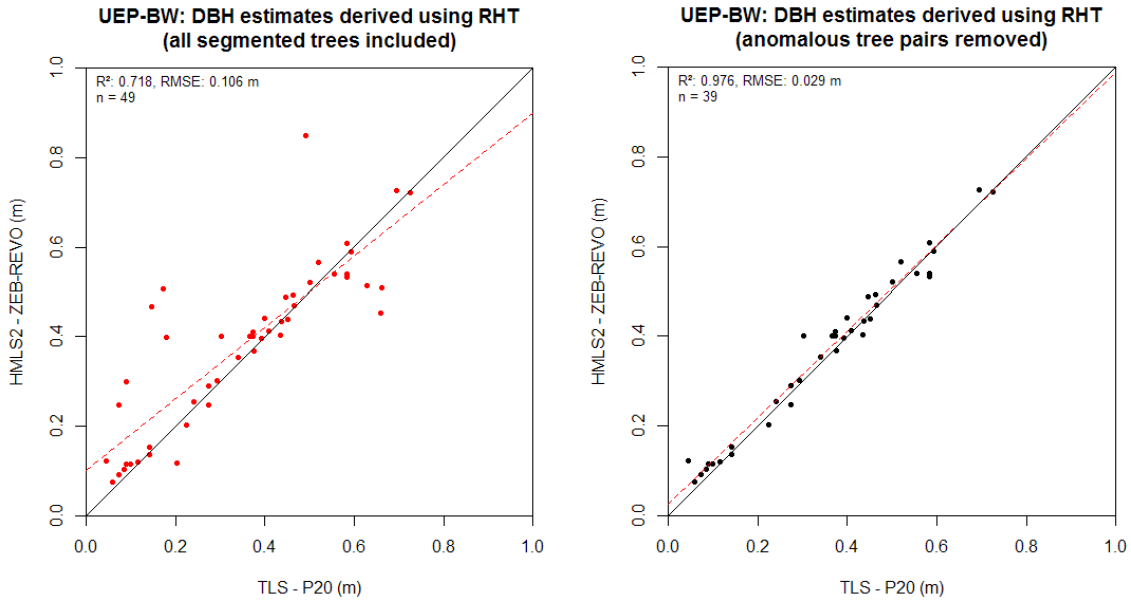

Epping Forest, post-holly clearance: HMLS2 (ZEB-REVO) vs TLS

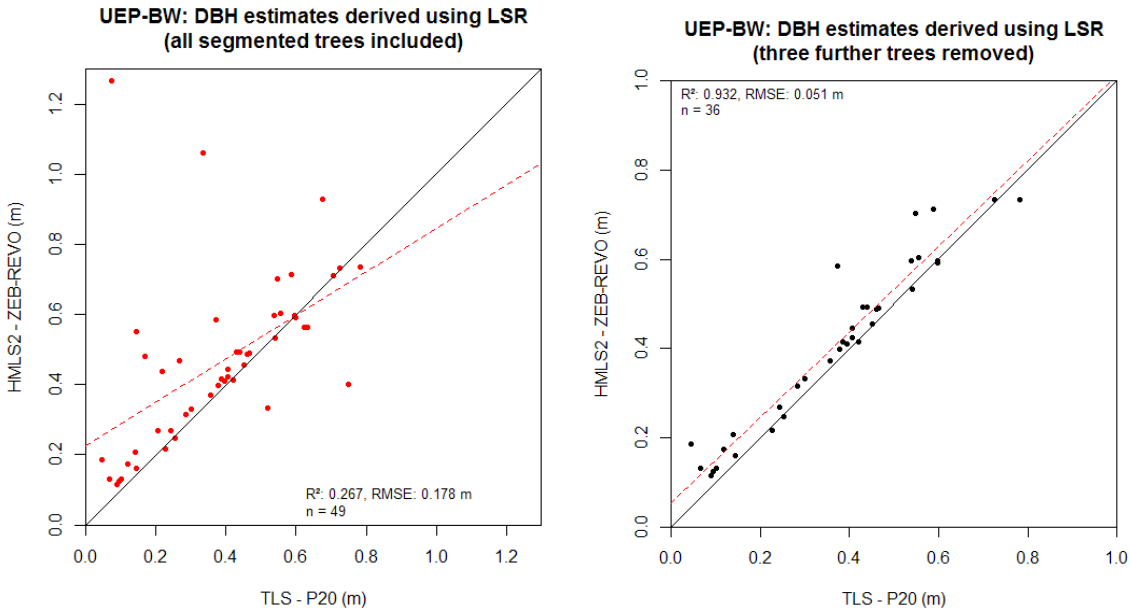

Figure 4.14: Scatterplots illustrating the relationship between TLS and HMLS2 RHT-derived DBH estimates.

Top-left: 'raw' dataset of 49 segmented trees common to both scans. Top-right: 'pruned' subset from which 10 trees were removed.

Bottom: LSR-derived DBH compared with TLS before (left) and after (right) removal of outlier data.

There was a broader range of DBH values where derived using the LSR algorithm. This was less a consequence of a methodological weakness (e.g. laser inaccuracy) and more a function of physical tree structure (branches, twigs) confounding the DBH estimation algorithm. Removing these outliers led to improved R^2 and reduced RMSE, suggesting RHT is a superior approach to DBH estimation. This suggestion would seem to confirm observations by Krůček et al. (2017). Using LSR instead of RHT (**Figure 4.14,** previous page), R^2 decreased slightly from 0.267 to 0.248. RMSE also showed a slight decrease, falling from 0.178 to 0.176 m. When three outliers were removed, R^2 was significantly boosted from 0.248 to 0.932. This implied a much better fit with the reference TLS data. Meanwhile RMSE decreased from 0.176 to 0.051 m. This error was much closer to anticipated systematic error (Ryding et al., 2015; Bauwens et al., 2016; GeoSLAM, 2018) associated with the inferior-quality laser of HMLS2 (Bosse et al., 2012) compared with the TLS system (Leica Geosystems AG, 2014).

Stratfield Brake

DBH was successfully extracted for each of the thirty-one stems across datasets acquired with all three sensors (HMLS1, HMLS2 and the reference TLS dataset). Several estimates proved to be unrealistic as a result of complex structural variation at DBH height, with some HMLS-derived estimates more than ten times greater than TLS equivalents. As a consequence, despite a mean DBH (TLS; RHT) of 0.224 m, RMSE varied by between 0.118 and 0.239 m. Contradicting results observed in the other field plots, the greatest accuracy was found in the HMLS2 data using the LSR algorithm: R^2 was 0.847 and RMSE 0.118 m.

Tilgate Forest: TLS and HMLS2

Of the segmented objects in both TLS and HMLS2 subplots, 25 were identified as trees suitable for analysis for which DBH was plotted (**Figure 4.15**, overleaf). One clearly anomalous value in LSR-derived DBH estimates was excluded from analysis.

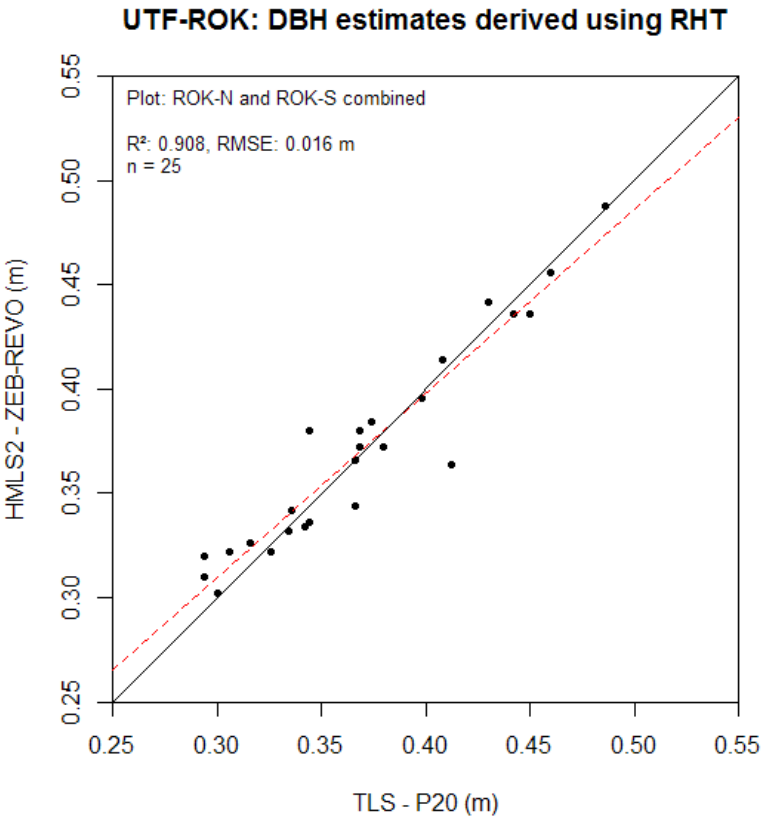

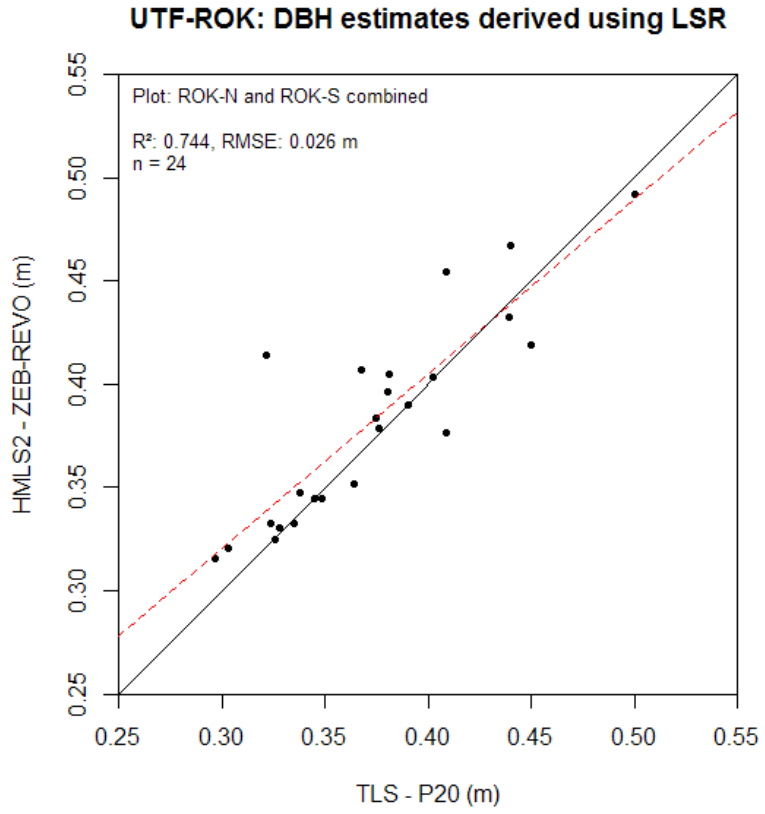

Figure 4.15: Scatterplots indicating DBH for each tree, derived from both TLS (P20) and HMLS2 (ZEB-REVO) sensors. An anomalous value was removed from the LSR dataset hence *n* = 24 in the right-hand plot.

Combined DBH estimates from multiple plots

To derive a 'true' accuracy assessment of DBH estimation for each sensor, data were aggregated from all field plots, with sample sizes varying a little (e.g. to reflect pre- and post-clearance of holly). Accordingly, two 'combined' datasets were created, with anomalous values (those where HMLS DBH varied from TLS DBH by more than 0.25 m) excluded. Per sensor, these were:

- HMLS1: comprising USB, UTF and *pre*-holly clearance UEP segments (n = 52)
- HMLS2: comprising USB, UTF and *post*-holly clearance UEP segments (n = 76)

Across the sites, 52 trees were sampled by TLS, HMLS1 and HMLS2. At UEP-BW, a further 24 trees were scanned by TLS and HMLS2 post-holly clearance – stems previously hidden by dense holly in the understorey. The data were plotted in two scatterplots (**Figure 4.16**, page 125) with R^2 values of 0.919 and 0.978, and RMSE of 0.060 m and 0.031 m, for HMLS1 (ZEB-1) and HMLS2 (ZEB-REVO) respectively. Descriptive statistics for the 52 trees scanned by all sensors are presented in **Table 4.6** below.

Table 4.6: Descriptive statistics for RHT-derived DBH estimates

Descriptive statistic	**TLS** (reference)	**HMLS1** (ZEB-1)	**HMLS2** (ZEB-REVO)
Mean	0.310	0.318	0.315
Standard Error	0.036	0.038	0.033
Median	0.240	0.234	0.254
Mode	0.110	0.098	0.104
Standard Deviation	0.255	0.270	0.235
Sample Variance	0.065	0.073	0.055
Kurtosis	0.284	2.812	-0.144
Skewness	1.019	1.560	0.848
Range	0.946	1.202	0.858
Minimum	0.044	0.046	0.052
Maximum	0.990	1.248	0.910
Sum	15.810	16.224	16.224

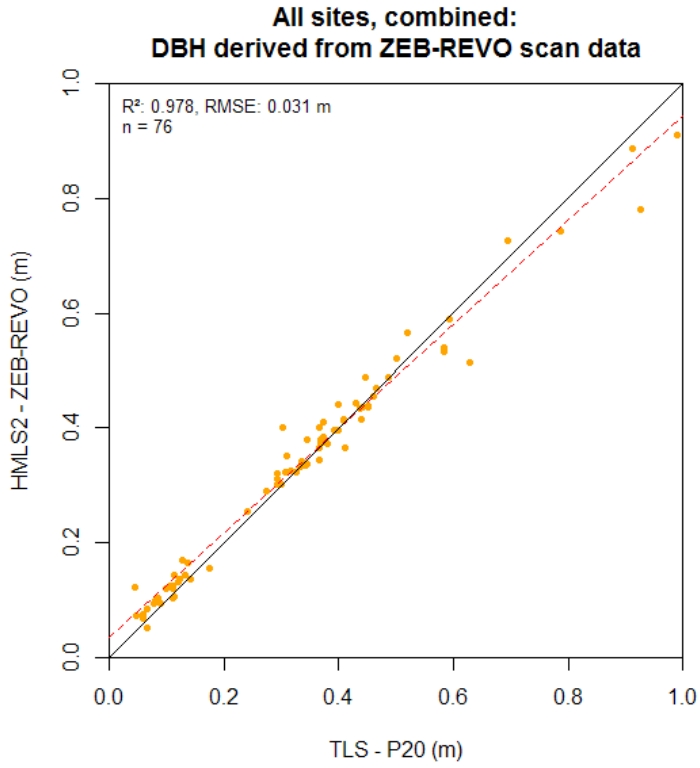

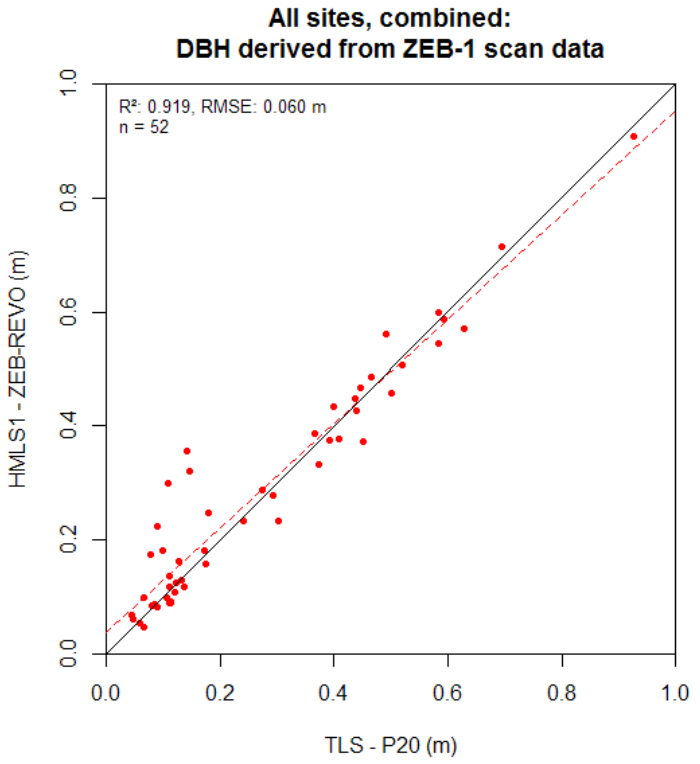

Figure 4.16: Scatterplots of aggregated DBH estimates derived using the superior RHT algorithm. Statistically, ZEB-REVO diameters appear more accurate than those derived from the ZEB-1 instrument, as one might expect from the newer-specification sensor. However, it also appears that the ZEB-1 plot is biased by noisier DBH values in the 0.1 to 0.4 m range, dominated by USB tree segments.

Tilgate Forest: TLS and manual inventory

DBH was directly sampled for nineteen red oak (Q. rubra) trees within two ten-metre circular inventory plots within the UTF-ROK study site. These were directly compared (**Figure 4.17**, below; **Figure 4.18**, following page) with DBH estimates extracted from TLS data using the RHT algorithm within *3D Forest*. **Figure 4.19** (page 128) depicts these results graphically as a scatterplot.

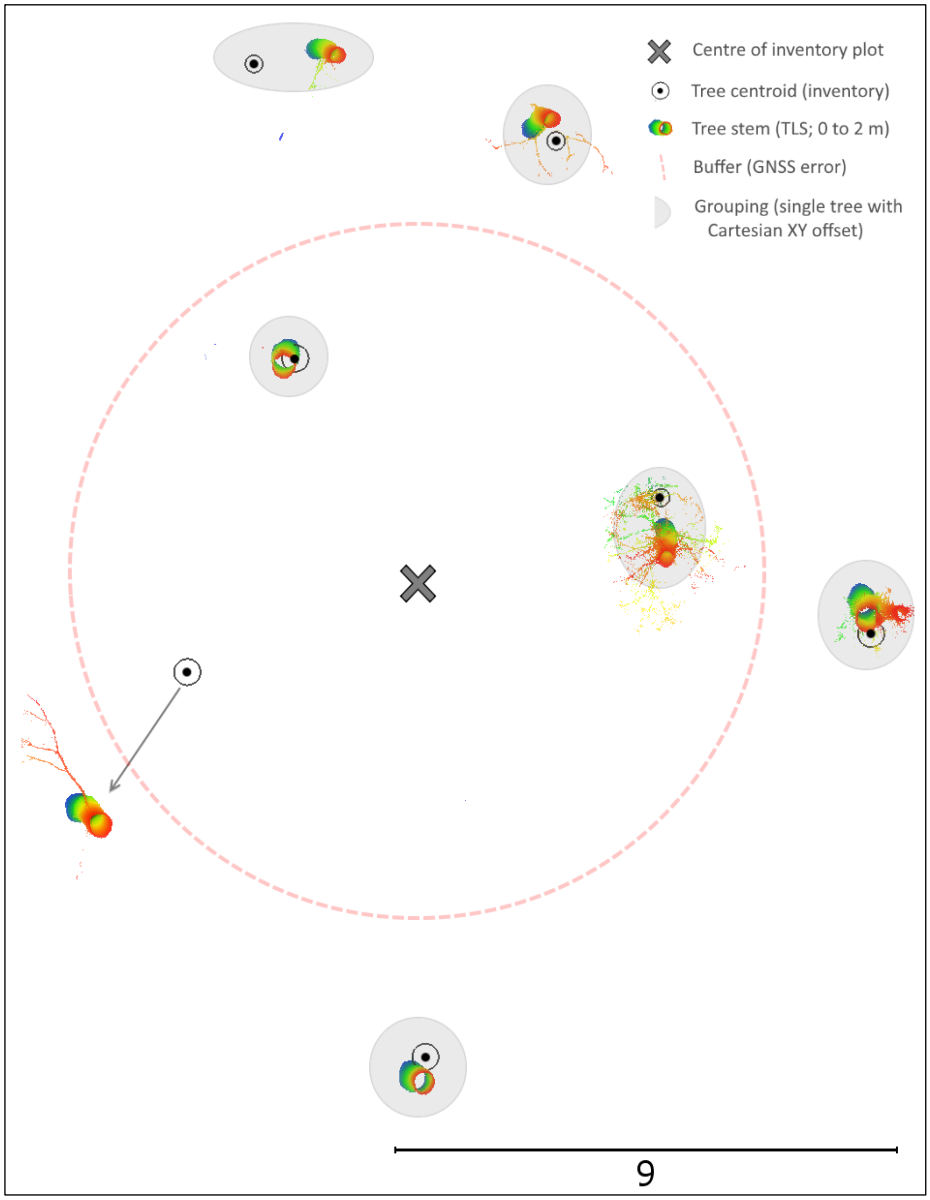

Figure 4.17: DBH 'stem map' for i004 plot as identified in TLS data (point cloud sections, coloured by height) and manual DBH observations, with Cartesian locations determined by logging range (tape measure from plot centre) and azimuth (angle clockwise of north, determined with a handheld compass).

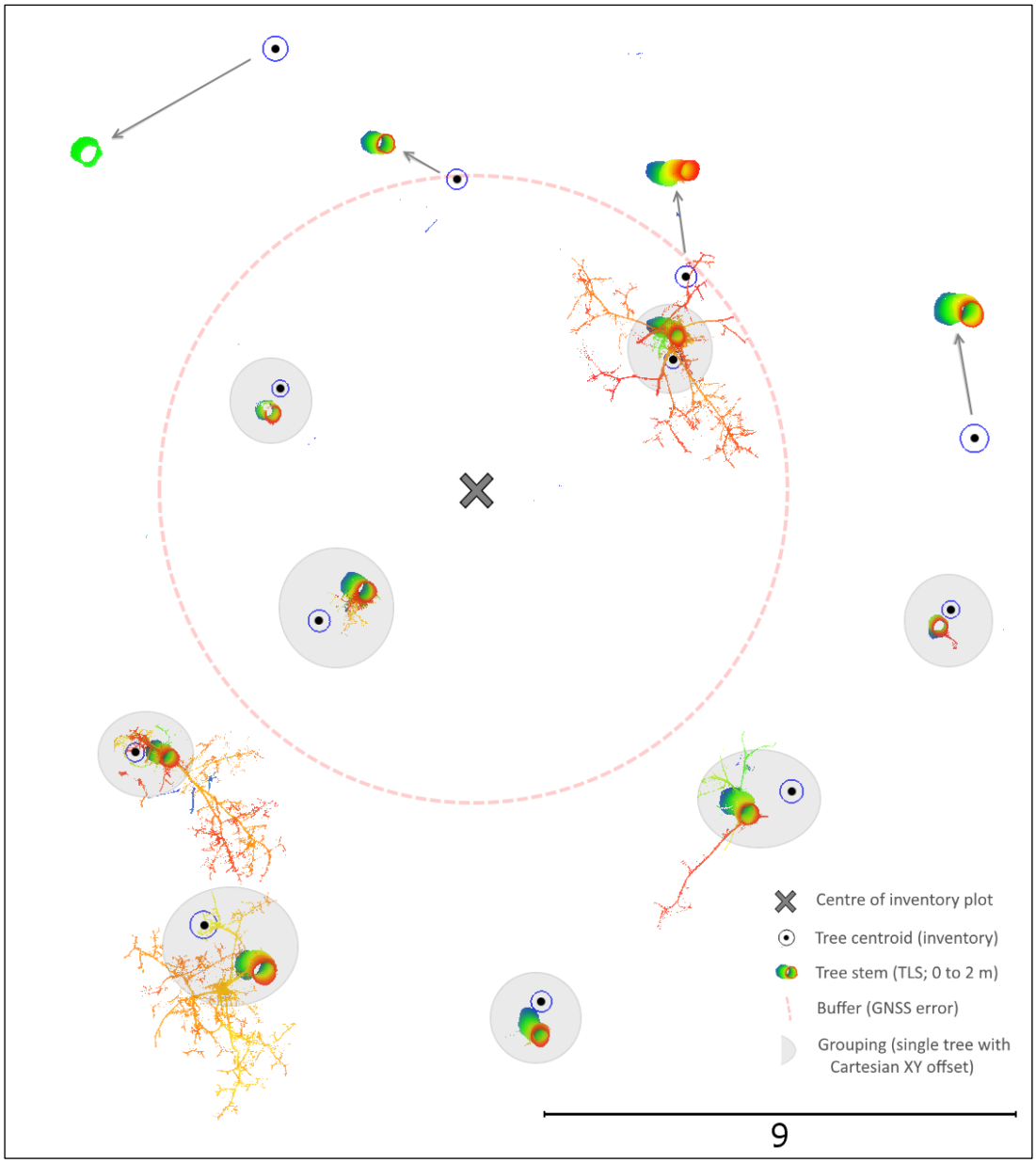

Figure 4.18: As per previous figure, but with data from the i006 plot.

In both **Figure 4.17** (previous page) and **4.18** (above), GNSS error (dashed, red circle) and XY error (indicated by arrows) are plotted. GNSS error was attributed to (a) use of a low-accuracy consumer grade GPS unit and (b) multipath error common when attempting to triangulate a GNSS position in an area where the signal is reflected (e.g. beneath trees and between tall buildings). Whilst it ultimately proved possible to translate the inventory stems to fit HMLS data, it is clear there is a spatial disconnect. It seems HMLS-based approaches to stem mapping are superior – more accurate and consistent – than traditional methods.

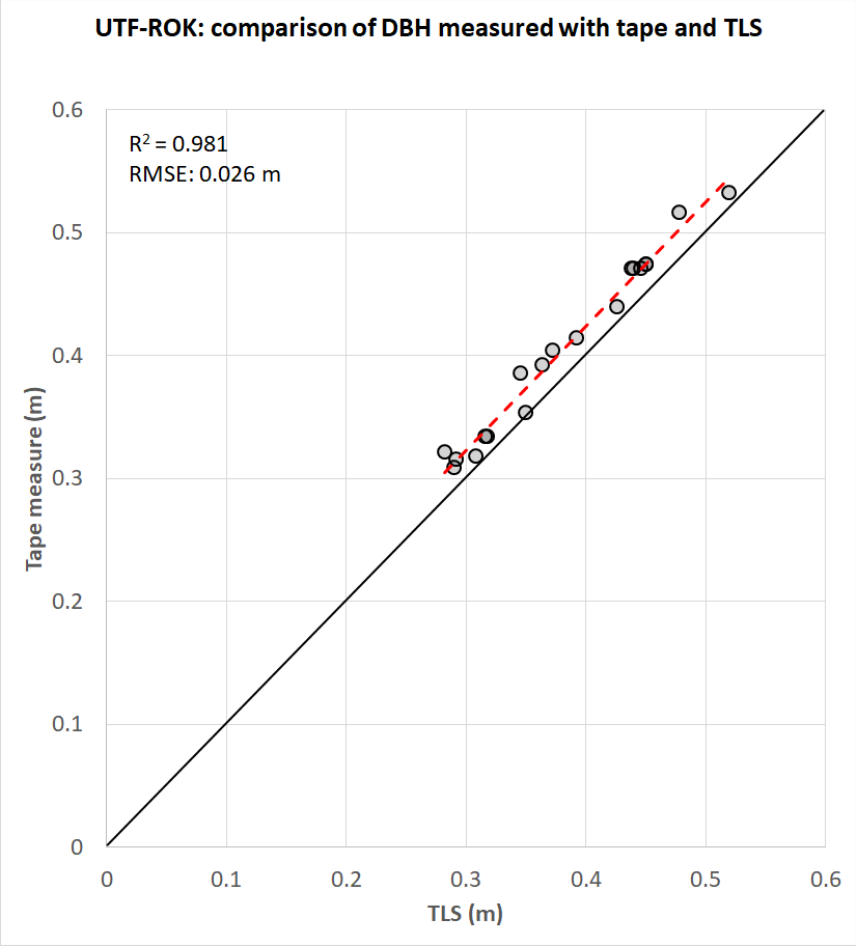

Figure 4.19: Scatterplot showing the relative accuracy of direct, tape measured DBH and indirect, semi-automated estimation of DBH in *3D Forest* as applied to TLS data. *N* = 19.

An R^2 value of 0.981 (**Figure 4.19**, above) suggests a good degree of agreement between the datasets but it is clear tape-measured diameters consistently exceed those derived from the TLS dataset. It is important to note that whilst an RMSE of 0.026 m might imply poor performance of the TLS data-derived estimates, there are several confounding factors. Manual, tape measurements were logged in November 2015 whilst TLS scans were acquired in May 2017. Whilst every effort was made to ensure trees could be re-located for subsequent surveys, systemic error (e.g. varying GNSS accuracy) introduced a level of uncertainty regarding cross-referencing individual stems (see **Figures 4.17** and **4.18;** pages 126 and 127). *3D Forest* estimates DBH by fitting circles to cross-sectional slices of point data; in reality, none of the stems were perfectly circular. These results compare well with the literature and validate that TLS-derived DBH estimates are a suitable reference dataset for assessment of HMLS accuracy.

4.3.4 Tree height

In this section, results are presented in the form of tables (**Table 4.7** below; **4.8**), graphs (**Figure 4.20** below and **4.23**), as two-dimensional profile renders of point cloud data per-sensor (**Figures 4.21** and **4.24**) and with rose diagrams (**Figure 4.21** and **4.25**) from page 129 to 133. Analyses focussed on maximum height of segmented trees from both UEP-BW and UTF-ROK subplots. USB-C was omitted from tree height analysis as the subplot was restricted to a height of 2.5 m. In any case, it proved difficult to detect top-of-tree height at this study site so results would have been influenced by canopy occlusion.

Table 4.7: Descriptive statistics for UEP-BW tree heights (m)

	TLS	HMLS1	HMLS2
Mean	13.756	10.407	11.059
Median	17.900	12.660	12.060
SD	7.647	4.653	5.552
Range	19.640	13.210	15.990
Minimum	2.320	2.480	2.460
Maximum	21.960	15.690	18.450

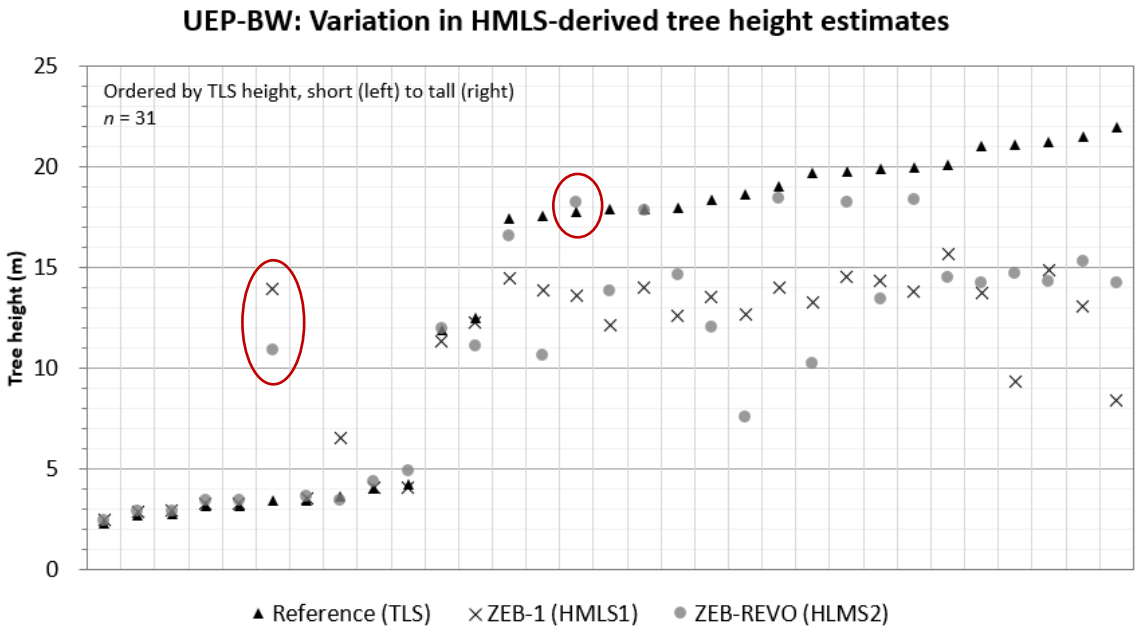

Figure 4.20: Graph showing top-of-tree heights within the UEP-BW subplot. Trees sorted by TLS-derived height. Note the circled values, where HMLS height > TLS height.

Figure 4.21: Visual comparison of tree heights within the UEP-BW subplot, rendered from a north-facing projection. From top: TLS (black), HMLS2 (orange) and HMLS1 (red). Neither HMLS sensor appears to have detected upper crown structure with HMLS1 data appearing the least-useful from a tree reconstruction perspective.

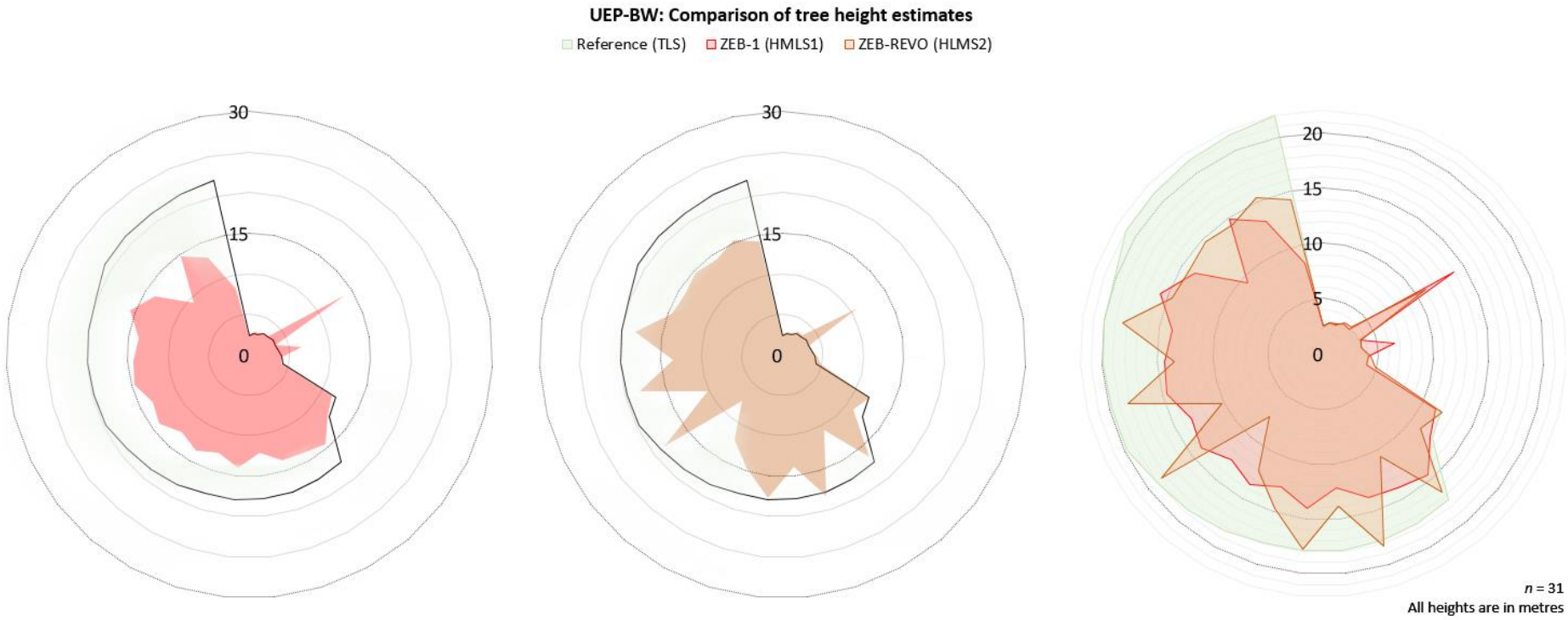

Figure 4.22: Rose diagrams illustrating the height of trees within the UEP-BW subplot as scanned by TLS (green), HMLS1 (red) and HMLS2 (orange) sensors. Trees are sorted (clockwise) by TLS-derived height. It is clear that neither HMLS sensor accurately resolves height. It appears HMLS2 has greater range (evidenced by spikes) than HMLS1 although this is inconsistent and perhaps due to noisy data.

Table 4.8: Descriptive statistics for UTF-ROK tree heights (m)

	TLS	HMLS2
Mean	26.237	16.523
Median	26.220	15.630
SD	0.901	3.220
Range	3.680	12.400
Minimum	24.320	12.510
Maximum	28.000	24.910

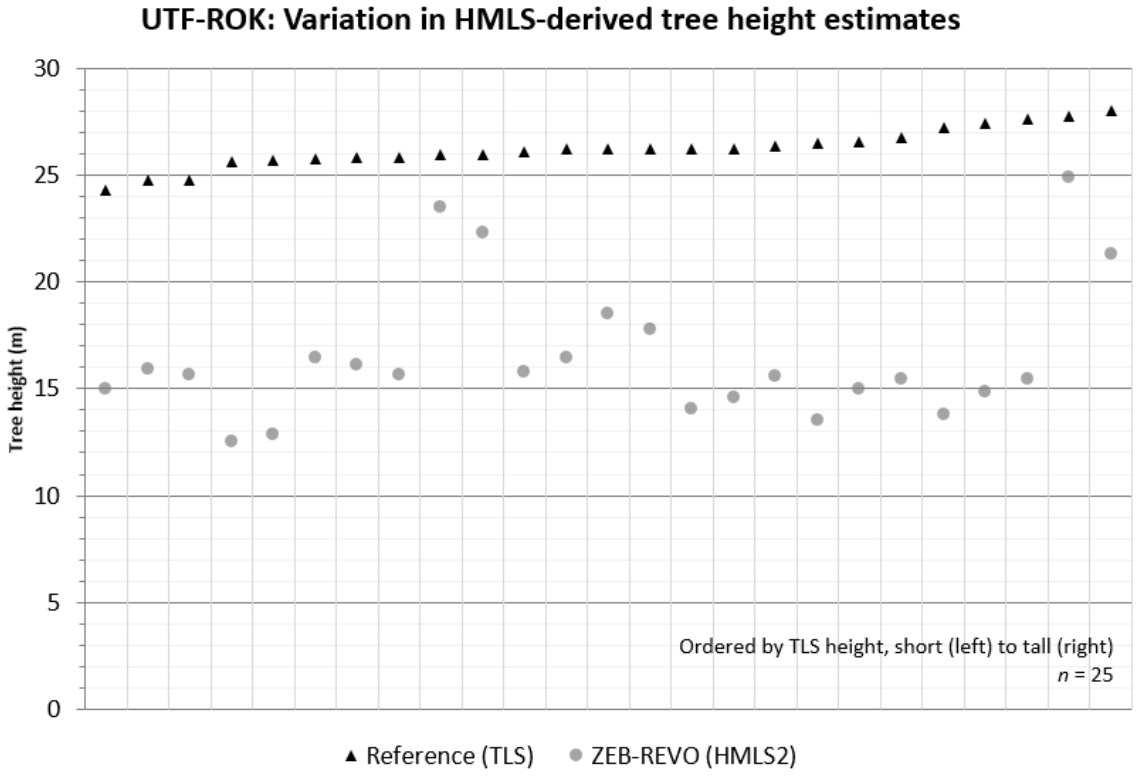

Figure 4.23: Graph illustrating maximum tree height derived from TLS and HMLS2 data, ordered by TLS-derived height. HMLS2 appears to have height range of 15 – 18 m (minus height of scanner above ground – typically 1.4 to 1.7 m).

Figure 4.24: As per **Figure 4.21** (page 130), a side-by-side, visual comparison of trees within the two UTF-ROK subplots rendered from TLS (black; **left**) and HMLS2 (orange; **right**) scans.

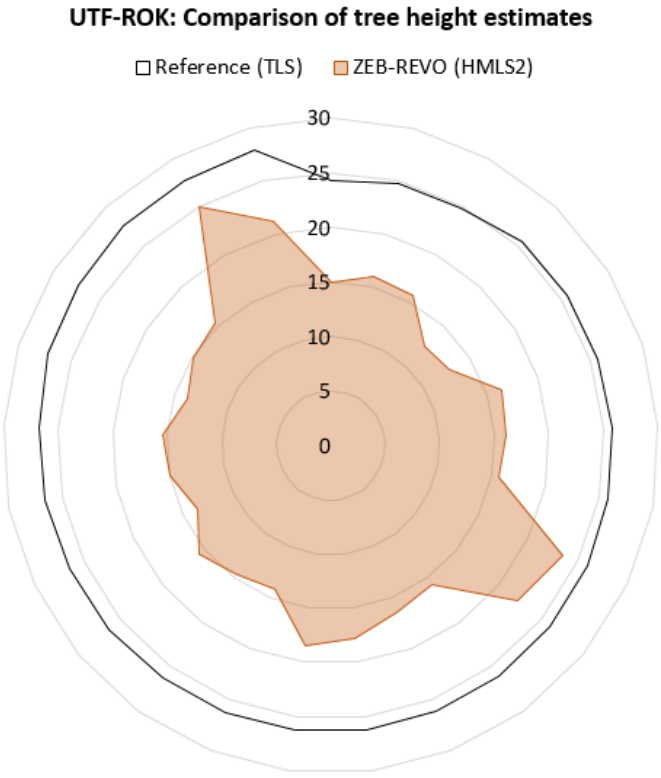

Figure 4.25: TLS and HMLS2 heights from combination of UTF-ROK north and south subplots. HMLS2 underestimates tree height – possibly a function of limited laser range.

4.3.5 Stem volume

Efforts to model stems as 3D meshes were very computationally intensive and led to mixed results (**Figure 4.26**, below; **Figures 4.27** and **4.28**, overleaf).

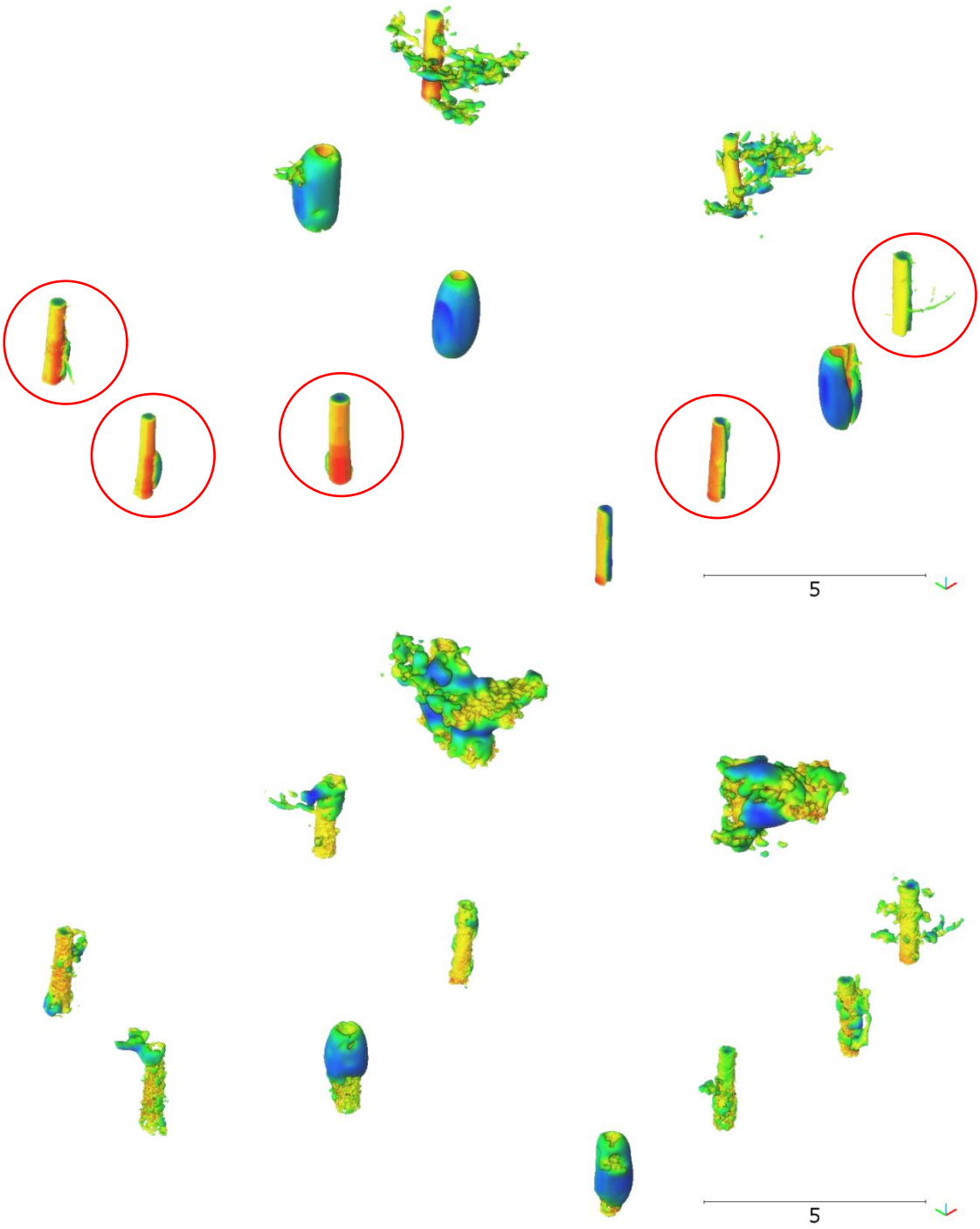

Figure 4.26: 3D meshes of 10 tree stem sections extracted from TLS (top pane) and HMLS (bottom pane) scans acquired within the UTF-ROK study site. The 5 meshes with most consistent volume estimates across the two datasets are circled (red) and expanded in **Figure 4.27** overleaf.

Of the ten stems modelled, only five seemed to bear a strong resemblance to what would typically be considered a tree stem – cylindrical meshes with texture. These five are reproduced below. Note that inconsistencies in point spacing or normal computation led the Poisson surface reconstruction algorithm to overestimate volume (note: 'growths' and 'speckle'). The derived volume for all ten stems, across both datasets, are compared in scatterplot format in **Figure 4.28,** below.

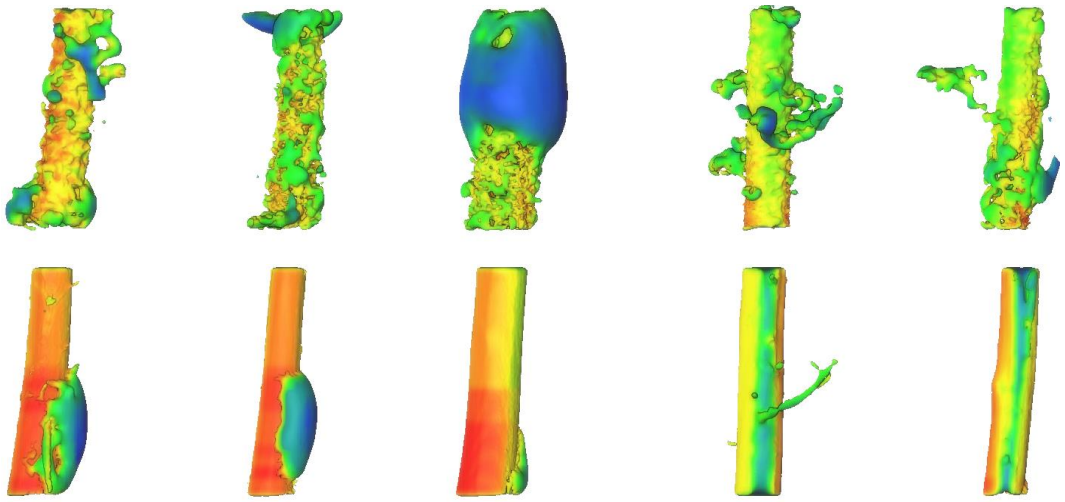

Figure 4.27: Meshes of tree stem sections computed on HMLS2 data (top) and TLS data (bottom). Each section is 2 m tall.

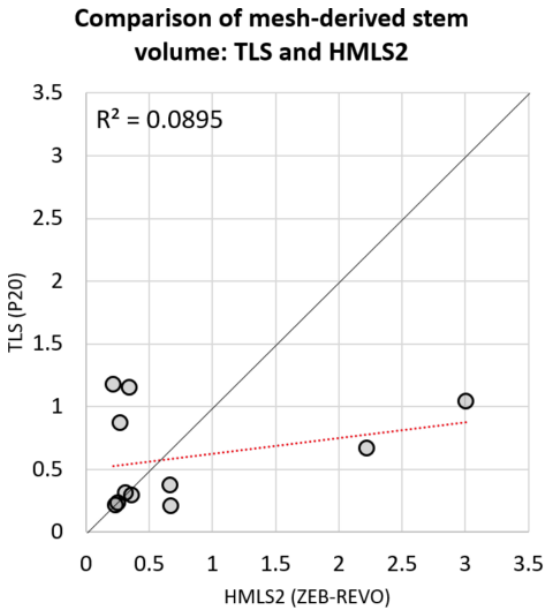

Figure 4.28: Scatterplot comparing mesh-derived volume of stem sections scanned using both the TLS and HMLS2 sensors and the Poisson surface reconstruction algorithm.

4.3.6 Tree crown: 2D geometry

The results on the following pages encompass three sub-plots from two field sites: Epping Forest (UEP-BW) and Tilgate Forest (ROK North and South). Crown geometry is presented as two-dimensional projected polygons using both the convex and concave hull methods exploring correlation, accuracy and limitations within and between observations (**Figure 4.29** below, **Figures 4.30** to **4.36** over the following pages). Summary tables for these parameters can be found in the ***Appendix***.

Epping Forest

To mitigate edge effects, trees with arbitrarily clipped crowns (those cropped during subplot extraction) were removed from analysis. As a result, 39 of 56 individual trees were retained from the segmented TLS-derived data. In each instance, at least 95% of 2D crown area was retained within point data. Of these 39 trees, only 21 were also recorded in HMLS datasets. The below results refer to these 21 trees.

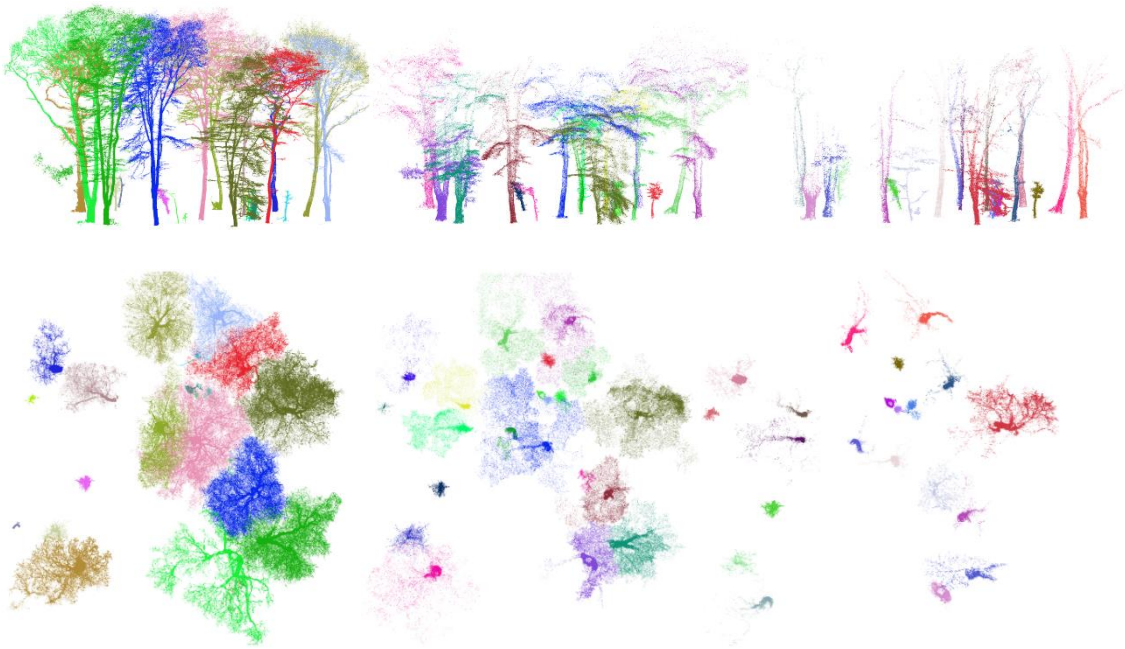

Figure 4.29: Profile (**top** row) and plan (**bottom** row) renders of segmented trees from the UEP-BW subplot acquired via TLS (**left**), HMLS2 (**centre**) and HMLS1 (**right**). Individual segments are coloured separately but colours may be repeated in adjacent plots. It is clear that crown structure is not fully resolved in the two HMLS scans.

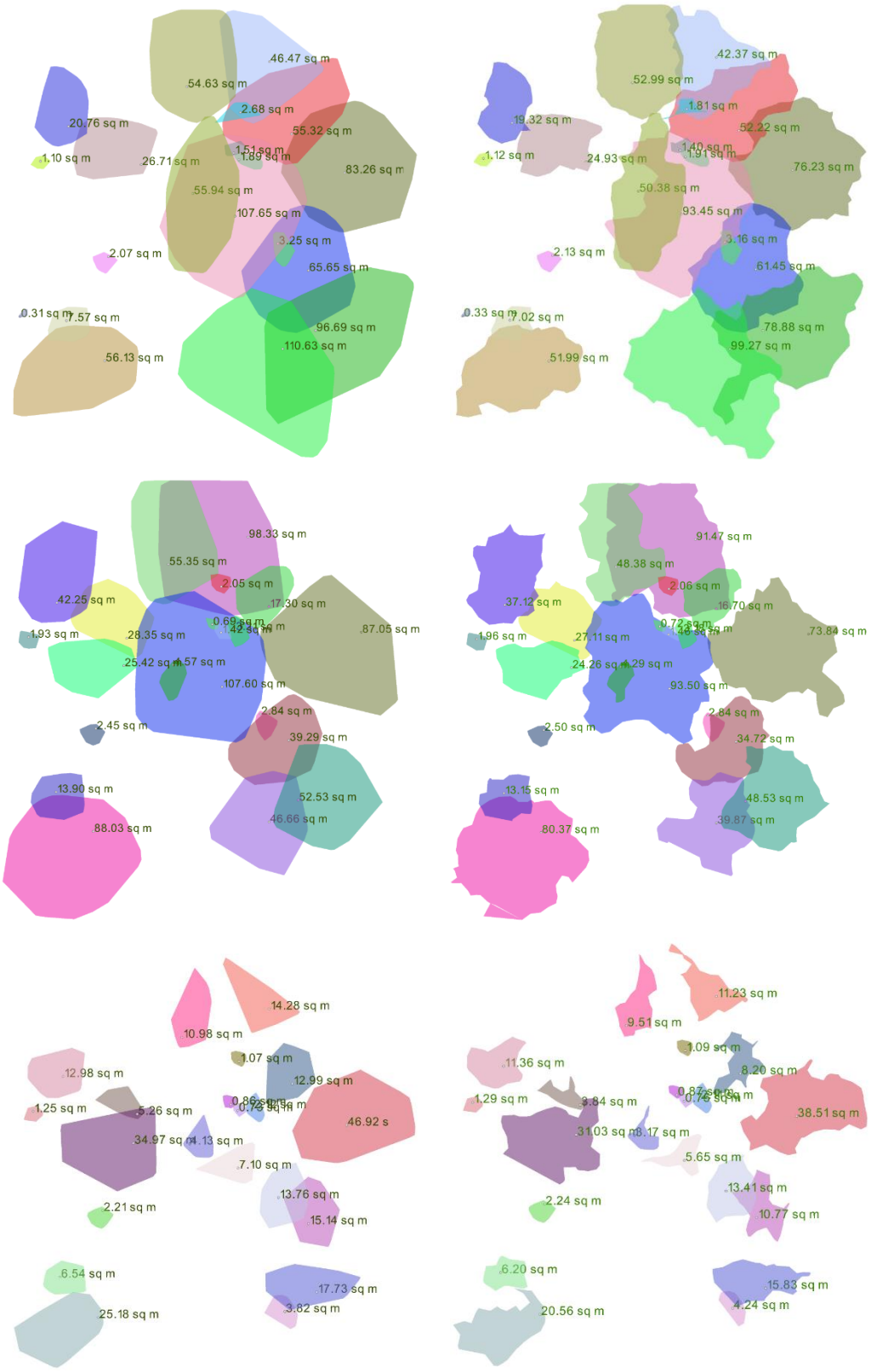

Figure 4.30: 2D crown projection polygons derived from TLS (**top** row), HMLS2 (**middle**) and HMLS1 (**bottom**) via convex hull (**left** panels) and concave hull (**right** panels) techniques. Clearly, crown surface area estimates are markedly different.

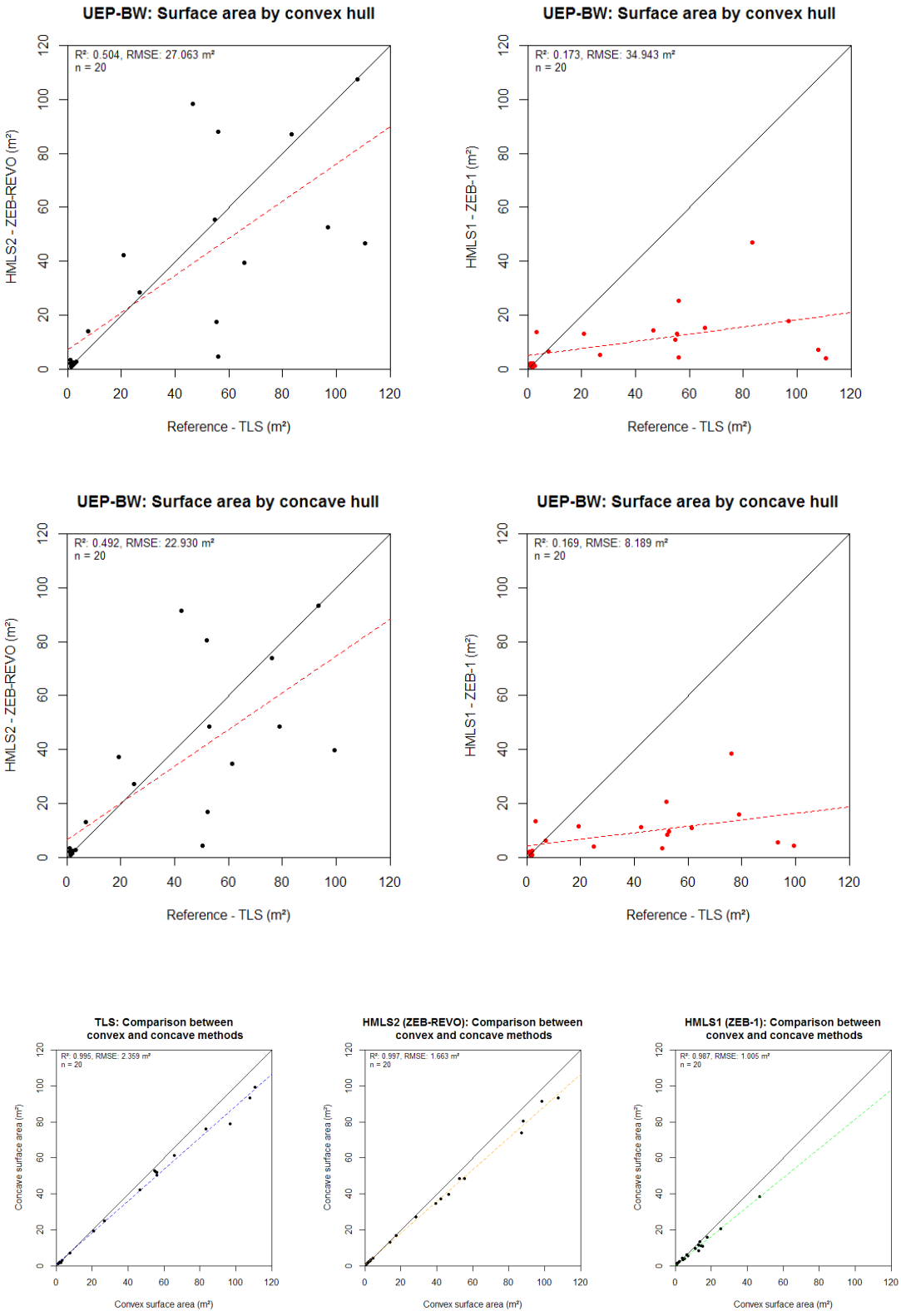

Figure 4.31: Scatterplots (a) exploring the relationship between multi-sensor crown area extents and (b) comparing the two techniques for estimating crown area.

Tilgate Forest: UTF-ROK North

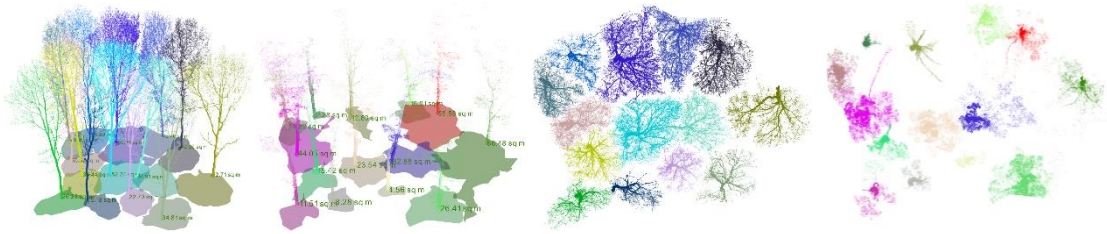

Figure 4.32: 14 trees extracted from data acquired in the UTF-ROK-N (north) sub-plot at Tilgate Forest. From **left**: TLS from oblique angle; HMLS2 from oblique angle; TLS in plan view coloured by tree segment; HMLS2 in plan view, coloured by tree segment.

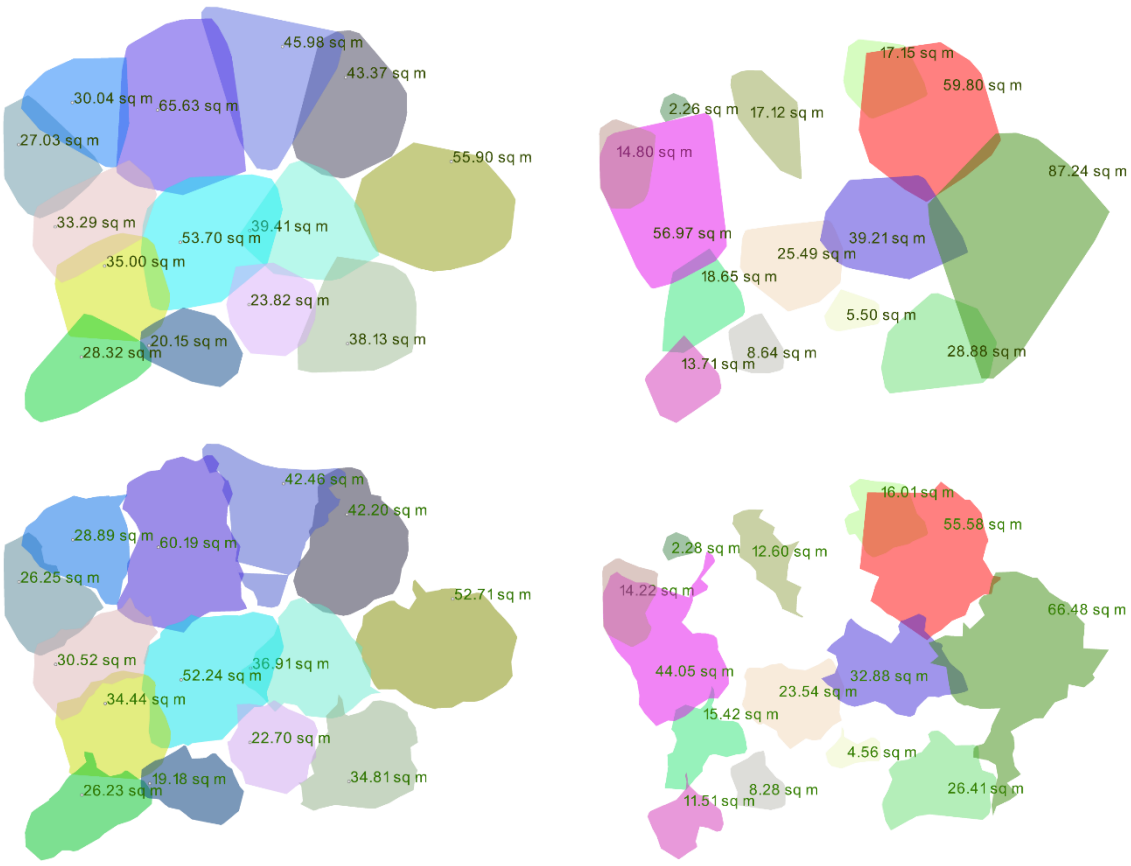

Figure 4.33: Convex (**top**) and concave (**bottom**) hull polygons for TLS (**left** panels) and HMLS2 (**right** panels) datasets. Polygon values are summarised in **Table 1.1**.

Tilgate Forest: UTF-ROK South

Figure 4.34: 11 trees extracted from data acquired in the UTF-ROK-S (south) sub-plot at Tilgate Forest. From left: TLS from oblique angle; HMLS2 from oblique angle; TLS in plan view coloured by tree segment; HMLS2 in plan view, coloured by tree segment.

Figure 4.35: 2D convex and concave hulls of the 11 tree segments scanned at UTF-ROK south. Although less marked than the UEP-BW equivalent, HMLS2 surface area is still significantly under-reported (**right** panels) compared with TLS (**left**).

Tilgate Forest: UTF-ROK Combined

To plot relationships between the two sensors and two projected crown surface area approaches, the 14 trees of UTF-ROK North and 11 of UTF-ROK South were combined. **Figure 4.36** shows a poor degree of correlation between TLS and HMLS-derived surface areas for the two techniques. It highlights a strong correlation between convex and concave hull-derived measurements, irrespective of sensor.

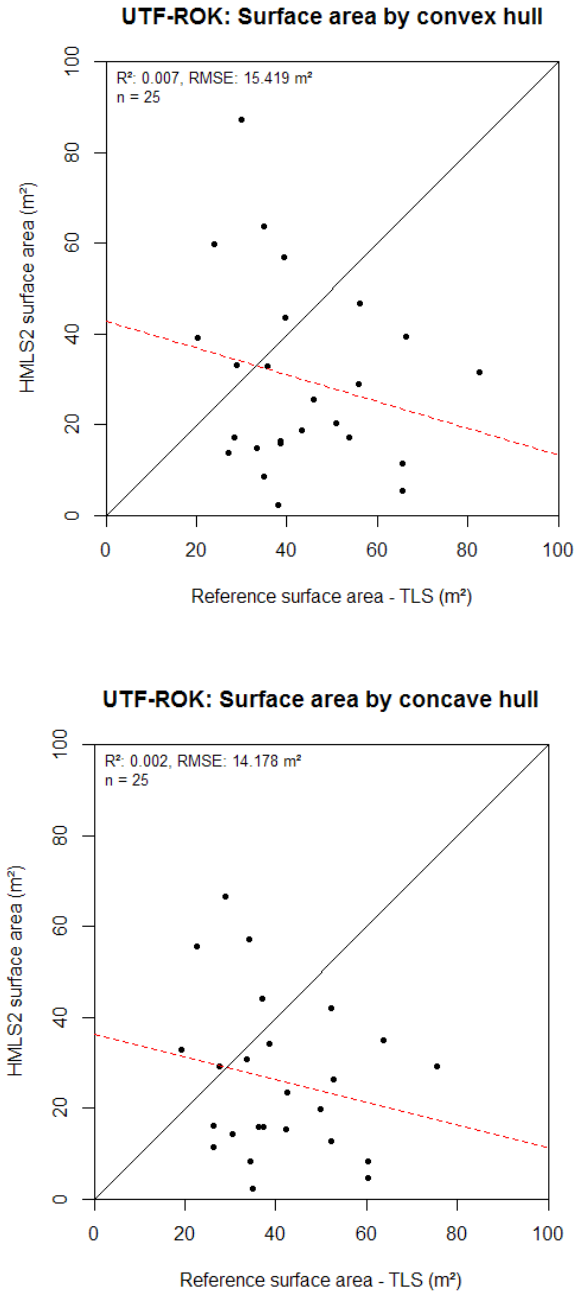

Figure 4.36: Scatterplots illustrating very weak correlation in projected crown surface area between sensors (upper two panels).

4.3.7 Tree crown: 3D geometry

Here, analysis focussed on the UEP-BW plots due to availability of data from all three sensors (P20 TLS; ZEB-1 and ZEB-REVO HMLS). To again mitigate for edge effects, only those trees with 95% of their crown (by area) within the UEP-BW sub-plot were retained. Initially, twenty trees were sampled from UEP-BW data (TLS, HMLS1, HMLS2) and twenty-five from UTF-ROK (TLS and HMLS2). Due to glitches in the *3D Forest* processing workflow, four trees were jettisoned from the UEP-BW dataset culminating in a sample size of sixteen. Despite this, data still captured a broad range of crown volumes (**Table 4.9**). Results are variously presented one site at a time through a combination of graphs, tables and projections of three-dimensional volumetric meshes.

Epping Forest

Table 4.9 summarises crown volume estimates by estimation technique.

Table 4.9: Summary of UEP-BW tree crown volumes

	Voxel (m^3)			Convex hull (m^3)			Cross-sectional (m^3)		
	TLS	HMLS1	HMLS2	TLS	HMLS1	HMLS2	TLS	HMLS1	HMLS2
Mean	7.03	0.66	2.01	441.97	52.72	235.18	233.75	22.10	130.46
Standard error	1.49	0.22	0.49	99.43	20.43	57.60	50.11	8.48	32.10
Median	7.28	0.43	1.23	407.85	27.93	211.54	212.95	14.23	108.21
SD	5.97	0.90	1.96	397.74	81.71	230.40	200.44	33.92	128.34
Kurtosis	-1.17	14.5	1.19	-1.00	10.62	-0.96	-1.45	11.85	-1.07
Skewness	0.40	3.73	1.26	0.49	3.11	0.59	0.30	3.31	0.71
Range	16.58	3.92	6.83	1174.56	334.01	680.19	552.60	140.11	341.41
Minimum	0.04	0.05	0.15	0.49	1.10	1.76	0.82	1.73	1.72
Maximum	16.62	3.96	6.98	1175.05	335.11	681.95	553.42	141.84	343.13
Sum	112.49	10.54	32.20	7071.57	843.60	3762.82	3740.04	353.35	2087.43
Count	16								

The sixteen trees sampled from UEP-BW data are displayed below, both as cross-sectional renders with terrain (**Figure 4.37**, overleaf) and as plan view renderings of concave hull

meshes and mesh intersection (**Figures 4.38** to **4.40**). A limitation was found in *3D Forest*: it was not possible to disable or format annotation text.

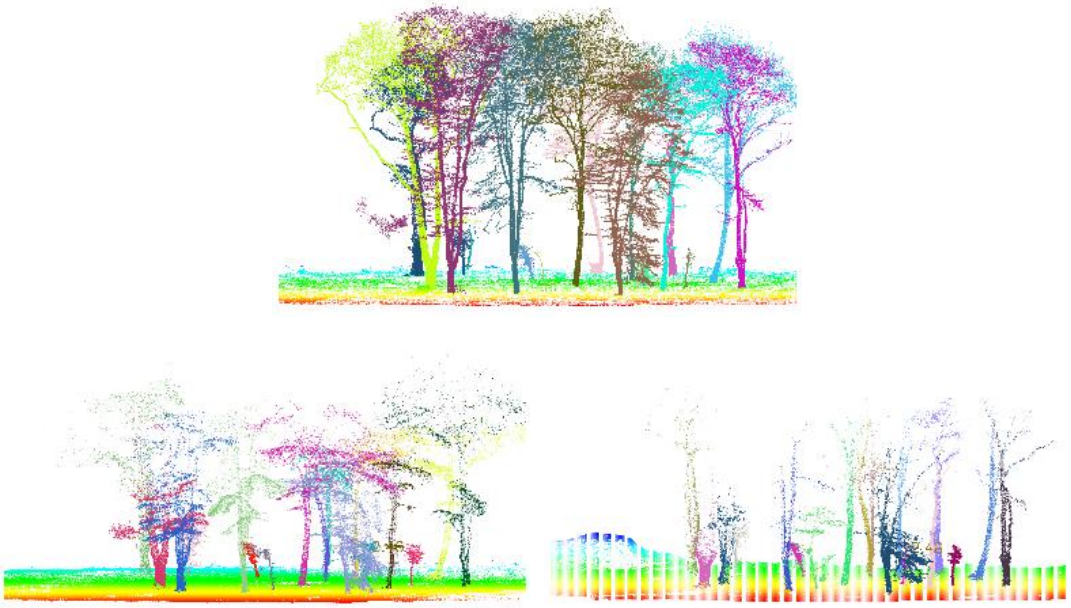

Figure 4.37: Cross-section renders of 16 tree segments as acquired by TLS (**left**), HMLS2 (**centre**) and HMLS1 (**right**) sensors at UEP-BW. Note that all trees are to scale.

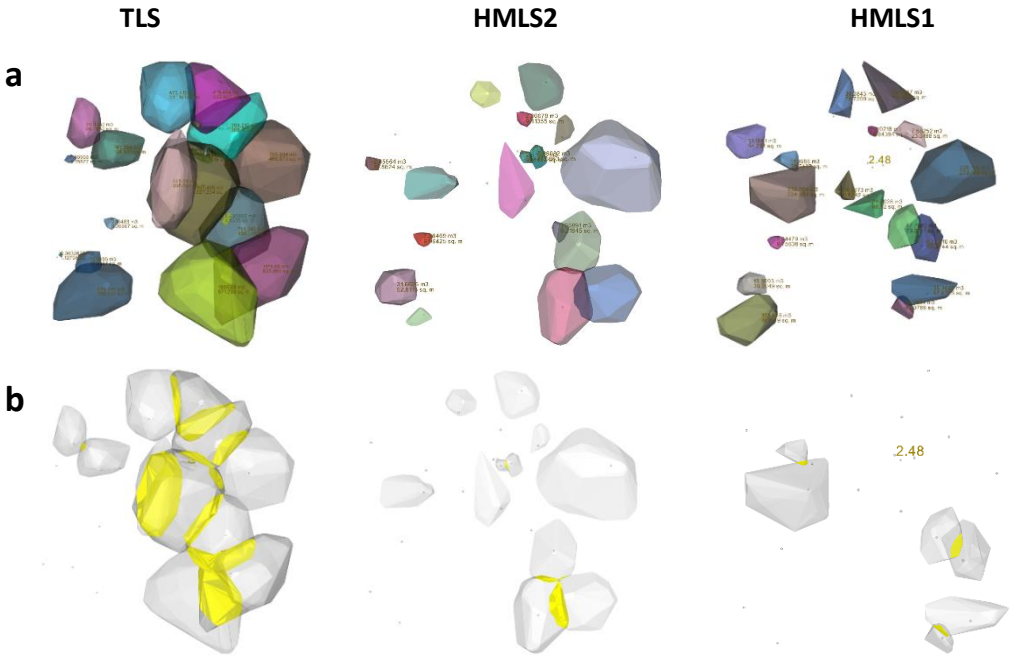

Figure 4.38: Plan view renders of (**a**) concave hull meshes for crowns as scanned by TLS (**left**), ZEB-REVO (HMLS2; **centre**) and ZEB-1 (HMLS1; **right**) sensors; and (**b**) meshes indicating intersectional crown meshes.

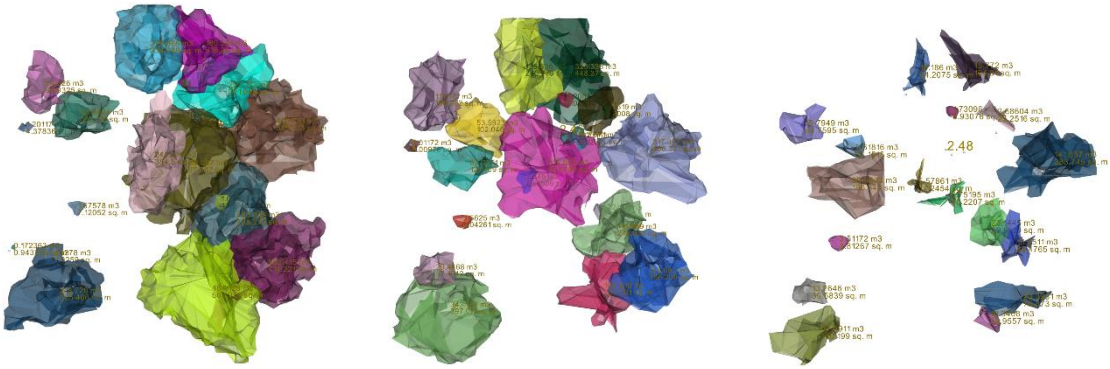

Figure 4.39: Meshes created from cross-section extracted from tree crowns. Note the 'tighter' fit, more akin to shrink-wrapping than a simple convex hull. Panels illustrate TLS (**left**), ZEB-REVO (HMLS2; **centre**) and ZEB-1 (HMLS1; **right**)-derived meshes.

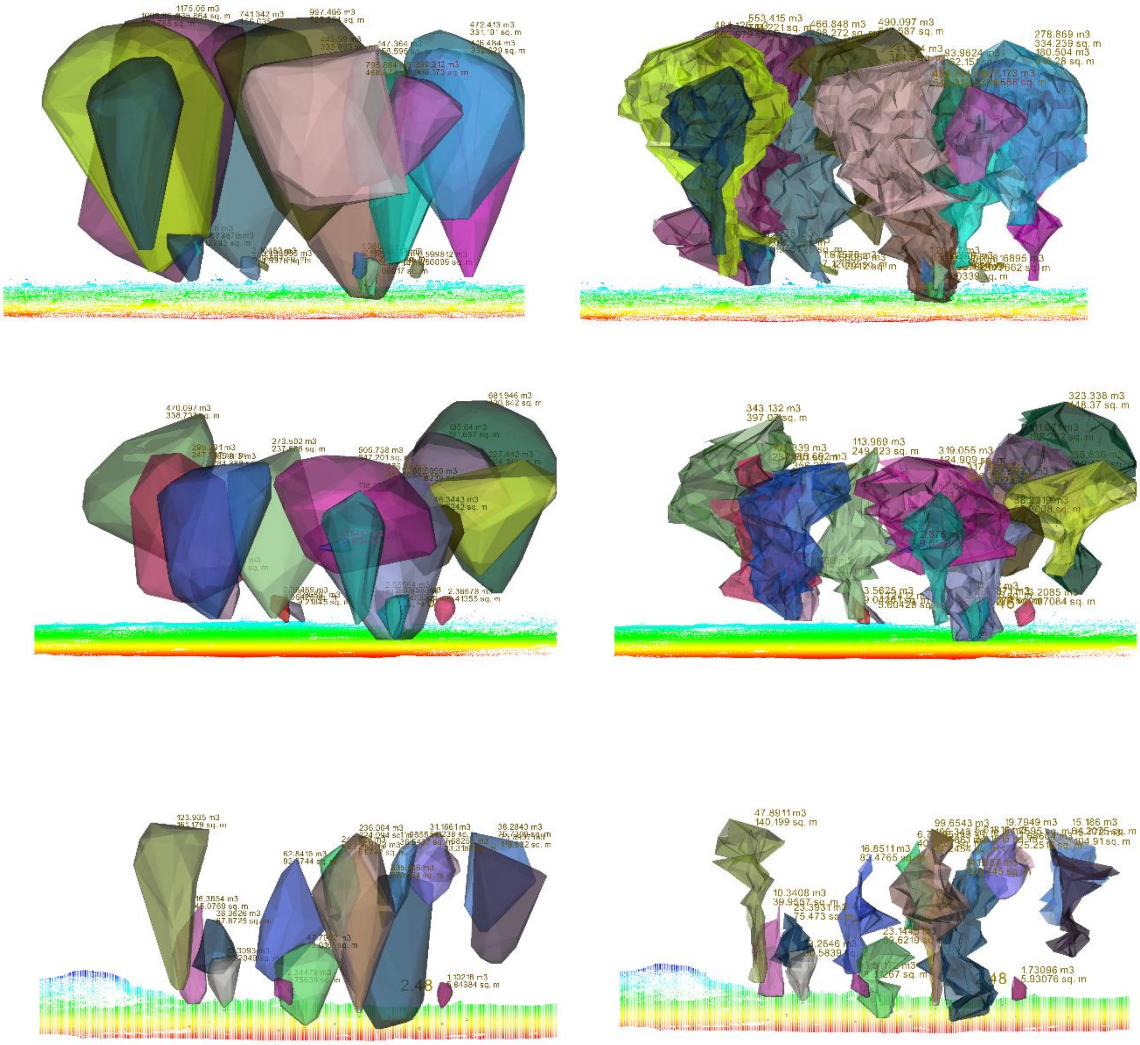

Figure 4.40: Side profile renders of convex hull **(left** panel) and cross-sectional (**right** panel) meshes. **Top** row: TLS. **Middle** row: HMLS2 (REVO). **Bottom** row: HMLS1 (ZEB-1).

The graphs on the following pages present collated UEP-BW crown height by sensor (**Figure 4.41,** below), estimated crown volume by sensor and technique (**Figure 4.42**, below), and crown mesh surface area by sensor and technique (**Figure 4.43**, below).

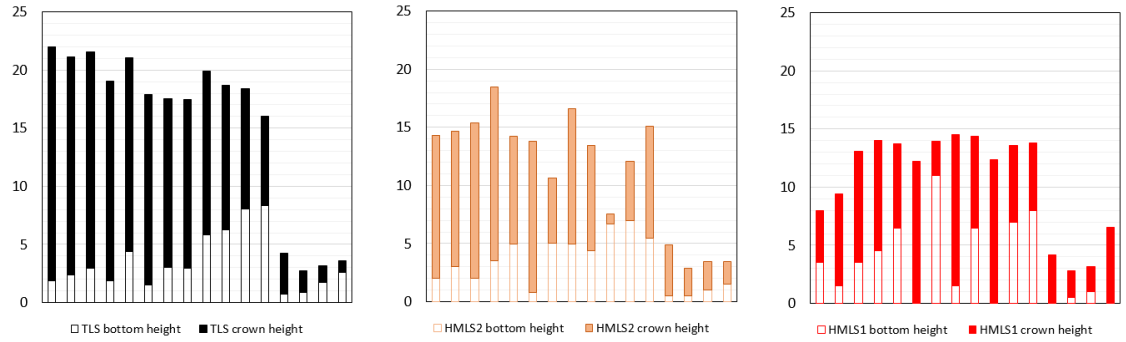

Figure 4.41: Stacked bar charts illustrating crown bottom height (hollow bars) and crown height (solid bars) for the UEP-BW subplot. 'Bottom' height is the height-above-ground of the first branch of a tree. 'Crown height' is therefore the height from this point to top-of-a-tree. It is notable that bottom height varies between sensors.

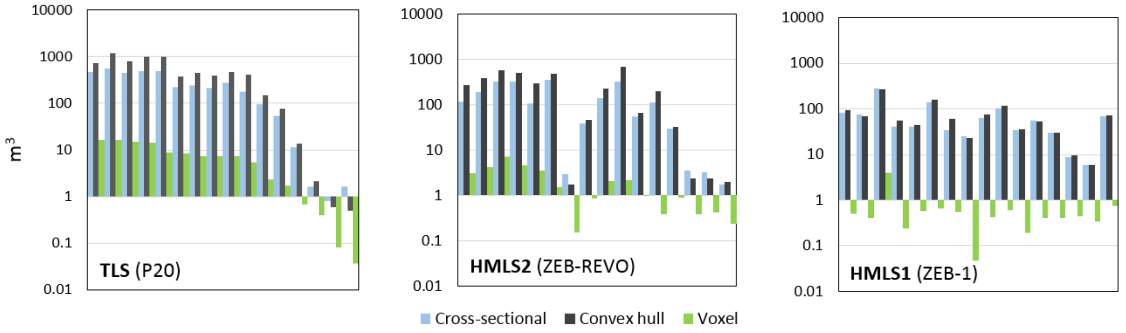

Figure 4.42: Estimated crown volumes; logarithmic scale used due to large range.

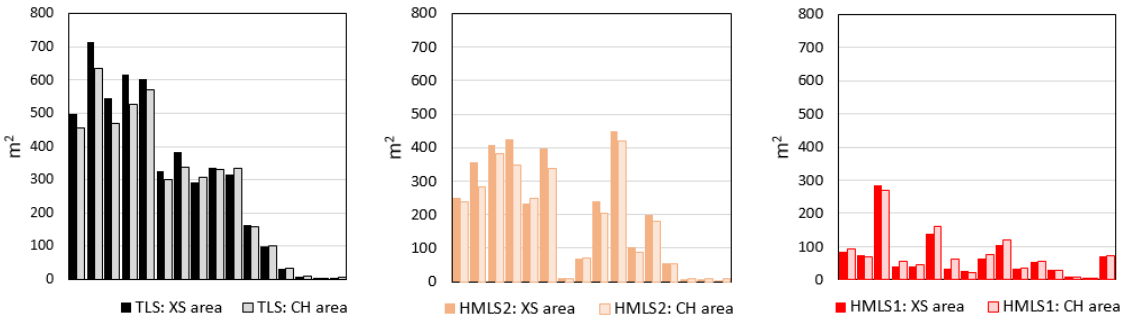

Figure 4.43: Surface area of volumetric meshes created using the cross-sectional (XS) and convex hull (CH) methodologies. Clearly, there is significant variation in estimated volume between sensors, whilst the two techniques estimate similar volumes.

Finally, a series of variables were plotted against one other (**Figure 4.44**, below).

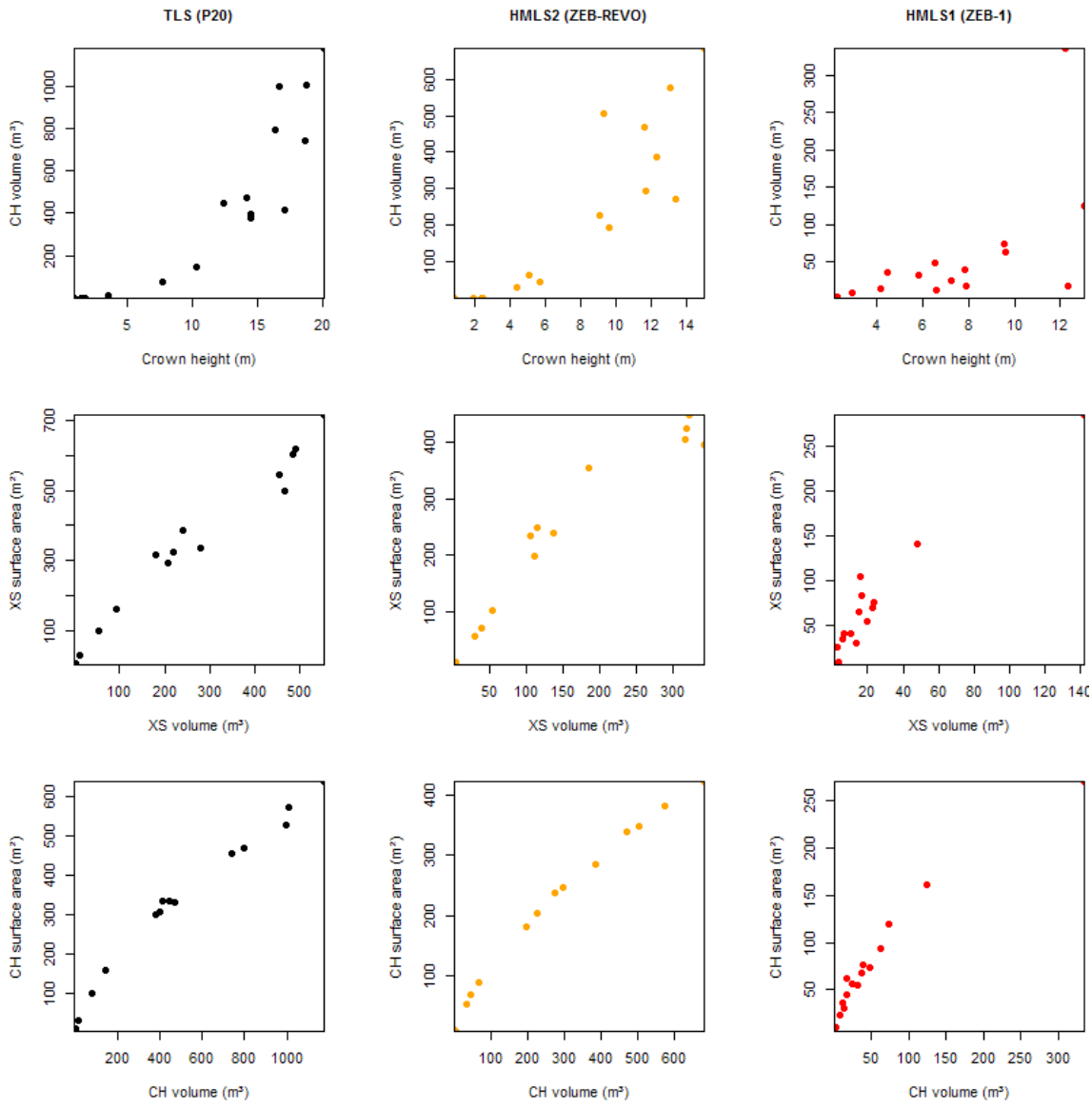

Figure 4.44: Scatterplots determining whether there might be relationships between crown height and convex-hull derived volume (top row), cross-sectional surface area and cross section-derived volume (middle row) and convex hull surface area and convex hull-derived volume (bottom row).

There are positive correlations in all instances. Interestingly, there appear to be negative exponential relationships in the two sets of volume vs. surface area plots.

Points are coloured by sensor: black (TLS), orange (HMLS2) and red (HMLS1).

4.4 Summary

The principle aim of this chapter was to assess the performance of HMLS sensors in object detection and measurement within different types of forest. Two HMLS sensors – the GeoSLAM ZEB-1 and ZEB-REVO – were put through their paces. Point clouds acquired with these sensors were compared with reference TLS data, as well as a variety of manual field validation measurements such as caliper and tape-derived DBH and range and azimuth-derive stem mapping. Data had to be subsampled to mitigate limitations at the data processing stage (i.e. RAM limited the volume of data which could be ingested) but nonetheless, valid results were achieved.

The data was generally suitable for semi-automated segmentation, although the systemic noise – manifested as a 'fuzziness' extending up to 0.05 m toward the scanner – tended to negatively impact separation of closely located tree components. Where accurate segmentation was achieved, stem maps proved reliable, with error limited to <0.1 m. Instances of more substantial error were largely due to the presence of understorey vegetation affecting the 'centre of gravity' of low laying points at ground-level.

Both HMLS systems proved capable of tree stem detection and in most cases, DBH could be derived from HMLS point data. Error (RMSE) was typically in the order of 0.02 to 0.05 m, in line with previous studies, with the Randomized Hough Transform algorithm in *3D Forest* found to be the best-performing. HMLS sensors could *not* detect tree height, irrespective of tree density or leaf coverage, suggesting limited range had a greater effect than anticipated. In addition, the two devices were of minimal use regarding extracting realistic crown metrics – especially volume.

The following chapter seeks to address technical limitations identified here by isolating individual parameters deemed most likely to negatively affect HMLS data utility and quality.

5. HMLS sensor performance in controlled conditions

At the time this research began (October 2014), HMLS systems were in their infancy. Ryding et al. (2015) were the first to report on the quality of HMLS data in a forested area, followed by Bauwens et al. (2016). HMLS scanning remains state-of-the-art technology and at the time of writing (September 2018), has been explored in fewer than ten studies. To date, no study has sought to characterise dominant parameters likely to influence the performance of HMLS techniques in an experimental setting.

In ***Chapter 4***, both the ZEB-1 (HMLS1) and ZEB-REVO (HMLS2) were deployed in forested environments with a view to assessing range, accuracy and quality of the resulting point clouds. The GeoSLAM HMLS sensor deployed in this chapter (HMLS1; the GeoSLAM ZEB-1) had a maximum specified range of 30 m 'indoors', falling to 20 m 'outdoors' (Bosse et al., 2012; Cabo et al., 2018; GeoSLAM, 2018). These specifications were described alongside a recommendation that surveys were limited to 0.5 hours in length and undertaken at typical walking pace (GeoSLAM, 2018), estimated to be 5 km h^{-1}. Beyond this, there was no information on likely point density, swath extent or minima for object detection. In conducting fieldwork for ***Chapter 4*** and analysing the data, it became clear that the sensor specification was optimistic in certain conditions and range was less than expected (12 m, rather than the quite 20 m 'outdoors'). In addition, an element of sensor drift was observed – meaning the mapping of tree stems was much less accurate than the TLS approaches used to generate benchmark data.

Questions began to emerge: how should this type of scanner be used in-the-field? How might user decisions affect SLAM registration? At what point does its usefulness as a tool to quickly measure trees degrade, given reliance on an IMU without GNSS? What limitations are applied to this type of data, given that severe error propagation was observed during several field scans?

5.1 Research aims

This chapter documents the process of defining minimum, and optimum, survey requirements to adequately and consistently capture sufficient spatial data in forest environments. Specifically, the aim was to define 'best practice' in the use of HMLS and similar sensors in acquiring data at the highest-possible detail with least effort and minimal cost.

Several experiments were designed to have broader applicability to future sensors based on SLAM registration, similar laser hardware or operated in a handheld manner. A series of scans were acquired, under controlled conditions, to better-understand the factors that influence the utility of HMLS sensors in forest mensuration. A reference scan was acquired in accordance with the GeoSLAM (2018) manual and informed by experiences gained through the wider context of this PhD research. Previous work in this area, including research by Ryding et al. (2015), Bauwens et al. (2016) and Oveland et al., (2018), characterised the accuracy of the ZEB-1 in extracting diameter at breast height in temperate woodlands. However these studies did not go as far as assessing scan geometry beyond detailing the scan trajectory they each followed. Furthermore, none of the three studies quantified the vertical distribution of points or sought to determine an optimal scanning strategy.

5.2 Research question

The research question for this chapter was:

> *RQ2: How does HMLS sensor range and proximity to a target influence point density and distribution? Is it possible to increase point density in areas of marginal sensor range by increasing scan repetition alone?*

5.3 Results for RQ2

The results within this chapter encompass a variety of themes: point density, point distribution and SLAM performance (indicated as 'quality'). Analyses were devised for each theme to test the effect of scan distance, repetition and velocity on the resulting point cloud data. These isolated-variable scans were compared with a high-detail HMLS and reference TLS scan. **Figure 5.1** (overleaf) illustrates the interconnectivity of the three themes (colour coded where appropriate). In total, twelve HMLS scans were acquired within the UVP field site. Of these, two encountered unrecoverable errors at the cloud processing stage – perhaps due to unfavourable geometry (A. Rak, *pers. comm*., Dec 19, 2017) or a lack of features in 3D space. Ten processed point clouds were downloaded from the GeoSLAM Cloud server, all showing major registration errors. These were 'flagged' for re-processing by a GeoSLAM engineer and of these scans, only nine (eight excluding the 'reference' scan) proved possible to remedy. The trajectories of these eight scans overlay one another and were aligned with the reference scan. Each scan is illustrated in side profile (**Figure 5.2**; page 152) and from an aerial perspective (**Figure 5.3**; page 153), coloured by height with a typical blue-green-yellow-red colour ramp. **Table 5.1** describes the specifics of each scan.

Group	Variable	Comment	Target distance (m)	Date	Start	End
Ref	Reference scan	Reference scan building on pilot study approach	Variable	13/12/2017	13:14:55	13:22:42
A	Loop - repetition	1 loop around buffer margin	2	19/12/2017	10:23:10	10:24:55
A	Loop - repetition	2 loops around buffer margin	2	19/12/2017	10:26:15	10:28:30
A	Loop - repetition	5 loops around buffer margin	2	19/12/2017	10:30:10	10:34:30
A	Loop - repetition	10 loops around buffer margin	2	19/12/2017	10:37:00	10:44:45
A	Loop - repetition	20 loops around buffer margin	2	19/12/2017	10:51:05	11:04:30
B	Loop - distance	1 loop at 5 m from trees	5	19/12/2017	11:13:18	11:15:16
B	Loop - distance	1 loop at 10 m from trees	10	19/12/2017	11:33:34	11:36:16
B	Loop - distance	1 loop at 20 m from trees	20	19/12/2017	11:46:45	11:51:06
C	Number of passes	Passing on SOUTH offset 11 m; two passes (E to W; W to E)	11	19/12/2017	11:53:16	11:55:29
C	Number of passes	Passing on SOUTH offset 11 m; one passes (E to W)	11	19/12/2017	11:57:53	12:00:00
D	Velocity	1 loop, very fast walking speed	5	19/12/2017	11:17:00	11:18:35
D	Velocity	1 loop, very slow walking speed	5	19/12/2017	11:19:53	11:23:18

Table 5.1: Table summarising the scans performed for the UVP field site experiments. Orange rows suffered problems during processing; red rows could not be processed at all.

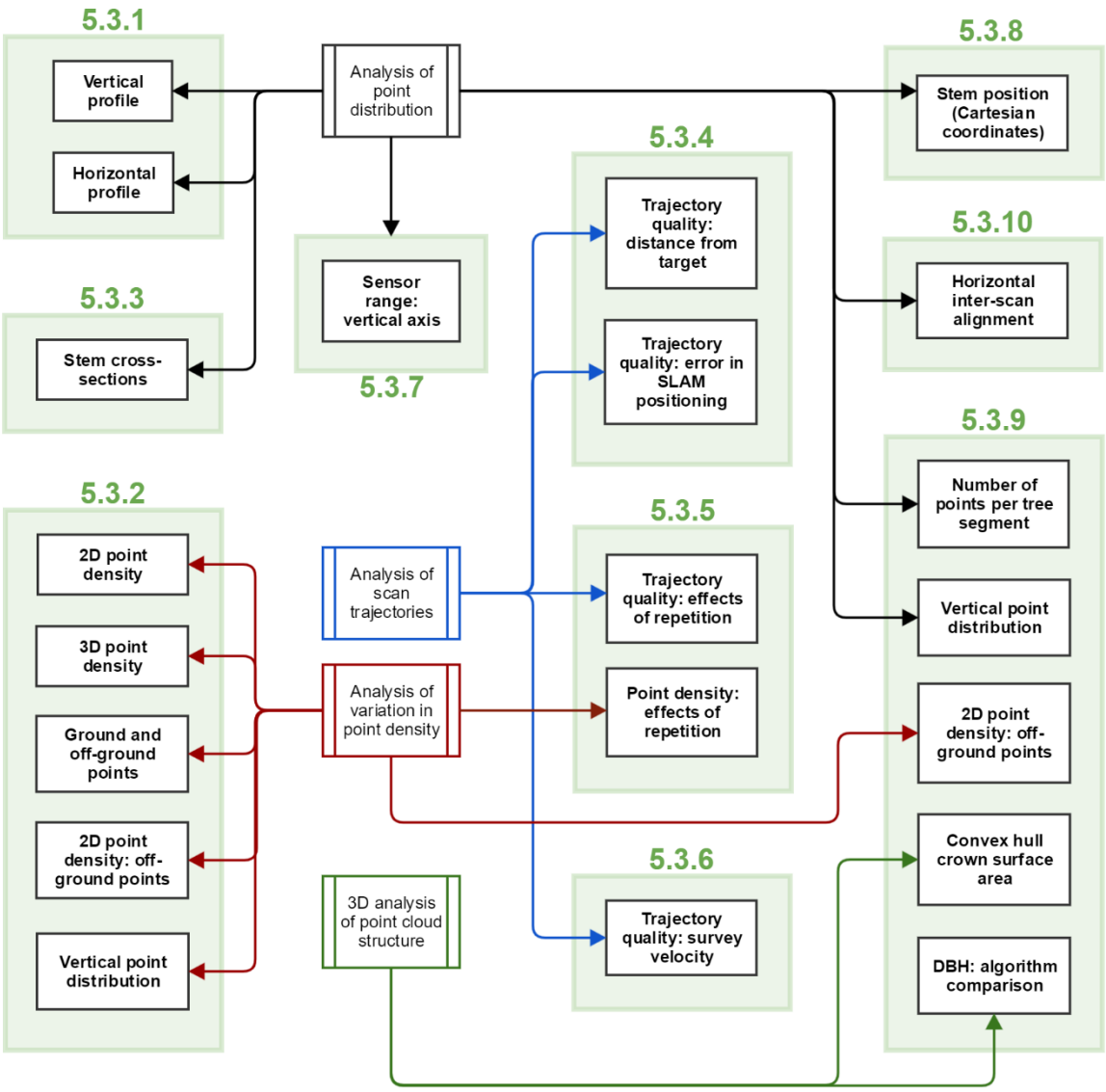

Figure 5.1: Schematic showing the interconnectivity between results in this chapter.

5.3.1 Side-by-side: vertical and horizontal profiles

Point clouds, 3D by nature, are very difficult to present in 2D media. However, they can be described both visually – through a variety of 2D plots – and statistically. Clouds were coloured by height (using default settings) and the SSAO (screen space ambient occlusion; OpenGL engine) shader was applied. 2D renders of each cloud were created, with a zoom set to 5x, and are reproduced in **Figure 5.2** and **5.3** on the following pages. These renders illustrate each cloud from aerial and east-facing perspectives. In side profile, north is towards the left; in the aerial projections (**Figure 5.3**), north is up.

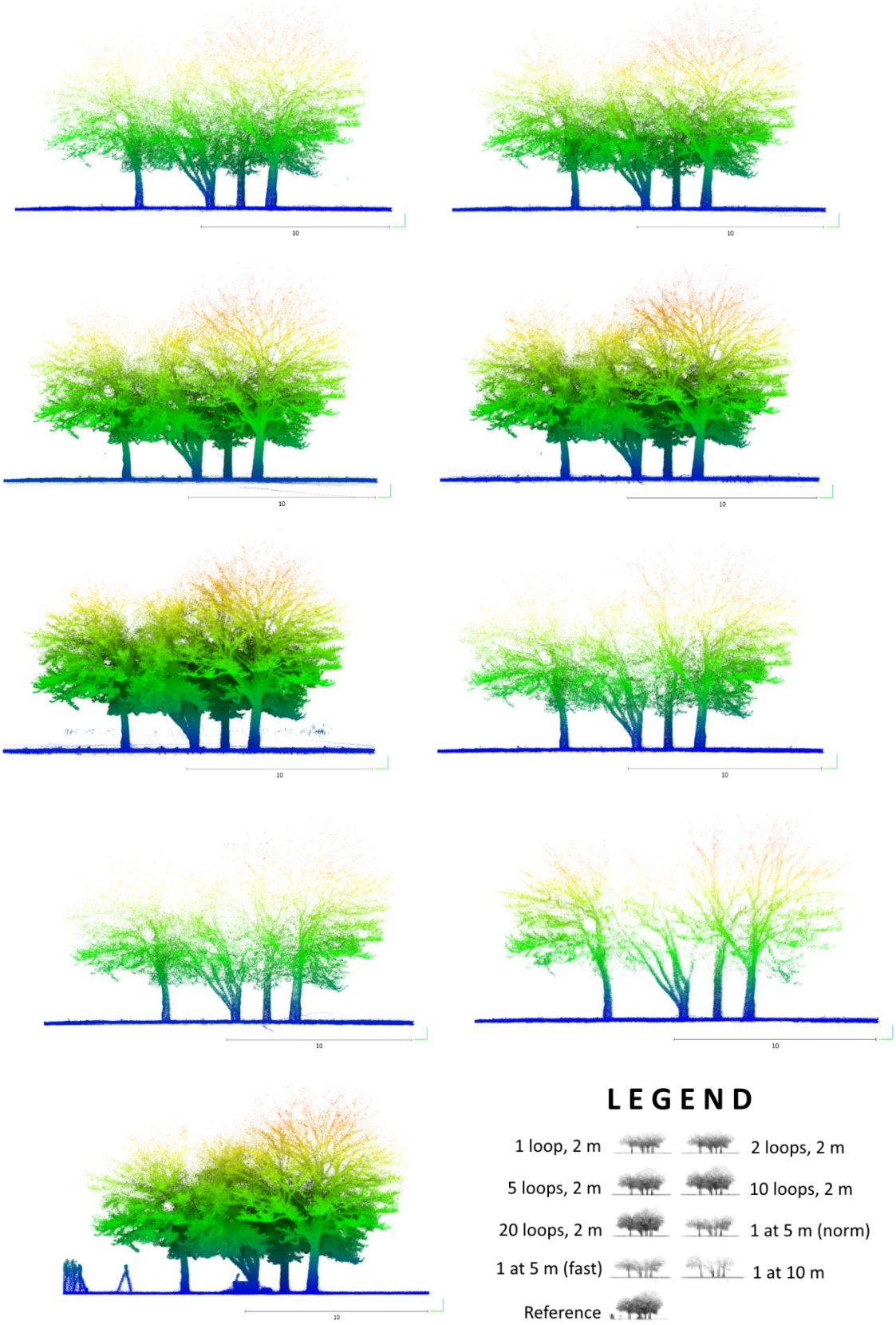

Figure 5.2: East-facing projections of the 9 successful HMLS scans as acquired at the UVP field site. Coloured by height sharing the same colour ramp. Blue: 0 m; green: 7.5 m; red: 15 m. Due to low point densities >8 m, point reproduction proved difficult here.

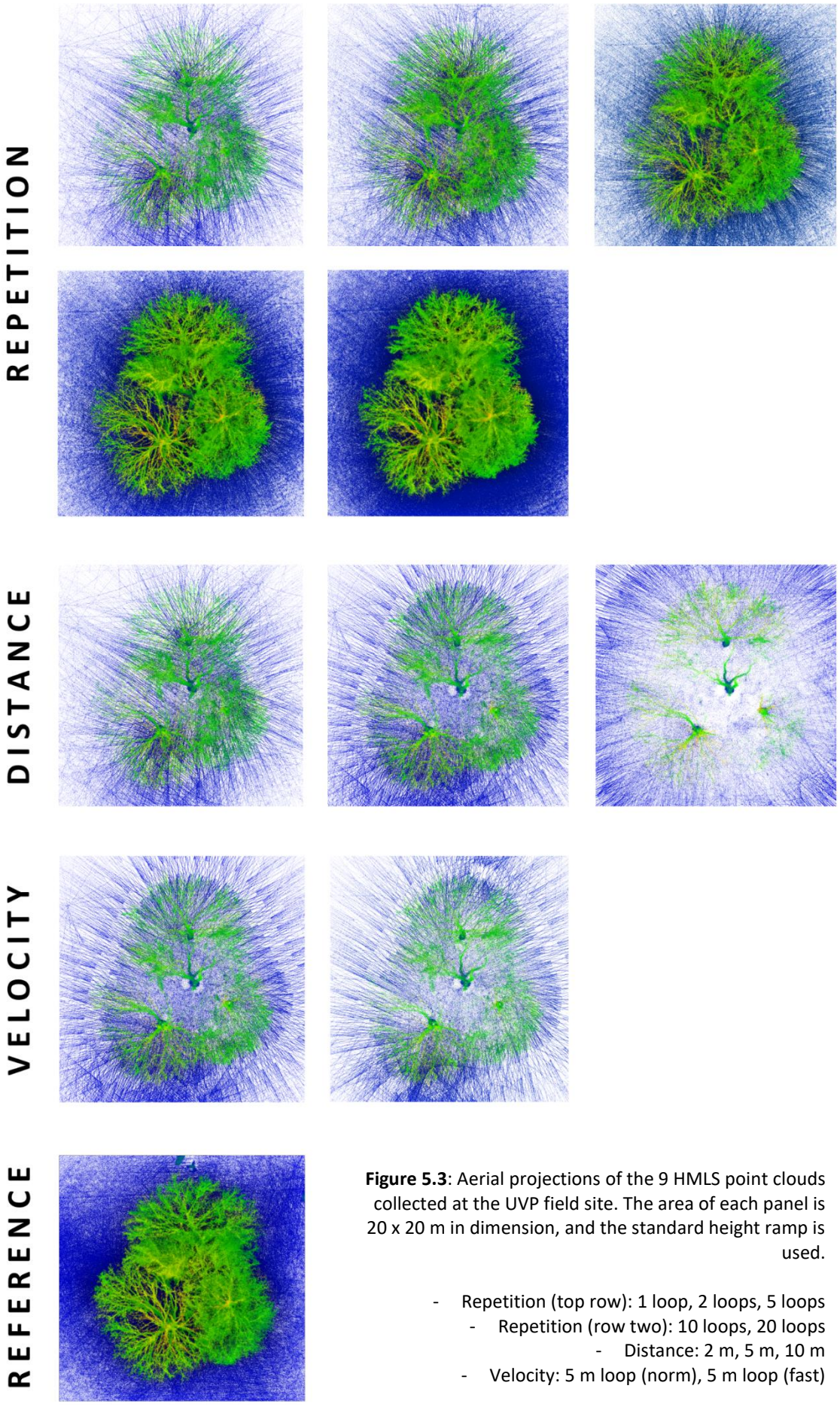

Figure 5.3: Aerial projections of the 9 HMLS point clouds collected at the UVP field site. The area of each panel is 20 x 20 m in dimension, and the standard height ramp is used.

- Repetition (top row): 1 loop, 2 loops, 5 loops
- Repetition (row two): 10 loops, 20 loops
- Distance: 2 m, 5 m, 10 m
- Velocity: 5 m loop (norm), 5 m loop (fast)

5.3.2 Point count, density and distribution

Processed point clouds for each of the nine successful scans were downloaded directly from *GeoSLAM Cloud* software in ISPRS .LAS (1.4) format. These .LAS files were imported into a single *CloudCompare* project and combined in a .BIN file within an organised hierarchy. Information from the headers of these files included information on scan geometry as well as a gross point count for each scan. *Point count* is "the number of 3D measurements captured during a scan". Together, *point distribution* and *point density* describe the spatial distribution of these measurements as well as any clustering or other spatial patterns that may exist. Here, the term point density refers to either a 2D or 3D point count, in raster cells (**Figure 5.4**, overleaf) or in cross-sections extracted from data where three-dimensional density was calculated with a moving, spherical kernel (**Figure 5.5** on page 156). Point distribution describes the relative density of points in the vertical axis (ground to the upper crown).

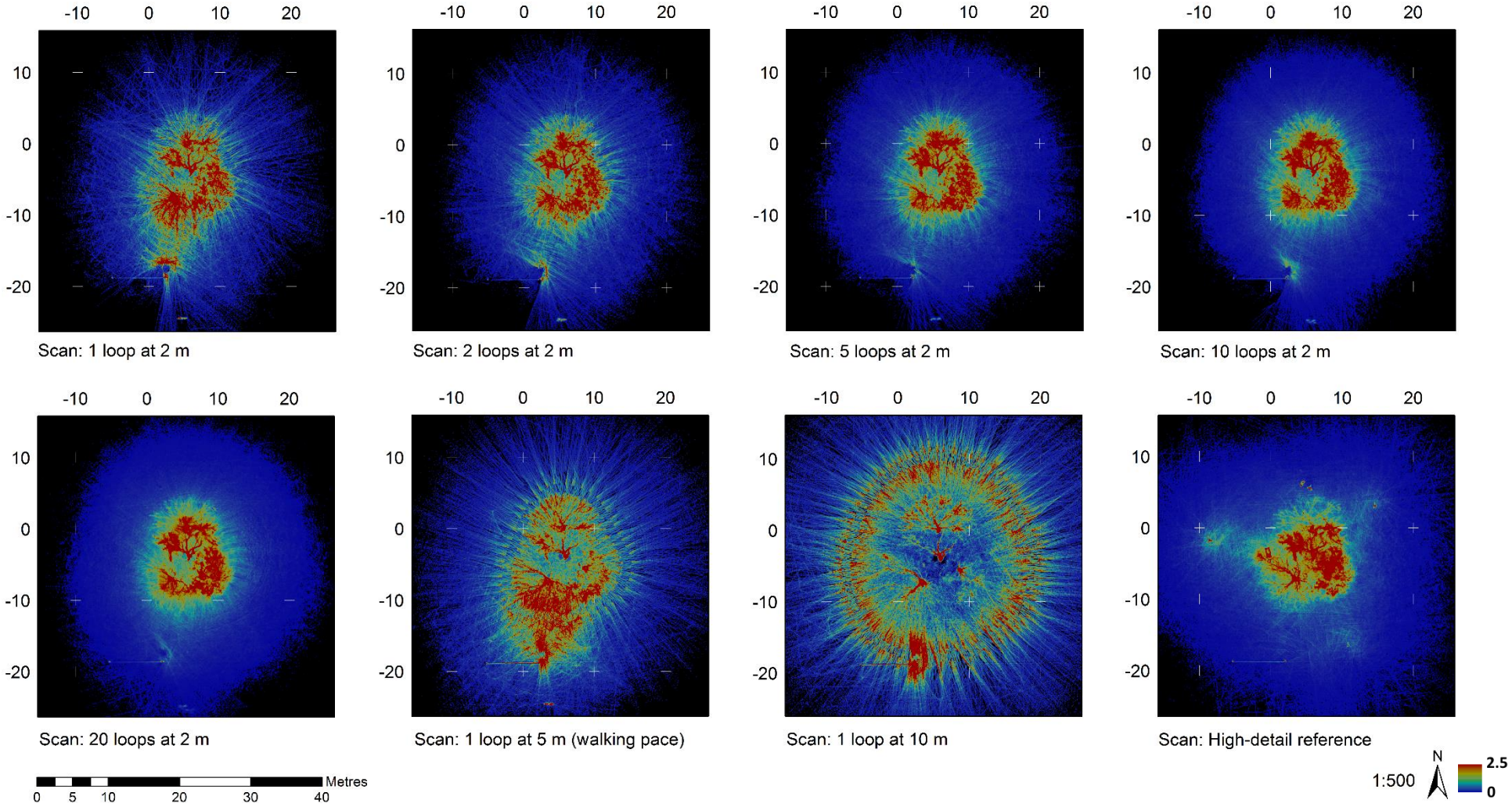

Figure 5.4: Two-dimensional point density, per 0.1 m pixel, for the scans undertaken with varying amounts of repetition and distance. Coloured by standard deviation (n = 2.5) ranging from low (0: deep blue) through to high (2.5: bright red). Black indicates '*NoData*' values.

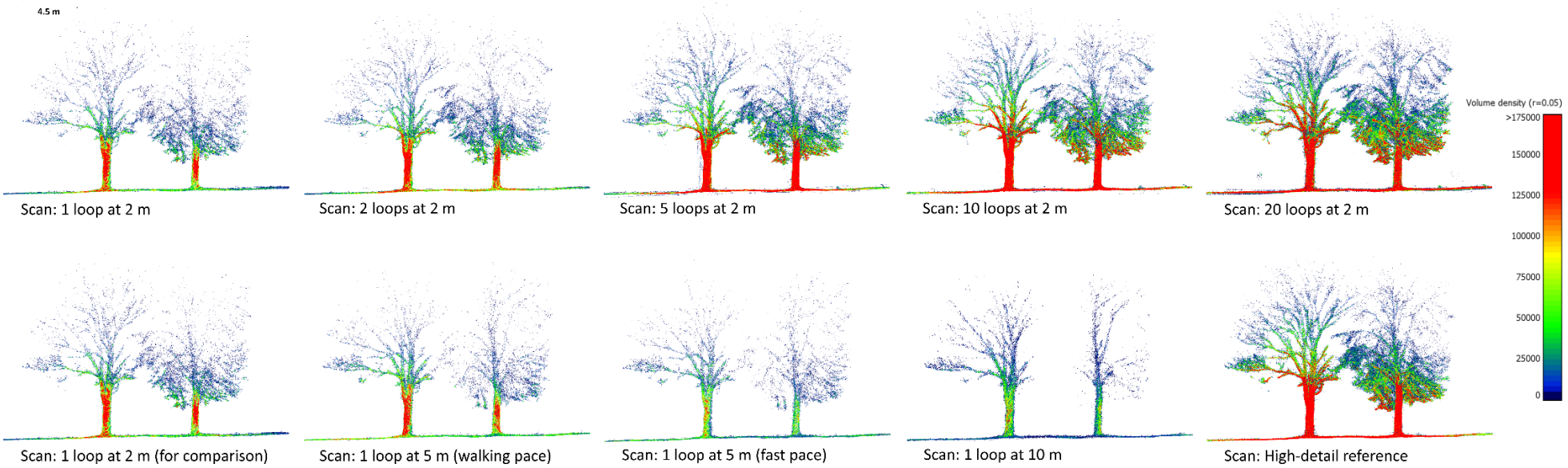

Figure 5.5: Side-by-side renderings of co-aligned east-west cross-sections extracted from all HMLS scans collected in the Victoria Park field site. Each rendering uses the same colour ramp, which describes number of points recorded within a sphere of 0.05 m radius. Due to the disparity of point density across the scans, the ramp is clamped at its upper bound to a value of 175 000 points; beyond this, the red shading persists.

Once density had been calculated, a *Cloth simulation filter* (CSF) classification was used to automatically classify points as 'ground' or 'non-ground' (Zhang et al., 2016). This was done as the majority of points in each scan depicted ground and would bias any analysis on vertical point distribution. **Figure 5.6** describes gross 'before' and 'after' point counts and their relationship as a function of this plug-in.

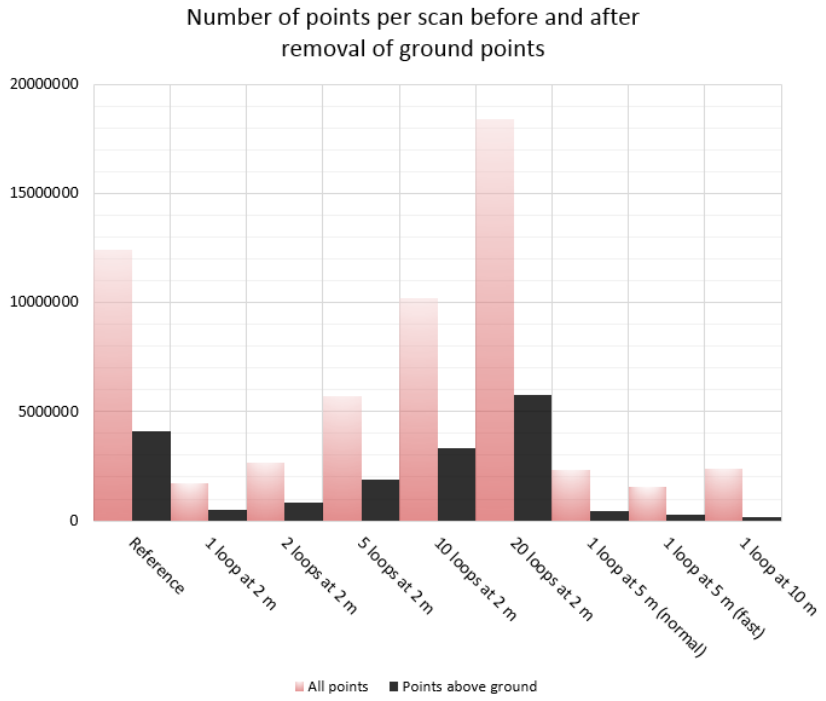

Figure 5.6: Graph showing point count per scan before and after application of the CSF plug-in. More points were acquired in the reference scan than in all but one scan.

As is clear in **Figure 5.6**, above, and **Figure 5.7** overleaf, point density varied quite substantially between scans and was much lower in varied-distance scans generally. For each of the nine controlled-condition scans, two histograms describing the vertical distribution of points were created. The first of these, **Figure 4.5.10**, shows the relative distribution of non-ground points in each of the nine scans. In each, the y axis has been preserved to best display the huge disparity in point density. In **Figure 4.5.11**, the same information was plotted but in terms of the proportion of all points logged per scan, as percentages. This allowed a side-by-side comparison of subtle variation in the height at which most points are focussed.

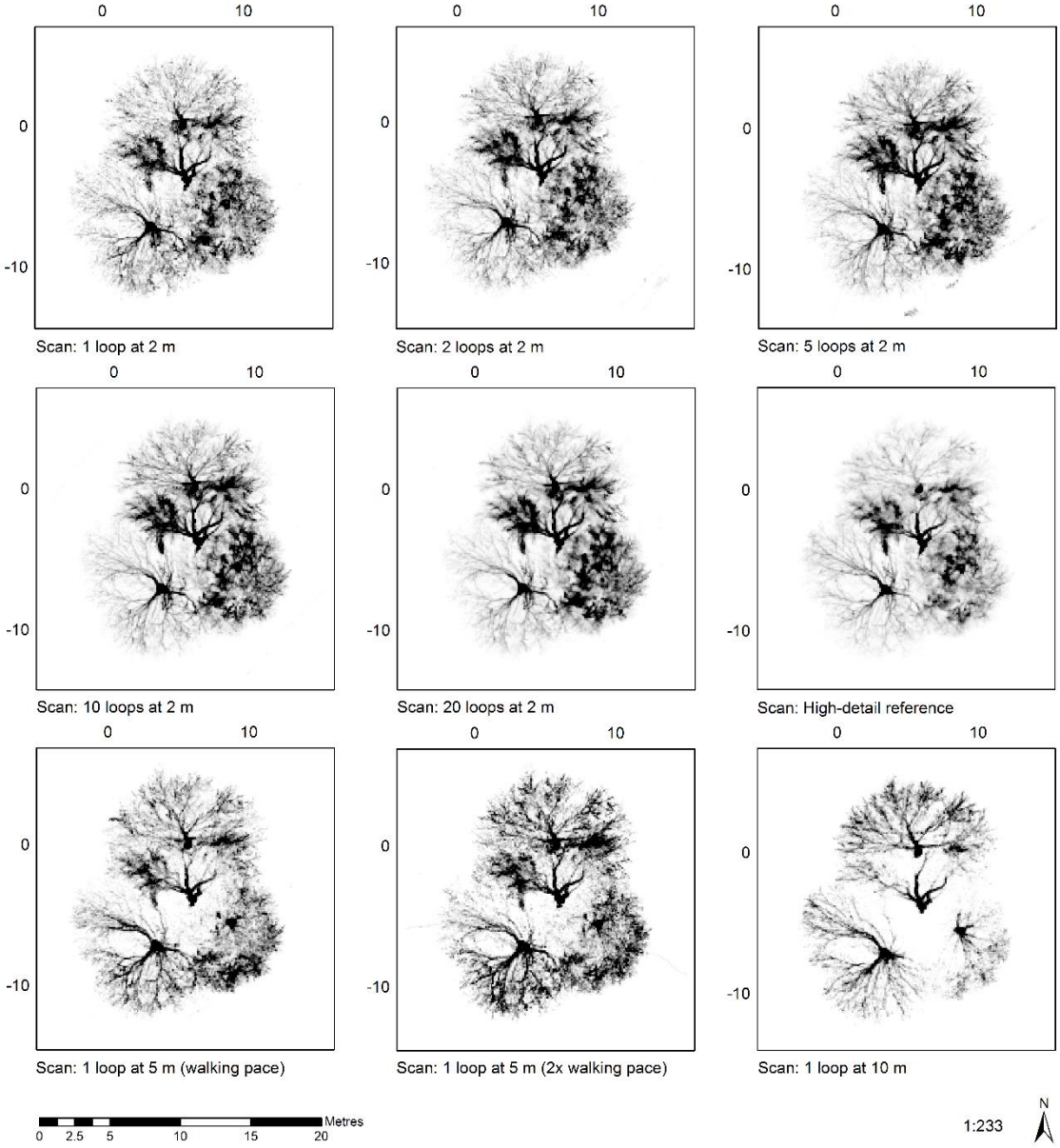

Figure 5.7: Two-dimensional point density, per 0.1 m pixel, for the scans undertaken with varying amounts of repetition, distance and speed. Coloured by standard deviation (n = 1) ranging from low (0: white) through to high (1: black). White indicates 'NoData' values.

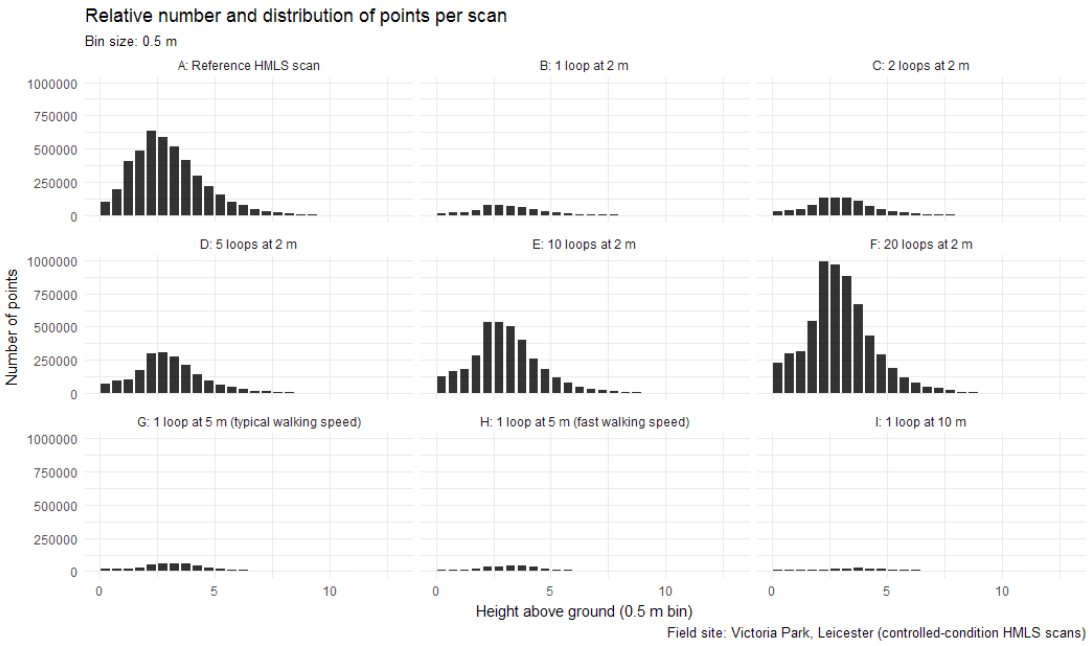

Figure 5.8: Histograms showing the distribution of non-ground points in 0.5 m bins in each of the scans. Generally speaking, these graphs share similar distribution with a majority of points acquired between 2 and 4 m of the terrain-normalised ground surface.

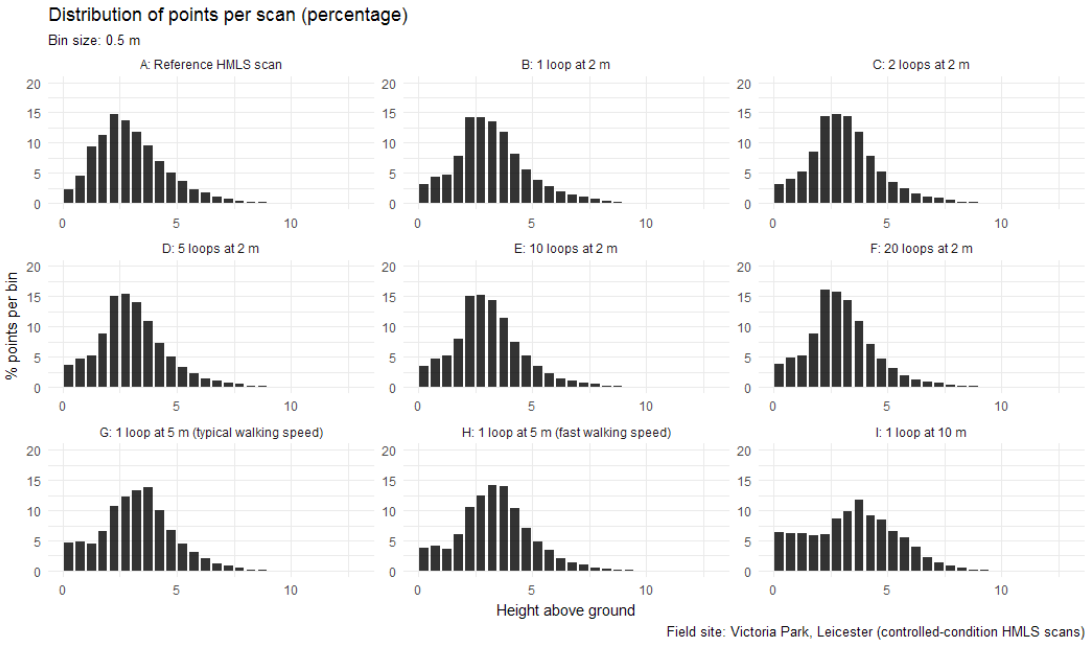

Figure 5.9: Histograms showing the percentage-based distribution of non-ground points in 0.5 m bins in each of the scans. Normalising the plots by percentage (compared with **Figure 5.8**), subtle variations become apparent. In all cases, skewness is in favour of the ground. At distances >5 m from the trees, the dominant height shifts from 2.5 to 4 m.

5.3.3 Side-by-side stem cross-sections

The density of points in each scan greatly varied. To better-understand these differences, horizontal cross-sections were extracted from each point cloud. These sections were 0.5 m deep (z axis) and include data at heights between 0.75 and 1.25 m above a terrain-normalised surface. Grouped by user-controlled variable, the cross-sections are presented in **Figure 5.10**, below and **5.11** overleaf.

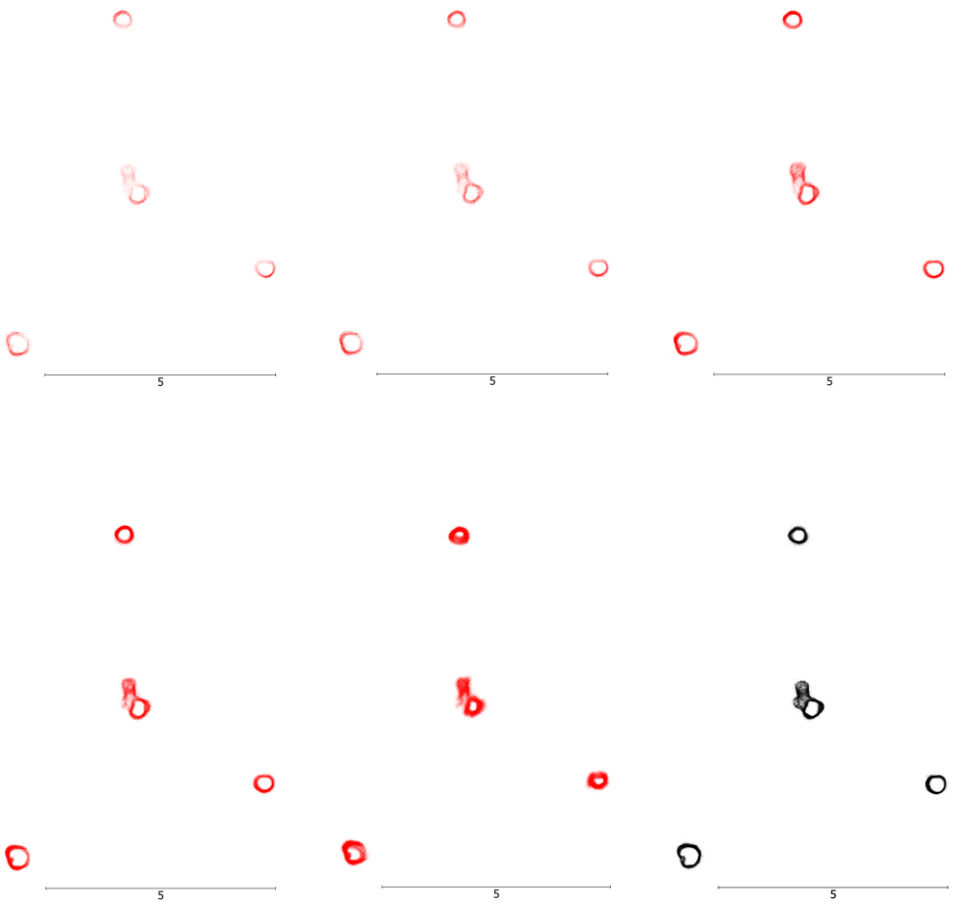

Figure 5.10: Cross-sections extracted from the varied-repetition scans of the UVP site captured at a constant distance of 2 m from target trees. Top row, from left: 1 loop, 2 loops and 5 loops. Bottom row, from left: 10 loops, 20 loops and reference scan.

The cross-sections from the single-loop scan (**Figure 5.10**, top-left) look partially-complete in terms of circumference – especially the middle tree. Meanwhile, sections

presented in the 20-loop scan look to have a high level of noise. Visually, the 5-loop scan looks closest to the reference dataset, suggesting 5 loops may sit nearest an 'optimal' scan protocol. Assessing varied-distance scans (**Figure 5.11**) and considering slices extend 0.5 m in the vertical axis, it looks as if the 10 m scan may lack enough points to perform a full circumferential measurement. It also became clear that point density diminished as velocity increased given the fixed pulse rate (40 Hz; Bosse et al., 2012) of the HMLS1 scanner.

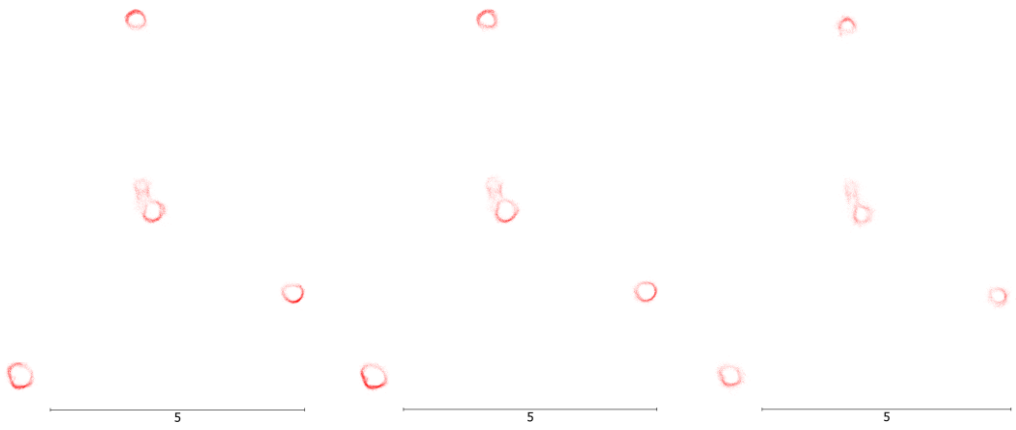

Figure 5.11: Cross-sections extracted from the varied-distance scans of the UVP site. From left, distances were 2 m, 5 m and 10 m.

5.3.4 Effect of varied sensor-target distance on tree reconstruction

In total, four scans were made of the UVP field site to assess the effect of distance on tree reconstruction. The scans followed a geometric loop offsetting the trees by 2, 5, 10 and 20 m (radius) respectively. Of these, the first three were successful and their trajectories are plotted in Figure **5.12**, overleaf. The 20-metre scan processed erroneously. GeoSLAM Cloud was unable to repair the raw data. The part-processed trajectory is presented in **Figure 5.13**, also overleaf. Intriguingly, some point data was recorded but the shape of the data did not match the real-world geometry of the scan.

Figure 5.12: Varied-distance scan trajectories illustrating 2 m (left), 5 m (central) and 10 m (right) buffer distance from the nearest tree to a given point. The start and end point of each scan were identical. Tree stems depicted as stars.

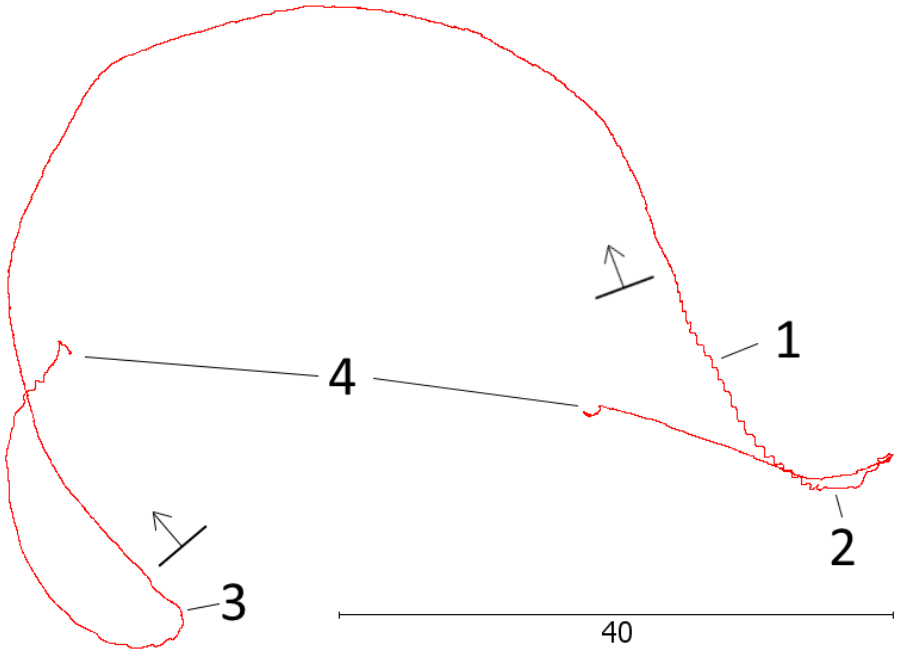

Figure 5.13: The trajectory of the scan conducted with 20 m radius, which GeoSLAM Cloud could not process. Most of the survey was co-registered correctly (between **3** and **1**). However, the relative lack of complex 3D features within range of the sensor may have impacted SLAM performance (e.g. **2** and **3**). Whilst as with all UVP surveys this scan had a common start and end point, post-SLAM processing, the start and end points somehow appear approximately 38 m apart (**4**).

5.3.5 Effect of number of passes on tree reconstruction

Five scans were acquired with varying amounts of repetition – passes of each target – ranging from 1 loop through to 20. Trajectories of each scan are illustrated in **Figure 5.14**.

Figure 5.14: Trajectories for each scan showing (from left) 1, 2, 5, 10 and 20 loops of the target trees. SLAM registration quality within the loops of the target trees appears moderate to good (green to blue) and degrades to poor (red) over open field.

Predictably, SLAM registration was successful in all scan scenarios. Just as predictably, point density increased with repetition although this was non-linear. Without access to the inner workings of this implementation of SLAM, it proved impossible to unpick where points may be removed or consolidated in overlapping trajectory loops. However, it was clear that tree reconstruction improved with increasing repetition (refer back to **Figures 5.2** to **5.5** plus **5.7**; refer to **Figure 5.15** over the page).

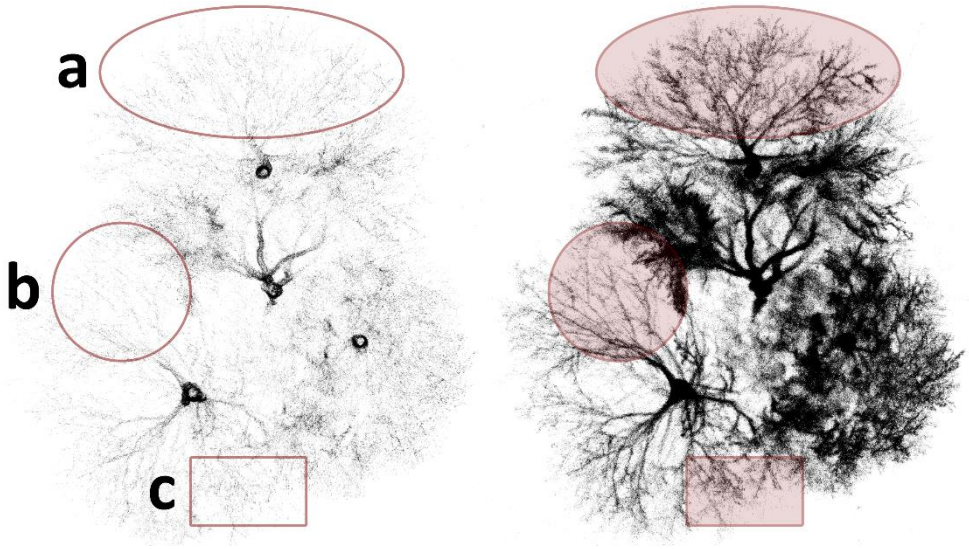

Figure 5.15: Post-CSF, non-ground-point density renders of the 1-loop (**left**) and 20-loop (**right**) UVP scans. Three areas showing the most marked variation in tree reconstruction have been highlighted (**a**, **b** and **c**) Even at this scale, it is clear that loop repetition is required to build the fullest picture of branch structure.

5.3.6 Effect of variation in rate-of-progress on tree reconstruction

Three scans were conducted at specific velocities: (**a**) typical (1.4 m s^{-1}), (**b**) a 'fast' (2.8 m s^{-1}) and (c) a 'slow' (0.7 m s^{-1}) walking pace. Of these, two scans generated successful results and one failed to process. The trajectories of the two successful scans are illustrated in **Figure 5.16** overleaf. Note that the faster scan required a secondary loop due to a degradation in SLAM positioning (annotated). Bizarrely, the 'slow' scan somehow failed to process correctly and misshapen, unrealistic point cloud and trajectory files were exported from *GeoSLAM Cloud*.

Density plots for the 'normal' and 'fast' scans (referring back to **Figures 5.5**; **5.7**) clearly demonstrate that the faster scan resulted in a much-reduced density of points. Furthermore, there appeared to be greater noise and an uneven density of individual scan lines, perhaps suggesting a somewhat intermittent variation in survey speed.

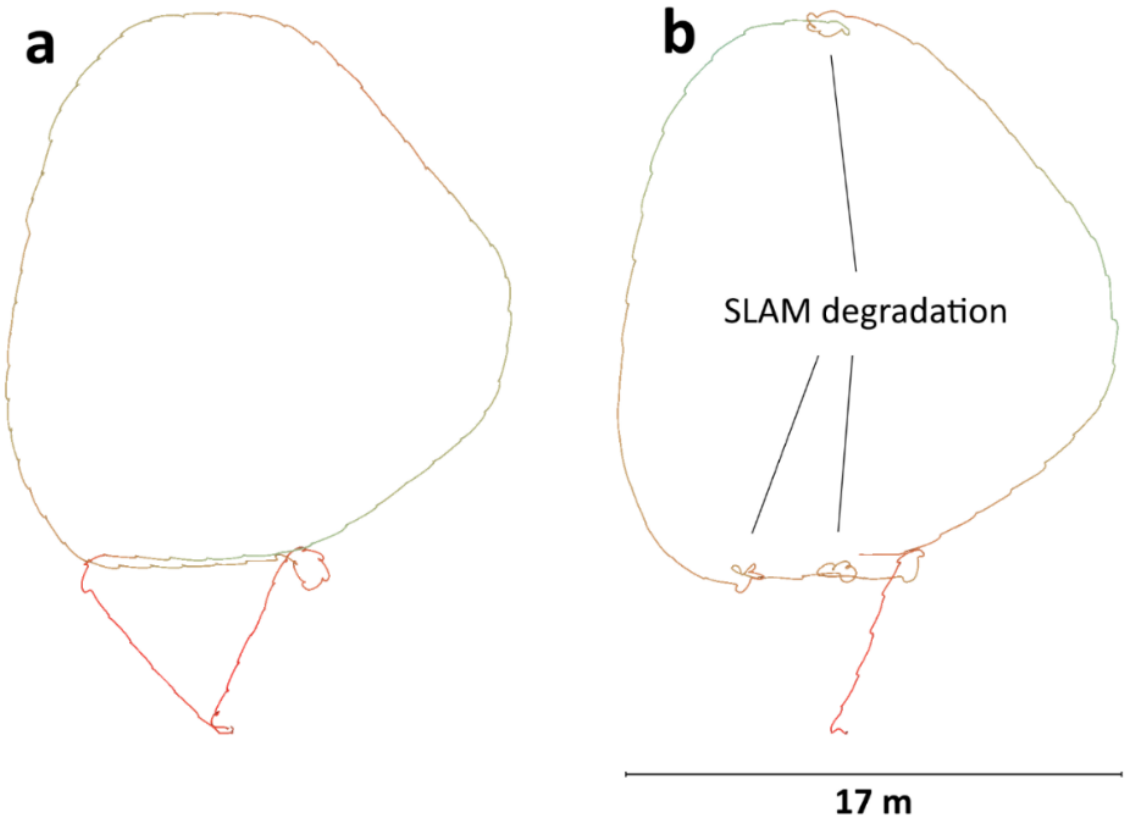

Figure 5.16: Trajectories, coloured by condition, of two 'varied velocity' scans. Both scans followed the same 5-metre buffer around the target trees, with the normal velocity scan (**a**) leading to a better-quality product than a scan conducted at twice the velocity (**b**). North is up; scale bar applies to both scans.

5.3.7 Effective sensor range

GeoSLAM (2018) suggested a theoretical sensor range, outdoors, of 20 m. In practice, it was found that effective range – the distance at which an object could be visually identified as a particular feature – was nearer 10 m. **Figures 5.5** and **5.7** suggest 12 m may be the most appropriate figure in terms of horizontal distance-from-target.
In terms of vertical range, **Figure 5.17** (next page) shows two height values for each scan – an absolute maximum height (above ground, where ground is defined as a terrain-normalised surface) and a height at the 99th percentile of all points. Strangely, two trends were identified. Absolute maximum detected height appeared to increase with repetition – and with distance-from-target, too. Yet whilst absolute maximum height is shown to increase, 99th-percentile height decreases. To better-understand

these unexpected trends, the point clouds were each trimmed at a height of 10 m above terrain-normalised ground. To highlight the inherent 'noisiness' of HMLS data at heights >10 m above ground, the reference scan was plotted alongside the P20 TLS validation dataset. With reference to the colour bar, it is clear looking at **Figure 5.17** (below) that the HMLS scan achieved a maximum detected height of 12.3 m whilst the TLS detected height in excess of 13.5 m. The overlay illustrates that the HMLS was unable to visibly resolve tree structure at heights above 10 m – further backed-up by the 'scattered' nature of the uppermost HMLS points, as visualised over the page in **Figure 5.18**.

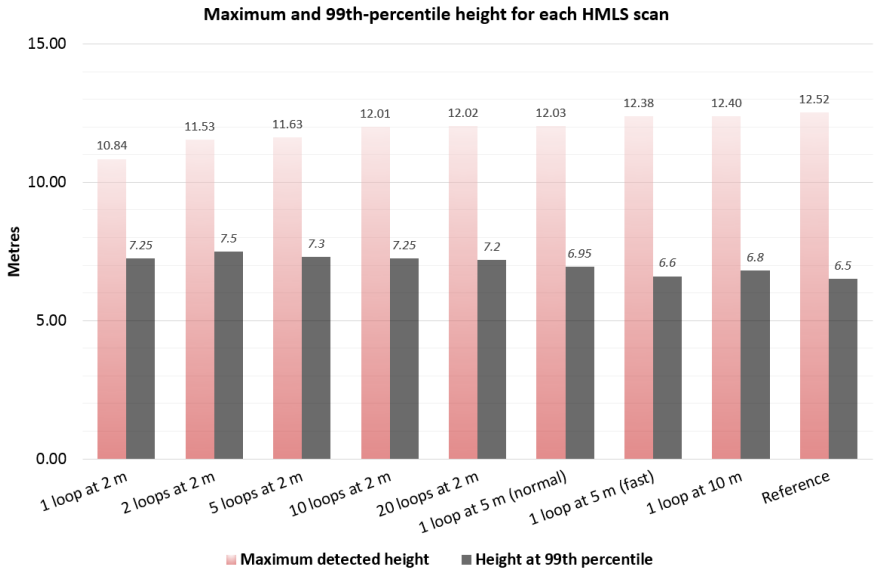

Figure 5.17: Bar chart showing maximum height, per scan, and 99th percentile height per scan. The latter heights were extracted as statistics calculated within *CloudCompare* and are included to highlight disparity between maximum and real-world heights.

Heights for the four trees were validated using the ikeGPS IKE4 in summer 2019 (*tree A*: 9.739 m; *tree B*: 10.072 m; *tree C*: 12.734 m; *tree D*: 12.089 m). However, whilst the comparative variation in height seemed plausible based on TLS heights (refer to ***Appendix***), the results are of limited use given that 18 months had elapsed between surveys. This demonstrates one of the major pitfalls of multi-sensor forest surveying: it is rare that all sensors can be deployed within a small temporal window.

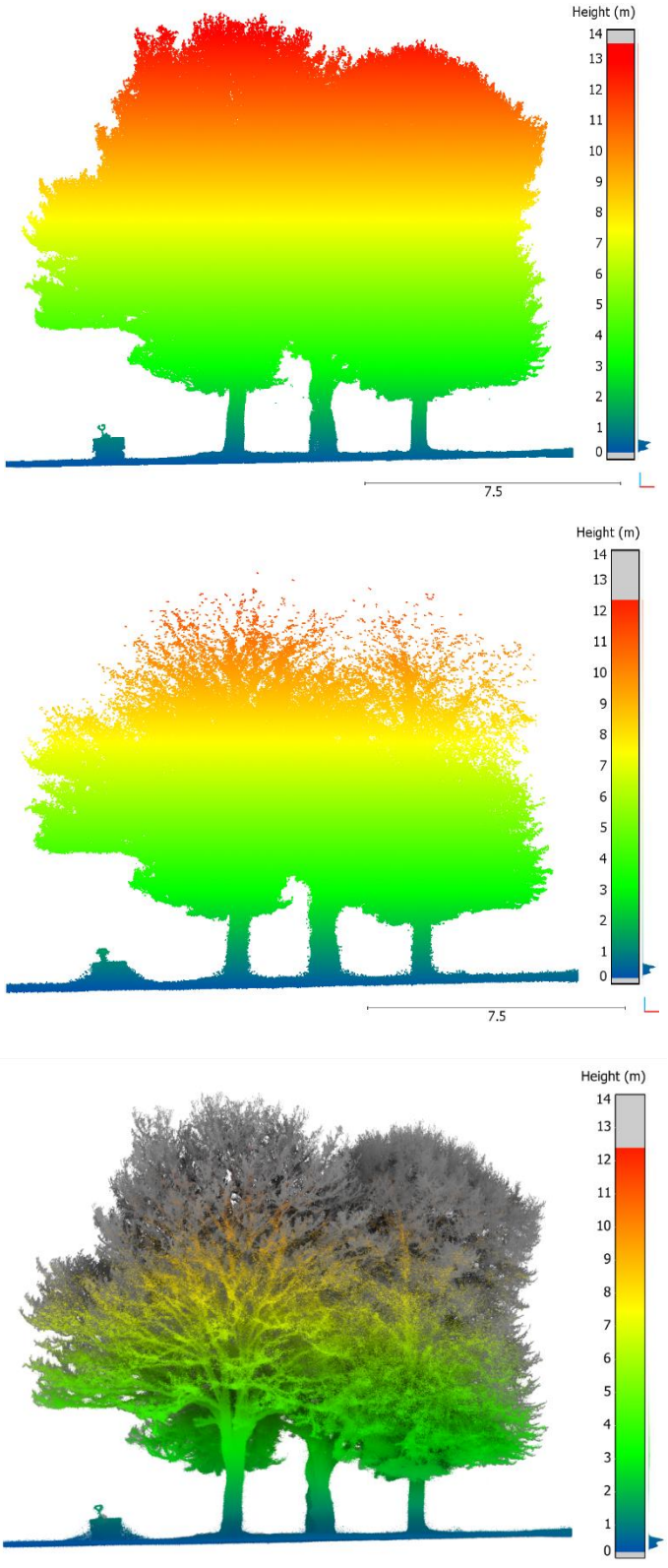

Figure 5.18: East-facing projection of (top) TLS, (b) high-detail HMLS and (c) combined point clouds illustrating the vertical distribution of points in terms of height above the terrain-normalised LCS.

5.3.8 Relative position of tree stem centroids

Four trees were segmented then isolated from non-tree points and stored within the software as individual, per-tree point clouds respectively named “Tree A”, “B”, “C” and “D”. Three methods were used to calculate centroids (as described in section 3 of this chapter): *lowest point*, *least-squares regression*, and *Hough transform*.

Figure 5.19 (page 169) presents the centroids at UVP plot-level, serving as a map of tree locations in the context of a local coordinate system (where the point *0,0,0* reflects the start-end point of the UVP reference scan). It is immediately clear that the cluster of centroids depicting Tree B has the greatest spread. Tree B is furthest from the trajectory of all UVP scans bar the ‘reference’, suggesting that positional accuracy may (at least in part) be a function of distance from scanner. The same four tree centroid clusters are each presented to a higher degree of zoom in **Figure 5.20** (page 170).

Based on a visual assessment, the ‘lowest point’ algorithm seemed to deliver the most realistic coordinates for each tree centroid. **Figure 5.21** (page 171), focusses on this approach, with estimated stem centre coloured by scan. Centroids extracted from the ‘reference’ scan are displayed as black points within a thin black buffer. The relative positions of the reference centroids and their isolated-variable counterparts consistently show erroneous tree position, under-reporting distance-from-scanner by up to 0.2 m.

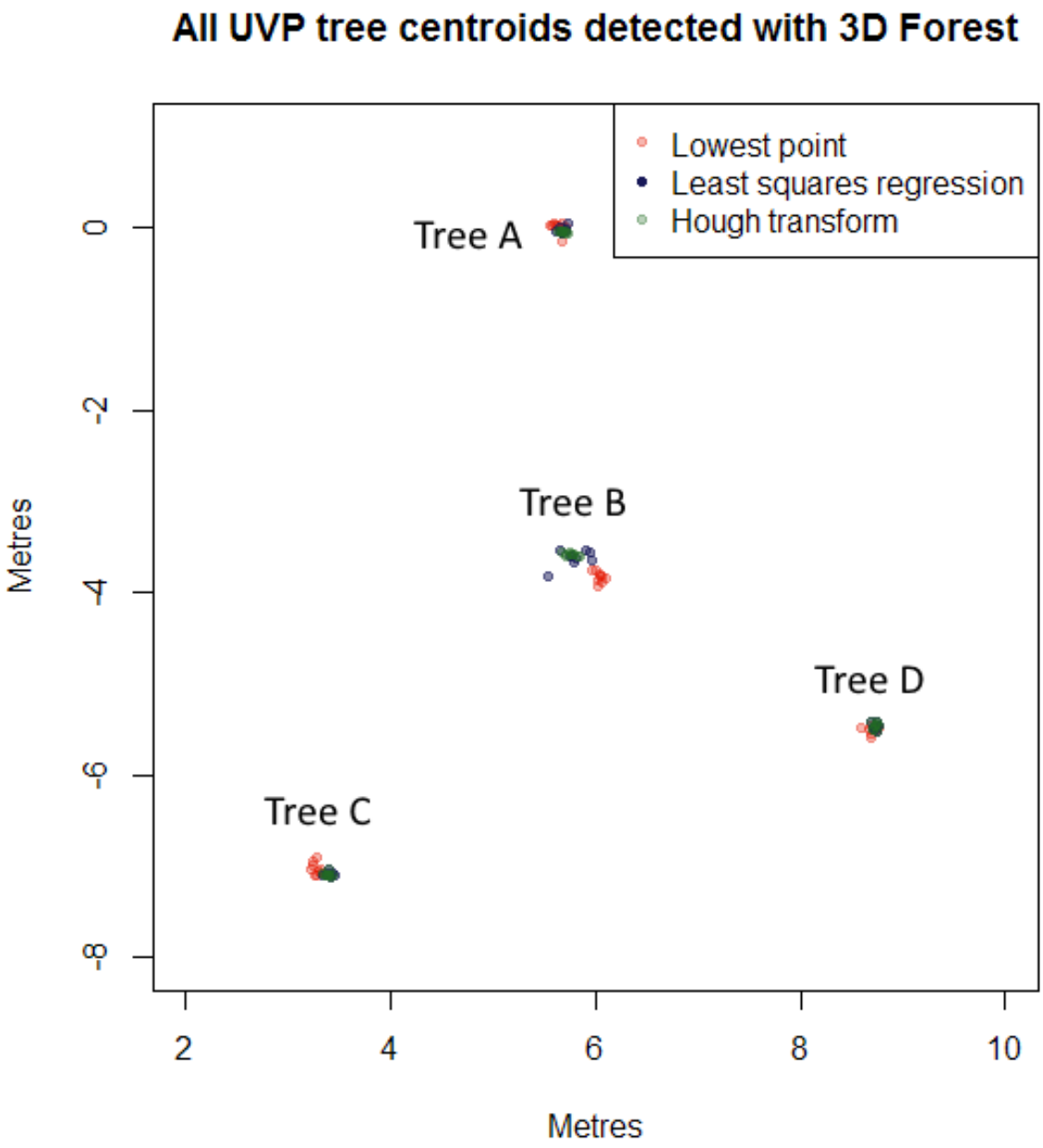

Figure 5.19: Scatterplot showing all detected stem centroids for each of the four trees within the UVP field site, coloured by the method used to detect centroid position. The uppermost cluster centre on *6,0* is "Tree A". The central cluster centred on *6,-4* is "Tree B". Meanwhile, the points at *3.5,-7* depict "Tree C" and *8.75,-5.25* illustrates "Tree D". Tree B shows the lowest level of agreement in tree position and is also the tree furthest from scan trajectories.

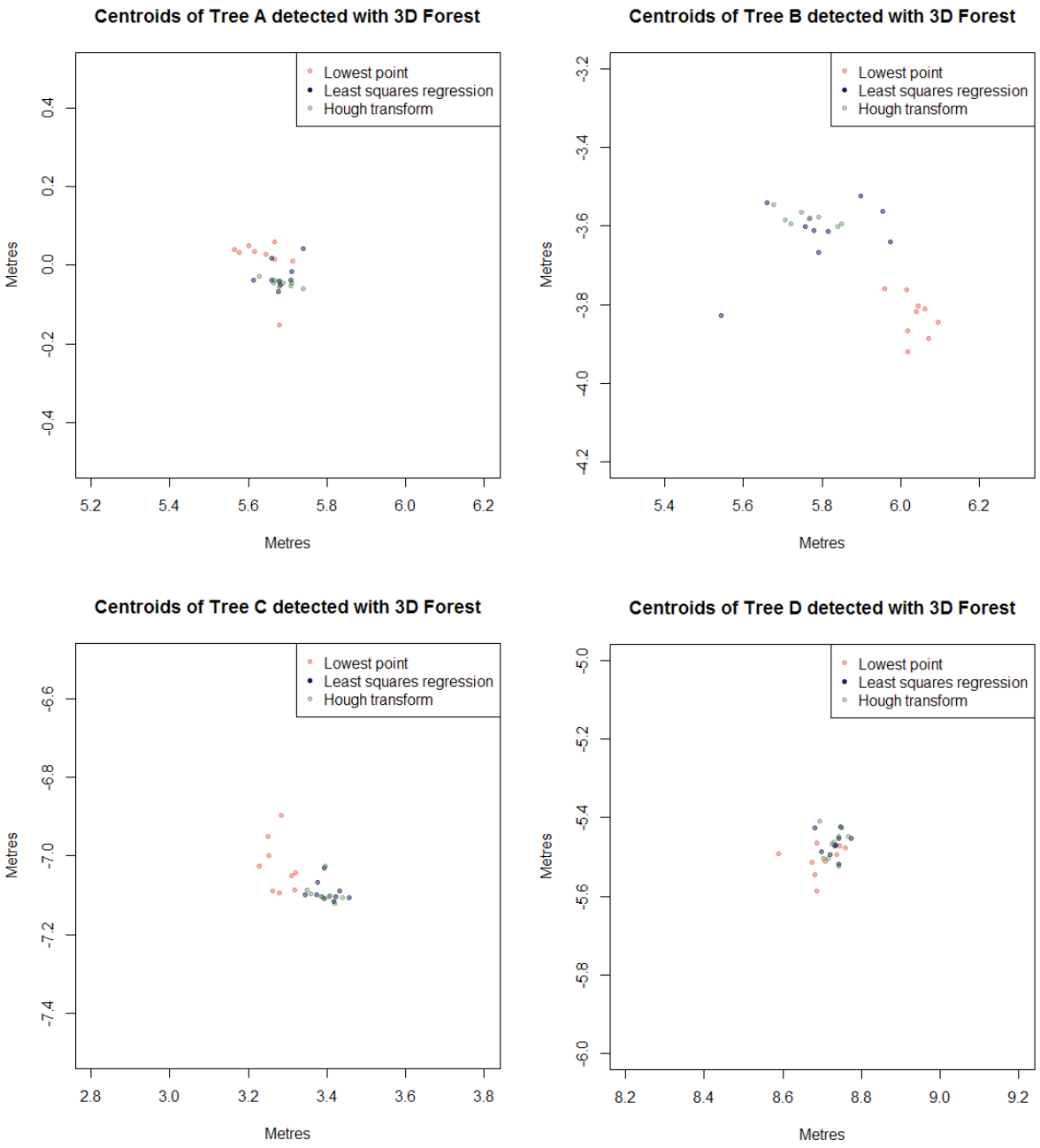

Figure 5.20: 'Zoomed-in' scatterplots showing the stem centroids for each of the four trees within the UVP field site and for each scan. The centroids are coloured by stem centroid detection method. Each plot is 1 x 1 m in extent. It is now especially clear that tree B has the greatest variation in apparent position, with positions varying by as much as 0.65 and 0.4 m in the *X* and *Y* axes respectively.

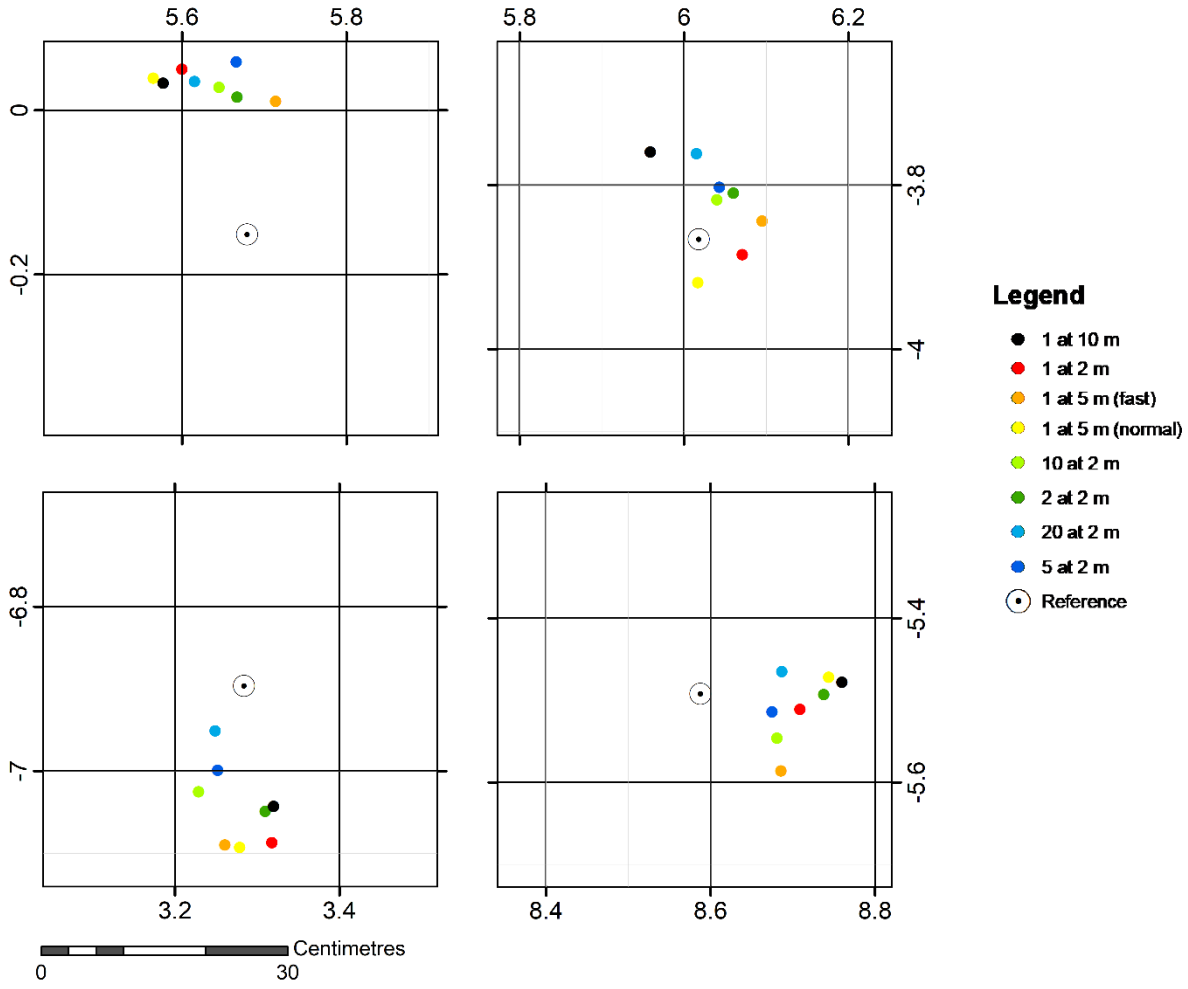

Figure 5.21: Extreme close-up plots of stem centroids coloured by scan rather than method of centroid detection. Here, the 'lowest point' algorithm was applied. Panels: top left: tree **A**; top right: tree **B**; bottom right: tree **C**; bottom left: tree **D**.

5.3.9 Semi-automated extraction of biophysical parameters

As previously described, all nine of the HMLS scans collected in the Victoria Park, Leicester (UVP) site were individually imported into *3D Forest* (Krůček et al., 2016; Trochta et al., 2017) where segmentation was performed. This was followed by tree variable (height, DBH, projected canopy area) estimation. The optimal algorithm parameters (e.g. thresholds, searching distances) as used in these analyses were previously described. Refer to the ***Appendix*** for a summary table detailing the variables estimated within *3D Forest* for each of trees A, B, C and D.

Figure 5.22 (overleaf) illustrates that the number of points per tree in each scan varied substantially and, upon comparison, consistently. In terms of gross point count, the reference scan sits somewhere between 10 and 20-loop scans. In the case of tree B, point count is highest as this is the scan that not only achieved the closest proximity but also looped it repeatedly. Most points were acquired for tree D, which also had the most substantial structure in terms of the lower canopy.

In terms of DBH estimation, **Figures 5.10** and **5.11** suggest that a sufficient point density exists in all scans except the single-loop, 10 m variation. **Figure 5.7**, however, highlights tree construction seriously deteriorates with distance from object (e.g. the 5 m and 10 m loops). This is further evidenced by **Figure 5.15** (page 164), which demonstrates beyond doubt that a single-loop scan at typical walking speed is insufficient even to infer structure of low-level branches within <5 m of the scanner. Ultimately, this suggests that any relationship between point count and tree reconstruction will be complex. A similarly complex relationship can be seen in **Figure 5.23** overleaf, which describes the projected surface area of each tree's canopy as estimated with two similar techniques (each described in 4.3 Methods and materials). In the upper pane, a high R^2 value indicates a strong relationship between the two canopy surface area techniques. In the lower pane, points were coloured by tree ID. All four trees seem to have a broad distribution of surface areas dependant on scan geometry. Overall, tree C had the greatest canopy surface area; trees B and D were similar.

In terms of DBH estimation both the Hough Transform (HT) and Least Squares Regression (LSR) algorithms, as applied in *3D Forest*, were broadly similar. Considering the mean value per tree, DBH derived via the Least Squares approach was slightly greater. Scatterplots of DBH 'pairs' are included in **Figure 5.24** (page 174). Recall that Tree B had a complex morphology and comprised two limbs at DBH height, which meant *3D Forest* calculated DBH as the diameter of the entire tree (not limb) at its widest point. Removing Tree B from the analysis yielded an R^2 value of 0.931.

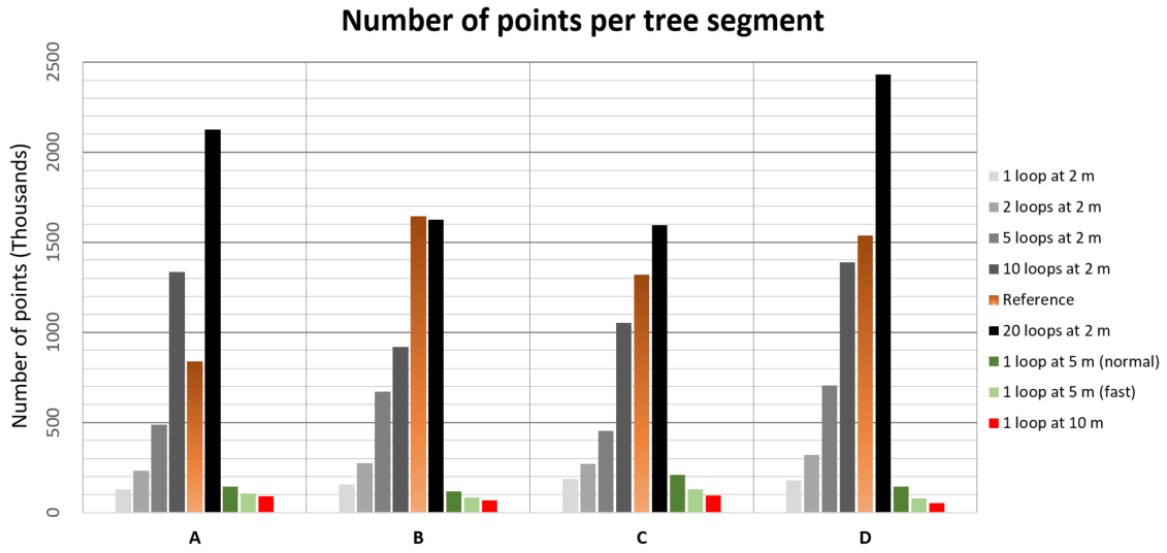

Figure 5.22: Simple bar chart illustrating the gross point count per tree and per scan. The greatest number of points is seen in the 20-loop (at 2 m) scan of tree D, which also contained the greatest extent of branch structure. The fewest points were also acquired for tree D, in the 10 m, single-loop scan.

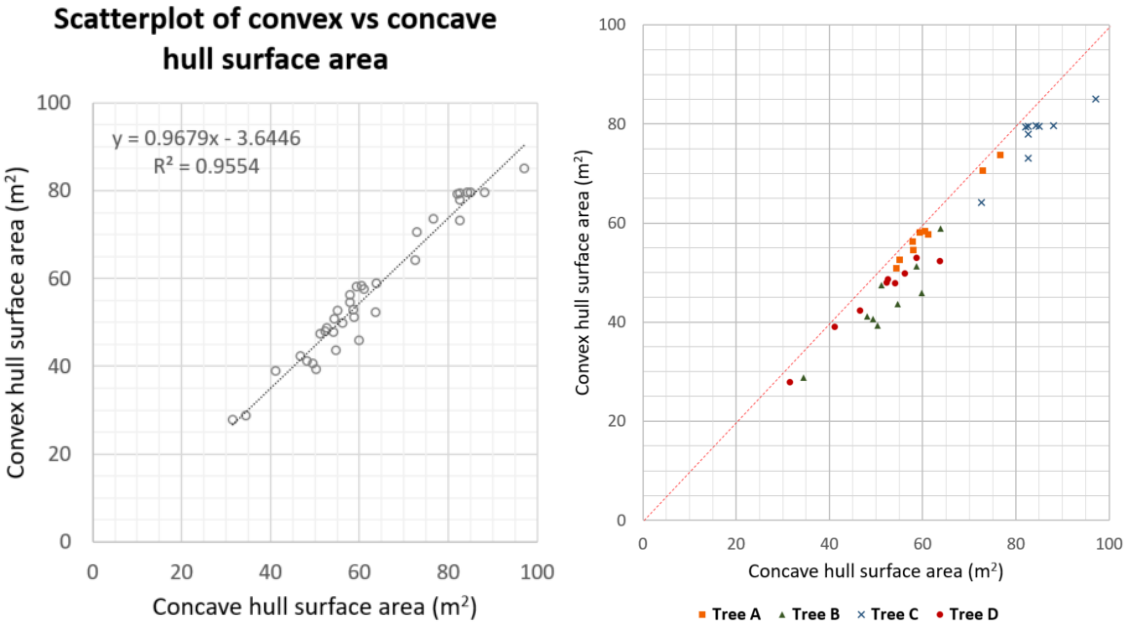

Figure 5.23: Scatterplots of projected canopy surface area measured with both the convex hull, and concave hull, algorithms within *3D Forest*.
Left: all points, with R^2 and equation. **Right**: all points, coloured by tree ID. Here, all points lie below the 1:1 line (red line), indicating that in all instances (all four trees, all nine scans) the concave hull area estimates were the greater of the two estimates.

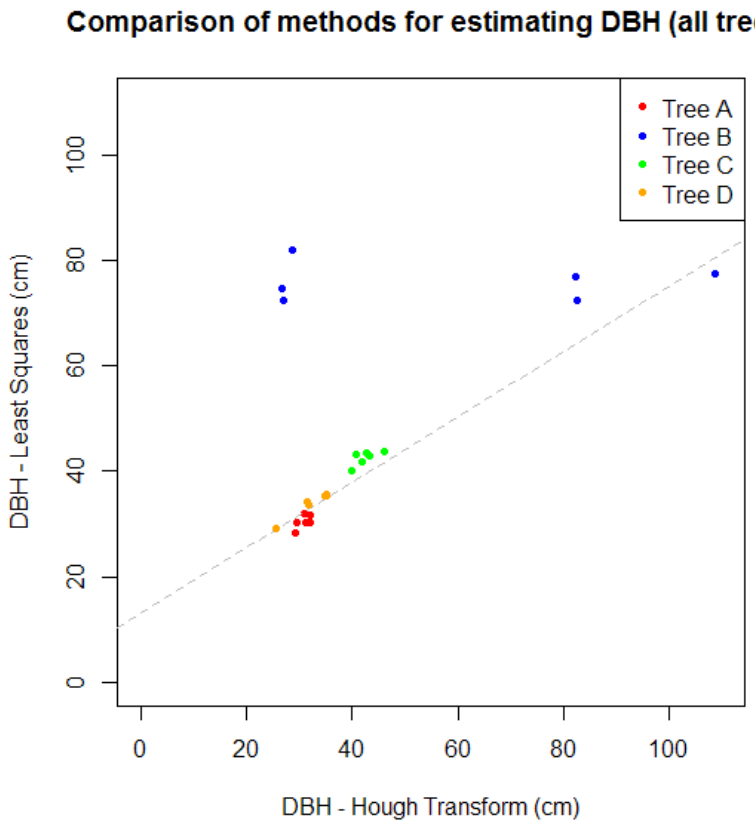

Figure 5.24: Scatterplot comparing DBH estimated by both HT and LSR techniques captured in varied-repetition scans. Omitting Tree B, an R^2 value of 0.931 was achieved.

5.3.10 Comparison of horizontal alignment between scans

Inter-scan alignment is represented in experimental, vertically exaggerated cross-sections (**Figures 5.25** and **5.26**, on the following two pages). These results were only intended to be indicative – alignment is difficult to quantify on reasonably flat topographies such as the UVP field site. In all cross-sections, the 'reference' dataset is displayed as a semi-transparent black point cloud and the comparison scan in red.

Where overlap is imperfect, alignment is also imperfect. This is largely to be expected, given the UVP scans were designed to explore the effect of a single variable on the dataset. A typical HMLS scan would include close-loop scans and intersections (see: However, these analyses were designed to highlight the nature of misalignment.

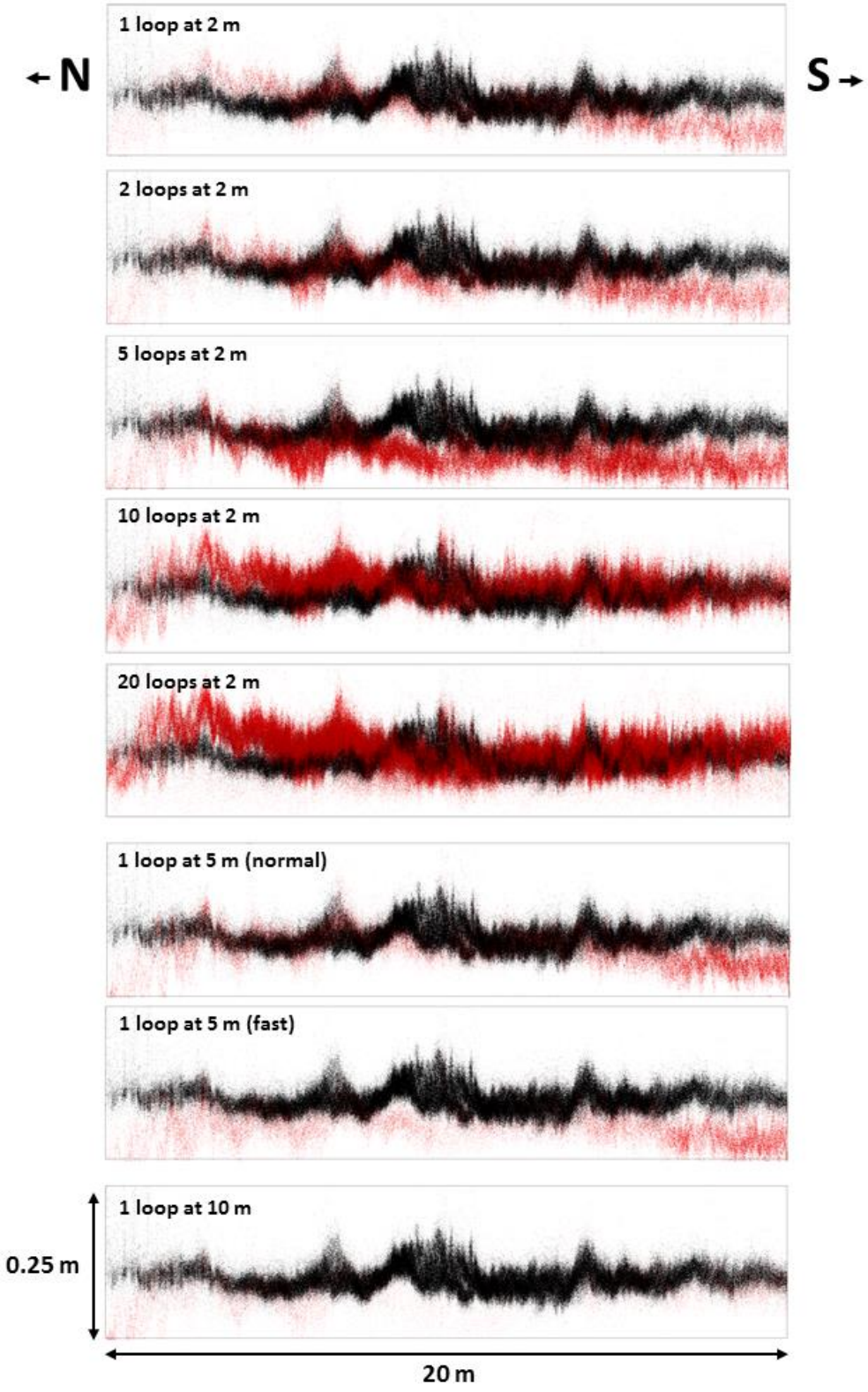

Figure 5.25: North (left) to south (right) cross-sections through vertically exaggerated HMLS scans. Black points indicate 'reference'; red denotes a given isolated-variable scan. All scans show a degree of misalignment but this is most marked in multiple-loop scans 2 m from the target trees.

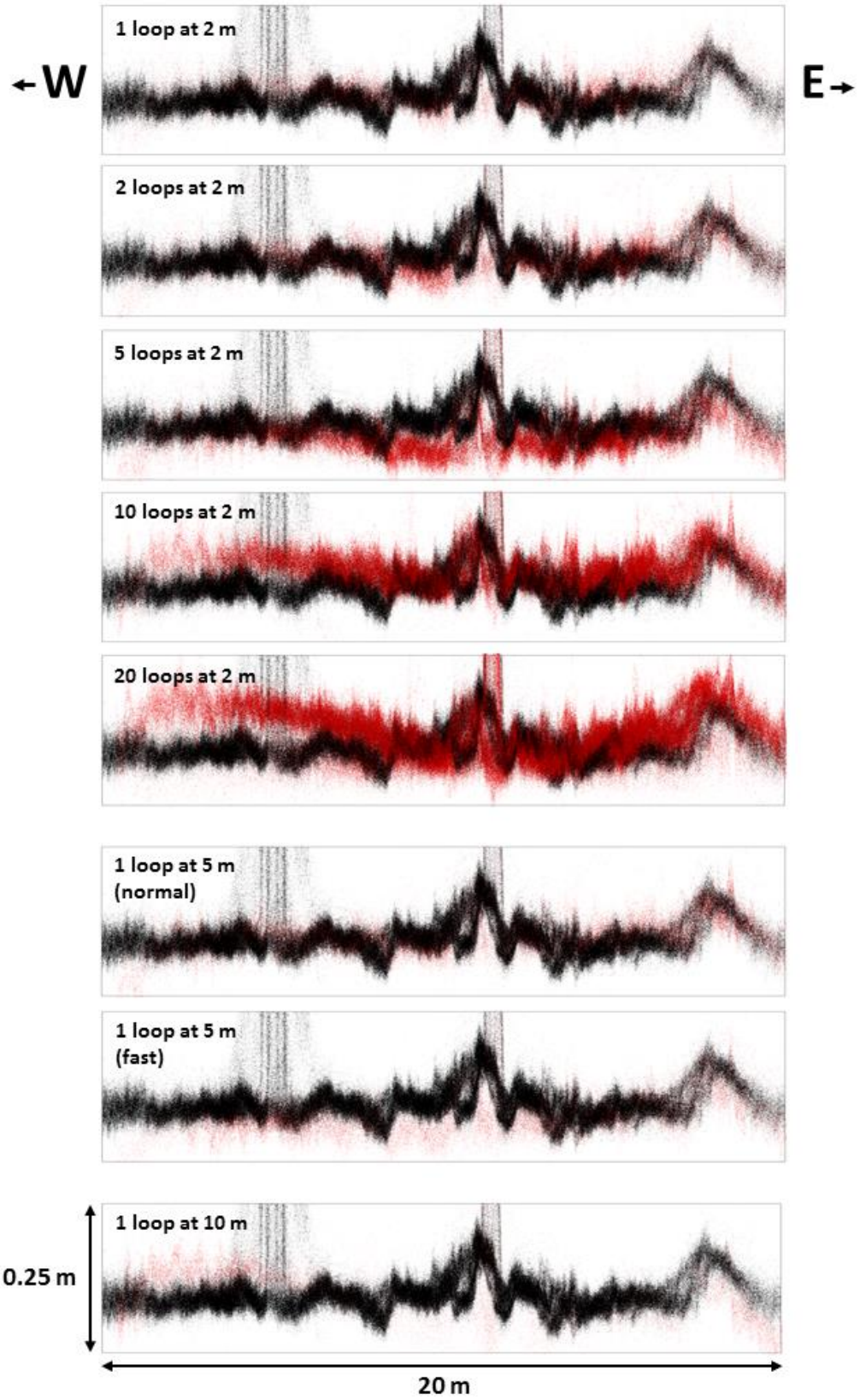

Figure 5.26: West (left) to east (right) cross-sections through the same vertically exaggerated HMLS scans. As in 4.5.35, black points indicate 'reference' and red isolated-variable scan clouds. Alignment, once again, appears to degrade mostly as a function of scan length/duration (i.e. with increasing loop iteration).

5.4 Summary

The overarching aim for this chapter was to define 'best practice' when using current generation HMLS sensors to map trees and forest. The research question set out to determine the likely impact of sensor range – and sensor proximity from target trees – on point density and point distribution. It also sought to test whether repetition (i.e. multiple passes of a target) could increase point density such that it could mitigate the effect of poor sensor range.

At the time of writing, current generation HMLS sensors did not offer a 'real time' data visualisation tool, so scans were conducted blind. This meant detailed planning of scan trajectories was required – and achieved by following pre-determined paths through the field site, staked out with plastic pegs. By following these paths, it was possible to isolate a single variable at a time. Such variables comprised of distance from target, target repetition, and velocity of survey. The results showed that survey trajectory repetition had a positive impact on point cloud density and point distribution – especially in areas at the marginal end of sensor range (8 – 12 m).

Other results included the discovery that edge case scans where data were collected in marginal conditions very quickly degraded. The quality indicator rapidly declined and some scans failed to process altogether. An interesting finding was that alignment very visibly degraded with frequency of repeat pass. Given that these scans were performed on a fixed trajectory with no intermediate loop closure, this perhaps implies error propagation is a dominant factor affecting SLAM data registration. A useful insight upon which to develop a forest survey protocol in itself.

6. Exploring the potential role of HMLS within multi-sensor 3D forest mapping: a data fusion approach

High-resolution, 3D forest mapping facilitates the extraction of spatial attributes and biophysical parameters, but the resolution and precision of these extracted metrics is directly impacted by the scanning hardware employed. ***Chapters 4*** and ***5*** demonstrated that some metrics can be acquired using HMLS sensors alone. However other metrics commonly used in forestry and forest inventory – such as tree height, canopy height, crown area and crown volume – require an accurate top-of-crown dataset. Whilst TLS workflows are often used to extract such metrics, such survey techniques are expensive and time-consuming. The results presented in ***Chapters 4*** and ***5*** also confirm that where HMLS data were acquired with optimised workflows, derived results were consistent. Whilst precision is lacking, error in data is both systematic and predictable.

6.1 Research aims

This chapter aims to define the role HMLS can play mapping forest in tandem with other sensors. In addition, it seeks to determine whether this multi-sensor 'data fusion' approach can address the limitations in HMLS range identified in previous chapters. HMLS data is co-registered and fused with EA ALS data. Theoretically, the fusion of 'ground up' HMLS data with ALS (which 'looks down from above') should lead to a holistic dataset. In turn, this 'fused' dataset should support the extraction of additional biophysical parameters which HMLS alone cannot capture.

6.2 Research question

The research question posed for this chapter was:

> *RQ3: To what extent can a fusion of HMLS and ALS data address limitations in the range of HMLS sensors? What 2D and 3D forest inventory measurements can be extracted from a fused dataset and how do they compare to TLS-derived measurements?*

6.3 Results for RQ3

The results presented (with their corresponding processing steps and sequencing in terms of chapter layout described in **Figure 6.1**, overleaf) build on those presented in ***Chapter 4***, fusing ALS with the HMLS2 data acquired in the UTF-ROK site as described earlier. To answer the research question, fused data were examined using *3D Forest* using the same methods previously employed within this research. Results were limited by the performance of *3D Forest* software on a Microsoft Surface 4 workstation – only a small quantity of data could be ingested at a time.

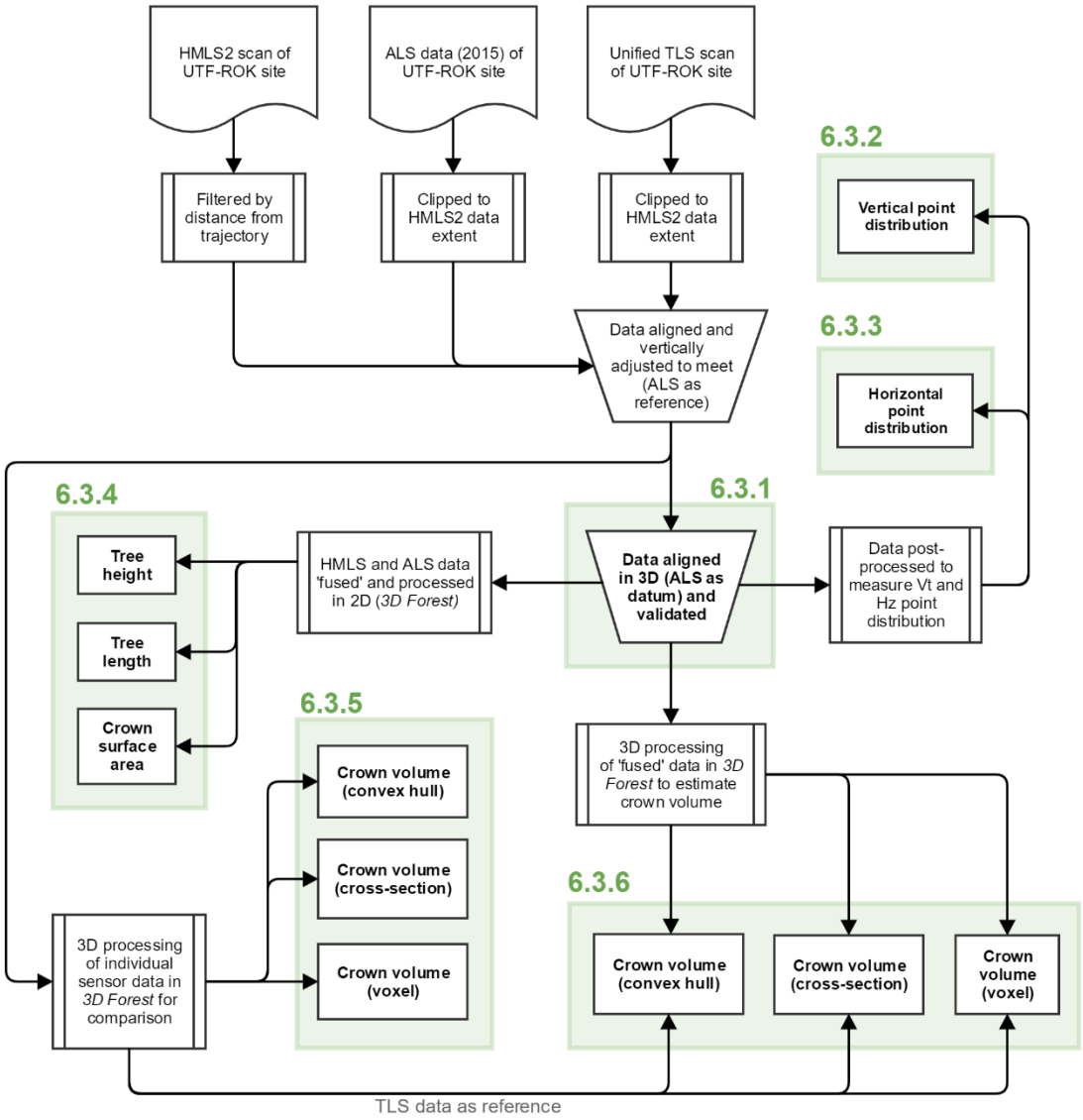

Figure 6.1: schematic flowchart illustrating the results presented in this chapter and the data fusion and processing steps which link them.

6.3.1 Validation of TLS and 'fused' HMLS-and-ALS datasets

LiDAR data from all sensors was passed through the Cloth Simulation Function (or CSF) algorithm (Zhang et al., 2016) plug-in in *CloudCompare*. This tool separated data into 'ground' and 'off-ground' categories. 'Ground' points were then turned into meshes to form bare earth DTM surfaces. DTMS from multiple sensors were compared and adjusted (vertical plane) to correct one dataset to a datum established by the other.

DTMs were also used to terrain-normalise data, i.e. when calculating heights above ground. *3D Forest* applied a similar process during the extraction of variables.

Following are results of an alignment check between ALS and HMLS data acquired in March 2014 and July 2016 respectively. The HMLS data preserved the structure of understorey vegetation whilst ALS 'last return' points depicted a bare-earth surface. Consequently, the resultant difference in height layer was biased and the apparent magnitude of change was as much as 2.75 m – the maximum height of the vegetation. **Figure 6.2** (overleaf) illustrates this comparison.

A network of smoothed paths and bridleways, apparently less prone to vertical change than surrounding vegetation, crossed this site and were used as vertical reference 'control surfaces'. After manual alignment with ALS data, HMLS data was filtered and only points within a 10 m 'distance-from-nearest-trajectory-point' threshold were retained. Filtered data is illustrated in **Figure 6.3** (also overleaf) coloured by height (left) and distance from trajectory (right). Vertical separation of footpaths can be seen to fall within the region of 0 to 0.05 m (shaded white) with a majority of points in the range 0.2 to 0.5 m. These latter values indicate height offset caused by understorey vegetation captured in HMLS, but not ALS, data.

TLS data were also aligned with ALS data and showed remarkably similar crown structure despite the three-year temporal baseline between acquisitions (ALS: March 2014; TLS: April 2017). **Figure 6.4** (page 183) illustrates this alignment in three dimensions. **Figure 6.5** (page 184) depicts the range of heights achieved using TLS, HMLS and HMLS-fused-to-ALS datasets. The fused *HMLS+ALS* dataset appears to record greater tree heights than the TLS reference despite validated vertical alignment; possibly an artefact, as ALS ground points had not been removed from analysis.

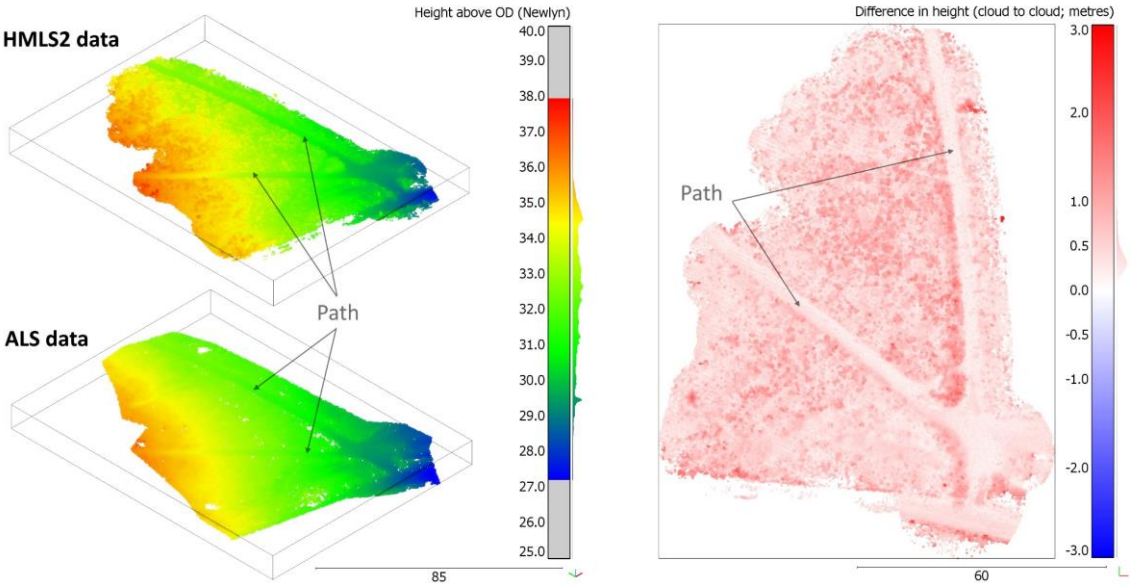

Figure 6.2: 3D projection of HMLS2 and ALS heights (left) and map of height differences (right). HMLS2 data appears much rougher than ALS due to presence of understorey vegetation which led to bias in mean height.

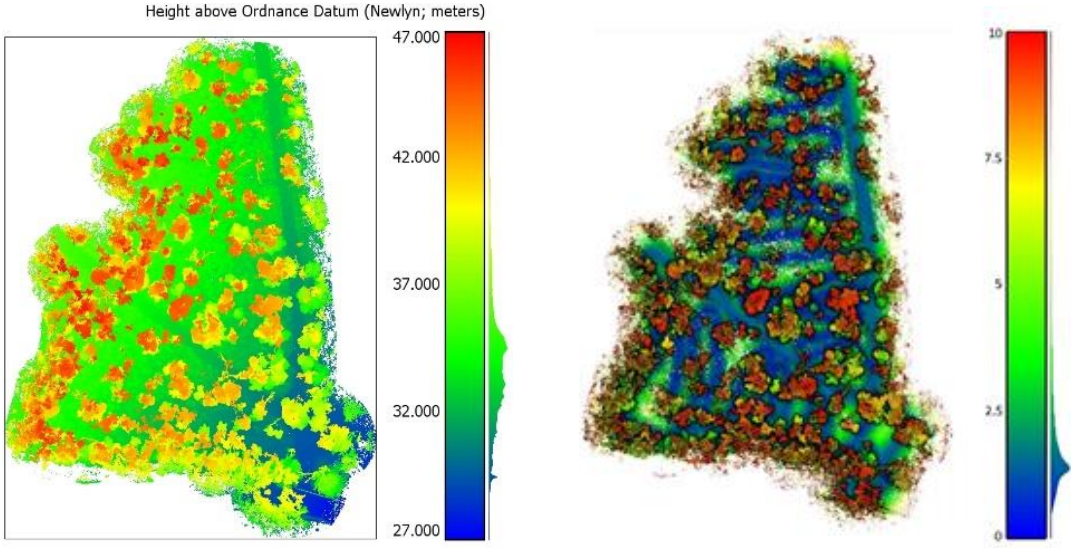

Figure 6.3: HMLS data acquired within the UTF-ROK study site and filtered by distance from trajectory. Coloured by height (**left**) and distance from trajectory (**right**).

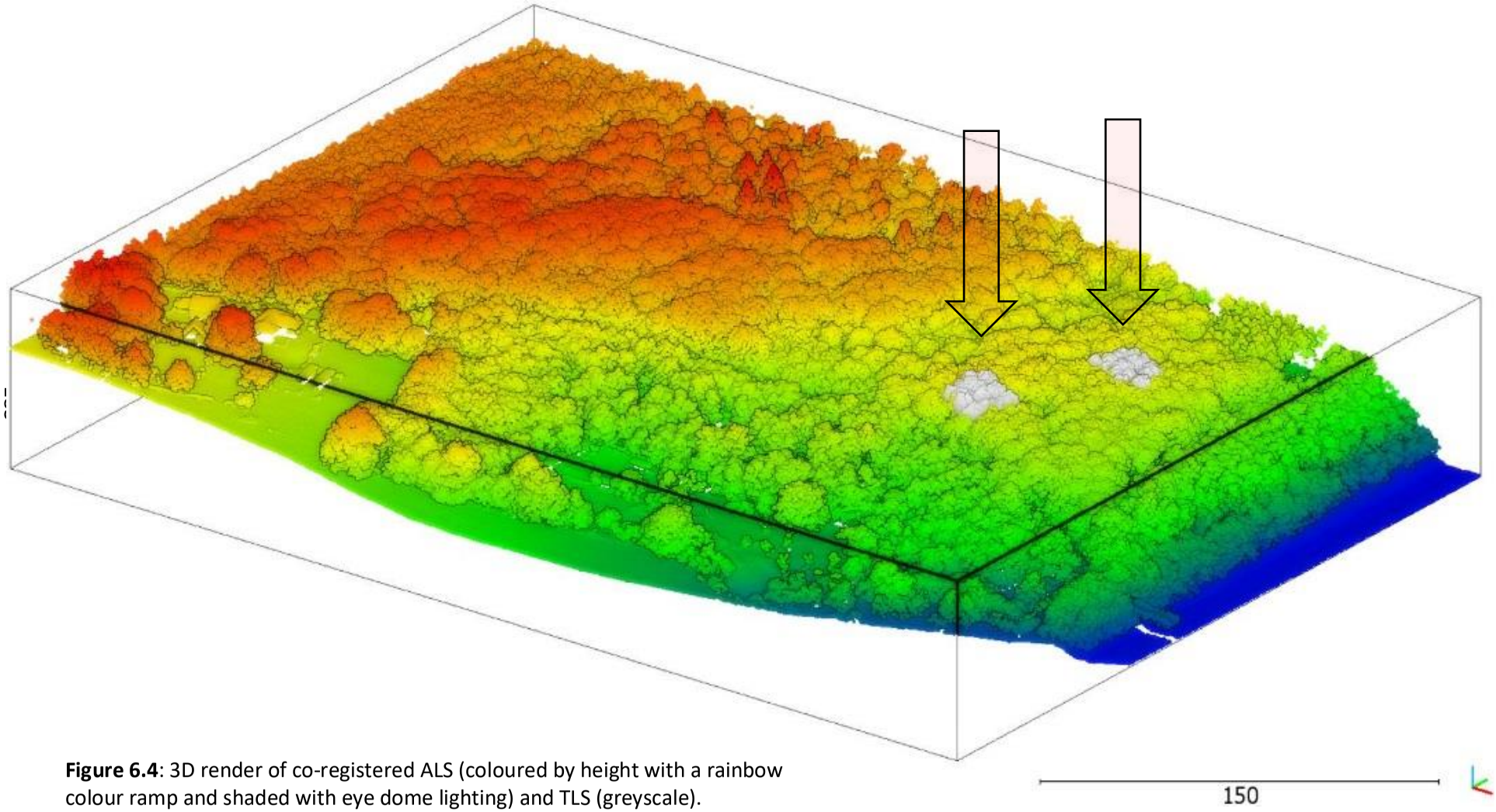

Figure 6.4: 3D render of co-registered ALS (coloured by height with a rainbow colour ramp and shaded with eye dome lighting) and TLS (greyscale).

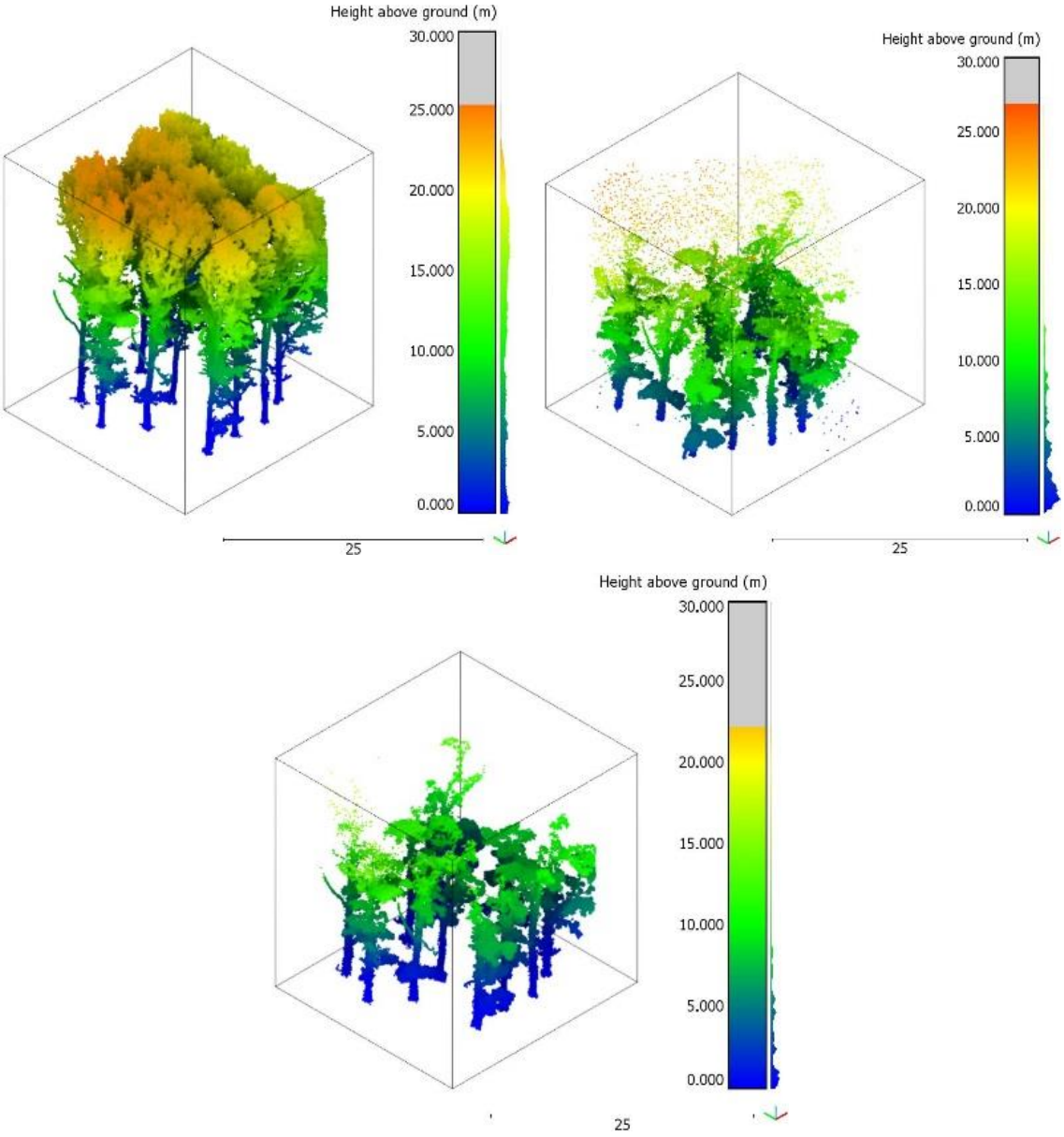

Figure 6.5: TLS (top left), HMLS + ALS (top right) and HMLS only (bottom) datasets. The respective colour ramps include histograms which illustrate the vertical distribution of points. Meanwhile the colour ramp extents define height range in each figure.

6.3.2 Comparison: vertical point distribution

Figure 6.6 (below) compares vertical point distribution in a TLS and a 'fused' point cloud, both after CSF filtering to derive 'off-ground' points. It is clear the fused dataset has less than half the point density of the TLS dataset at its greatest magnitude (6 m above ground) and the distribution falls away dramatically above this height. Maximum heights are broadly similar (2 m difference), a value perhaps exaggerated by the temporal interval between acquisitions (ALS: February 2015; TLS: April 2017) and seasonality (with leaf cover much greater in TLS scan, likely leading to physically higher components of trees in the plot).

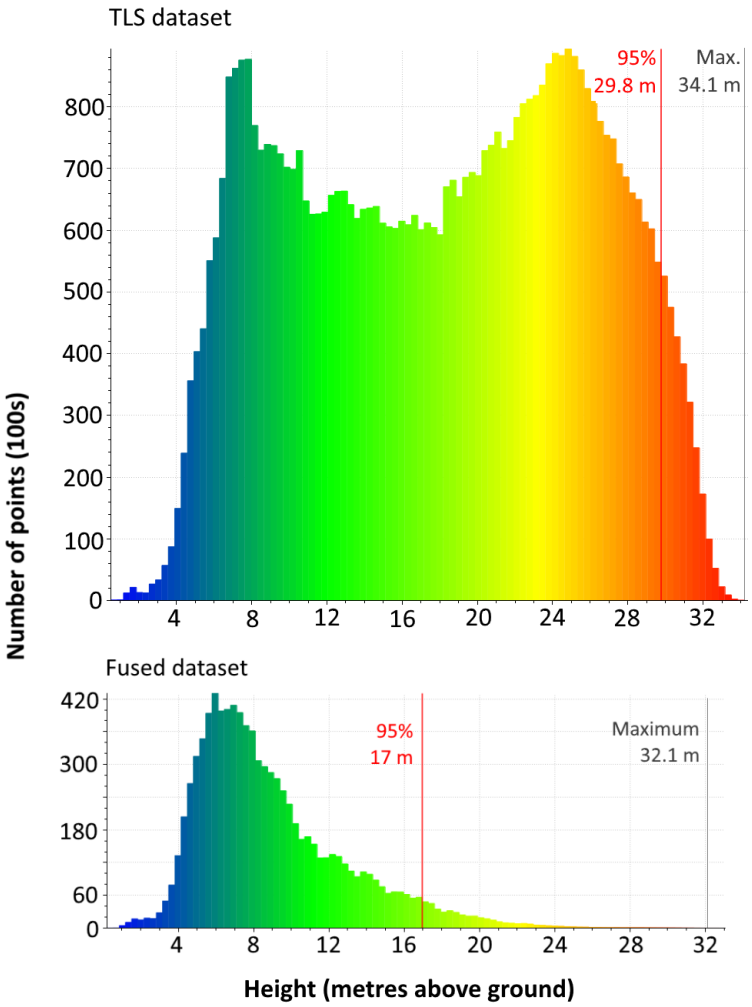

Figure 6.6: Histograms of vertical point distribution for 'off-ground' points acquired with the TLS system (**top**; maximum height: 34.2 m) and formed through the data fusion approach (**bottom**; maximum height: 32.1 m). Both histograms are reproduced to the same X and Y scales.

Both datasets were then subsampled using a voxel de-densification routine, with voxel edge size set to 1 m. This was intended to remove bias in the data structure associated with sensor-specific point cloud geometry (i.e. ALS acquired in parallel strips; TLS acquired in hemispheres) and to give a 'true' picture of 3D structure (**Figure 6.7**, below). Having done this, the vertical distributions of the two plots now look more comparable – indeed, heights at the 99th percentile are within 0.1 m. The vertical offset between maximum frequency (TLS: 25 m; 22 m) may even indicate tree growth between acquisitions.

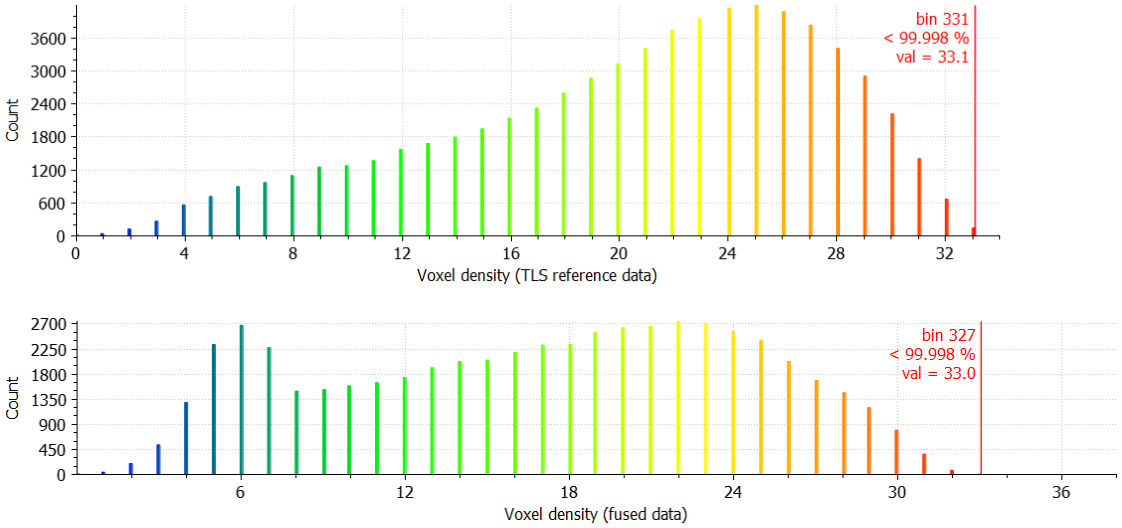

Figure 6.7: Histograms of vertical point density for TLS (**top**) and fused (**bottom**) datasets in the UTF-ROK study site, normalised through a 1 m voxel de-densification.

6.3.3 Comparison: horizontal point distribution

In a broadly similar approach, horizontal distribution of off-ground points is also measured in **Figure 6.8** (following page). Due to the TLS data having substantially higher point density across the site, the datasets were log10-transformed in order to share a colour ramp. ALS point distribution seems to visualise tree crowns, whilst TLS distribution clearly shows crown extent plus higher densities of points at the position of each tree stem. Fused data, meanwhile, seems to sit halfway between the two.

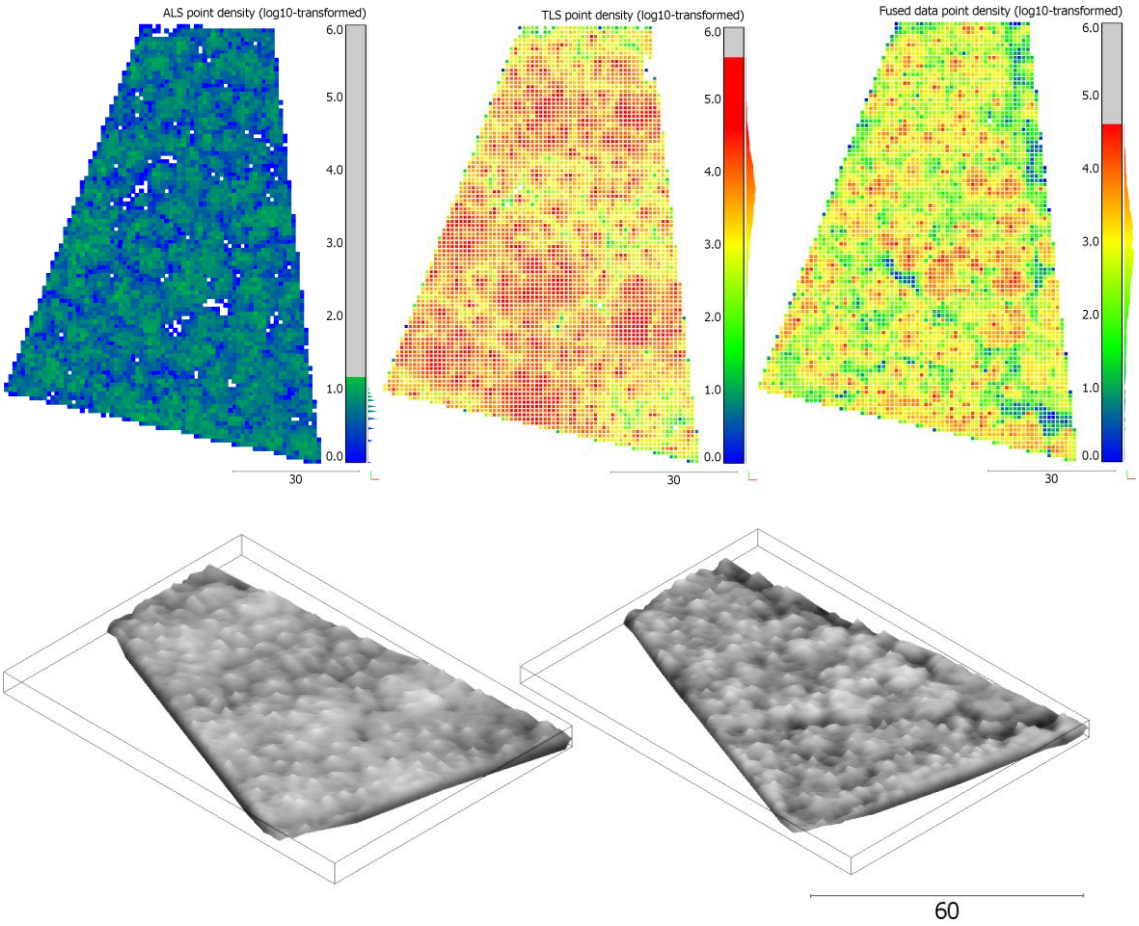

Figure 6.8: Above: point density distribution meshes for TLS (left) and fused (right) datasets, log10-transformed as per earlier figure. Stems correspond but crown data appears more extensive and 'smoother' in the TLS mesh due to higher point density.

6.3.4 2D tree-level metrics derived from fused data using *3D Forest*

Here, 2D measurements derived from fused HMLS2 and ALS data acquired at the UTF-ROK study site are compared with TLS-derived observations. **Figure 6.9** overleaf demonstrates that realistic tree heights were obtained despite limited HMLS range. The data is visualised in *3D Forest* software, with estimated tree height depicted with vertical 'poles' and heights rendered in text. Comparing values with those in ***Chapter 5***, it can be seen that data fusion improves tree height estimates in comparison with TLS-derived height (**Figure 6.11**; page 189). Meanwhile **Figure 6.10**, on the following page, illustrates projected crown area using the (a) convex and (b) concave cross-sectional method. Graphs presented in **Figure 6.12** (also on page 189) again suggest that data fusion can improve 2D crown characterisation.

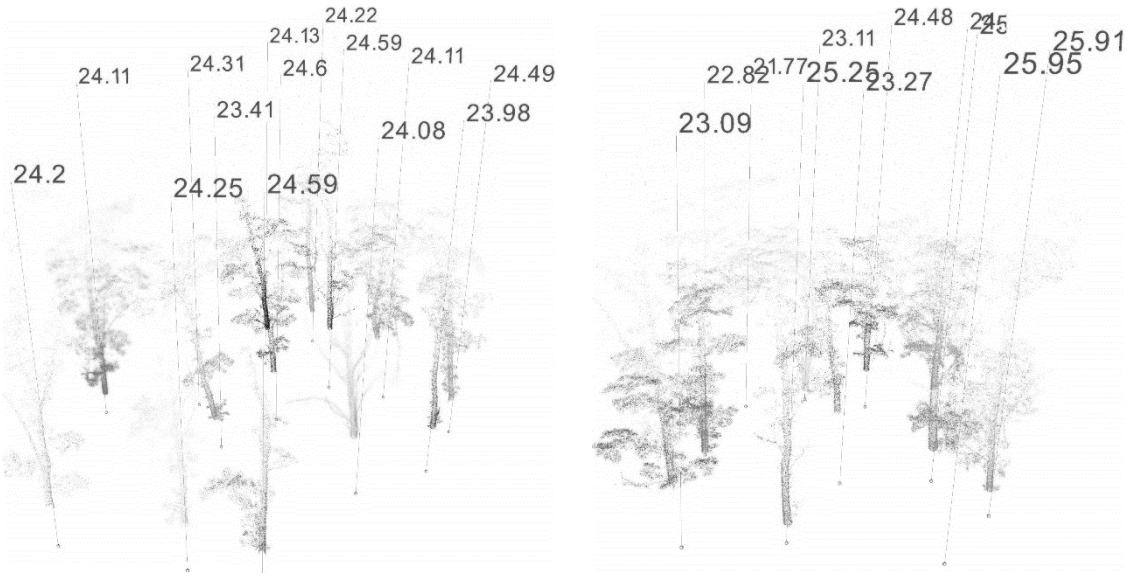

Figure 6.9: Three-dimensional render of two fused-data point clouds (HMLS data acquired at UTF-ROK using the ZEB-REVO HMLS sensor merged with ALS data).

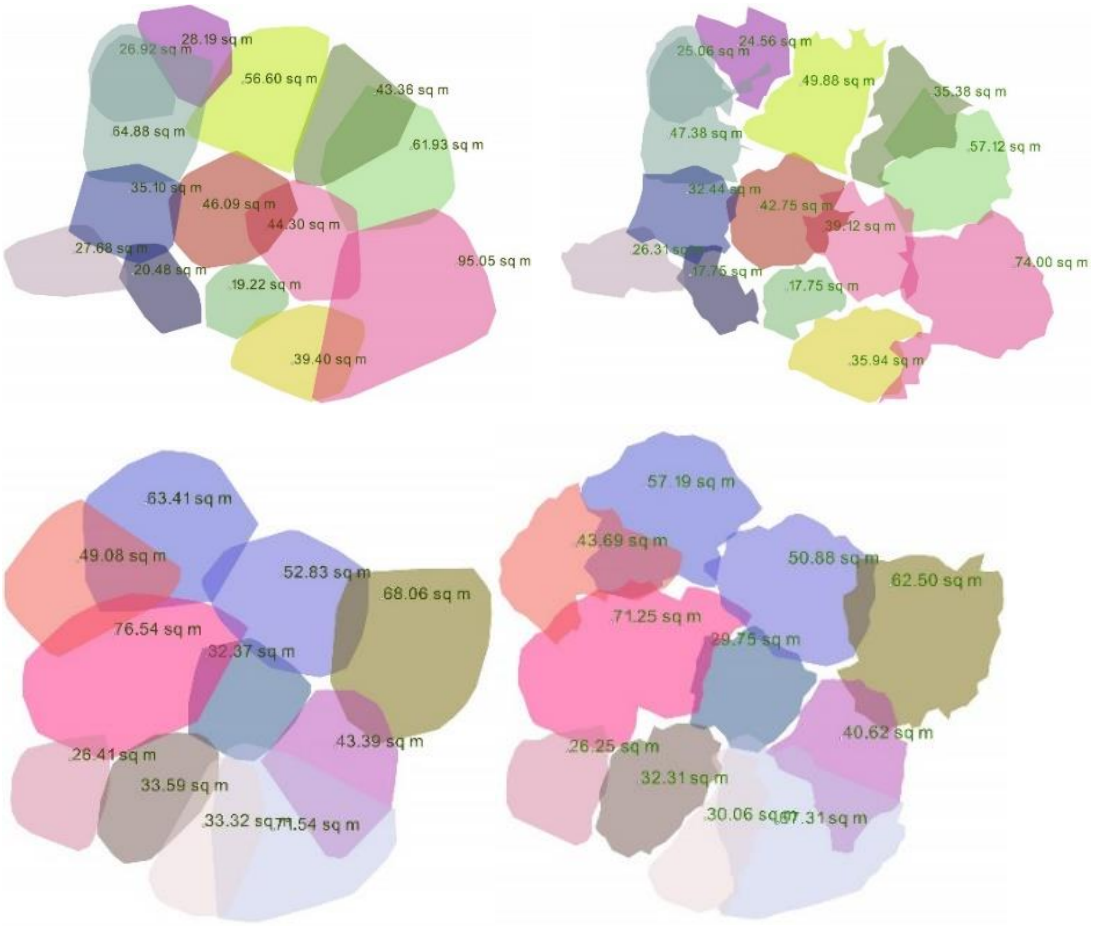

Figure 6.10: Two-dimensional plots of convex (**left**) and concave (**right**) hull-derived crown surface area estimates derived from the clouds presented in **Figure 6.9** above. Coloured by tree.

Figures 6.5.3 and **6.5.4** detail height, crown height and projected crown area in both the (i) native and (ii) multi-sensor fused datasets.

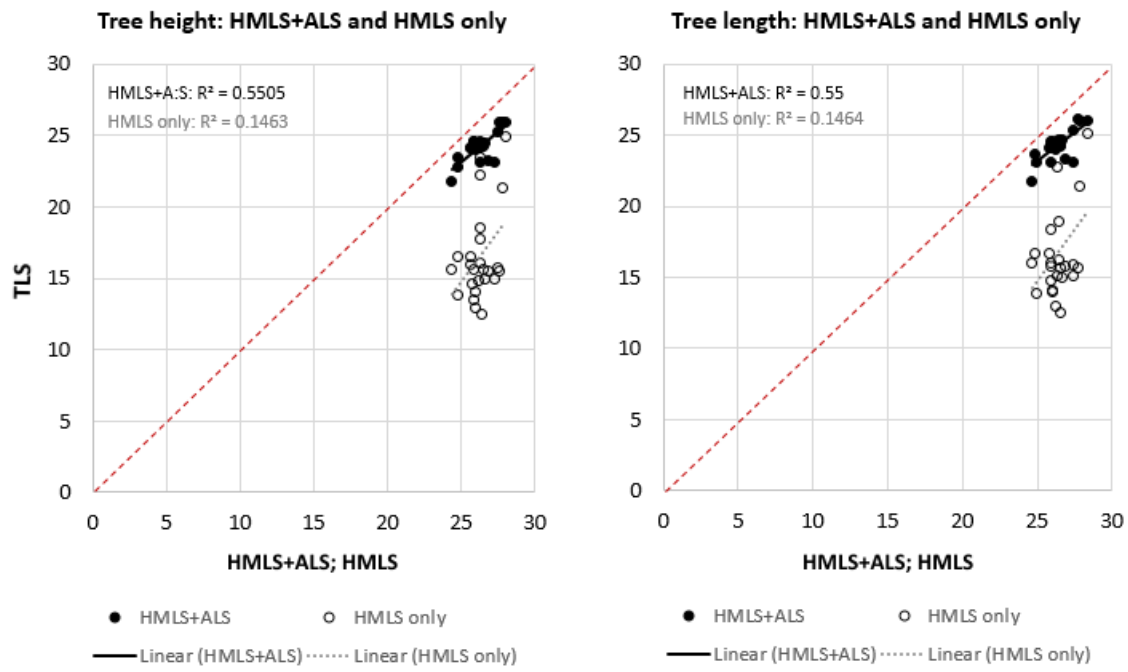

Figure 6.11: Scatterplots comparing TLS reference height (per tree) with HMLS+ALS and HMLS-only height estimates.

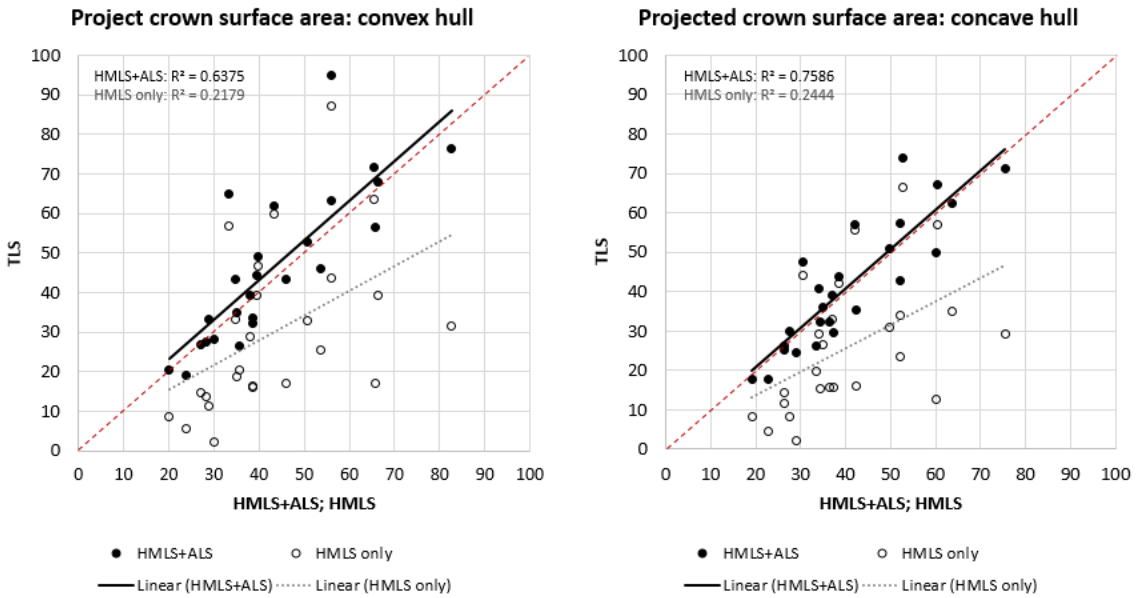

Figure 6.12: Scatterplots comparing TLS reference crown area with HMLS+ALS and HMLS-only crown area estimates. It is clear the data fusion approach can yield results which conform much more closely to TLS estimates than HMLS data can alone.

6.3.5 Comparison of TLS and HMLS crown volume

A summary of descriptive statistics encompassing crown volumes estimated for each of the twenty-five trees sampled from UTF-ROK data is presented in **Table 6.1**. This is followed with profile-view and plan-view renders of segmented point clouds and volumetric meshes (**Figures 6.13** to **6.16**; pages 191 to 194). These are presented per subplot – first the UTF-ROK North subplot, then UTF-ROK South. Finally, a series of graphs explore inter-sensor comparisons and methodological differences in crown volume estimation.

Table 6.1: Summary of UTF-ROK tree crown volumes

	Voxel (m^3)		**Convex hull (m^3)**		**Cross-sectional (m^3)**	
	TLS	HMLS2	TLS	HMLS2	TLS	HMLS2
Mean	9.10	1.88	529.79	225.47	281.69	117.72
Standard error	0.84	0.27	45.18	43.49	25.18	98.23
Median	8.17	1.48	447.30	149.20	241.54	98.23
SD	4.18	1.35	225.88	217.45	125.91	103.63
Kurtosis	0.11	-0.59	0.38	2.64	0.30	0.67
Skewness	0.88	0.70	0.89	1.58	0.89	1.13
Range	15.40	4.62	901.39	894.45	497.12	359.14
Minimum	3.39	0.24	204.20	7.86	99.99	4.33
Maximum	18.79	4.86	1105.59	902.31	597.11	363.46
Sum	227.41	47.04	13244.64	5636.82	7042.27	2943.03
Count	25					

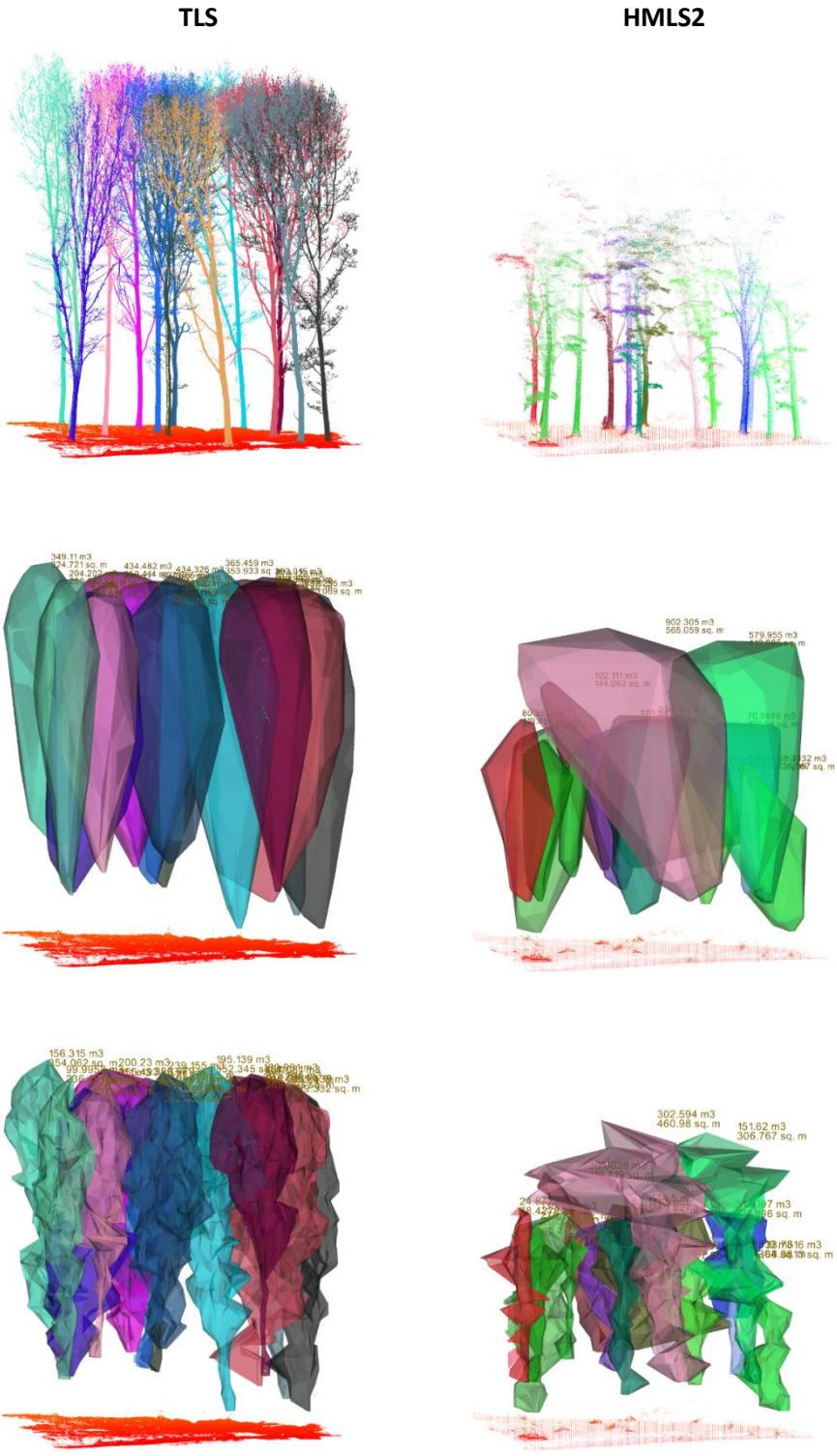

Figure 6.13: Profile views of (**top**) UTF-ROK North tree segments, (**middle**) convex hull volume meshes and (**bottom**) volume-by-cross section meshes.

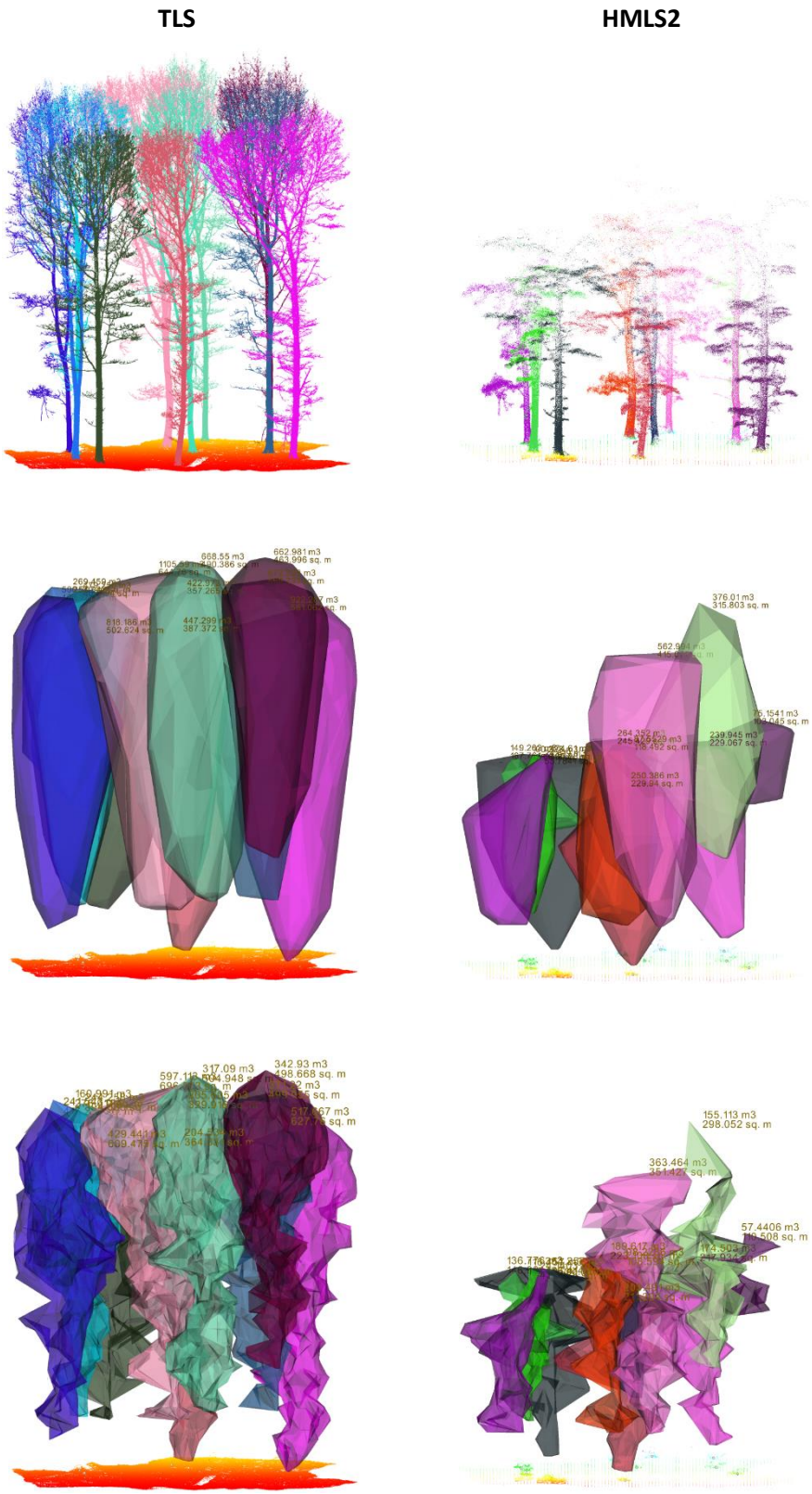

Figure 6.14: Profile views of (**top**) UTF-ROK South tree segments, (**middle**) convex hull volume meshes and (**bottom**) volume-by-cross section meshes.

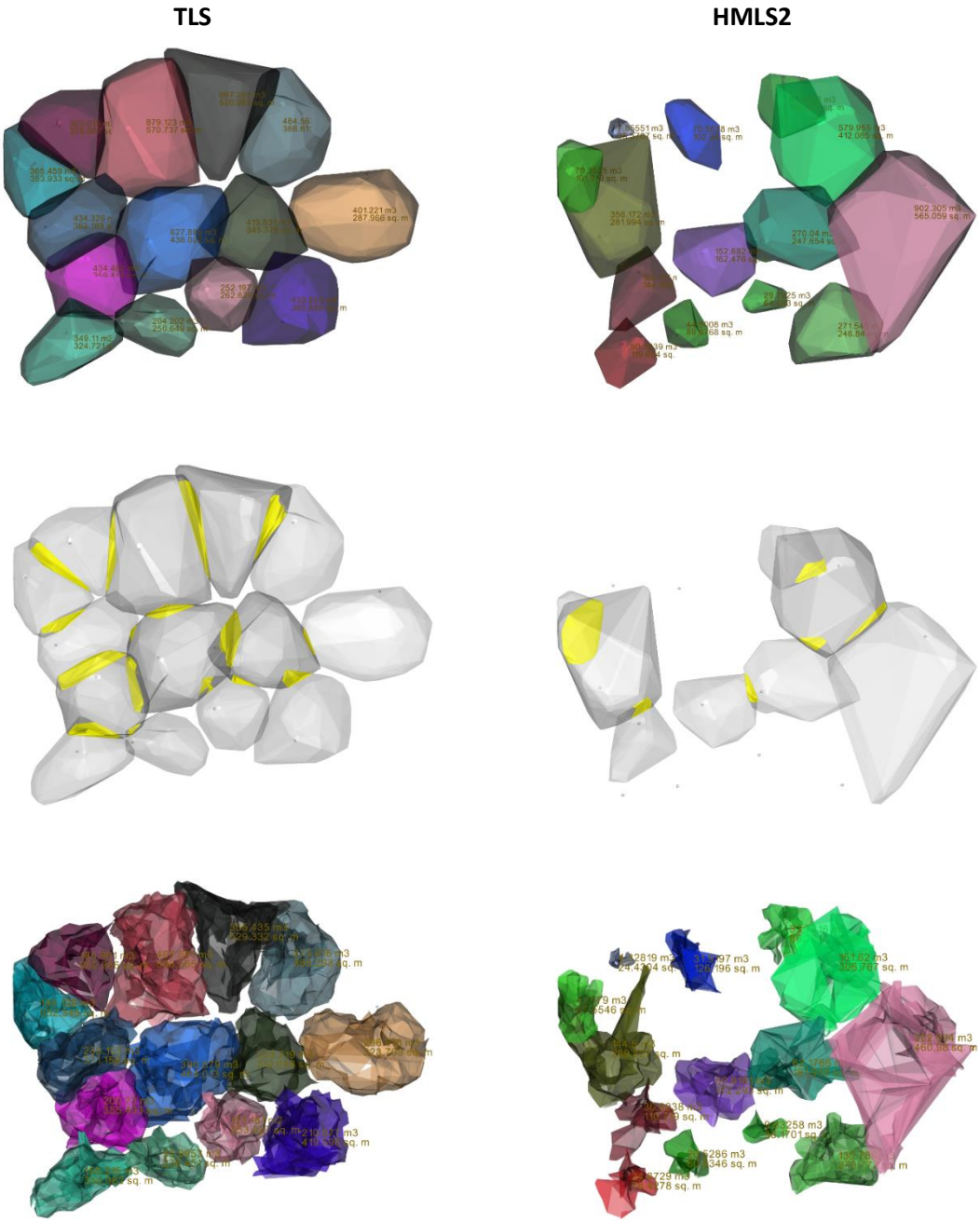

Figure 6.15: Plan views of (**top**) UTF-ROK North convex hull volume meshes, (**middle**) intersections – highlighted yellow – between convex hull volume meshes and (**bottom**) volume-by-cross section meshes.

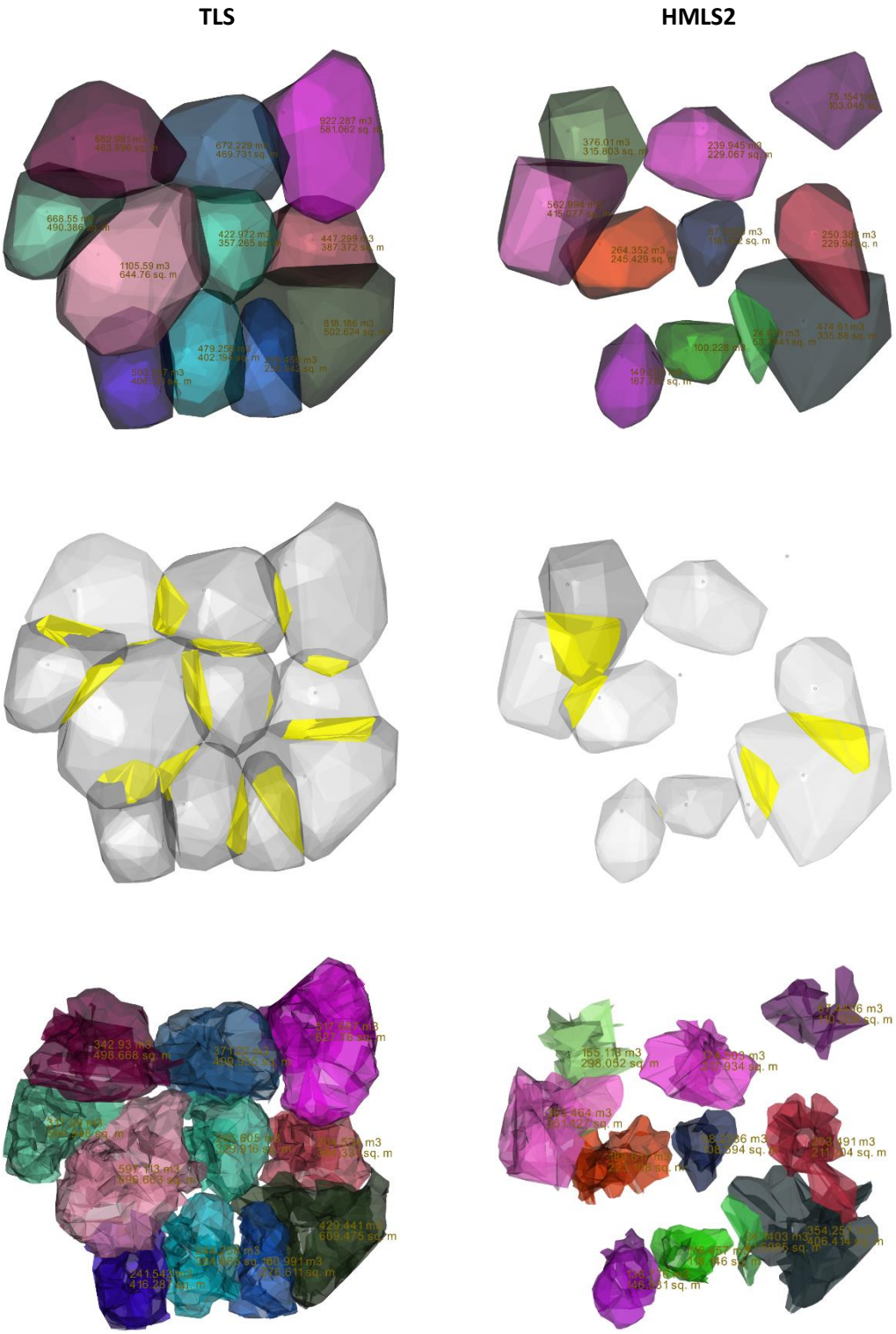

Figure 6.16: Plan views of (**top**) UTF-ROK South convex hull volume meshes, (**middle**) intersections – highlighted yellow – between convex hull volume meshes and (**bottom**) volume-by-cross section meshes.

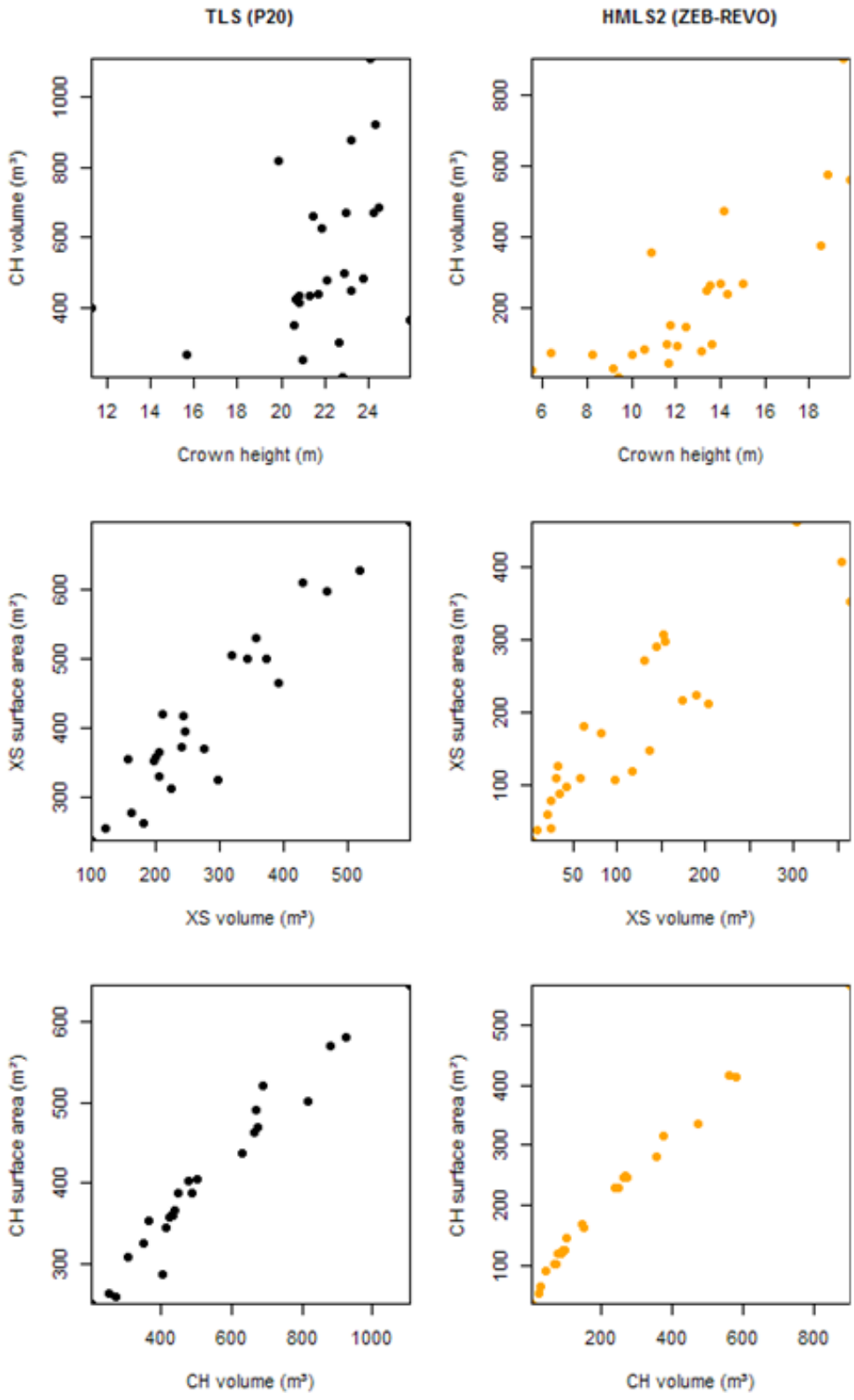

Figure 6.17: Final selection of scatterplots, this time plotted by sensor, exploring relationships between (**top**) crown height and convex hull-derived volume; (**middle**) cross-sectional surface area and cross section-derived volume; and (**bottom**) convex hull-derived volume and convex hull mesh surface area. As with UEP-BW, the latter four plots display a negative exponential relationship regardless of sensor used.

The results presented here were extracted from fused point clouds using *3D Forest.* As discussed in previous chapters, a major limitation in this approach was the maximum amount of data which could be imported into the software before it crashed. Unless and until such software is further developed to handle larger datasets, the retrieval of such metrics will be limited to small sub-plots.

6.3.6 3D tree-level metrics derived from fused data using *3D Forest*

In this section, 3D crown analyses are repeated. TLS data is compared with a fused HMLS2+ALS dataset. **Figure 6.18**, below, illustrates convex and concave hull (volume by section) approaches to crown volume estimation from a north-facing projection; **Figure 6.19** (page 197) shows this data in plan view. These variables are also plotted in **Figures 6.20** and **6.21** (page 198) to directly compare native and fused results.

Figure 6.18: Side profile projection of the convex hull (**top**) and volume-by-cross-section (**bottom**) meshes again derived from fused point clouds of the two UTF-ROK subplots.

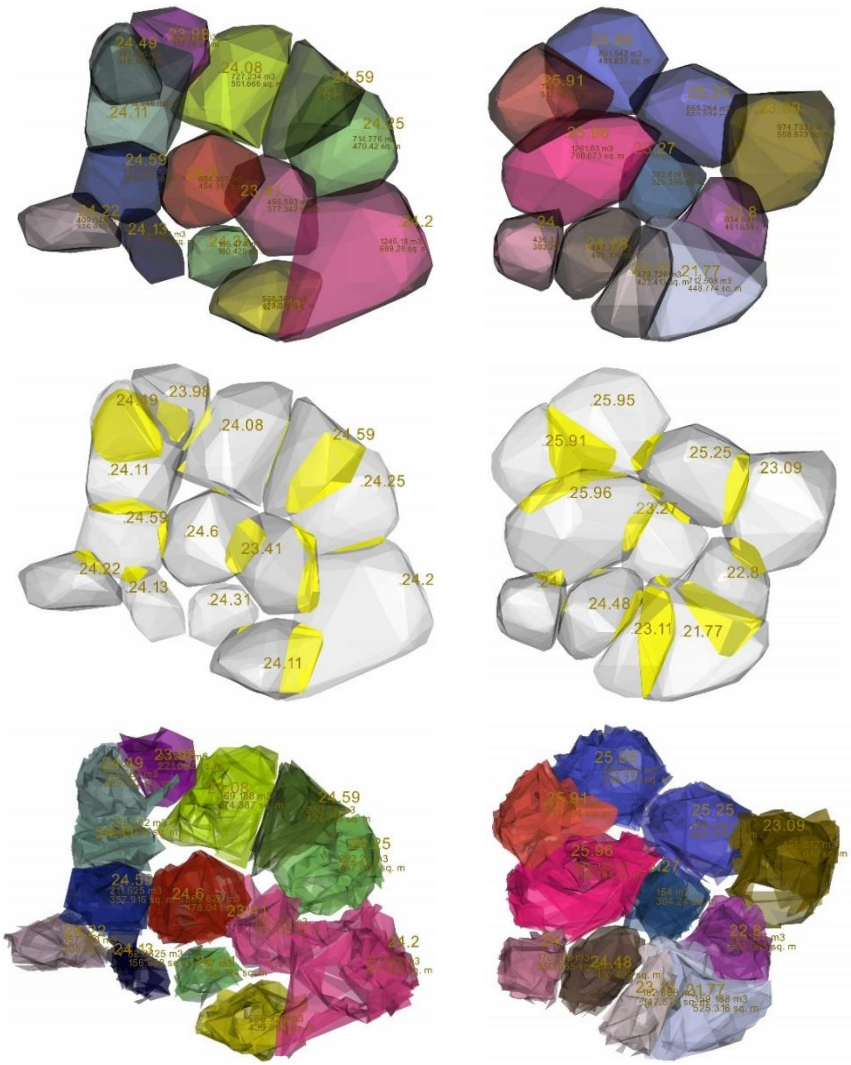

Figure 6.19: 3D meshes of UTF-ROK crown volume estimated through the convex hull (**top-left** and **top-right**; two plots side-by-side), convex hull intersecting overlap (**middle-left**; **middle-right**) and volume-by-cross-section (**bottom-left**; **bottom-right**) algorithms. Note: graphics included for reference purposes (display parameters cannot be modified).

Volume estimates are inaccurate in that the degree of noise in ALS data cannot be quantified, especially having been manually segmented 'by eye'. Despite this, comparable volumes to TLS-derived estimates were obtained via the data fusion approach (**Figure 6.20**, overleaf). A side-by-side comparison of the three approaches (**Figure 6.21**, overleaf) illustrates that the improvements achieved with this approach are inconsistent. Future work should certainly consider adopting a consistent, replicable, semi-automated approach to ALS crown segmentation such as the multi-scale approach described by Barnes et al. (2017).

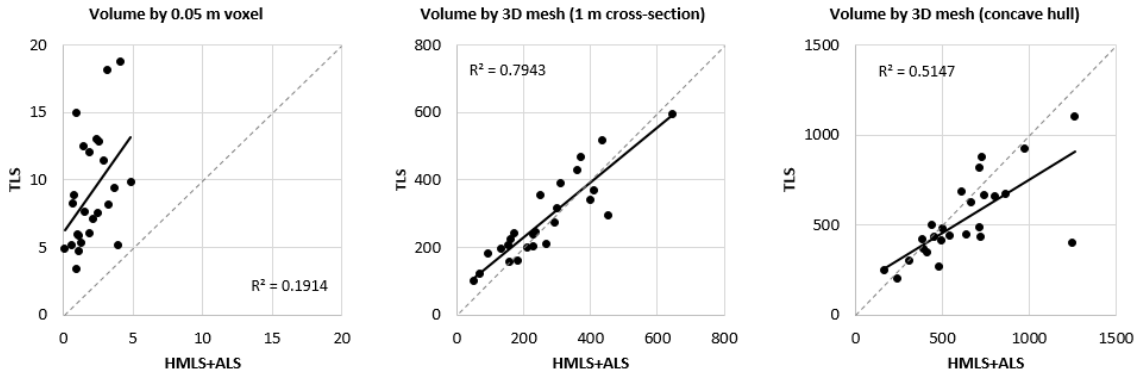

Figure 6.20: Scatterplots showing the relationship between TLS and HMLS+ALS (fused) crown volume estimates. The cross-section-derived approach to volume estimation shows the greatest potential (good fit to 1:1 line; $R^2 = 0.7943$.

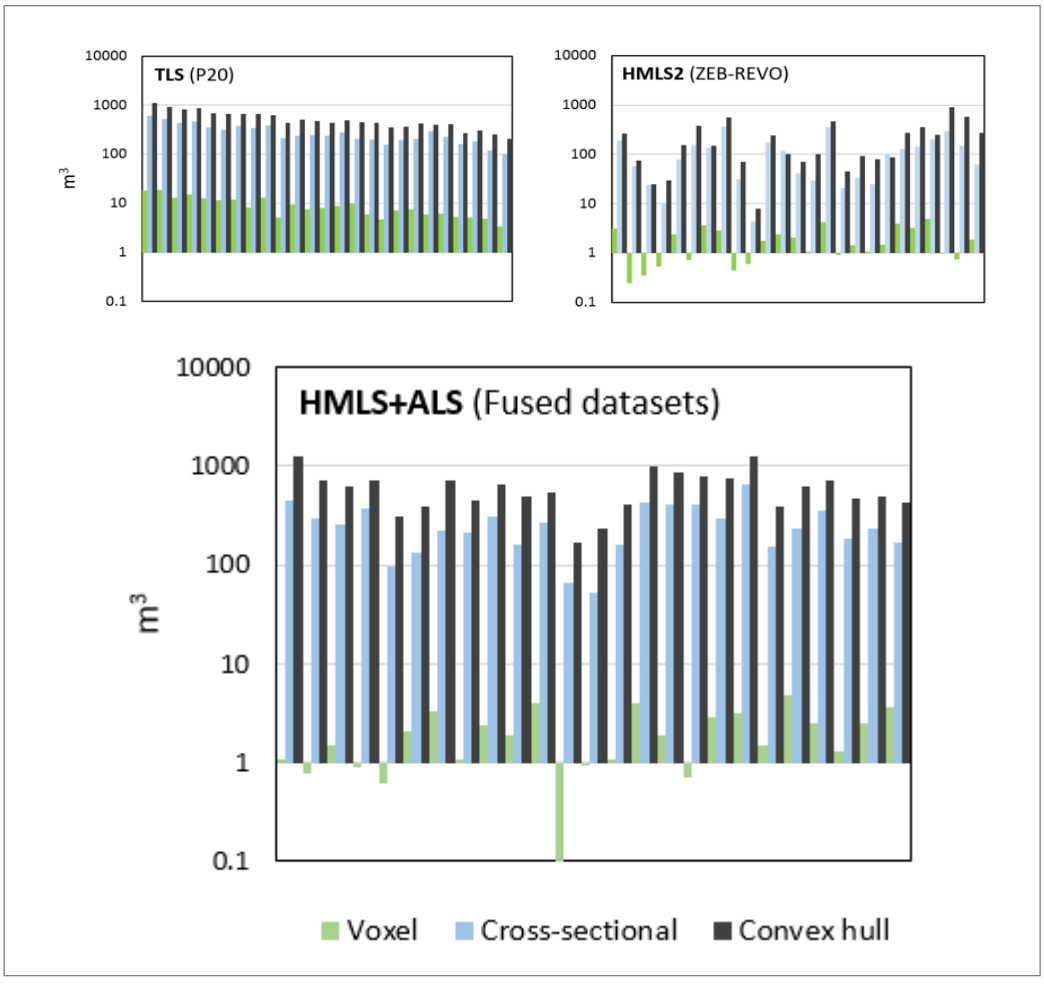

Figure 6.21: Side-by-side comparison of tree crown volumes estimated by (a) voxel count, (b) cross-sectional mesh and (c) convex hull mesh approaches applied to fused (HMLS+ALS) data.

6.4 Summary

The overarching objective of this chapter was to determine the role HMLS technology can play in acquisition of sub-canopy data for 2D, 3D and pseudo-3D forest mapping. HMLS sensors cannot measure canopy structure (***Chapter 4***; ***Chapter 5***) but the data presented and analysed within this chapter confirms the HMLS approach to forest mapping is potentially very useful for the rapid acquisition of rich, three-dimensional information tree parameters from ground to lower crown. Crucially, whilst the two sensor technologies exist in separate domains and ultimately resolve different forest components, there are parallels which manifest as spatially explicit relationships.

This chapter demonstrated that sensor fusion can indeed boost the utility of HMLS systems in several forest applications. However, there is only merit in fusing data where all datasets involved are of sufficiently high point density to discern tree structural components. Environment Agency (2018a) open LiDAR data is therefore unlikely to contribute complementary structural insight to an area of forest mapped with current-generation HMLS sensors. On the corollary, a combination of HMLS and UAV LiDAR acquisitions seems likely to offer the most efficient means of accurately mapping 2D and 3D forest structure.

7. Discussion

7.1 Introduction

This research sought to develop a protocol for the optimal use of HMLS in forests. When the project began in 2014, HMLS sensors had only recently become available in professional surveying and were yet to be assessed in forest environments. The pace of development in mobile laser scanning has increased over the years since, but HMLS sensors have remained under-represented throughout the literature.

7.2 Chapter structure

This chapter begins with a question-by-question analysis of the research questions posed – the main findings, specific results and broader implications raised by each of the three results chapters. These sections (***7.3*** to ***7.5***) include full analysis of all results achieved throughout this work, which are then examined in the context of existing research literature. Section ***7.6*** looks more generally at variation in positioning, precision and quality of HMLS data (in comparison with other methods and sensors) across all study sites. The limitations of this research are then discussed (***7.7***), leading to a section (***7.8***) which addresses both limitations and data quality through an applied analysis of operational considerations. Finally, section ***7.9*** proposes a hypothetical 'integrated forest inventory and assessment' protocol, within which it is anticipated HMLS technology would play a key role. The many merits of such systems are put into context in terms of the forestry variables they *can* readily detect and measure, whilst strategies to acquire a full suite of tree apex to forest floor datasets are also described.

7.3 RQ1: Comparison of tree mensuration derived from benchmark TLS and experimental HMLS scanning

RQ1 sought to determine how HMLS techniques compared with established, tried-and-tested TLS methods for measuring trees in two and three dimensions. Experiments were devised to identify which 'parts of a tree' the two HMLS sensors could resolve – and the precision of measurements subsequently derived from this data. Bespoke forestry-specific software was tested and information derived from HMLS data through this software was compared with a precise and reliable reference (TLS) dataset.

7.3.1 Main findings

The results and findings introduced here were designed to answer RQ1 and assess the many roles HMLS sensors can play in forest surveying, building on work performed by Ryding et al. (2015), Bauwens et al. (2016), Oveland et al. (2018), Cabo et al. (2018a) and others in this field. The main findings are presented per-measurement. To reiterate, two-dimensional variables included DBH, tree height, crown height and projected tree crown area. Three-dimensional variables focused on crown volume, estimated using three separate algorithms.

7.3.2 Subsets, classification and segmentation of HMLS point clouds

HMLS data generally lent itself well to object-based segmentation with the exception of the USB-C subplot (e.g. **Figure 4.9**; page 114) where tree crowns intersected one another. The very nature of HMLS surveying meant that points were distributed relatively-evenly throughout each scan (and hence subplot). This was in contrast with TLS techniques where a high density of points were acquired close to the scanner, density decreasing with distance. Individual points were more widely separated in HMLS than TLS data because of beam divergence angle and sensor resolution. This proved to be a double-edged sword; data density was lower but a larger minimum-distance-between-points threshold for HMLS clouds was thus necessary to facilitate semi-automated segmentation (**Table 4.5**; page 110). Ultimately, this meant that a high degree of manual adjustment was required. Fewer points were acquired per unit

area using HMLS than the TLS reference datasets. Thus, both the classification and segmentation algorithms ran more swiftly for HMLS than TLS data. **Figure 4.7** (page 112) illustrates this problem in the context of HMLS data acquired at UEP-BW.

For various reasons, *3D Forest* proved inconsistently unstable and often crashed. This seemed to be most common when the software attempted to classify point clouds exceeding 20 x 20 m (spatial limit) or 30 000 000 points (data volume) into terrain and vegetation layers. Accordingly, spatial subsets were extracted. This had the effect of shrinking sample size but enabling semi-automated extraction of biophysical parameters such as tree height, DBH, etc. Classification and segmentation were ultimately successful across all subplots although manual refinement was required. Not all scans were equal and not all user-defined parameters were applicable across all datasets. The structural definition of 'tree' therefore varied with sensor, site and survey methodology. As with any branch of science, it is key that data is processed consistently. This was adhered to as fully as possible but bias was identified after manual 'cleaning' of segments. Furthermore, classifying segments as 'tree' or 'other vegetation' was a necessarily manual task. At best, this aspect of processing could be described as '*semi*-automated'.

Recall that the anomalous values removed were those which exhibited unrealistic differences between RHT-derived DBH extracted from both the TLS and HMLS2 datasets. The distribution of points in **Figure 4.12** (p. 119; right-hand panel), even with three more pairs of DBH values excluded, remains greater than that illustrated in **Figure 4.14** (p. 121; bottom right-hand panel). This suggests that as a DBH estimation technique, LSR is less reliable than RHT. Later in this chapter, a much larger sample of DBH estimates is analysed. This incorporates a broader range of diameters and encompasses multiple forest plots across three separate forests.

The results presented in ***Chapter Four*** demonstrate that current-specification HMLS sensors cannot yet measure the full height of trees. However, they do confirm that it is possible to accurately ($R^2 > 0.85$ across three different forest types) derive DBH in scenarios where HMLS scans are performed optimally. Throughout this chapter, HMLS

was again compared with multiple TLS reference scans and where range was not relevant, results were found to be of high accuracy and good precision. Where measurements required information on tree structure at heights greater than 16 m (ZEB-REVO) or 12 m (ZEB-1) above ground, the data was of much less scientific utility. 2D and 2D crown mensuration proved problematic due to limited range, but workflows developed to assess these variables worked well. Future developments in mobile LiDAR technology look set to herald a second LiDAR revolution in forestry.

It is common knowledge that the size of tree structural components – branches, twigs, leaves - decrease broadly in line with distance from the ground. Given that HMLS sensors have limited range, and that beam separation is such that adjacent points may be several centimetres apart at crown height, it was perhaps predictable that such sensors did not prove capable of detecting crown structure in the experiments conducted here (***Chapter 4***, sections **4.3.6** and **4.3.7**; pages 136-146). **Figures 4.30** (p. 137), **4.33** (p. 139) and **4.35** (p. 140) illustrate how variables dependent on accurate determination of crown height and crown bottom height were also negatively affected by a limit in HMLS range. In particular **Figure 4.37** (page 143) and **4.31** (page 145) serve to highlight that crown height underestimation was not linear but perhaps random.

Scans were performed outdoors, where HMLS range was expected to fall between 10 and 15 m (Cabo et al., 2018a) or 15 to 20 m (GeoSLAM, 2018). The results presented in this research highlight a useful range of 16 m (HMLS2) and 12 m (HMLS1) in typical daylight conditions. Points were logged at heights above this but given diminishing resolution with distance from scanner, it proved impossible to determine whether these spurious points were tree or mere noise. Clipping heights at the 99th percentile reduced maximum height by several metres***.***

7.3.3 Diameter at breast height

The results presented in ***Chapter 4***, section **4.3.3,** suggest it is indeed possible to extract realistic DBH estimates using HMLS sensors subject to a certain tolerance. Mean RMSE values of 0.031 m (for the HMLS2 sensor) and 0.060 m (for HMLS1) were achieved across all three field sites. These results are negatively biased, for some trees, due to complex tree structure. Not all stems were 'clean' so results were demonstrably biased by the presence of surface noise and occasionally low branches, both at DBH height. Additionally, the *3D Forest* implementation of DBH-fitting algorithms seemed sub-optimal in the context of noisy stem point clouds, the least-squares (LSR) approach particularly. In the most-representative field site – UEP-BW, comprising the widest range of DBH values – an RMSE value of 0.029 m (HMLS2) was achieved once clearly-anomalous estimates were removed. These RMSE values, taken across all sites as a whole, compare fairly favourably with existing research comprised of similar analyses: 0.29 m (Ryding et al., 2015), 0.011 m (Bauwens et al., 2016) 0.031 m (Oveland et al., 2018) and 0.037 m (Forsman et al., 2016) for the HMLS1 system and 0.010 m (Cabo et al., 2018a) for the HMLS2 alternative.

Given manual 'cleaning' of tree stems within a point cloud prior to analysis, RMSE can realistically be expected to fall to 0.010 to 0.030 m. As data processing progressed, some segmented trees were omitted from analysis due to clear overestimation associated with noise, branches at DBH height or insufficient coverage in terms of stem circumference – e.g. because of occlusion. Other values were removed where equivalents in other sensor scans were unavailable. Where only 'clean' stems were sampled – for example the trees sampled from the UTF-ROK subplot (**Figure 4.15**; page 123) scanned with the HMLS2 device – RMSE reduced to 0.016 m (RHT) and 0.026 m (LSR).

RMSE for DBH derived from the HMLS1 datasets acquired at Stratfield Brake (USB) was greater than expected, biased by problems deriving DBH from the smaller trees within the plot. In future, such issues could be mitigated to some extent with manual

adjustment of DBH point clouds on a tree-by-tree basis within *3D Forest*. However, this may prove to be an unworkable solution given the time required for such work.

Mean DBH values (**Table 4.6**; page 124), across all sites, were 0.318 m (HMLS1) and 0.315 m (HMLS2). This compared favourably with mean TLS-derived DBH – 0.310 m. Meanwhile, standard error was 0.036 m, 0.038 m and 0.033 m for TLS, HMLS1 and HMLS2 respectively. So, when considered as a series of values, the two techniques compare well. A corollary to this argument is when minimum derived DBH is compared. For the TLS dataset, the smallest DBH value derived was 0.044 m. HMLS1-derived DBH for the same stem was 0.046 m – just 2 mm difference. However, minimum HMLS2-derived DBH was 0.052. In some instances, points in close proximity to a tree stem between 1.2 and 1.4 m above ground were incorrectly attributed as 'DBH cloud' points, irrespective of DBH algorithms (e.g. **Figures 7.1** for TLS and **7.2** for HMLS2; page 206). Unfortunately, the '*DBH cloud edit*' tool built-in to *3D Forest* was unable to modify the respective point clouds on-the-fly, so these anomalous values were removed from further analyses reducing sample size from 51 to 49.

An alternative technique was tested to potentially combat this overestimation of DBH, albeit with a substantial time penalty. A pair of trees were identified where the difference between TLS and HMLS2-derived DBH exceeded 0.1 m. The two trees were then manually 'pruned' of all non-stem points in the vicinity of breast height and the two DBH-estimating algorithms were re-ran. **Figure 7.3** (page 207) illustrates tree 33 before, during and after this process as applied to TLS data. The 'pruning' process for the tree highlighted in **Figure 7.3** took three minutes, requiring multiple detailed edits. This was in addition to time taken identifying 'incorrect' trees within the subplot and isolating points associated with that tree from all other points in the subplot cloud. As it would have proved inefficient to repeat the process on all trees where inter-sensor DBH estimates varied by more than a threshold amount (in this study, 0.1 m), these trees were instead removed from further analyses. DBH error was deemed to have been the result of the *3D Forest* algorithm rather than HMLS2 data quality. Consequently, a further 9 trees (**Figure 7.4**; page 207) were removed. Of the 51 trees segmented from TLS and HMLS data, a total of 39 were preserved.

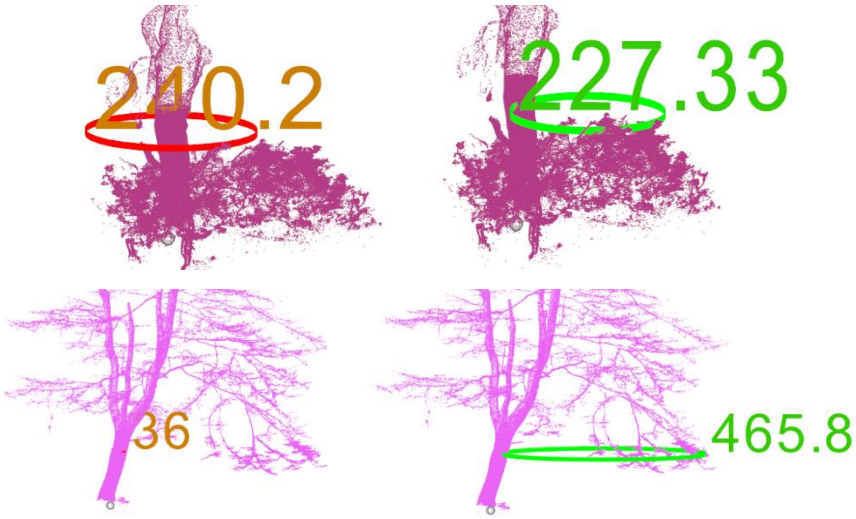

Figure 7.1: DBH estimates for tree number 45 (top) and 15 (bottom) as derived from P20 TLS data using RHT (red cylinder) and LSR (green cylinder) algorithms. Estimates here are shown as visualised within *3D Forest* software.

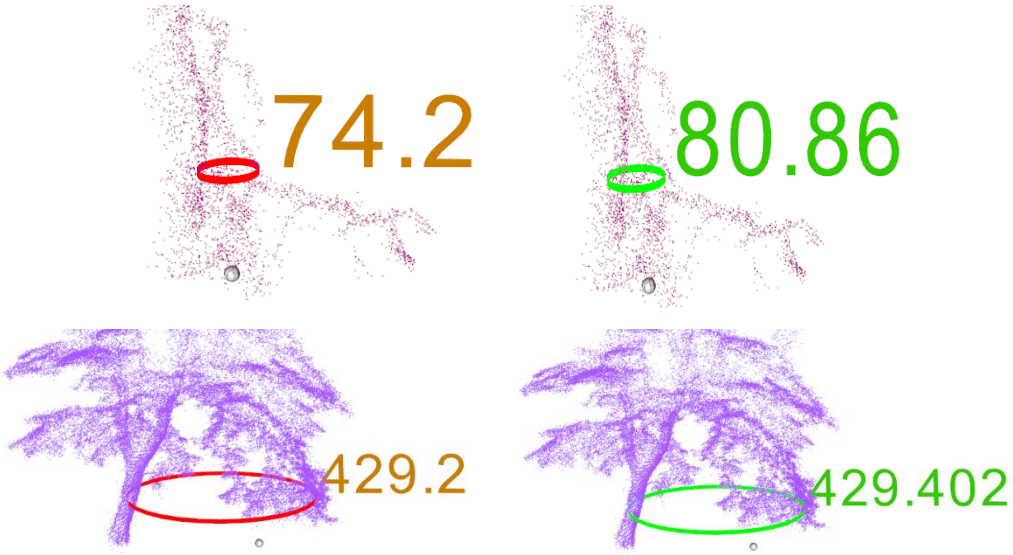

Figure 7.2: Further DBH estimates for tree 45 (top) and 15 (bottom), this time derived from ZEB-REVO (HMLS2) data using RHT (red cylinder) and LSR (green cylinder) algorithms. Estimates here are shown as visualised within *3D Forest* software.

Figure 7.3: Tree 33 extracted from the TLS dataset before (left), during (centre; orange denotes points to be discarded) and after (right) manual data pruning. As a result of the pruning, derived DBH decreased from 0.85 to 54.8 m. While removal of the minor twigs improved DBH estimation, the time expense rendered the approach inefficient within the scope of this research.

Cabo et al. (2018b) demonstrated algorithms which could derive accurate DBH estimated despite the presence of artefacts in point clouds at breast height. If such algorithms were applied to HMLS data, there is every chance the results in ***Chapters 4*** and ***5*** could be further improved. DBH estimation using unmanned ground vehicle-based LiDAR and SLAM processing achieved RMSE of 2.38 cm (Pierzchala et al., 2018). The results presented in ***Chapters 4*** and ***5*** compare favourably, especially when data artefacts are considered.

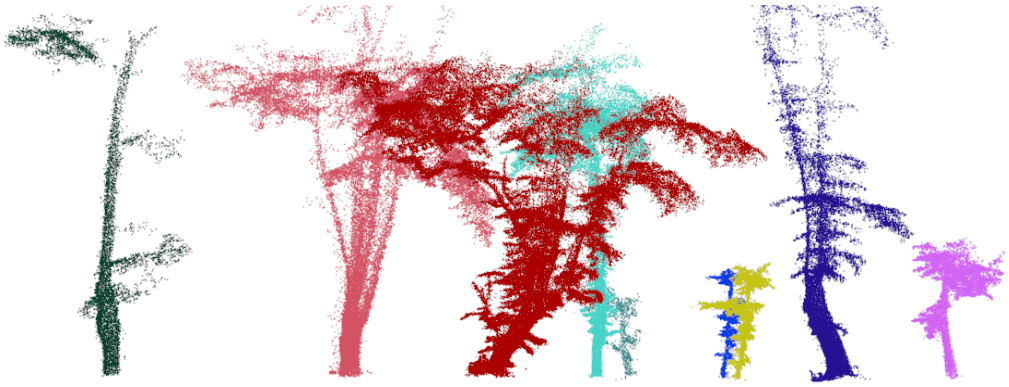

Figure 7.4: Trees as scanned with HMLS2 and removed from further analysis as they were deemed too structurally-complex for DBH estimation. In this instance, the presence of minor branches and dense leaves at DBH height affected the accuracy of the *3D Forest* cylinder-fitting.

7.3.4 Tree height

In terms of tree height, neither the HMLS1 nor HMLS2 sensor could resolve the height of trees >24.9 m as measured using TLS (**Table 4.7** and **4.8**; **Figure 4.20** and **4.23** – pages 129 and 132). The tree with the greatest height successfully detected in full by HMLS1 stood at 12.4 above ground. Whilst HMLS1 also recorded tree heights up to 15.7 m above ground, these points did not reflect true height. This implies a hard limit in sensor range between 12 and 13 m in typical conditions reflectively of a calm spring morning in the southern UK. This backs-up findings presented in ***Chapter 5*** (**Figures 5.17** and **5.18**; p. 166-167) - a maximum detected height of 12.5 m above ground. Meanwhile HMLS2 showed a mean height of 16.5 m within the UTF-ROK subplot where mean TLS height was 26.2 m – again implying a superior, but still limited, sensor range. Across both the UEP-BW and UTF-ROK sites, HMLS2 height estimates seemed to peak at roughly 15 m above ground. These figures are in line with Cabo et al. (2018a) which, at the time of writing (July 2018), was the only study to have assessed a ZEB-REVO within a forest environment.

7.3.5 Stem volume

Efforts to model tree stems as three-dimensional meshes to estimate individual tree stem volume – and potentially derive growing stock volume at the plot-level – were relatively unsuccessful. The technology exists to achieve this and indeed, several recent studies have leveraged TLS data and software such as *Computree* (Raumonen et al., 2013; Hackenberg et al., 2015; Calders et al., 2015; 2016; Sheppard et al., 2017; Stovall et al., 2017; 2018; Putman et al., 2018; Wilkes et al., 2018) to build quantitative structure models. However, the processing pipelines for achieving such models were lengthy and inefficient – perhaps best used for single-tree samples.

Whilst it proved possible to generate meshes, the process was very time-consuming. HMLS clouds were significantly noisier than TLS equivalents and spatial resolution was up to one order of magnitude lower. Stems were first manually-isolated from HMLS scans (ground, understorey vegetation and branches removed iteratively with

polygonal ‘fences’, as described in *CloudCompare* was then used to compute normals and the ‘*Poisson surface reconstruction’* plug-in called to generate a mesh. Meshes were subsequently adjusted by clamping the associated scalar field values. This had the net result of removing TIN mesh vertices not representative of the true tree stem. TINs were spatially complex and did not resemble stem geometry as accurately as TLS no indication of accuracy was available. As a consequence, a decision was made to jettison full-tree volume from this research given resource limitations. Voxel-based volume is briefly discussed in ***Chapter Six***.

7.3.6 2D and 3D tree crown geometry

An attempt was made to derive two-dimensional crown structure for variously sized trees from HMLS data. This was novel analysis not previously tested in published research. Unfortunately, neither HMLS1 nor HMLS2 proved capable of capturing sufficient crown structure to facilitate realistic estimation of two-dimensional crown size and shape. Crown geometric algorithms could only be usefully applied to data where individual trees could be segmented. This effectively meant that areas of forest where crowns intersected one another could not be used as segmentation relied, in part, on a minimum point separation. In intersecting crowns, points from adjacent trees often fell well within this threshold, especially where branches or twigs were in direct contact with one another. Therefore, to measure crown geometry a subset of the data acquired for this chapter was extracted. This subset included the UEP-BW and UTF-ROK subplots featuring tall, sparsely-planted trees and displaying a degree of ‘crown shyness’. Whilst the actual results generated significantly underestimated true crown shape and extent, considered as proof-of-concept they suggest substantial promise, particularly with anticipated development in terms of hardware.

Estimates derived from the UEP-BW subplot showed a weak correlation with respect to reference TLS-derived estimates: R^2 values of 0.173 (HMLS1) and 0.504 (HMLS2). Meanwhile estimates extracted from TLS and HMLS2 scans acquired at the UTF-ROK field site yielded an R^2 value of 0.007. Together, these results suggest that HMLS sensors are not useful in terms of reconstructing tree crown geometry. There seems to

be little benefit in attempting to derive crown width or projected surface area using such instruments. Similar attempts were made to examine the three-dimensional structure of the same tree samples using the same sensors. Again, the success of this approach was very limited due to the relatively limited range of the HMLS laser itself.

HMLS range was limited and no clear relationships were observed where HMLS and TLS volumes were directly compared (page 136 – 146). Yet across all subplots, a relationship was identified between convex hull volume and crown height for both TLS and HMLS2 sensors (**Figure 4.44**; page 146). Of greater interest was the apparent relationship – negatively exponential – between mesh surface area and surface volume, evidenced in both TLS and HMLS2 analyses (**Figure 4.44** again). Future research might detect subtly different exponents. If so, this may perhaps be a simple means of discriminating between tree types (e.g. coniferous; non-coniferous) or perhaps even species. However, the technique itself functioned well, suggesting that with a superior laser (e.g. enhanced range) the approach would be of merit mapping.

It remains to be seen whether the convex hull, or cross-sectional, approaches to three-dimensional crown volume estimation are of greater merit. Where both were applied to TLS data, derived volumes were significantly different (**Table 4.9**; p. 142). The voxel-based approach substantially underestimated volume. This is because the approach only created voxels where 3D measurements existed in XYZ space. Thus, as such measurements were predominantly captured within the outer edge of tree crowns, and biased towards the base of a crown (due to limited sensor range), few voxels were located within the crown. Voxel volume accuracy in this context was dependant on two parameters: voxel cell size and point density. With a cell size of 10 m, even a very sparse voxel plot would indicate high crown volume. Conversely, 0.01 m voxels are always going to under-report crown volume when point density is less than e.g. 1 000 000 points/m^3. Given the variance in point density as a function of (a) tree height, (b) distance-from-scanner, (c) occlusion and (d) scanner placement, it was impossible to create a continuous 3D reproduction of full tree structure.

The success of a similar approach could be improved using a mobile sensor with a high range (>50m), high pulse rate (>100MHz) and improved accuracy (<0.001m). This might include the GeoSLAM ZEB-HORIZON, Leica BLKGO or Leica Pegasus:Two systems. Such systems should also facilitate much-improved crown meshing, especially if fused with UAV-mounted LiDAR-derived datasets.

7.4 RQ2: Target reconstruction as a function of survey geometry

7.4.1 Sensor range

Looking at all scans side-by-side, from both a profile (**Figure 5.2**; p. 152) and an aerial (**Figure 5.3**; p. 153) perspective, variation in sensor range is clear to see. This becomes even more evident in **Figure 5.5** (p. 156) where the proportion of physical tree structure detected by the ZEB-1 visibly decreases. The obvious implication is that the scanner does not have an infinite range and the distance it can scan can be observed in datasets as small as the UVP site. To explore range in a more empirical manner, the vertical distribution of points was plotted in a series of histograms (**Figures 5.8** and **5.9**; p. 159). The size of each bin was set to 0.5 m, reflecting the z-axis dimension of horizontal slices extracted from each scan. Although the shape of each histogram is subtly different, each peaked in the range of 3.5 to 4 m above a terrain-normalised datum and each showed a maximum vertical height-above-datum of no greater than 9.5 m. On this evidence alone, range could naively be described as “up to 10 m outdoors”, some 10 m shy of the GeoSLAM (2018) specification. However, short of measuring ‘range’, this was more akin to an inferred determination of ‘maximum height’. It took no account of three-dimensional (angular) range.

Looking at density plots in **5.9** (p. 159), tree reconstruction between 2 m and 10 m scans is vastly different – yet in all scans, apparent maximum height is identical. This suggests that range exceeded 10 m, at least laterally, in all scans. It seemed prudent to re-evaluate maximum height. Maximum height was estimated for each scan (rather than tree), with values illustrated in bar chart form as **Figure 5.17** (p. 166). Maximum

height varied between 10.84 and 12.52 m – with the 'highest' points recorded in the 'reference' scan.

Intriguingly, the lowest-quality scans (in terms of SLAM registration) accounted for the next three greatest heights – the two 5 m (fast; steady) and 10 m scans. Suspicion grew that perhaps gross maximum height may not be the optimal measure, so additional heights were extracted at the 99th percentile of points above ground. Although not a *de* facto measure of height, this approach had a drastic effect on relative height values between the scans. Now, heights varied between 6.5 and 7.5 m, with height *decreasing* in line with quality of SLAM registration. Recalling that SLAM quality is a proxy for the quality of the data, this suggested that values extracted from low-quality scans were less reliable. The 'reference' scan had the lowest apparent height but was biased, in that a greater proportion of points were collected of ground given the complex trajectory (multiple, rather than a single, loop).

All HMLS scans significantly under-estimated tree height in comparison with the HMLS 'reference' (**Figure 5.17**; p. 166). Meanwhile the TLS data suggested maximum height in the region of 13.5 m, versus 12.5 m for the reference HMLS scan (**Figure 5.18**). Examining the figure in more detail it appears the HMLS point cloud structure degrades at heights exceeding 8 m or so. Tempting though it might be to suggest occlusion (shadowing of upper tree structure by lower branches blocking laser pulses), it is a factor common to both HMLS and TLS. Given the 'always on' nature of HMLS scanning, data was continuously captured from an almost-infinite number of angles. Perhaps it is more sensible to define a range of data quality degradation rather than an absolute value for maximum range. Useful sensor range appears to fall within the region of 10 to 12 m.

7.4.2 SLAM performance in feature-poor environments

It was hypothesised that SLAM may struggle where there was a lack of unique features within 5 – 10 m of the scanner. This appeared to have been the case in the 10 m scan. The football goalpost was successfully reconstructed, but remaining points bore no

relevance to on-the-ground physical structure. As suggested in **Figures 5.4** (p. 155) and **5.7** (p. 158), a 2D density raster might be the best way to visualise tree reconstruction. Although the 3D information is lost, these plots clearly show relative branch completeness (i.e. the portion of a given tree successfully detected in a single scan).

The 'hole' in the 10 m scan is more readily visible in **Figure 5.3** (page 153) which includes cross-sectional slices extracted from a 3D density plots generated from the varied-distance scans. This figure illustrates significant difference in the number of branches detected by the ZEB-1 HMLS in the three scans highlighted. In the case of the 10 m scan, almost no structure is visible between the two stems. Given that this void is >11 m from the scan trajectory, an obvious implication is that range may have been limited to <12 m. Even at the eastern (left) and western (right) extremities, much less of the lower branch structure was detected despite relative scanner proximity. For moderate-to-good quality SLAM registration, the trajectory of any given HMLS scan must loop features of interest at least once and in close (<5 m) proximity.

7.4.3 Point density and distribution

Figures 5.4, **5.5** and **5.7** illustrate density as a variable in each of the scans – measured in 2D (**5.4**; **5.7**) and 3D (**5.5**). Density is a metric that counts the number of 'hits' – LiDAR measurements – in a 'bin' (equal-area raster cell). Of interest here was whether there would be any pattern in density variation and if so, whether it was predictable and whether it was a function of a user-controlled survey parameter. The GeoSLAM ZEB-1 collects 41,000 points per second (GeoSLAM, 2018a) and typical walking speed for an adult human averages roughly 7 km h^{-1} (2 m s^{-1}). Assuming a horizontal range of 15 m either side of the scanner, HMLS swath width is roughly 30 m. Thus 41,000 points covering an area 2 x 30 m in extent will be logged per second.

If point spacing was equal, density would equate to 683 points per m^2. Of course, point spacing is a function of beam separation – increasing with distance from a scanner – and so not equal at all. Scan geometry varies dynamically, and point distribution is as much a product of sensor orientation and progress of the surveyor through a field site

as anything else. It therefore proved impossible to constrain any realistic estimate for point density. However, analysis of density across each scan and plot nonetheless yielded useful insight.

Unsurprisingly, the highest point density was recorded in the 20-loop scan (20 loops at a distance of 2 m from target trees). Lowest point density was recorded in the 1-loop-at-10-m scan – which showed a 'data gap' between the trees at heights above ground. In all single-loop scans, ground point density tended to show a somewhat striped distribution (**Figure 5.4**; p. 155). The data in this scan would require a high degree interpolation to build a coherent, smooth continuous surface model if required. The use of multiple loops mitigated this issue entirely, incorporating a multitude of scan angles into the dataset.

It is also clear that multiple (> 2) passes of a target object greatly increase the number of points acquired (**Figures 5.7** and **5.8**; pp. 157 and 159). However, this relationship is not linear – with more repetition, comparatively fewer points per pass are collected. Some points are potentially lost in the SLAM registration or other cloud-based processing method. In **Figure 5.9** (page 159), we can see the distribution of points in each height bin as a percentage of all points acquired per scan. Most points can be seen to have been captured at heights between 1.5 and 4.5 m and above ground. Density is biased by proximity to the HMLS sensor and consequential decrease in the effect of beam angles (e.g. at a distance of 2 m, two beams angled 1° apart will be much closer than at a distance of 10 m). This is further evidenced by focussing on the plot for "1 loop at 10 m", which shows much less bias. Proportionally, the effect of distance-from-sensor on beam separation is much less pronounced. The lower branches were 4 m above ground and in this particular scan were the reason why a majority of points were logged at this height bin.

Comparing stem cross-sections (**Figures 5.10** and **5.11**; pp. 160-161), the variation in density between scans is obvious. Of the scans that successfully processed, four seem to have incomplete stem reconstruction (i.e. point density is not continuous around tree circumference) – 1 loop at 2 m, 1 loop at 5 m (normal pace), 1 loop at 5 m (fast)

and 1 loop at 10 m. This suggests that repetition and distance both play a role in tree reconstruction, even at DBH height. This assertion is further validated by **Figure 5.5** (page 156) which highlights an enormous difference in point density and distribution. It also illustrates that in marginal scan range conditions, implied structure of a tree is lost. In its stead is an incoherent, relatively sparse distribution of points. These points homogenously fill a volume otherwise occupied by point clusters resembling first- and second-order branches, arbitrarily 'simplifying' tree structure.

Few (< 1000) points were logged more than 10 m above ground in five of the nine scans – and less than 500 in the 5 and 10 m-from-target scans. Once again, this variation in point distribution suggests a limited 'useful range', probably in the region of 10 or so metres.

7.4.4 Tree measurement under controlled conditions

Based on the results that comprise much of this chapter, it is clear HMLS sensors cannot be relied upon to detect tree height accurately and precisely. The specification supplied by the OEM suggested 20 m range outdoors and 30 m indoors. In forests, maximum range would theoretically lie somewhere between the two due to canopy closure attenuating sunlight. Both HMLS sensors struggled to depict forest structure at a distance beyond 12 m – 13 m and in some cases, even objects some 10 m from the sensor were poorly-resolved.

In terms of tree height metrics, it appears HMLS are unable to reconstruct even the lower canopy of typical temperate tree species given the performance observed here. Therefore, canopy geometry was inconsistent – convex and concave hull area varied quite considerably (**Figure 5.23**; page 173) by as much as 13.9 m^2. Some of this error, however, is attributable to the nature of segmentation in *3D Forest* given the overlap between the canopies of the UVP trees. Thus, in ***Chapter 5***, crown surface area is revisited with focus on non-overlapping trees.

In terms of estimating diameter at breast height, HMLS demonstrated promising results. Whilst there remain concerns about noisiness of the data, the algorithms available in *3D Forest* were able to extract DBH semi-automatically from each scan in three of the four trees. The fourth – tree B – was an exception as the stem branched into two limbs at more or less DBH height (1.33 m above ground), confounding circle-fitting. Comparing the LSR and RHT approaches to DBH estimation, there was some variation (R^2: 0.931; see **Figure 5.24** on page 174).

Stem detection was successful in all scans that were fully-processed (**Figures 5.19** – **5.21**; pages 169-171), although given only four trees were present, this was to be expected. When imported into *3D Forest*, centroid positions were estimated for all four trees in all scans – although the locations did vary by up to 0.65 m (**Figures 5.20** and **5.21**). The 20 m scan failed to process at all.

It is clear tree centroids were spread fairly widely with respect to the reference dataset – and in a perpendicular direction to the respective survey trajectory. For instance, tree A – the northernmost tree in the site – has a cluster of points distributed along a north-south axis to the north of where the reference scan positioned it. This would appear to be a hallmark of SLAM positioning in the absence of closed-loops or, for example, trajectory passes overlapping and intersecting one another (as per **Figure 7.6** on page 221).

Error accumulates (error propagation) while a scan is underway. This is because the IMU has no external reference data source such as GNSS positioning and functions as a dead-reckoning instrument. Every degree of rotation is subject to an error, and these errors continuously accumulate unless or until a loop is closed. In the context of HMLS methods, until a survey revisits an object previously surveyed (and ideally approached from a different angle). This error propagation seemed particularly pronounced in the continuously looping scans of the UVP site but was not the case in the reference scan. Error propagation is also the likely cause of misalignment as highlighted in **Figures 5.25** and **5.26** (pages 175 and 176). In these figures, alignment is at its poorest where scan separation (5 m; 10 m) is greatest or duration longest (5; 10; 20 loops).

In summary, the ZEB-1 HMLS system is capable of measuring DBH and tree position to acceptable degrees of accuracy and precision, but optimal use requires multiple passes of target objects within a range of 10 m at most and with repeat loop closure to mitigate excessive error propagation.

7.4.5 Effect of repetition within a single scan

For moderate-to-good quality SLAM registration, the trajectory of any given HMLS scan must loop features of interest at least once and in close proximity to guarantee coverage although 'useful' sensor range probably lies in the region of 10 to 12 m. Based on these results, it seems range is independent of ambient lighting condition and thus is unlikely to be effected through use of the system outdoors.

Point density varies enormously between scans. In most cases, repetition (multiple loops) mitigates data gaps sufficiently. To ensure an even and continuous spread of data from all angles, objects should be looped at least twice from a distance no greater than 10 m on each pass. The ZEB-1 HMLS systems is capable of measuring DBH and tree position to acceptable degrees of accuracy and precision, but optimal use requires multiple passes of target objects within a range of 10 m at most and with repeat loop closure to mitigate excessive error propagation.

7.5 RQ3: Evaluation of a 'data fusion' approach to forest mapping and modelling

The principle aim of this chapter was to determine the role HMLS sensors can play in sub-canopy forest mapping within multi-sensor mapping campaigns. The literature contains thousands of studies exploring forest structural mapping. Most studies focus on ALS, TLS or a combination of the two. There is a clear trade-off (**Figure 7.5,** overleaf) between speed and detail. As comprehensively discussed in ***Chapter 2: Literature review***, published research typically aligns to just one or two of several sensor methodologies. These include ALS, TLS, MLS and HMLS systems.

7.5.1 Multiple sensors, complementary roles

Each approach offers a distinct balance between two ends of a spectrum (**Figure 7.5**, below), 'speed' and 'detail', but it is rare for multiple approaches to be combined. As a useful rule of thumb, ALS offers rapid mapping of wide areas (100s of km^2 in a single flight) at the cost of resolution (5 to 20 points per m^2 footprint), whilst TLS offers very-high-resolution, highly-detailed, local models (>100 000 points per m^2 footprint and mm-scale precision) but with significant time penalty. Meanwhile MLS, HMLS, UAV-LiDAR and UAV-SfM methods alike occupy a fuzzy 'middle ground'. Techniques built around these sensing platforms allow quick capture of 3D data encompassing broad tracts of forest at cm-scale precision. This chapter aimed to identify where, on this spectrum, HMLS techniques sit.

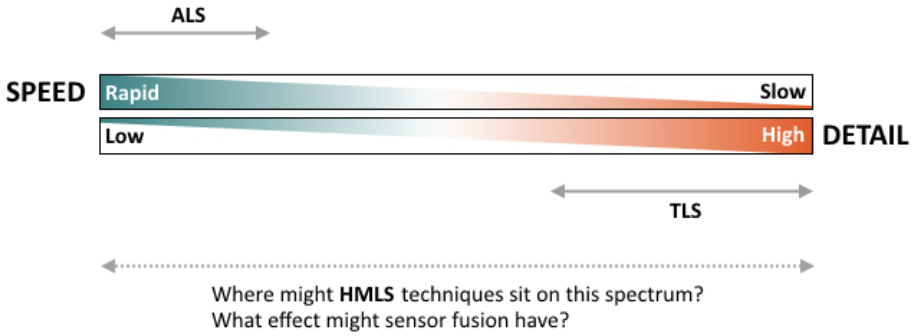

Figure 7.5: Visual representation of the 'spectrum' of 3D forest mapping showing a research gap between ALS and TLS techniques.

The results presented in ***Chapter 6*** are believed to be the first to fully-assess utility of HMLS in acquiring full-coverage 3D data to complement other 3D datasets (i.e. ALS). ***Chapters 4*** and ***5*** confirmed that HMLS scanners cannot obtain tree height or fine structural detail. However, results in the two chapters clearly demonstrate that HMLS is a great tool to quickly and reliably capture cm-scale forest features (DBH, trunk length, dimensions of first-order branches) at the plot and sub-compartment level. with tree parameters directly retrieved from HMLS point clouds. Internal (within-scan) SLAM-derived positioning is robust in forested environments, as found through the

goodness-of-fit of HMLS and ALS data to one another. Where HMLS scan quality is 'good', error is less than 0.1 m. Caution should be applied during HMLS data capture to ensure a good baseline point density and minimise error propagation.

There is a benefit in fusing HMLS and ALS data to combine high-resolution mapping of tree density, DBH and trunk height with crown architectural variables such as tree height, crown height, crown extent and canopy height. Basic data fusion was shown to be a viable means for deriving a complete set of crown variables in conjunction. **Figures 6.9** (page 188) through to **6.21** (page 198) confirmed fusion of ALS and HMLS point clouds can greatly-improve 2D and 3D tree mensuration. Where compared with reference TLS-derived variables, parameters extracted from fused (HMLS + ALS) data were more accurate than those extracted from HMLS data alone. HMLS sensors are demonstrably suitable for multiple roles in ongoing forest research.

7.5.2 Improvement in capability of 2D and 3D tree mensuration

When measuring tree height and length (**Figure 6.11**; p. 189), R^2 rose from 0.15 to 0.55 in both cases. R^2 of convex-hull derived crown surface area increased from 0.22 to 0.64 and concave hull-derived surface area saw R^2 values improve from 0.24 to 0.76, despite a temporal baseline of two years between ALS (2015) and HMLS (2017) data capture.

Voxel-based crown volume estimation was poor in all instances (**Figures 6.20** and **6.21** on page 198**)**, likely as voxels only depict tree surface area and not volume (Stovall et al., 2018). Cross-section-derived crown volume yielded the strongest relationship when compared with TLS-derived estimates: R^2 was 0.79. However, the data were biased in that segmentation of the 'fused' data was carried out manually by eye. In the future, more-sophisticated segmentation algorithms not reliant on homogenous point density may yield superior results.

7.6 HMLS data positioning, quality and precision

Imprecise positioning (e.g. **Figure 5.21** on page 171; **Figure 6.2** on page 182) presented wider problems throughout this research. Whilst visual registration in *CloudCompare* proved a successful means to co-align data, no peer-reviewed studies had explored the validity of this approach. The results presented here must be accepted with a caveat that intra-acquisition alignment is potentially incorrect. Only with the inclusion of well-distributed ground control can multi-sensor datasets be accurately co-aligned.

Results derived in ***Chapters 4*** and ***5*** indicated that target complexity (e.g. richness/abundance of significant 3D objects within scanning range) and trajectory geometry (e.g. number of passes, distance from object and speed of survey) have an impact on the accuracy of HMLS-derived forest mapping. Although a qualitative variable (i.e. with no defined scalar field or attribute), SLAM condition does describe the relative success of a scan. Where condition was observed to be 'high', tree centroid positions were accurate when compared with reference (e.g. TLS) datasets (**Figure 5.21**, p171; **Figure 7.6** overleaf; **Figure 7.7**, p223). Conversely, scans comprising several metres of 'poor' SLAM condition invariably incorporated positional error.

Once downloaded from *GeoSLAM Cloud*, HMLS-derived data came with little information on the quality of SLAM registration. Two such 'quality' files were provided alongside full-density 'full' point data: a reduced-density point cloud (hard-coded to retain 9% of all possible points - purely indicative) coloured by quality and a point-based scanner trajectory file coloured using the same colouration. These files were supplied with a quality flag-based colour ramp ranging from blue, through beige, to red. The implication was that blue implied 'successful' SLAM performance, red 'poor' and shades in between some fairly arbitrary quality. Poor registration was occasionally suggested though the ZEB-1 LED flashing orange. According to GeoSLAM (2018a), this could occur wherever the operator moved (i) too fast, (ii) too abruptly (e.g. when making a sudden turn, tripping, or otherwise moving too fast for the IMU to compensate) or (iii) through a relatively sparse, featureless environment.

The scans undertaken in the UVP field site were condition-controlled, meaning (i) and (ii) were fully mitigated by moving at a reasonable pace. By isolating the effects of speed, the net result was that the quality flag indicated SLAM performance – except for the varied-velocity scans. In all the scans acquired at a constant separation of 2 m from target trees, quality within 10 m of the trees remained good. This is validated by the trajectory acquired in the reference scan (**Figure 7.6**), where good quality (i.e. blue shading) applied throughout.

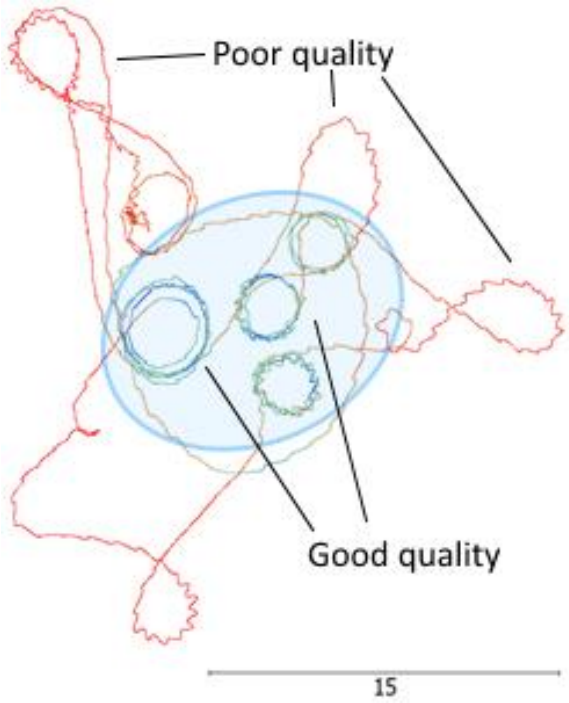

Figure 7.6: Modified schematic of the UVP 'reference' scan trajectory, coloured by SLAM registration quality. The blue shaded polygon highlights the area within 5 m of features (i.e. trees) where quality was flagged as 'good' in all 2 m-buffer scans. The area outside invariably saw poor SLAM registration across the board, likely due to a lack of 3D features within sensor range. North is aligned to the left in this schematic.

Where scans were carefully conducted, quality remained high in the vicinity of persistent features. To further verify this claim, all UVP HMLS scan trajectories were aligned in a single plot (**Figure 7.7**; page 223). Once again, a pattern emerged – good quality registration in the immediate vicinity of trees, with poor registration in outlying areas of each scan. The outermost loops are areas where the scan included TLS target

tripods. These objects were no more than 1 m above ground and surrounded by >10 m of flat, featureless terrain. This seems to confirm that SLAM requires an abundance of complex structure, viewed from multiple angles, to localise position on-the-fly.

Scans conducted at distances of 5 and 10 m from the target trees displayed moderate to poor SLAM quality. In the case of the 'fast' 5 m scan, the ZEB-1 LED blinked on two occasions and so a few retraced steps were taken. This suggests that speed, as well as distance from complex objects, is significant – perhaps the second most-important user-controlled variable. The 10 m scan was of poor quality throughout. Meanwhile, the 20 m scan failed to process as too few points associated with trees were recorded at all. Finally, two scans which saw the trajectory run east-west once, then twice, 11 m to the south of the trees triggered an 'error' in *GeoSLAM Cloud*. Evidently, the geometry of these scans was far too optimistic.

All HMLS point clouds showed systematic noise, especially visible in planar and cylindrical surfaces and likely a by-product of the low-cost laser itself (Bosse et al., 2012; Liang et al., 2018). HMLS data oversamples the true dimensions of smaller objects and there is a bias associated with noise. A consequence of this is that only objects equal to, or greater than, mean systematic error (RMSE = 0.03m; Ryding et al., 2015; ***Chapter Four*** and ***Five*** of this research) may be detected reliably. Even where objects were detected, bias must be considered. It is anticipated a noise reduction filter could improve accuracy of the technique where applied to HMLS data. However, in the case of trees with stem height within maximum range of HMLS sensors, the approach can potentially yield realistic stem volume estimates despite systematic noise. Adoption of the OHM algorithm proposed by Stovall et al. (2017) or the voxel-based approach described by Putman et al. (2018) would likely mitigate bias associated with this noise.

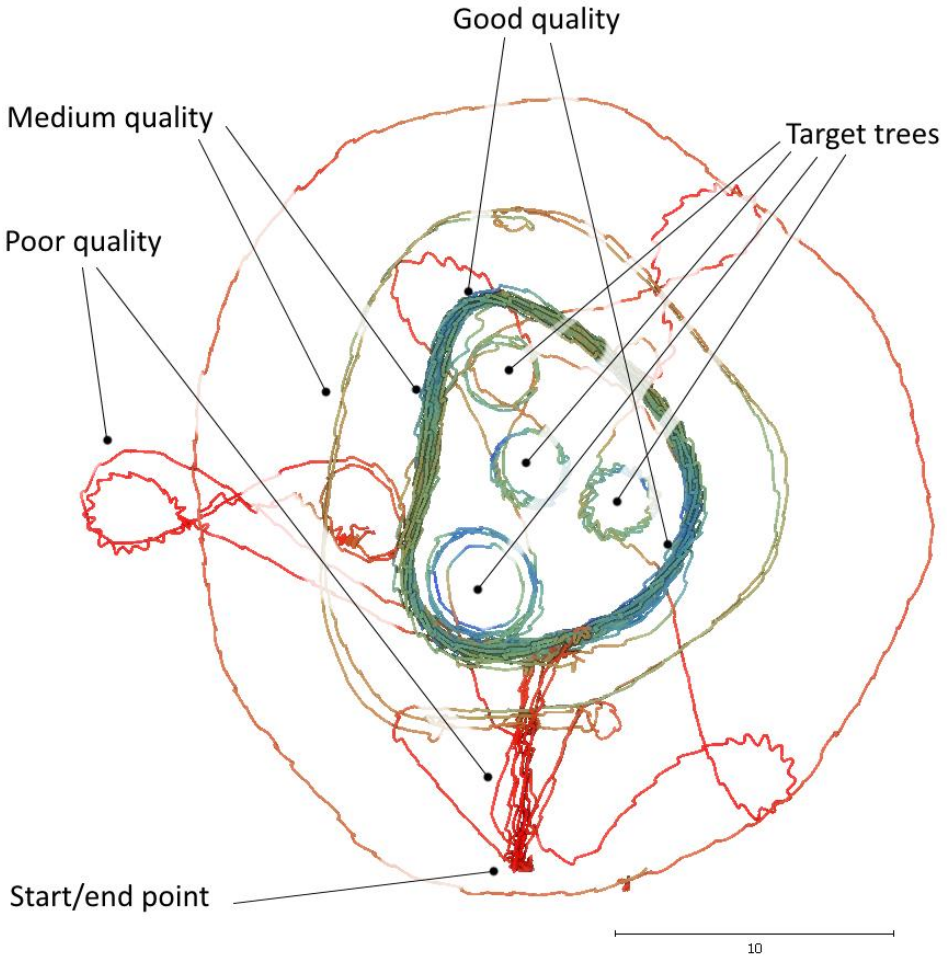

Figure 7.7: Co-aligned plot of all UVP HMLS scan trajectories, coloured by quality. Unfortunately, no index or colour ramp was supplied with this information.

7.7 Limitations of this research

7.7.1 HMLS sensor range

A possible factor affecting range may also have been ambient ultraviolet radiation (e.g. from the sun) known to negatively affect near-infrared radiation (A. Rak, *pers. comm.*, Dec 19, 2017). It remains difficult to ascertain the primary cause of underestimation at the individual tree level. This could be limited range, a side-effect of segmentation or even the result of scan geometry. For instance, adjacent trees may have been captured from very different sensor positions. This is especially likely where occlusion from certain angles was a factor, a common problem in forest laser scanning. With a laser range exceeding 50 m, all trees could theoretically be scanned from top-of-crown to

forest floor using HMLS sensors. In so doing, datasets comparable to Wilkes et al. (2017) and Calders et al. (2018) might be achieved. Compared with TLS, absolute accuracy would be inferior but spatial extent much greater.

7.7.2 Data processing bottlenecks

This research was in part frustrated by a patchy selection of software tools, few of which readily integrated with one another. At the same time, there are an abundance of processing modules and libraries in a multitude of libraries and programming languages ideally suited to specific tasks but which, with a few amendments, may prove useful in unrelated applications. For example, 2D object-based image analysis could assist in segmentation of 3D HMLS point clouds if data were first converted to a 2D density raster. Future research would derive enormous benefit by tackling an apparent disconnect between available software and intuitive workflows. Integrating multiple LiDAR classification, point cloud segmentation, parameter extraction and microwave scattering modules into a 'one-stop' software package would remedy many of the processing bottlenecks described in ***Chapter Six***.

At present, few software tools capable of deriving geometric variables from point clouds also facilitate batch processing, with *Computree* (Othmani et al., 2011) and the *SimpleTree* add-on module (Hackenberg et al., 2015) a notable exception. In parallel, necessary modification to certain point cloud objects (e.g. trees with low-hanging branches; dense understorey vegetation at DBH height) cannot be automated or sped-up through programming tweaks. Such edits are made in real-time; this level of user-interaction accounted for a considerable proportion of time (several months) dedicated to data processing and analysis for this research. However, semi-automated processing steps would certainly benefit from parallelisation in processing to maximise CPU efficiency. Further optimisation could include boosting available RAM or converting scripts to run with accelerated GPU, rather than conventional CPU, hardware.

When generating results for RQ2 (***Chapter 5***), major limitations in the performance of *3D Forest* software were identified (***Chapter 3***: **Figures 3.33** and **3.37**; pages 91 and 97) leading to issues in scale and sample size. Given that segmentation of UEP-BW alone in *3D Forest* took roughly seven hours per sensor, it is not difficult to see the need to carefully-balance the trade-off between processing time and sample size. Minimum sample size was set to 15 trees – with subplot dimensions tailored to suit. Despite processing with a powerful workstation, point clouds above spatial and memory thresholds seemed to continually crash the software.

Major processing bottlenecks were also reported in Liang et al. (2018), especially in the case of tree height estimation and stem detection in areas of dense forest. This agrees with what was found in ***Chapter 5***, especially the USB field site. Liang et al. (2018) identified operator error as a primary cause of omission error when acquiring forest data with mobile scanning systems. The HMLS data capture protocols presented throughout ***Chapters 3*** to 6 here go some way to addressing this. Certainly, by specifying a 'minimal trajectory separation' and filtering point clouds by distance from trajectory, the quality of retained data was enhanced and redundant points (in this instance, points outside the AOI as defined by distance) were removed without undue delay.

7.7.3 Lack of real-time data coverage or quality indication

At the time of writing (May 2018), a real-time module for the ZEB-REVO (HMLS2) was available but had not been tested in forests. Prior to this innovation, HMLS data were captured 'blind'. The only interactivity between surveyor and hardware was a solitary LED on the scanner. Coloured green, it indicated data were being captured at acceptable SLAM quality. Flashing amber, the indication was that SLAM quality had degraded. No other real-time feedback was available. The surveyor would not discover artefacts, misalignment or gaps in data coverage until they had left the field and processed data. This was a major weakness of the HMLS systems tested in this research but addressed in similar products soon to enter the sensor marketplace.

7.7.4 Temporal separation of data capture

Limited availability of ALS data further reduced opportunities to fully-explore data fusion. Whilst the availability of EA ALS data is a substantial benefit to science, the nature of its capture meant a broad range of acquisition dates. Surveys were flown to encompass discrete polygonal areas in specific temporal windows. Necessarily, these could not overlap with HMLS capture. Hence ALS and HMLS surveys were separated by 2 to 4 years. In this period, sampled trees grew at varying rates and upper canopy structure invariably changed. Future research could explore simultaneous capture of airborne and terrestrial dataset to minimise this effect.

7.7.5 Complications co-aligning data from multiple sensors

Given the reliance necessarily invested in handheld GPS devices, it is perhaps unsurprising that absolute spatial agreement between TLS and HMLS sensors proved difficult. The handheld Garmin GPS unit used in the field reported accuracy as high as 1 m, deteriorating to between 3 to 8 m depending on canopy cover. As a consequence, georeferencing of individual scans was based on ALS data. HMLS scans were shifted horizontally (to match tree crowns and corner structures, e.g. buildings, fences) and vertically (aligning footpaths and tarmac surfaces) within *CloudCompare*. This visual registration approach did not yield real-world accuracy assessments, which would have been problematic in any case due to spatial distortion associated with SLAM. The GeoSLAM Cloud implementation of SLAM is 'black box' – with no user-adjustable parameters. Whilst its strength lies in mapping non-uniform areas of spatial heterogeneity, hence its performance in certain forested areas, the algorithm has a tendency to propagate error through dead reckoning without sufficient loop closure. Unfortunately, data were captured 'blind' and where resulting point clouds were sub-optimal, data were discarded.

To assess HMLS-and-ALS data fusion and compare with TLS data (RQ3), multi-sensor datasets had to be fused. This was done using a manual, visual registration approach. Whilst largely regarded as an acceptable method when aligning terrestrial LiDAR, the

approach usually includes fixed-position targets for precise alignment once visual registration is undertaken. This approach is much less-frequently used (if at all) when combining data from multiple sensor types. In the case of this research, accuracy was further constrained by a lack of fixed targets and thus became an exercise of judgment and user-interpretation. Data were extracted from ALS by overlaying TLS data and cutting polygonal fences from the fused data using TLS crown structure as a guide. There may be bias due to this sampling method. Furthermore, this manual segmentation-by-polygon was only possible as the UTF red oak compartment showed signs of 'crown shyness'. Multi-layer crowns are much more complex and require multiple polygonal fences from a limitless number of 3D perspectives.

It is important to note that ALS data were acquired in February 2015 and fused with HMLS data acquired in 2016. These fused data were compared with TLS data acquired in 2017. In this instance, no additional data on tree growth rates was available. Even with knowledge of tree growth, it is impossible to fully account for temporal variation in height. These errors must therefore be accounted for in any future work fusing data from multiple sensors and acquisition dates.

7.8 Operational considerations using HMLS in forested areas

In forestry, HMLS remains a relatively recent addition to the toolkit and at the time of writing, only a few research papers had been published assessing GeoSLAM HMLS sensors in this context. Accordingly, there was a need to assess the factors that may optimise or constrain their operational usage. Here, the principal benefits and disadvantages of the ZEB-1 HMLS system are described operationally in comparison with more-traditional TLS methods.

7.8.1 Efficiency: time and cost

An obvious benefit using HMLS in a forest is the time efficiency of this scanning technique. Using HMLS instead of ALS or TLS, substantial time saving is possible. ALS

data capture campaigns acquire vast swathes of data very rapidly but to the detriment of detail. Aircraft typically cruise at a rate of 150 to 200 knots at altitudes of around 1 000 m. Swath width in the ALS data obtained for this study (Environment Agency, 2018a; 2018b) was 240 m, including 40 m overlap with adjacent survey lines on each side parallel to direction of flight. As a coarse estimate, such ALS sensors can capture 18 000 to 24 500 m^2 of 3D data per second. However, mean point densities tend to vary between 10 and 30 points per metre. At such coarse resolution, the detection of individual trees is difficult – and stems are almost impossible to detect. In most cases, data is biased toward the upper canopy. Understorey vegetation is poorly represented and where present in any abundance, can also negatively influence the accuracy of ground detection.

Conversely, terrestrial laser scanning is inherently time-consuming yet offers almost-limitless spatial resolution from the forest floor to the top of the tallest tree. This is especially the case with modern laser scanners such as the Leica Geosystems P20 (used to validate findings in this research) and P40 and equivalent systems from Riegl Gmbh (VZ-400i; Calders *et al*., 2016a; 2016b; Wilkes *et al*., 2018) with >100 m range. The TLS technique requires complex sensor set-up at each scan station, and assistance from multiple field scientists. Individual scans take 3 to 15 minutes each and multiple scans are required per plot (refer to ***2. Literature review*** and ***3. Methods*** for detail) to mitigate occlusion. There are further bottlenecks in terms of data import, registration and processing (Liang et al., 2018) – especially in higher-density scans.

As suggested by the few relevant studies in the literature (Ryding et al., 2015; Bauwens et al., 2016; Aijazi et al., 2017; Huerta-Garcia et al., 2017; Cabo et al., 2018a; Oveland et al., 2018) the principle benefit of HMLS, compared with TLS, is relatively-rapid data acquisition (in terms of area-based coverage). This research agreed, further establishing that data capture rate was primarily limited by the speed of the surveyor. As described in ***Chapter 5***, the HMLS approach proved capable of deriving results comparable to those acquired with TLS. For example when estimating DBH, HMLS-derived parameter RMSE was in the region of 0.03 m when compared with TLS

observations of the same trees. This places HMLS systems to the right of a 'level of detail' spectrum such as **Figure 7.8**, below.

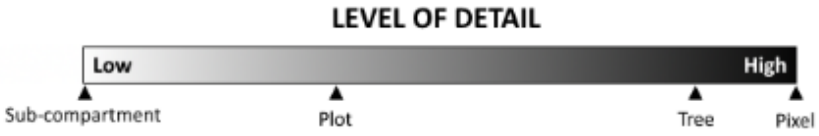

Figure 7.8: Graphical depiction of the varying levels of detail achieved with the sensors analysed in this research

Each of the nine HMLS scans collected in the UVP field site took less than 15 minutes – with cloud-based processing equally rapid, processing undertaken at a 1:1 ratio with duration of field capture. This data allowed creation an accurate stem map (centroids) within minutes of data import. The equivalent TLS survey required eight scan stations and took three hours. TLS data processing was non-trivial, too, requiring bespoke software (*Leica Cyclone*) and involving a two-hour delay while raw data loaded to the *Cyclone* database. It currently (May 2018) costs £0.32 per 2 m^2 'unit' to process HMLS data via GeoSLAM Cloud. In contrast, TLS data processing attracts no charge assuming the operator has at least basic experience and their time is not chargeable. However, TLS data processing requires specialist, proprietary, commercially leased software (*Leica Cyclone*) which in itself requires a certain level of expertise and significant processing time. It is therefore difficult to apportion cost, software licence depreciation and to value the time of the data processor. TLS data processing is as laborious or straightforward as the survey specification necessitates.

In the TLS-based UVP field survey, black-and-white tripod-mounted targets were used to provide common reference points in each of the eight scans. These reference points were successfully used to align the scans, to a gross RMSE of 0.002 m. The entire processing chain first required the import of raw scan data into Cyclone, running behind-the-scenes over several hours. This was followed by a quick automatic-alignment-of-targets which took several seconds. A final 'registration' was performed

to derive a co-registered point cloud. This entire processing workflow took a full working day but could have taken much longer. HMLS data processing and alignment, meanwhile, was simple. Thanks to SLAM, data was delivered 'pre-aligned' with no user intervention required. Automated processing was done using GeoSLAM Cloud and co-registered, processed data were downloaded as single point cloud files within an hour of upload. Alignment of individual scans to a common local coordinate system took the form of manual translation and rotation in *CloudCompare* and was completed within an hour. With the use of spherical targets in the field, this could be reduced to minutes (GeoSLAM, 2018b).

7.8.2 Recording geometry and minimising occlusion

Given that an HMLS sensor can be moved into an almost limitless number of positions, occlusion is almost entirely mitigated. The prerequisite is that a conscious effort is made, during survey, to ensure the HMLS unit is operated well within its documented range in close proximity with all target trees. Thus, in a relatively open forest a scan should be performed such that opposing survey lines fall within 20 m of one another. In so doing, all objects will be within 10 m of the scanner and reconstruction of any given tree should prove practical.

Given, also, that an HMLS scans continuously and registers points in an almost spherical manner about the surveyor, there is no need to manually aim it at targets. Simply following a trajectory at a steady pace should ensure capture of sufficient data to perform similar analyses to those described in 4.5 Results for RQ1. However, a key constraint is that the HMLS sensors (the ZEB-1 and ZEB-REVO) available at the time of writing did not ship with any real-time display of scan trajectory or data logged. So some form of on-the-fly positioning is required to guarantee coverage. This might take the form of a pre-measured 'grid', or even the use of field spotters to track progress relative to an X and Y axis. From summer 2018, an upgraded HMLS – the ZEB-REVO RT – is likely to be available. This will ship with real-time SLAM processing and live data display, mitigating this problem (GeoSLAM, 2018c).

7.8.3 Placing HMLS in the context of precise forest mapping

Based on the evidence presented in this chapter, it is clear HMLS systems offer substantial value in a multitude of sub-canopy forest mapping. However, where do HMLS systems fit in the context of precise forest mapping, specifically? **Figure 7.9** (below) builds on the 'level of detail' concept (**Figure 7.8**; page 229). It proposes a continuum – a defined range – in which HMLS systems are suitable. The scale is logarithmic, ranging from coarse level-of-detail (100 m, consistent with typical wall-to-wall biomass maps) to extremely high detail (0.001 m, the precision and accuracy with which individual leaves are routinely mapped with survey-grade laser scanners). The orange-to-green gradient indicates the pseudo-spectral bandwidth at which this research suggests HMLS sensors may operate. Meanwhile the feint orange shading to the left outlines the spatial extent of coarser-resolution EO data (e.g. Landsat 8, Sentinel1/2).

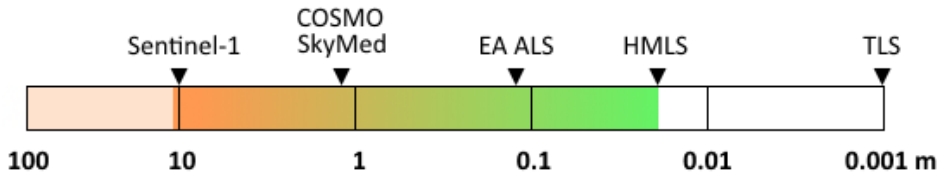

Figure 7.9: A continuum of high-resolution and VHR sensor system resolution.

Upon reflection, HMLS sensors seem to offer an impressive bandwidth in the sense that numerous precision forestry measurements are achievable. The colour gradient highlights that this range extends from 0.03 m (typical RMSE of HMLS measurements such as DBH when compared with reference TLS data, as per ***Chapter 4*** and ***Chapter 5***) to 12 m (maximum useful range outdoors, in bright sunlight, as per ***Chapter 5***). In between, they are perhaps the perfect sensor for mapping ground-level forest attributes at the pixel-level, for instance mapping stem density beneath a mosaic of 1.2 m COSMO-SkyMed (Spotlight-2) or 10 to 20 m Sentinel-1 pixels. HMLS data fits ALS, such as the EA (Environment Agency, 2018a) data explored here – very well, with propagated error in planar dimensions of HMLS scans well within horizontal tolerance specified for the EA data.

Where HMLS performs poorly is where objects < 0.05 m are scanned – leaves, twigs and grass become homogenous 'clumps' within the point cloud. Additionally, the systematic noise in HMLS data precludes these sensors from being useful in measuring fine-scale surface roughness or topography. Despite this, HMLS sensors are excellent instruments for measuring forest floor topography. The primary limitation is that data require some form of filtering and, perhaps, noise reduction – which has the clear dis-benefit of reducing point density and introducing some kind of interpolation. The results presented here determined that topography derived from HMLS data and filtered using the CSF algorithm (Zhang et al., 2016) was of comparable detail and precision to TLS and ALS-derived data.

7.9 Integrated forest inventory and assessment

This research has demonstrated that HMLS systems are of mixed utility in forest mapping: there are measurements for which they are capable tools, and measurements for which they are inappropriate. To what extent can these systems - and the workflows described in this thesis - play a role in forest inventories and mapping beneath the canopy? The findings described throughout this thesis suggest there is a clear supporting role for HMLS sensors in the context of an integrated, multi sensor approach to forest inventory and assessment.

7.9.1 Comparison of sensor suitability by forest biophysical parameter

Table 7.1 on the following page lists the key forest biophysical parameters identified and discussed throughout this research and gives each sensor a qualitative, relative ranking (from 3 to 1) in suitability for the retrieval of each parameter. A ranking of three implies the sensor is very well-specified for retrieval of a given parameter. A ranking of two suggests good, if sub-optimal, results might be expected based on research conducted and results gathered within this thesis. A ranking of one proposes that the respective sensor is *capable* of making the measurement, but with an expectation that accuracy will be lost through omission or commission.

For example, TLS instruments have repeatedly been demonstrated as optimal tools to measure true tree height (subject to the effects of occlusion). Meanwhile, the UAV imagery-based structure-from-motion has been shown to be a good technique for crown modelling, but as crowns below mean crown height are poorly reconstructed, output is sub-optimal. At the far end of the spectrum, it is potentially possible to calculate AGB using DBH and a measurement of stem taper from HMLS sensors but this is limited to trees with heights within sensor range. Furthermore, range noise manifested as systematic 'fuzzy' noise precludes an accurate estimate of DBH.

Table 7.1: Assessment of sensor suitability per forest biophysical parameter

Parameter	ALS	UAV-SfM	TLS	HMLS	Inventory
AGB	●●	●●	●●●	●	●●
Basal area			●●●	●●●	●●●
Crown area/extent	●●●	●●	●●		●
Canopy cover	●●●	●●●	●●		●
Canopy height	●●●	●	●●		●
Canopy profile	●●	●	●●		●
Crown height	●●●		●●		●
Crown radius	●●●	●●●	●●		●
Crown volume	●●●	●●	●●		●
DBH			●●●	●●●	●●●
Growing stock volume			●●●	●●	●
Leaf area index	●	●●●	●●		●●●
Stand complexity	●●		●●		●
Stem density			●●	●●●	●●
Stem location			●●●	●●	●
Stem taper			●●●	●●	●
Tree density	●	●	●●	●●●	●●
Tree height	●●	●●	●●●		●
Topography	●●	●	●●	●●●	

●●● indicates an optimal sensor platform

●● indicates 'good results some of the time'

● indicates 'inconsistent'

Absence of ● suggests the sensor is not capable of measuring this specific parameter

7.9.2 Multi-sensor forest mapping

Based on the analysis above, HMLS sensors are an optimal tool for the capture of DBH and subsequent calculation of basal area. What they lack in absolute precision (i.e. due to systematic noise/range error), they compensate for in terms of the spatial extent at which data can be acquired in a fixed time interval. Whilst TLS instruments are evidently more precise, coverage is constrained by (a) capture time, (b) density of scan set-ups and (c) effects of occlusion integral to a fixed station methodology. HMLS instruments, inherently mobile in nature, offer an almost infinite number of capture 'set-ups' and flexible survey geometry. In a similar vein, HMLS sensors can complement airborne sensors. Airborne laser scanners below densities of around 100 points $m^{2\,-1}$ cannot typically 'see' tree stems, nor indeed much in the way of tree structure between the upper crown and the forest floor. Current generation HMLS can 'see' the forest floor, tree stems and lower branches – but not tree crowns. Logically, fusion of these two datasets leads to a more holistic point cloud broadly comparable to mid-range TLS scanners (as shown in ***Chapter 6***). This suggests HMLS are perhaps the best sensor to map stem/tree density and forest floor topography – addressing a functionality gap in ALS approaches. Overall, HMLS sensors are perhaps a single tool in an ever-expanding toolbox but a tool likely to offer functionality which benefits a broad variety of 3D mapping techniques.

7.9.3 Multi-temporal forest mapping

A principle benefit of the HMLS approach to forest mapping is that efficiencies can be propagated over time. The time and costs saved using HMLS rather than TLS for a survey are multiplied each time a forest plot or stand is scanned. Given that scan trajectory overlap is not essential, unlike TLS surveys which ideally need identical scan station set-ups, repeat surveys are constrained purely by logistics (access, surveyor availability and scanner availability). A surveyor simply needs to turn-up, initialise the sensor, scan, then demobilise. In practical terms, handheld consumer GPS way pointing is sufficiently precise to give a ballpark estimate where a repeat scan should be located. If scans are conducted using the same protocol, with considerations made

for effective loop-closure to minimise IMU/SLAM drift, then multiple-epoch datasets should overlay one another without issue to decimetre levels of precision.

This ultimately means that an HMLS scan be organised and conducted with minimal lead time. This is a huge benefit in many forest mapping applications. Chief among these is likely to be in calibration-validation ("cal/val") campaigns, such as those currently in operation for the forthcoming BIOMASS P-band SAR mission. Experience gained during this research led to the awareness that TLS surveys require a lot of pre-planning, coordination and field assistance. HMLS surveys, on the other hand, can be performed by a lone worker. Where opportunistic surveys can help a broader scientific mission – e.g. if a SAR satellite is due to overpass a specific area of forest immediately after an unexpected event such as a storm – an HMLS scanner can be immediately dispatched with a forest surveyor. Data can be captured within hours – rather than weeks and months. In a related vein, repeat surveys can be tasked at a fraction of the cost – useful in tying 3D scans with SAR repeat-pass intervals. ESA Sentinel-1A and 1B have a 6-day repeat period.

8. Conclusion

8.1 Mapping forests with HMLS: strengths

The results in this research demonstrate what can be achieved with HMLS and consumer-grade positioning. Along with increasing laser range, modern positioning equipment is also subject to continued development. Handheld GNSS solutions are now available which can acquire 3D positional information to millimetric precision almost instantaneously, subject to an RTK-GPS subscription and mobile data coverage (Leica Geosystems, 2018b). Naturally, such technology enables increased precision in HMLS scan co-registration by accurately locating physical targets and prominent objects (e.g. walls, fence posts) in real-world coordinates. Physical targets could be established common to HMLS, airborne and spaceborne platforms and precisely positioned using RTK-GPS sensors and survey-grade total stations.

Like many LiDAR applications, TLS and HMLS seem to sit at different points on a spectrum from 'quick and cheap' to 'precise and expensive'. These results suggest that current-generation HMLS scanners can facilitate very good quality results. Whilst not comparable to TLS sensors, which remain the 'gold standard' in forest mapping, it is demonstrably possible to rapidly acquire useful forest metrics over a wider spatial area. Using HMLS sensors, this can be achieved with less sensor 'bias' or occlusion due to a dynamic, continually changing scan position. The pace of technological development suggests that HMLS and similar systems will integrate higher-quality lasers with extended range in the not-too-distant future, building on ground established by sensors such as Leica's *Pegasus: Backpack* (Lehtola et al., 2017) and 3D Laser Mapping (2018)'s ROBIN system, GeoSLAM's ZEB-HORIZON and Leica Geosystems' forthcoming BLK2GO among others.

There is likely to be a proliferation of research projects assessing these systems in forested areas in the forthcoming months. Calders et al. (2018) and Wilkes et al. (2018)

demonstrated rigorous, robust and repeatable workflows for the modelling of individual trees at large scale (plots of 1 Ha or greater) to inform a new generation of radiative transfer models. Whilst the precision and range of the HMLS sensors tested in this research preclude such detail, the results suggest HMLS technology remains suitable for some aspects of large-scale forest mapping for SAR calibration and validation.

8.2 Mapping forests with HMLS: weaknesses

As described in **7.4.3**, fusion of HMLS with some form of airborne dataset can mitigate limited range in current-generation HMLS sensors. However, the relevance of this approach diminishes where large temporal baselines exist between the fused data. Seasonal variation – particularly canopy defoliation – can be expected to influence forest structure as detected from airborne platforms. Therefore future research should focus on adopting extended-range sensors. With increased range, sensors will be able to detect tree components at any height. However, in addition, factors such as occlusion can be greatly reduced as much more structural information can be acquired from a given sensor position. This will lead to much greater overlap between adjacent trajectories and ensure a given tree is detected in several, rather than two-to-three, passes.

HMLS data capture within the research described was limited by a lack of real-time information on scan coverage or quality. Data were acquired blindly in the expectation that by following protocols developed for this work, quality would be optimised. At the time of writing, GeoSLAM are now marketing the ZEB-REVO RT ('real-time') which integrates a tablet computer to visualise (i) trajectory and (ii) a sparse (9% of points) point cloud as a surveyor navigates a scene (GeoSLAM, 2018). The ZEB-REVO RT is yet to be used in active research but is anticipated to mitigate most limitations identified in ***Chapter Four*** as point density and coverage can be optimised on-the-go. For the first

time, foresters using such sensors could acquire and access a complete, quality-controlled 3D dataset within hours of entering a study site.

8.3 Recommendations for future research

Recent radar missions including the first ICEYE microsatellite and the S-band NovaSAR-1 satellite (launched in January and September 2018 respectively) will require some form of ground calibration and validation data. Meanwhile the forthcoming BIOMASS P-band SAR satellite is anticipated to launch in 2021. In the case of ICEYE, simultaneous SAR and HMLS acquisition becomes possible not just weekly (as per Sentinel-1) or semi-regularly (e.g. COSMO-SkyMed) but multiple times per day (ICEYE, 2018). Future work in the field of HMLS may wish to focus on the role HMLS sensors might play in collecting high volumes of data, over wide (forest stand rather than forest plot) areas, in multi-temporal windows coincident with SAR data take opportunities.

If HMLS technology development keeps pace with TLS, it is possible mobile scanners will offer range (>100 m) and precision (<0.001 m error at distances of 10 m) equivalent to 2018-era TLS instruments. If so, HMLS sensors may prove to be ideal instruments for calibration and validation in a representative sample of Earth's forest biomass magnitude. Once range is addressed, tree height and crown structure can be resolved as rapidly as DBH and stem positions have been in the research presented here. Coupled with UAV-LiDAR, we may soon reach the point where full vertical forest structure can be mapped rapidly, efficiently and precisely.

8.4 Summary

At the time this research began (October 2014), no studies had explored use of HMLS systems in forests. Ryding et al. (2015), a proof-of-concept and the first such study, was published in January 2015. To date (July 2018), it had been cited just twenty-five

times and over the period, just fewer than ten papers on the topic of HMLS in forests (Bauwens et al., 2016; Oveland et al., 2018; Cabo et al., 2018a; 2018b) had been published. The research presented in this PhD was designed to build on the work of Ryding et al. (2015) and Bauwens et al. (2016) in applying similar methods but on a broader scale in multiple forest types. This novelty persists: none of the aforementioned papers explicitly considered different species, species compositions or forest types. Of these papers, only Cabo et al. (2018a) assessed performance of the GeoSLAM ZEB-REVO. Indeed, this research was limited to just two compartments of a single city centre park so cannot truly be considered as a benchmark study.

At the time of writing (late July 2018), the first benchmarking exercise to compare software capable of deriving forest inventory information from TLS data was published (Liang et al., 2018). This introduced several novel algorithms designed to estimate stem volume. Of these, all but one utilised both stem curvature and tree height to achieve this. Future work should therefore adopt a similar approach, this time focussing on HMLS data, to assess the applicability of both HMLS hardware and aforementioned software in estimating stem volume. Whilst the results presented in this research indicate current HMLS sensors cannot reliably estimate tree heights >12 m, there remains potential for utilising the lower portion of tree stems to forward-model whole-tree volume. This could perhaps be enhanced through the inclusion of species-specific allometric models which describe the relationship between stem curve or stem taper and tree height.

In due course, hardware developments are likely to facilitate HMLS systems (e.g. ZEB-HORIZON; BLK2GO) which offer enhanced range and cleaner data. With the continual move towards multi-core ‘big data’ processing, LiDAR segmentation and classification software will inevitably improve too. This will increase the extent of data which can be processed in a single pass, and the time required to do this. Given these, it is reasonable to predict portable and handheld LiDAR systems will soon become a dominant tool for the mapping and measurement of forests alongside high-precision TLS scanners.

9. References

3D Laser Mapping. (2018, July 17). ROBIN: Walk, Drive, Fly. Retrieved from https://www.3dlasermapping.com/wp-content/uploads/2017/12/ROBIN-DATASHEET-WEB.pdf

Adão, T., Hruška, J., Pádua, L., Bessa, J., Peres, E., Morais, R., & Sousa, J. J. (2017). Hyperspectral imaging: A review on UAV-based sensors, data processing and applications for agriculture and forestry. *Remote Sensing*, *9*(11). https://doi.org/10.3390/rs9111110

Ahmed, O. S., Franklin, S. E., Wulder, M. A., & White, J. C. (2015). Characterizing stand-level forest canopy cover and height using Landsat time series, samples of airborne LiDAR, and the Random Forest algorithm. *ISPRS Journal of Photogrammetry and Remote Sensing*, *101*(September), 89–101. https://doi.org/10.1016/j.isprsjprs.2014.11.007

Aijazi, A., Checchin, P., Malaterre, L., & Trassoudaine, L. (2017). Automatic Detection and Parameter Estimation of Trees for Forest Inventory Applications Using 3D Terrestrial LiDAR. *Remote Sensing*, *9*(9), 946. https://doi.org/10.3390/rs9090946

Ashcroft, M. B., Gollan, J. R., & Ramp, D. (2014). Creating vegetation density profiles for a diverse range of ecological habitats using terrestrial laser scanning. *Methods in Ecology and Evolution*, *5*(3), 263–272. https://doi.org/10.1111/2041-210X.12157

Asner, G. P., Brodrick, P. G., Philipson, C., Vaughn, N. R., Martin, R. E., Knapp, D. E., … Coomes, D. A. (2018). Mapped aboveground carbon stocks to advance forest conservation and recovery in Malaysian Borneo. *Biological Conservation*, *217*(June 2017), 289–310. https://doi.org/10.1016/j.biocon.2017.10.020

Asner, G. P., & Mascaro, J. (2014). Mapping tropical forest carbon: Calibrating plot estimates to a simple LiDAR metric. *Remote Sensing of Environment*, *140*, 614–624. https://doi.org/10.1016/j.rse.2013.09.023

Avitabile, V., Baccini, A., Friedl, M. A., & Schmullius, C. (2012). Capabilities and limitations of Landsat and land cover data for aboveground woody biomass estimation of Uganda. *Remote Sensing of Environment*, *117*, 366–380. https://doi.org/10.1016/j.rse.2011.10.012

Baccini, A., Goetz, S. J., Walker, W. S., Laporte, N. T., Sun, M., Sulla-Menashe, D., … Houghton, R. A. (2012). Estimated carbon dioxide emissions from tropical deforestation improved by carbon-density maps. *Nature Climate Change*, *2*(3), 182–185. https://doi.org/10.1038/nclimate1354

Balzter, H. (2001). Forest mapping and monitoring with interferometric synthetic aperture radar (InSAR). *Progress in Physical Geography*, *25*(2), 159–177. https://doi.org/10.1191/030913301666986397

Balzter, H., Cox, R., Rowland, C., & Saich, P. (2003). Forest canopy height mapping from dual-wavelength SAR interferometry. In *Applications of SAR Polarimetry and Polarimetric Interferometry* (Vol. 529).

Bauwens, S., Bartholomeus, H., Calders, K., & Lejeune, P. (2016). Forest inventory with terrestrial LiDAR: a comparison of static and hand-held mobile laser scanning. *Forests*, *7*(6), 127.

Bauwens, S., Fayolle, A., Gourlet-Fleury, S., Ndjele, L. M., Mengal, C., & Lejeune, P. (2017). Terrestrial photogrammetry: a non-destructive method for modelling irregularly shaped tropical tree trunks. *Methods in Ecology and Evolution*, *8*(4), 460–471. https://doi.org/10.1111/2041-210X.12670

Bienert, A., Scheller, S., Keane, E., Mullooly, G., & Mohan, F. (2006). Application of Terrestrial Laser Scanners for The Determination of Forest Inventory Parameters. *International Archives of Photogrammetry , Remote Sensing and Spatial Information Science*, *36*, 5. https://doi.org/10.1111/jam.12647

Bienert, A., Georgi, L., Kunz, M., Maas, H.-G., & von Oheimb, G. (2018). Comparison and Combination of Mobile and Terrestrial Laser Scanning for Natural Forest Inventories. *Forests*, *9*(7), 395. https://doi.org/10.3390/f9070395

Blakey, R. V., Law, B. S., Kingsford, R. T., & Stoklosa, J. (2017). Terrestrial laser scanning reveals below-canopy bat trait relationships with forest structure. *Remote Sensing of Environment*, *198*, 40–51. https://doi.org/10.1016/j.rse.2017.05.038

Bolton, D. K., Coops, N. C., & Wulder, M. A. (2013). Measuring forest structure along productivity gradients in the Canadian boreal with small-footprint Lidar. *Environmental Monitoring and Assessment*, *185*(8), 6617–6634. https://doi.org/10.1007/s10661-012-3051-9

Bosse, M., Zlot, R., & Flick, P. (2012). Zebedee: Design of a spring-mounted 3-D range sensor with application to mobile mapping. *IEEE Transactions on Robotics*, *28*(5), 1104–1119. https://doi.org/10.1109/TRO.2012.2200990

Bouvet, A., Le Toan, T., & Mermoz, S. (2010). An above-ground biomass map of African savannas at a resolution of 100 meters using ALOS PALSAR data, (1).

Bouvet, A., Mermoz, S., Ballère, M., Koleck, T., & Le Toan, T. (2018). Use of the SAR shadowing effect for deforestation detection with Sentinel-1 time series. *Remote Sensing*, *10*(8), 1–19. https://doi.org/10.3390/rs10081250

Brandtberg, T. (2007). Classifying individual tree species under leaf-off and leaf-on conditions using airborne lidar. *ISPRS Journal of Photogrammetry and Remote Sensing*, *61*(5), 325–340. https://doi.org/10.1016/j.isprsjprs.2006.10.006

Brede, B., Lau, A., Bartholomeus, H. M., & Kooistra, L. (2017). Comparing RIEGL RiCOPTER UAV LiDAR derived canopy height and DBH with terrestrial LiDAR. *Sensors (Switzerland)*, *17*(10), 1–16. https://doi.org/10.3390/s17102371

Breiman, L. (2001). Random forests. *Machine Learning*, *45*(1), 5–32. https://doi.org/10.1023/A:1010933404324

Brolly, G., Király, G., & Czimber, K. (2013). Mapping forest regeneration from terrestrial laser scans. *Acta Silvatica et Lignaria Hungarica*, *9*(1), 135–146. https://doi.org/10.2478/aslh-2013-0011

Brown, S., Gillespie, A. J. R., & Lugo, A. E. (1989). Biomass estimation methods for tropical forests with applications to forest inventory data. *Forest Science*. Retrieved from http://www.ingentaconnect.com/content/saf/fs/1989/00000035/00000004/art00003

Cabo, C., Del Pozo, S., Rodríguez-Gonzálvez, P., Ordóñez, C., & González-Aguilera, D. (2018a). Comparing terrestrial laser scanning (TLS) and wearable laser scanning (WLS) for individual tree modeling at plot level. *Remote Sensing*, *10*(4). https://doi.org/10.3390/rs10040540

Cabo, C., Ordóñez, C., López-Sánchez, C. A., & Armesto, J. (2018b). Automatic dendrometry: Tree detection, tree height and diameter estimation using terrestrial laser scanning. *International Journal of Applied Earth Observation and Geoinformation*, *69*(November 2017), 164–174. https://doi.org/10.1016/j.jag.2018.01.011

Cai, S., Zhang, W., Qi, J., Wan, P., Shao, J., & Shen, A. (2018). Applicability analysis of cloth simulation filtering algorithm for mobile LiDAR point cloud. *International Archives of the Photogrammetry, Remote Sensing and Spatial Information Sciences - ISPRS Archives*, *42*(3), 107–111. https://doi.org/10.5194/isprs-archives-XLII-3-107-2018

Calders, K., Burt, A., Origo, N., Disney, M., Nightingale, J., Raumonen, P., & Lewis, P. (2016). Large-area virtual forests from terrestrial laser scanning data. *International Geoscience and Remote Sensing Symposium (IGARSS)*, *2016–Novem* (July), 1765–1767. https://doi.org/10.1109/IGARSS.2016.7729452

Calders, K., Armston, J., Newnham, G., Herold, M., & Goodwin, N. (2014). Implications of sensor configuration and topography on vertical plant profiles derived from terrestrial LiDAR. *Agricultural and Forest Meteorology*, *194*, 104–117. https://doi.org/10.1016/j.agrformet.2014.03.022

Calders, K., Disney, M. I., Armston, J., Burt, A., Brede, B., Origo, N., … Nightingale, J. (2017). Evaluation of the range accuracy and the radiometric calibration of multiple terrestrial laser scanning instruments for data interoperability. *IEEE Transactions on Geoscience and Remote Sensing*, *55*(5), 2716–2724. https://doi.org/10.1109/TGRS.2017.2652721

Calders, K., Newnham, G. J., Armston, J. D., Disney, M. I., Schaaf, C. B., & Paynter, I. (2015). Terrestrial LIDAR for forest monitoring. *A Sourcebook of Methods and Procedures for Monitoring and Reporting Anthropogenic Greenhouse Gas Emissions and Removals Associated with Deforestation, Gains and Losses of Carbon Stocks in Forests Remaining Forests, and Forestation*, (NOVEMBER).

Calders, K., Newnham, G., Burt, A., Murphy, S., Raumonen, P., Herold, M., … Kaasalainen, M. (2015). Nondestructive estimates of above-ground biomass using terrestrial laser scanning. *Methods in Ecology and Evolution*, *6*(2), 198–208. https://doi.org/10.1111/2041-210X.12301

Calders, K., Origo, N., Burt, A., Disney, M., Nightingale, J., Raumonen, P., … Lewis, P. (2018). Realistic forest stand reconstruction from terrestrial LiDAR for radiative transfer modelling. *Remote Sensing*, *10*(6), 1–15. https://doi.org/10.3390/rs10060933

Campos, M. B., Tommaselli, A. M. G., Honkavaara, E., Prol, F. dos S., Kaartinen, H., El Issaoui, A., & Hakala, T. (2018). A backpack-mounted omnidirectional camera with off-the-shelf navigation sensors for mobile terrestrial mapping: Development and forest application. *Sensors (Switzerland)*, *18*(3), 1–18. https://doi.org/10.3390/s18030827

Cao, L., Coops, N. C., Hermosilla, T., Innes, J., Dai, J., & She, G. (2014). Using small-footprint discrete and full-waveform airborne LiDAR metrics to estimate total biomass and biomass components in subtropical forests. *Remote Sensing*, *6*(8), 7110–7135. https://doi.org/10.3390/rs6087110

Carbomap. (2017, July 10). The F-Lux UAS Brings Lidar Forest Mapping to Developing Nations. Retrieved from https://www.spar3d.com/news/lidar/carbomap-f-lux-uas-brings-lidar-forest-mapping-to-developing-nations/

Cartus, O., Kellndorfer, J., Rombach, M., & Walker, W. (2012). Mapping canopy height and growing stock volume using airborne lidar, alos palsar and landsat ETM+. *Remote Sensing*, *4*(11), 3320–3345. https://doi.org/10.3390/rs4113320

Cartus, O., Kellndorfer, J., Walker, W., Franco, C., Bishop, J., Santos, L., & Fuentes, J. M. M. (2014). A national, detailed map of forest aboveground carbon stocks in Mexico. *Remote Sensing*, *6*(6), 5559–5588. https://doi.org/10.3390/rs6065559

Carvalhais, N., Forkel, M., Khomik, M., Bellarby, J., Jung, M., Migliavacca, M., … Reichstein, M. (2014). Global covariation of carbon turnover times with climate in terrestrial ecosystems. *Nature*, *514*(7521), 213–217. https://doi.org/10.1038/nature13731

Chave, J., Andalo, C., Brown, S., Cairns, M. A., Chambers, J. Q., Eamus, D., … Yamakura, T. (2005). Tree allometry and improved estimation of carbon stocks and balance in tropical forests. *Oecologia*, *145*(1), 87–99. https://doi.org/10.1007/s00442-005-0100-x

Chave, J., Condit, R., Aguilar, S., Hernandez, A., Lao, S., & Perez, R. (2004). Error propagation and scaling for tropical forest biomass estimates. *Philosophical Transactions of the Royal Society B: Biological Sciences*, *359*(1443), 409–420. https://doi.org/10.1098/rstb.2003.1425

Chave, J., Muller-landau, H. C., Baker, T. R., Easdale, T. a, & Webb, C. O. (2014). Regional and Phylogenetic Variation of Wood Density across 2456 Neotropical Tree Species REGIONAL AND PHYLOGENETIC VARIATION OF WOOD DENSITY ACROSS 2456 NEOTROPICAL TREE SPECIES, *16*(6), 2356–2367.

Chave, J., Réjou-Méchain, M., Búrquez, A., Chidumayo, E., Colgan, M. S., Delitti, W. B. C., … Vieilledent, G. (2014). Improved allometric models to estimate the aboveground biomass of tropical trees. *Global Change Biology*, *20*(10), 3177–3190. https://doi.org/10.1111/gcb.12629

Chen, Q., Vaglio Laurin, G., & Valentini, R. (2015). Uncertainty of remotely sensed aboveground biomass over an African tropical forest: Propagating errors from trees to

plots to pixels. *Remote Sensing of Environment*, *160*, 134–143. https://doi.org/10.1016/j.rse.2015.01.009

Chowdhury, T. A., Thiel, C., & Schmullius, C. (2014). Growing stock volume estimation from L-band ALOS PALSAR polarimetric coherence in Siberian forest. *Remote Sensing of Environment*, *155*, 129–144. https://doi.org/10.1016/j.rse.2014.05.007

Clark, D. B., & Kellner, J. R. (2012). Tropical forest biomass estimation and the fallacy of misplaced concreteness. *Journal of Vegetation Science*, *23*(6), 1191–1196. https://doi.org/10.1111/j.1654-1103.2012.01471.x

CloudCompare (version 2.9.1) [GPL software]. (2018). Retrieved from http://www.cloudcompare.org/

Coomes, D. A., Dalponte, M., Jucker, T., Asner, G. P., Banin, L. F., Burslem, D. F. R. P., … Qie, L. (2017). Area-based vs tree-centric approaches to mapping forest carbon in Southeast Asian forests from airborne laser scanning data. *Remote Sensing of Environment*, *194*, 77–88. https://doi.org/10.1016/j.rse.2017.03.017

Dalponte, M., Ørka, H. O., Ene, L. T., Gobakken, T., & Næsset, E. (2014). Tree crown delineation and tree species classification in boreal forests using hyperspectral and ALS data. *Remote Sensing of Environment*, *140*, 306–317. https://doi.org/10.1016/j.rse.2013.09.006

Danson, A., Mark Danson, F., Hetherington, D., Morsdorf, F., Koetz, B., & Allgöwer, B. (2007). Forest canopy gap fraction from terrestrial laser scanning. *IEEE Geoscience and Remote Sensing Letter*s, 4(1). https://doi.org/10.1109/LGRS.2006.887064

Danson, F. M., Sasse, F., & Schofield, L. A. (2018). Spectral and spatial information from a novel dual-wavelength full-waveform terrestrial laser scanner data for forest ecology. *Interface Focus*.

Dassot, M., Colin, A., Santenoise, P., Fournier, M., & Constant, T. (2012). Terrestrial laser scanning for measuring the solid wood volume, including branches, of adult

standing trees in the forest environment. *Computers and Electronics in Agriculture*, *89*, 86–93. https://doi.org/10.1016/j.compag.2012.08.005

de Sassi, C., Joseph, S., Bos, A. B., Duchelle, A. E., Ravikumar, A., & Herold, M. (2015). Towards integrated monitoring of REDD+. *Current Opinion in Environmental Sustainability*, *14*, 93–100. https://doi.org/10.1016/j.cosust.2015.04.003

Deng, S., Katoh, M., Guan, Q., Yin, N., & Li, M. (2014). Estimating forest aboveground biomass by combining ALOS PALSAR and WorldView-2 data: A case study at Purple Mountain National Park, Nanjing, China. *Remote Sensing*, *6*(9), 7878–7910. https://doi.org/10.3390/rs6097878

Díaz-Vilariño, L., Verbree, E., Zlatanova, S., & Diakité, A. (2017). Indoor modelling from SLAM-based laser scanner: Door detection to envelope reconstruction. *International Archives of the Photogrammetry, Remote Sensing and Spatial Information Sciences - ISPRS Archives*, *42*(2W7), 345–352. https://doi.org/10.5194/isprs-archives-XLII-2-W7-345-2017

Disney, M. I., Kalogirou, V., Lewis, P., Prieto-Blanco, A., Hancock, S., & Pfeifer, M. (2010). Simulating the impact of discrete-return lidar system and survey characteristics over young conifer and broadleaf forests. *Remote Sensing of Environment*, *114*(7), 1546–1560. https://doi.org/10.1016/j.rse.2010.02.009

Disney, M., Lewis, P., & Saich, P. (2006). 3D modelling of forest canopy structure for remote sensing simulations in the optical and microwave domains. *Remote Sensing of Environment*, *100*(1), 114–132. https://doi.org/10.1016/j.rse.2005.10.003

Dobson, M. C. (n.d.). Preliminary Analysis of ERS-1 SAR for Forest Ecosystem Studies.

Donoghue, D. N. M., Watt, P. J., Cox, N. J., & Wilson, J. (2007). Remote sensing of species mixtures in conifer plantations using LiDAR height and intensity data. *Remote Sensing of Environment*, *110*(4), 509–522. https://doi.org/10.1016/j.rse.2007.02.032

Eichhorn, M. P., Ryding, J., Smith, M. J., Gill, R. M. A., Siriwardena, G. M., & Fuller, R. J. (2017). Effects of deer on woodland structure revealed through terrestrial laser

scanning. *Journal of Applied Ecology*, *54*(6), 1615–1626. https://doi.org/10.1111/1365-2664.12902

Eloy, C. (2011). Leonardo's rule, self-similarity, and wind-induced stresses in trees. Physical Review Letters, 107(25), 258101.

Ene, L. T., Næsset, E., Gobakken, T., Gregoire, T. G., Ståhl, G., & Nelson, R. (2012). Assessing the accuracy of regional LiDAR-based biomass estimation using a simulation approach. *Remote Sensing of Environment*, *123*, 579–592. https://doi.org/10.1016/j.rse.2012.04.017

Englhart, S., Keuck, V., & Siegert, F. (2011). Aboveground biomass retrieval in tropical forests - The potential of combined X- and L-band SAR data use. *Remote Sensing of Environment*, *115*(5), 1260–1271. https://doi.org/10.1016/j.rse.2011.01.008

Englhart, S., Keuck, V., & Siegert, F. (2012). Modeling aboveground biomass in tropical forests using multi-frequency SAR data-A comparison of methods. *IEEE Journal of Selected Topics in Applied Earth Observations and Remote Sensing*, *5*(1), 298–306. https://doi.org/10.1109/JSTARS.2011.2176720

Englund, O., Sparovek, G., Berndes, G., Freitas, F., Ometto, J. P., Oliveira, P. V. D. C. E., … Lapola, D. (2017). A new high-resolution nationwide aboveground carbon map for Brazil. *Geo: Geography and Environment*, *4*(2), 1–12. https://doi.org/10.1002/geo2.45

Environment Agency (2018a). Survey Open Data portal. https://environment.data.gov.uk/ds/survey/#/survey. Accessed: 01/09/2018.

Environment Agency. (2018b). Environment Agency LIDAR data: Technical Note (March 2016, v5). Retrieved from https://www.geostore.com/environment-agency/docs/Environment_Agency_LIDAR_Open_Data_FAQ_v5.pdf

ESA SNAP (version 5.00) [GPL software]. (2018). Retrieved from http://step.esa.int/main/download/previous-versions/

FAO. (2000). Global Forest Resources Assessment 200. Retrieved from http://www.fao.org/docrep/004/y1997e/y1997e00.htm

Fayad, I., Baghdadi, N., Bailly, J.-S., Barbier, N., Gond, V., Hajj, M., … Bourgine, B. (2014). Canopy Height Estimation in French Guiana with LiDAR ICESat/GLAS Data Using Principal Component Analysis and Random Forest Regressions. *Remote Sensing*, *6*(12), 11883–11914. https://doi.org/10.3390/rs61211883

Feliciano, E. A., Wdowinski, S., & Potts, M. D. (2014). Assessing Mangrove Above-Ground Biomass and Structure using Terrestrial Laser Scanning: A Case Study in the Everglades National Park. *Wetlands*, *34*(5), 955–968. https://doi.org/10.1007/s13157-014-0558-6

Ferraz, A., Saatchi, S., Mallet, C., Jacquemoud, S., Gonï¿½alves, G., Silva, C. A., … Pereira, L. (2016). Airborne lidar estimation of aboveground forest biomass in the absence of field inventory. *Remote Sensing*, *8*(8), 1–18. https://doi.org/10.3390/rs8080653

Ferraz, A., Bretar, F., Jacquemoud, S., Gonçalves, G., Pereira, L., Tomé, M., & Soares, P. (2012). 3-D mapping of a multi-layered Mediterranean forest using ALS data. *Remote Sensing of Environment*, *121*, 210–223. https://doi.org/10.1016/j.rse.2012.01.020

Forestry Commission. (2018, June 7). National Forest Inventory Woodland England. Retrieved from http://data-forestry.opendata.arcgis.com/datasets/national-forest-inventory-woodland-england

Forest Research. (2018, September 25). Woodland statistics. Retrieved from https://www.forestresearch.gov.uk/tools-and-resources/statistics/statistics-by-topic/woodland-statistics/

Forsman, M., Börlin, N., Olofsson, K., Reese, H., & Holmgren, J. (2018). Bias of cylinder diameter estimation from ground-based laser scanners with different beam widths: A simulation study. *ISPRS Journal of Photogrammetry and Remote Sensing*, *135*, 84–92. https://doi.org/10.1016/j.isprsjprs.2017.11.013

Forsman, M., Holmgren, J., & Olofsson, K. (2016). Tree stem diameter estimation from mobile laser scanning using line-wise intensity-based clustering. *Forests*, *7*(9). https://doi.org/10.3390/f7090206

García, M., Gajardo, J., Riaño, D., Zhao, K., Martín, P., & Ustin, S. (2015). Canopy clumping appraisal using terrestrial and airborne laser scanning. *Remote Sensing of Environment*, *161*, 78–88. https://doi.org/10.1016/j.rse.2015.01.030

García, M., Saatchi, S., Casas, A., Koltunov, A., Ustin, S., Ramirez, C., & Balzter, H. (2017). Extrapolating Forest Canopy Fuel Properties in the California Rim Fire by Combining Airborne LiDAR and Landsat OLI Data. *Remote Sensing*, *9*(4), 394. https://doi.org/10.3390/rs9040394

García, M., Saatchi, S., Ustin, S., & Balzter, H. (2018). Modelling forest canopy height by integrating airborne LiDAR samples with satellite Radar and multispectral imagery. *International Journal of Applied Earth Observation and Geoinformation*, *66*(November 2017), 159–173. https://doi.org/10.1016/j.jag.2017.11.017

GeoSLAM. (2018, September 22). ZEB-REVO User Manual v3.0.0. Retrieved from https://geoslam.com/wp-content/uploads/2018/02/ZEB-REVO-User-Guide-V3.0.0.pdf?x97867

Google. (2018). Google Earth Pro (v 7.3.2.5491). Retrieved from https://www.google.com/earth/download/gep/agree.html

Gorelick, N., Hancher, M., Dixon, M., Ilyushchenko, S., Thau, D., & Moore, R. (2017). Google Earth Engine: Planetary-scale geospatial analysis for everyone. *Remote Sensing of Environment, 202*, 18-27.

Görgens, E. B., Packalen, P., da Silva, A. G. P., Alvares, C. A., Campoe, O. C., Stape, J. L., & Rodriguez, L. C. E. (2015). Stand volume models based on stable metrics as from multiple ALS acquisitions in Eucalyptus plantations. *Annals of Forest Science*, *72*(4), 489–498. https://doi.org/10.1007/s13595-015-0457-x

Graham, A., Coops, N., Wilcox, M., & Plowright, A. (2019). Evaluation of ground surface models derived from unmanned aerial systems with digital aerial photogrammetry in a disturbed conifer forest. Remote Sensing, 11(1), 84.

Grainger, A. (2010). Uncertainty in the construction of global knowledge of tropical forests. *Progress in Physical Geography*, *34*(6), 811–844. https://doi.org/10.1177/0309133310387326

Haahr, M. (2018, September 26). RANDOM.ORG: True Random Number Service. Retrieved from https://www.random.org

Hackenberg, J., Spiecker, H., Calders, K., Disney, M., & Raumonen, P. (2015). SimpleTree - An efficient open source tool to build tree models from TLS clouds. *Forests*, *6*(11), 4245–4294. https://doi.org/10.3390/f6114245

Hackenberg, J., Wassenberg, M., Spiecker, H., & Sun, D. (2015). Non-destructive method for biomass prediction combining TLS derived tree volume and wood density. *Forests*, *6*(4), 1274–1300. https://doi.org/10.3390/f6041274

Hall, F. G., Bergen, K., Blair, J. B., Dubayah, R., Houghton, R., Hurtt, G., … Wickland, D. (2011). Characterizing 3D vegetation structure from space: Mission requirements. *Remote Sensing of Environment*, *115*(11), 2753–2775. https://doi.org/10.1016/j.rse.2011.01.024

Hansen, A. J., Phillips, L. B., Dubayah, R., Goetz, S., & Hofton, M. (2014). Regional-scale application of lidar: Variation in forest canopy structure across the southeastern US. *Forest Ecology and Management*, *329*, 214–226. https://doi.org/10.1016/j.foreco.2014.06.009

Hansen, E. H., Gobakken, T., Bollandsås, O. M., Zahabu, E., & Næsset, E. (2015). Modeling aboveground biomass in dense tropical submontane rainforest using airborne laser scanner data. *Remote Sensing*, *7*(1), 788–807. https://doi.org/10.3390/rs70100788

Hansen, M. C., Potapov, P. V., Moore, R., Hancher, M., Turubanova, S. A., Tyukavina, A., … Townshend, J. R. G. (2013). High-resolution global maps of 21st-century forest cover change. *Science*, *342*(6160), 850–853. https://doi.org/10.1126/science.1244693

Harris, N. L., Brown, S., Hagen, S. C., Saatchi, S. S., Petrova, S., Salas, W., … Lotsch, A. (2012). Baseline Map of Carbon Emissions from Deforestation in Tropical Regions, *2005*(June), 1573–1576.

Heinzel, J., & Koch, B. (2011). Exploring full-waveform LiDAR parameters for tree species classification. *International Journal of Applied Earth Observation and Geoinformation*, *13*(1), 152–160. https://doi.org/10.1016/j.jag.2010.09.010

Herold, M., Román-Cuesta, R. M., Mollicone, D., Hirata, Y., Van Laake, P., Asner, G. P., … MacDicken, K. (2011). Options for monitoring and estimating historical carbon emissions from forest degradation in the context of REDD+. *Carbon Balance and Management*, *6*(1), 13. https://doi.org/10.1186/1750-0680-6-13

Hess, C., Bienert, A., Härdtle, W., & Von Oheimb, G. (2015). Does tree architectural complexity influence the accuracy of wood volume estimates of single young trees by terrestrial laser scanning? *Forests*, *6*(11), 3847–3867. https://doi.org/10.3390/f6113847

Holdridge, L. R. (1967). Life zone ecology. *Life zone ecology.*, (rev. ed.)).

Hopkinson, C., Chasmer, L., Young-Pow, C., & Treitz, P. (2004). Assessing forest metrics with a ground-based scanning lidar. *Canadian Journal of Forest Research*, *34*(3), 573–583. https://doi.org/10.1139/x03-225

Hosoi, F., & Omasa, K. (2006). Voxel-Based 3-D Modeling of Individual Trees for Estimating Leaf Area Density Using. *Ieee Transactions on Geoscience and Remote Sensing*, *44*(12), 3610–3618. https://doi.org/Doi 10.1109/Tgrs.2006.881743

Huerta-García, R. E., Ramírez-Serrat, N. L., Yépez-Rincón, F. D., & Lozano-García, D. F. (2018). Precision of remote sensors to estimate aerial biomass parameters: portable

LIDAR and optical sensors. *Revista Chapingo Serie Ciencias Forestales y Del Ambiente*, *24*(2), 219–235. https://doi.org/10.5154/r.rchscfa.2017.09.059

Hyyppä, J., Virtanen, J. P., Jaakkola, A., Yu, X., Hyyppä, H., & Liang, X. (2017). Feasibility of Google Tango and kinect for crowdsourcing forestry information. *Forests*, *9*(1), 1–14. https://doi.org/10.3390/f9010006

ICEYE. (2018, Jan 12). ICEYE Successfully Launches World's First SAR Microsatellite and Establishes Finland's First Commercial Satellite Operations. Retrieved from https://www.iceye.com/press/press-releases/iceye-successfully-launches-worlds-first-sar-microsatellite-and-establishes-finlands-first-commercial-satellite

Ioki, K., Tsuyuki, S., Hirata, Y., Phua, M. H., Wong, W. V. C., Ling, Z. Y., … Takao, G. (2014). Estimating above-ground biomass of tropical rainforest of different degradation levels in Northern Borneo using airborne LiDAR. *Forest Ecology and Management*, *328*, 335–341. https://doi.org/10.1016/j.foreco.2014.06.003

Kaasalainen, S., Holopainen, M., Karjalainen, M., Vastaranta, M., Kankare, V., Karila, K., & Osmanoglu, B. (2015). Combining lidar and synthetic aperture radar data to estimate forest biomass: Status and prospects. *Forests*, *6*(1), 252–270. https://doi.org/10.3390/f6010252

Kazhdan, M., & Hoppe, H. (2013). Screened Poisson surface reconstruction. ACM Transactions on Graphics (ToG), 32(3), 29.

Kellndorfer, J. M., Pierce, L. E., Dobson, M. C., & Ulaby, F. T. (1998). Toward consistent regional-to-global-scale vegetation characterization using orbital SAR systems. IEEE Transactions on Geoscience and Remote Sensing, 36(5), 1396-1411.

Kellndorfer, J. M., Walker, W. S., LaPoint, E., Kirsch, K., Bishop, J., & Fiske, G. (2010). Statistical fusion of lidar, InSAR, and optical remote sensing data for forest stand height characterization: A regional-scale method based on LVIS, SRTM, Landsat ETM+, and ancillary data sets. *Journal of Geophysical Research: Biogeosciences*, *115*(G2), n/a-n/a. https://doi.org/10.1029/2009JG000997

Kellndorfer, J., Cartus, O., Bishop, J., Walker, W., & Holecz, F. (2014). Large Scale Mapping of Forests and Land Cover with Synthetic Aperture Radar Data. *Land Applications of Radar Remote Sensing*. https://doi.org/10.5772/58220

Koreň, M. (n.d.). DendroCloud.

Koreň, M., Mokroš, M., & Bucha, T. (2017). Accuracy of tree diameter estimation from terrestrial laser scanning by circle-fitting methods. *International Journal of Applied Earth Observation and Geoinformation*, *63*(July), 122–128. https://doi.org/10.1016/j.jag.2017.07.015

Krůček, M., Trochta, J., & Král, K. (2016). 3D Forest User Guide, 38.

Khorrami, R., Naeimi, Z., Tabari, M., & Eslahchi, M. R. (2018). A new method for detecting individual trees in aerial LiDAR point clouds using absolute height maxima. Environmental monitoring and assessment, 190(12), 708.

Kukko, A., Kaijaluoto, R., Kaartinen, H., Lehtola, V. V., Jaakkola, A., & Hyyppä, J. (2017). Graph SLAM correction for single scanner MLS forest data under boreal forest canopy. *ISPRS Journal of Photogrammetry and Remote Sensing*, *132*, 199–209. https://doi.org/10.1016/j.isprsjprs.2017.09.006

Kunz, M., Hess, C., Raumonen, P., Bienert, A., Hackenberg, J., Maas, H. G., … Von Oheimb, G. (2017). Comparison of wood volume estimates of young trees from terrestrial laser scan data. *IForest*, *10*(2), 451–458. https://doi.org/10.3832/ifor2151-010

Latifi, H., Fassnacht, F. E., Hartig, F., Berger, C., Hernández, J., Corvalán, P., & Koch, B. (2015). Stratified aboveground forest biomass estimation by remote sensing data. *International Journal of Applied Earth Observation and Geoinformation*, *38*, 229–241. https://doi.org/10.1016/j.jag.2015.01.016

Le Toan, T., Beaudoin, A., Riom, J., & Guyon, D. (1992). Relating forest biomass to SAR data. *IEEE Transactions on Geoscience and Remote Sensing*, *30*(2), 403-411.

Le Toan, T., Quegan, S., Davidson, M. W. J., Balzter, H., Paillou, P., Papathanassiou, K., … Ulander, L. (2011). The BIOMASS mission: Mapping global forest biomass to better understand the terrestrial carbon cycle. *Remote Sensing of Environment*, *115*(11), 2850–2860. https://doi.org/10.1016/j.rse.2011.03.020

Leica Geosystems AG. (2014, November 29). Leica ScanStation P20: Industry's Best Performing Ultra-High Speed Scanner. Retrieved from https://w3.leica-geosystems.com/downloads123/hds/hds/scanstation_p20/brochures-datasheet/leica_scanstation_p20_dat_en.pdf

Leica Geosystems. (2017a, December 05). The Leica BLK360. Retrieved from https://lasers.leica-geosystems.com/uk/blk360

Leica Geosystems. (2017b, December 05). Leica Pegasus:Backpack Wearable Mobile Mapping Solution. Retrieved from https://leica-geosystems.com/en-GB/products/mobile-sensor-platforms/capture-platforms/leica-pegasus-backpack

Leica Geosystems. (2018, September 16). Leica RTC360 3D Laser Scanner. Retrieved from https://leica-geosystems.com/en-GB/products/laser-scanners/scanners/leica-rtc360

Leica HDS. (2017, December 05). Leica Cyclone 3D Point Cloud Processing Software. Retrieved from https://hds.leica-geosystems.com/en/Leica-Cyclone_6515.htm

Lehtola, V. V., Kaartinen, H., Nüchter, A., Kaijaluoto, R., Kukko, A., Litkey, P., … Hyyppä, J. (2017). Comparison of the selected state-of-the-art 3D indoor scanning and point cloud generation methods. *Remote Sensing*, *9*(8), 1–26. https://doi.org/10.3390/rs9080796

Liang, X., Hyyppä, J., Kaartinen, H., Lehtomäki, M., Pyörälä, J., Pfeifer, N., … Wang, Y. (2018). International benchmarking of terrestrial laser scanning approaches for forest inventories. *ISPRS Journal of Photogrammetry and Remote Sensing*, *144*(December 2017), 137–179. https://doi.org/10.1016/j.isprsjprs.2018.06.021

Liang, X., Jaakkola, A., Wang, Y., Hyyppä, J., Honkavaara, E., Liu, J., & Kaartinen, H. (2014). The use of a hand-held camera for individual tree 3D mapping in forest sample plots. *Remote Sensing*, *6*(7), 6587–6603. https://doi.org/10.3390/rs6076587

Liu, C., Xing, Y., Duanmu, J., & Tian, X. (2018). Evaluating different methods for estimating diameter at breast height from terrestrial laser scanning. *Remote Sensing*, *10*(4), 1–20. https://doi.org/10.3390/rs10040513

Lu, X., Guo, Q., Li, W., & Flanagan, J. (2014). A bottom-up approach to segment individual deciduous trees using leaf-off lidar point cloud data. *ISPRS Journal of Photogrammetry and Remote Sensing*, *94*, 1–12. https://doi.org/10.1016/j.isprsjprs.2014.03.014

Lucas, R., Lee, A., & Williams, M. (2005). The role of LiDAR data in understanding the relation between forest structure and SAR imagery. *International Geoscience and Remote Sensing Symposium (IGARSS)*, *3*(C), 2101–2104. https://doi.org/10.1109/IGARSS.2005.1526431

Mascaro, J., Asner, G. P., Davies, S., Dehgan, A., & Saatchi, S. (2014a). These are the days of lasers in the jungle. *Carbon Balance and Management*, *9*(1), 1–3. https://doi.org/10.1186/s13021-014-0007-0

Mascaro, J., Asner, G. P., Knapp, D. E., Kennedy-Bowdoin, T., Martin, R. E., Anderson, C., … Chadwick, K. D. (2014b). A tale of two “Forests”: Random Forest machine learning aids tropical Forest carbon mapping. *PLoS ONE*, *9*(1), 12–16. https://doi.org/10.1371/journal.pone.0085993

Mermoz, S., Réjou-Méchain, M., Villard, L., Le Toan, T., Rossi, V., & Gourlet-Fleury, S. (2015). Decrease of L-band SAR backscatter with biomass of dense forests. *Remote Sensing of Environment*, *159*, 307–317. https://doi.org/10.1016/j.rse.2014.12.019

Mitchard, E. T. A. (2018). The tropical forest carbon cycle and climate change. *Nature*, *559*(7715), 527–534. https://doi.org/10.1038/s41586-018-0300-2

Mitchard, E. T. A., Feldpausch, T. R., Brienen, R. J. W., Lopez-Gonzalez, G., Monteagudo, A., Baker, T. R., … Phillips, O. L. (2014). Markedly divergent estimates of Amazon forest carbon density from ground plots and satellites. *Global Ecology and Biogeography*, *23*(8), 935–946. https://doi.org/10.1111/geb.12168

Mitchell, A. L., Tapley, I., Milne, A. K., Williams, M. L., Zhou, Z. S., Lehmann, E., … Held, A. (2014). C- and L-band SAR interoperability: Filling the gaps in continuous forest cover mapping in Tasmania. *Remote Sensing of Environment*, *155*, 58–68. https://doi.org/10.1016/j.rse.2014.02.020

Morsdorf, F., Kötz, B., Meier, E., Itten, K. I., & Allgöwer, B. (2006). Estimation of LAI and fractional cover from small footprint airborne laser scanning data based on gap fraction. *Remote Sensing of Environment*, *104*(1), 50–61. https://doi.org/10.1016/j.rse.2006.04.019

Muir, J., Phinn, S., Eyre, T., & Scarth, P. (2018). Measuring plot scale woodland structure using terrestrial laser scanning. *Remote Sensing in Ecology and Conservation*. https://doi.org/10.1002/rse2.82

Ni, W., Zhang, Z., Sun, G., Guo, Z., & He, Y. (2014). The penetration depth derived from the synthesis of ALOS/PALSAR InSAR data and ASTER GDEM for the mapping of forest biomass. *Remote Sensing*, *6*(8), 7303–7319. https://doi.org/10.3390/rs6087303

Ningthoujam, R. K., Balzter, H., Tansey, K., Feldpausch, T. R., Mitchard, E. T. A., Wani, A. A., & Joshi, P. K. (2017). Relationships of S-band radar backscatter and forest aboveground biomass in different forest types. *Remote Sensing*, *9*(11), 1–17. https://doi.org/10.3390/rs9111116

Ningthoujam, R. K., Balzter, H., Tansey, K., Morrison, K., Johnson, S. C. M., Gerard, F., … Bermejo, J. P. (2016). Airborne S-band SAR for forest biophysical retrieval in temperate mixed forests of the UK. *Remote Sensing*, *8*(7), 1–22. https://doi.org/10.3390/rs8070609

Ningthoujam, R. K., Joshi, P. K., & Roy, P. S. (2018). Retrieval of forest biomass for tropical deciduous mixed forest using ALOS PALSAR mosaic imagery and field plot data. *International Journal of Applied Earth Observation and Geoinformation*, *69*(April), 206–216. https://doi.org/10.1016/j.jag.2018.03.007

Ningthoujam, R. K., Tansey, K., Balzter, H., Morrison, K., Johnson, S. C. M., Gerard, F., … Blythe, T. (2016). Mapping forest cover and forest cover change with airborne S-band radar. *Remote Sensing*, *8*(7). https://doi.org/10.3390/rs8070577

Nocerino, E., Menna, F., Remondino, F., Toschi, I., & Rodríguez-Gonzálvez, P. (2017). Investigation of indoor and outdoor performance of two portable mobile mapping systems, (June), 103320I. https://doi.org/10.1117/12.2270761

Ørka, H. O., Bollandsås, O. M., Hansen, E. H., Næsset, E., & Gobakken, T. (2018). Effects of terrain slope and aspect on the error of ALS-based predictions of forest attributes. Forestry: An International Journal of Forest Research, 91(2), 225-237.

Othmani, A., Piboule, A., Krebs, M., & Stolz, C. (2011). Towards automated and operational forest inventories with T-Lidar. *SilviLaser*, 1–9. Retrieved from https://hal.archives-ouvertes.fr/hal-00646403/

Oveland, I., Hauglin, M., Gobakken, T., Næsset, E., & Maalen-Johansen, I. (2017). Automatic estimation of tree position and stem diameter using a moving terrestrial laser scanner. *Remote Sensing*, *9*(4), 1–15. https://doi.org/10.3390/rs9040350

Oveland, I., Hauglin, M., Giannetti, F., Kjørsvik, N. S., & Gobakken, T. (2018). Comparing three different ground based laser scanning methods for tree stem detection. *Remote Sensing*, *10*(4), 1–17. https://doi.org/10.3390/rs10040538

Palace, M. W., Sullivan, F. B., Ducey, M. J., Treuhaft, R. N., Herrick, C., Shimbo, J. Z., & Mota-E-Silva, J. (2015). Estimating forest structure in a tropical forest using field measurements, a synthetic model and discrete return lidar data. *Remote Sensing of Environment*, *161*, 1–11. https://doi.org/10.1016/j.rse.2015.01.020

Pierzchała, M., Giguère, P., & Astrup, R. (2018). Mapping forests using an unmanned ground vehicle with 3D LiDAR and graph-SLAM. *Computers and Electronics in Agriculture*, *145*(December 2017), 217–225. https://doi.org/10.1016/j.compag.2017.12.034

Pueschel, P., Newnham, G., Rock, G., Udelhoven, T., Werner, W., & Hill, J. (2013). The influence of scan mode and circle fitting on tree stem detection, stem diameter and volume extraction from terrestrial laser scans. *ISPRS Journal of Photogrammetry and Remote Sensing*, *77*, 44–56. https://doi.org/10.1016/j.isprsjprs.2012.12.001

Putman, E. B., Popescu, S. C., Eriksson, M., Zhou, T., Klockow, P., Vogel, J., & Moore, G. W. (2018). Detecting and quantifying standing dead tree structural loss with reconstructed tree models using voxelized terrestrial lidar data. *Remote Sensing of Environment*, *209*(August 2017), 52–65. https://doi.org/10.1016/j.rse.2018.02.028

Raumonen, P., Kaasalainen, M., Åkerblom, M., Kaasalainen, S., Kaartinen, H., Vastaranta, M., … Lewis, P. (2013). Fast Automatic Precision Tree Models from Terrestrial Laser Scanner Data. *Remote Sensing*, *5*(2), 491–520. https://doi.org/10.3390/rs5020491

Reitberger, J., Schnörr, C., Krzystek, P., & Stilla, U. (2009). 3D segmentation of single trees exploiting full waveform LIDAR data. *ISPRS Journal of Photogrammetry and Remote Sensing*, *64*(6), 561–574. https://doi.org/10.1016/j.isprsjprs.2009.04.002

Rodríguez-Veiga, P., Saatchi, S., Tansey, K., & Balzter, H. (2016). Magnitude, spatial distribution and uncertainty of forest biomass stocks in Mexico. *Remote Sensing of Environment*, *183*, 265–281. https://doi.org/10.1016/j.rse.2016.06.004

Rodríguez-Veiga, P., Wheeler, J., Louis, V., Tansey, K., & Balzter, H. (2017). Quantifying Forest Biomass Carbon Stocks From Space. *Current Forestry Reports*, *3*(1), 1–18. https://doi.org/10.1007/s40725-017-0052-5

Ryding, J., Williams, E., Smith, M. J., & Eichhorn, M. P. (2015). Assessing handheld mobile laser scanners for forest surveys. *Remote Sensing*, *7*(1), 1095–1111. https://doi.org/10.3390/rs70101095

Saatchi, S., Houghton, R. A., Dos Santos Alvalá, R. C., Soares, J. V., & Yu, Y. (2007). Distribution of aboveground live biomass in the Amazon basin. *Global Change Biology*, *13*(4), 816–837. https://doi.org/10.1111/j.1365-2486.2007.01323.x

Saatchi, S., Marlier, M., Chazdon, R. L., Clark, D. B., & Russell, A. E. (2011). Impact of spatial variability of tropical forest structure on radar estimation of aboveground biomass. *Remote Sensing of Environment*, *115*(11), 2836–2849. https://doi.org/10.1016/j.rse.2010.07.015

Saatchi, S., Mascaro, J., Xu, L., Keller, M., Yang, Y., Duffy, P., … Schimel, D. (2014). Seeing the forest beyond the trees. *Global Ecology and Biogeography*, n/a-n/a. https://doi.org/10.1111/geb.12256

Saatchi, S., Ulander, L., Williams, M., Quegan, S., Letoan, T., Shugart, H., & Chave, J. (2012). Forest biomass and the science of inventory from space. *Nature Climate Change*, *2*(12), 826–827. https://doi.org/10.1038/nclimate1759

Salach, A., Bakuła, K., Pilarska, M., Ostrowski, W., Górski, K., & Kurczyński, Z. (2018). Accuracy assessment of point clouds from LidaR and dense image matching acquired using the UAV platform for DTM creation. ISPRS International Journal of Geo-Information, 7(9), 342.

Sagang, L. B. T., Momo, S. T., Libalah, M. B., Rossi, V., Fonton, N., Mofack, G. I., … Barbier, N. (2018). Using volume-weighted average wood specific gravity of trees reduces bias in aboveground biomass predictions from forest volume data. *Forest Ecology and Management*, *424*(May), 519–528. https://doi.org/10.1016/j.foreco.2018.04.054

Santoro, M., Wegmüller, U., & Askne, J. (2018). Forest stem volume estimation using C-band interferometric SAR coherence data of the ERS-1 mission 3-days repeat-interval

phase. *Remote Sensing of Environment*, *216*(April), 684–696. https://doi.org/10.1016/j.rse.2018.07.032

Satellite Applications Catapult. (2016, November 16). COSMO-SkyMed Radar Science and Innovation Research (CORSAIR) Programme. Retrieved from https://sa.catapult.org.uk/our-opportunities/opportunities/corsair/

Shugart, H. H., Saatchi, S., & Hall, F. G. (2010). Importance of structure and its measurement in quantifying function of forest ecosystems. Journal of Geophysical Research: Biogeosciences, 115(G2).

Schimel, D., & Keller, M. (2015). Big questions, big science: meeting the challenges of global ecology. *Oecologia*, *177*(4), 925–934. https://doi.org/10.1007/s00442-015-3236-3

Shendryk, I., Broich, M., & Tulbure, M. G. (2018). Multi-sensor airborne and satellite data for upscaling tree number information in a structurally complex eucalypt forest. *International Journal of Applied Earth Observation and Geoinformation*, *73*(April), 397–406. https://doi.org/10.1016/j.jag.2018.07.011

Sheppard, J., Morhart, C., Hackenberg, J., & Spiecker, H. (2017). Terrestrial laser scanning as a tool for assessing tree growth. *IForest - Biogeosciences and Forestry*, *10*(1), 172–179. https://doi.org/10.3832/ifor2138-009

Sheridan, R., Popescu, S., Gatziolis, D., Morgan, C., & Ku, N.-W. (2014). Modeling Forest Aboveground Biomass and Volume Using Airborne LiDAR Metrics and Forest Inventory and Analysis Data in the Pacific Northwest. *Remote Sensing*, *7*(1), 229–255. https://doi.org/10.3390/rs70100229

Shimada, M., Itoh, T., Motooka, T., Watanabe, M., Shiraishi, T., Thapa, R., & Lucas, R. (2014). New global forest/non-forest maps from ALOS PALSAR data (2007-2010). *Remote Sensing of Environment*, *155*, 13–31. https://doi.org/10.1016/j.rse.2014.04.014

Shugart, H. H., Saatchi, S., & Hall, F. G. (2010). Importance of structure and its measurement in quantifying function of forest ecosystems. *Journal of Geophysical Research: Biogeosciences*, *115*(4), 1–16. https://doi.org/10.1029/2009JG000993

Sileshi, G. W. (2014). A critical review of forest biomass estimation models, common mistakes and corrective measures. *Forest Ecology and Management*, *329*, 237–254. https://doi.org/10.1016/j.foreco.2014.06.026

Simpson, J., Smith, T., & Wooster, M. (2017). Assessment of errors caused by forest vegetation structure in airborne LiDAR-derived DTMs. Remote Sensing, 9(11), 1101.

Sinha, S., Jeganathan, C., Sharma, L. K., & Nathawat, M. S. (2015). A review of radar remote sensing for biomass estimation. *International Journal of Environmental Science and Technology*, *12*(5), 1779–1792. https://doi.org/10.1007/s13762-015-0750-0

Small, D. (2011). Flattening gamma: Radiometric terrain correction for SAR imagery. *IEEE Transactions on Geoscience and Remote Sensing*, *49*(8), 3081–3093. https://doi.org/10.1109/TGRS.2011.2120616

Solberg, S., Næsset, E., Gobakken, T., & Bollandsås, O. M. (2014). Forest biomass change estimated from height change in interferometric SAR height models. *Carbon Balance and Management*, *9*(1), 1–12. https://doi.org/10.1186/s13021-014-0005-2

Staats, B. R., Diakité, A. A., Voûte, R. L., & Zlatanova, S. (2017). AUTOMATIC GENERATION of INDOOR NAVIGABLE SPACE USING A POINT CLOUD and ITS SCANNER TRAJECTORY. *ISPRS Annals of the Photogrammetry, Remote Sensing and Spatial Information Sciences*, *4*(2W4), 393–400. https://doi.org/10.5194/isprs-annals-IV-2-W4-393-2017

Stovall, A. E. L., & Shugart, H. H. (2018). Improved Biomass Calibration and Validation With Terrestrial LiDAR: Implications for Future LiDAR and SAR Missions. *IEEE Journal of Selected Topics in Applied Earth Observations and Remote Sensing*, 1–11. https://doi.org/10.1109/JSTARS.2018.2803110

Stovall, A. E. L., Shugart, H. H., Stovall, A. E. L., Anderson-Teixeira, K. J., & Anderson-Teixeira, K. J. (2018). Assessing terrestrial laser scanning for developing non-destructive biomass allometry. *Forest Ecology and Management*, *427*(May), 217–229. https://doi.org/10.1016/j.foreco.2018.06.004

Stovall, A. E. L., Vorster, A. G., Anderson, R. S., Evangelista, P. H., & Shugart, H. H. (2017). Non-destructive aboveground biomass estimation of coniferous trees using terrestrial LiDAR. *Remote Sensing of Environment*, *200*(July), 31–42. https://doi.org/10.1016/j.rse.2017.08.013

Takagi, K., Yone, Y., Takahashi, H., Sakai, R., Hojyo, H., Kamiura, T., … Oguma, H. (2015). Forest biomass and volume estimation using airborne LiDAR in a cool-temperate forest of northern Hokkaido, Japan. *Ecological Informatics*, *26*(P3), 54–60. https://doi.org/10.1016/j.ecoinf.2015.01.005

Tansey, K., Selmes, N., Anstee, A., Tate, N. J., & Denniss, A. (2009). Estimating tree and stand variables in a Corsican Pine woodland from terrestrial laser scanner data. *International Journal of Remote Sensing*, *30*(19), 5195–5209. https://doi.org/10.1080/01431160902882587

Trochta, J., Kruček, M., Vrška, T., & Kraâl, K. (2017). 3D Forest: An application for descriptions of three-dimensional forest structures using terrestrial LiDAR. *PLoS ONE*, *12*(5), 1–17. https://doi.org/10.1371/journal.pone.0176871

Tsui, O. W., Coops, N. C., Wulder, M. A., & Marshall, P. L. (2013). Integrating airborne LiDAR and space-borne radar via multivariate kriging to estimate above-ground biomass. *Remote Sensing of Environment*, *139*, 340–352. https://doi.org/10.1016/j.rse.2013.08.012

Tucci, G., Visintini, D., Bonora, V., & Parisi, E. (2018). Examination of Indoor Mobile Mapping Systems in a Diversified Internal/External Test Field. *Applied Sciences*, *8*(3), 401. https://doi.org/10.3390/app8030401

Ulaby, F. T., McDonald, K., Sarabandi, K., & Dobson, M. C. (1988). Michigan Microwave Canopy Scattering Models (MIMICS). *International Geoscience and Remote Sensing Symposium, "Remote Sensing: Moving Toward the 21st Century"*., *2*(August 1988), 1009–1009. https://doi.org/10.1109/IGARSS.1988.570506

Whittow J. (1984). The Penguin Dictionary of Physical Geography. Harmondsworth: Penguin.

Wilkes, P., Lau, A., Disney, M., Calders, K., Burt, A., Gonzalez de Tanago, J., … Herold, M. (2017). Data acquisition considerations for Terrestrial Laser Scanning of forest plots. *Remote Sensing of Environment*, *196*, 140–153. https://doi.org/10.1016/j.rse.2017.04.030

Wilkes, P., Disney, M., Vicari, M. B., Calders, K., & Burt, A. (2018). Estimating urban above ground biomass with multi-scale LiDAR. *Carbon Balance and Management*, *13*(1), 1–20. https://doi.org/10.1186/s13021-018-0098-0

Woodhouse, I. H., Mitchard, E. T. A., Brolly, M., Maniatis, D., & Ryan, C. M. (2012). Radar backscatter is not a "direct measure" of forest biomass. *Nature Climate Change*, *2*(8), 556–557. https://doi.org/10.1038/nclimate1601

Woodland Trust. (2014). Stratfield Brake Management Plan 2014-2019. Retrieved from http://www.woodlandtrust.org.uk/woodfile/777/management-plan.pdf

Woodland Trust. (2018). Stratfield Brake site leaflet. Retrieved from https://www.woodlandtrust.org.uk/mediafile/100047964/stratfield-brake-site-leaflet.pdf

Wu, B., Yu, B., Yue, W., Shu, S., Tan, W., Hu, C., … Liu, H. (2013). A voxel-based method for automated identification and morphological parameters estimation of individual street trees from mobile laser scanning data. *Remote Sensing*, *5*(2), 584–611. https://doi.org/10.3390/rs5020584

Wulder, M. A., White, J. C., Alvarez, F., Han, T., Rogan, J., & Hawkes, B. (2009). Characterizing boreal forest wildfire with multi-temporal Landsat and LIDAR data. *Remote Sensing of Environment*, *113*(7), 1540–1555. https://doi.org/10.1016/j.rse.2009.03.004

Wulder, M. A., Han, T., White, J. C., Sweda, T., & Tsuzuki, H. (2007). Integrating profiling LIDAR with Landsat data for regional boreal forest canopy attribute estimation and change characterization. *Remote Sensing of Environment*, *110*(1), 123–137. https://doi.org/10.1016/j.rse.2007.02.002

Yao, W., Krzystek, P., & Heurich, M. (2012). Tree species classification and estimation of stem volume and DBH based on single tree extraction by exploiting airborne full-waveform LiDAR data. *Remote Sensing of Environment*, *123*, 368–380. https://doi.org/10.1016/j.rse.2012.03.027

Zhang, W., Qi, J., Wan, P., Wang, H., Xie, D., Wang, X., & Yan, G. (2016). An easy-to-use airborne LiDAR data filtering method based on cloth simulation. *Remote Sensing*, *8*(6), 1–22. https://doi.org/10.3390/rs8060501

Appendix

Tree measurements (*3D Forest*) for the UVP study site:

Scan	Tree	Points	Height (m)	DBH (cm)			2D surface area (m^2)		
				RHT	LSR	LSR-RHT	Convex hull	Concave hull	Difference
Reference	A	840171	8.30	29.60	30.35	0.75	57.85	56.32	1.53
1 at 2 m	A	129010	8.91	32.20	31.81	-0.39	57.94	54.60	3.34
2 at 2 m	A	233248	8.89	32.00	30.33	-1.67	59.38	58.13	1.25
5 at 2 m	A	488386	8.01	31.00	31.93	0.93	55.02	52.62	2.40
10 at 2 m	A	1334703	9.49	31.20	30.15	-1.05	72.84	70.64	2.20
20 at 2 m	A	2126986	9.18	29.20	28.33	-0.87	76.68	73.68	3.00
1 at 5 m (normal)	A	144478	8.35	27.80	31.64	3.84	61.12	57.65	3.47
1 at 10 m	A	89276	8.85	28.80	28.85	0.05	54.39	50.86	3.53
1 at 5 m (fast)	A	105559	8.26	31.20	31.42	0.22	60.46	58.39	2.07
Mean		*610202*	*8.69*	*30.33*	*30.54*	*0.20*	*61.74*	*59.21*	*2.53*
Reference	B	1646048	8.77	82.60	72.50	-10.10	58.73	51.23	7.50
1 at 2 m	B	155764	8.57	28.60	81.88	53.28	54.68	43.62	11.06
2 at 2 m	B	271816	9.12	82.40	76.86	-5.54	50.29	39.32	10.97
5 at 2 m	B	670146	8.43	26.80	74.59	47.79	63.87	58.87	5.00
10 at 2 m	B	919492	9.12	27.00	72.32	45.32	59.83	45.89	13.94
20 at 2 m	B	1624273	9.12	108.60	77.45	-31.15	34.50	28.74	5.76
1 at 5 m (normal)	B	118159	8.15	94.40	78.18	-16.22	49.42	40.68	8.74
1 at 10 m	B	67500	7.83	76.80	75.63	-1.17	48.13	41.19	6.94
1 at 5 m (fast)	B	81495	8.26	87.40	76.26	-11.14	51.17	47.39	3.78
Mean		*617188*	*8.60*	*68.29*	*76.19*	*7.90*	*52.29*	*44.10*	*8.19*
Reference	C	1318854	10.78	43.40	42.93	-0.47	82.62	77.95	4.67
1 at 2 m	C	186575	10.66	42.80	43.53	0.73	84.24	79.59	4.65
2 at 2 m	C	268451	10.71	42.00	41.70	-0.30	84.98	79.56	5.42
5 at 2 m	C	453600	9.76	46.00	43.64	-2.36	82.57	73.13	9.43
10 at 2 m	C	1050861	11.27	40.80	43.10	2.30	82.60	79.51	3.09
20 at 2 m	C	1594414	11.31	40.00	40.08	0.08	82.10	79.33	2.77
1 at 5 m (normal)	C	208611	10.29	45.40	43.50	-1.90	88.13	79.70	8.43
1 at 10 m	C	95552	10.27	40.00	40.04	0.04	72.54	64.20	8.34
1 at 5 m (fast)	C	129352	9.83	49.20	46.50	-2.70	97.13	85.05	12.08
Mean		*589586*	*10.54*	*43.29*	*42.78*	*-0.51*	*84.10*	*77.56*	*6.54*
Reference	D	1537180	9.51	35.20	35.42	0.22	58.65	52.95	5.70
1 at 2 m	D	178616	9.77	35.00	35.30	0.30	63.65	52.26	11.39
2 at 2 m	D	319344	10.05	31.80	33.70	1.90	54.09	47.83	6.26
5 at 2 m	D	704412	9.76	35.20	35.73	0.53	52.59	48.67	3.91
10 at 2 m	D	1389031	10.47	31.60	34.13	2.53	56.14	49.85	6.28
20 at 2 m	D	2430086	10.44	25.60	29.07	3.47	52.26	48.00	4.26
1 at 5 m (normal)	D	141933	9.83	37.20	35.91	-1.29	46.63	42.32	4.31
1 at 10 m	D	50699	10.03	35.20	31.87	-3.33	31.46	27.83	3.63
1 at 5 m (fast)	D	77345	10.21	31.80	33.75	1.95	41.10	39.00	2.10
Mean		*758738*	*10.01*	*33.18*	*33.88*	*0.70*	*50.73*	*45.41*	*5.32*

Derived 2D crown surface areas (UEP-BW)
All surface areas are reported in m^2

Convex hull approach			**Concave hull approach**		
TLS	HMLS1	HMLS2	TLS	HMLS1	HMLS2
83.257	46.921	87.051	76.229	38.513	73.840
65.655	15.143	39.286	61.448	10.771	34.717
96.687	17.726	52.534	78.879	15.834	48.534
55.318	12.995	17.298	52.220	8.199	16.702
3.254	13.762	2.835	3.155	13.406	2.845
110.630	3.822	46.658	99.266	4.243	39.867
46.466	14.281	98.326	42.371	11.229	91.465
1.887	0.734	1.422	1.915	0.745	1.462
1.511	0.865	0.690	1.405	0.874	0.717
107.652	7.101	107.603	93.446	5.645	93.504
2.681	1.071	2.046	1.811	1.094	2.055
54.632	10.982	55.352	52.990	9.511	48.384
26.712	5.257	28.351	24.932	3.837	27.105
2.066	2.210	2.455	2.130	2.245	2.495
56.133	25.185	88.030	51.989	20.557	80.371
20.764	12.982	42.253	19.319	11.359	37.125
7.566	6.541	13.900	7.016	6.202	13.151
55.943	4.128	4.566	50.375	3.172	4.292
1.097	1.249	1.930	1.123	1.294	1.964
1.074	2.124	3.209	1.096	2.106	3.179
40.049	***10.254***	***34.790***	***36.156***	***8.542***	***31.189***

Derived 2D crown surface areas (UTF-ROK N&S)
All surface areas are reported in m^2

Convex hull approach		**Concave hull approach**	
TLS	HMLS2	TLS	HMLS2
55.902	28.884	52.712	26.408
34.790	63.614	34.167	57.062
82.633	31.656	75.451	29.114
33.292	14.801	30.519	14.223
30.036	87.243	28.890	66.481
56.133	46.600	52.111	41.950
23.815	59.799	22.703	55.580
20.151	39.214	19.182	32.883
65.544	11.288	60.377	8.345
43.368	18.649	42.201	15.423
45.977	25.487	42.456	23.537
28.921	33.120	27.540	29.144
66.289	39.422	63.620	34.858
65.629	5.501	60.188	4.559
39.408	56.971	36.908	44.054
38.463	15.948	36.281	15.814
53.697	17.118	52.244	12.597
50.735	20.355	49.850	19.838
38.645	16.477	37.311	15.834
35.003	8.640	34.443	8.275
35.683	32.866	33.484	30.830
27.026	13.714	26.247	11.505
39.71	46.639	38.451	34.031
28.318	17.155	26.228	16.007
38.131	2.258	34.811	2.278
43.092	**30.017**	**40.735**	**26.025**